Ollscoil na hÉireann, Corcaigh

National University of Ireland, Cork

Analysing Curved Optical Waveguides Using the Finite Difference Beam Propagation Method

Thesis presented by

Tommy Murphy, BSc

for the degree of

Master of Science

University College Cork

School of Science

Department of Physics

Head of Department: Prof. John McInerney

Supervisor: Prof. Frank Peters

September 2020

Research supported by SFI

I, Tommy Murphy, certify that this thesis is my own work and has not been submitted for another degree at University College Cork or elsewhere.

Tommy Murphy

Contents

Abstract

Photonic integrated circuits (PICs) integrate optical components on a single semiconductor chip. As time has progressed, advances have been made allowing the components of these PICs to become smaller and smaller. It is now possible to place many of these components on a single PIC. As these components can contain, or be connected by, bending waveguides, it is desirable to make these waveguide bends with as small a radius of curvature as possible to allow many components to fit on the single PIC. Unfortunately, as the radius of curvature decreases, the power loss through the bend increases due to the waveguide's fundamental mode shifting towards the outside of the bend, causing large loss from the transition between the straight and curved waveguides. The power from the shifted mode also leaks as the fields propagate through the bend.

Therefore, the aim of this thesis was to reduce the loss caused by these bends at small radii of curvature, allowing the bends to take up less space on a PIC. This involved designing the waveguide bends to have curvature profiles other than the conventional circular waveguide bend. The propagating fields through the bends were then analysed by numerical simulations using a program utilising the 3D finite difference beam propagation method, which was created and optimised over the course of the research, to investigate if the different curvature profiles could reduce the loss caused by bends in ridge waveguides. It was found that much lower loss could be achieved for curved deep-etched ridge waveguides with small radii of curvature by designing the bend to have a section where the curvature of the waveguide linearly changes.

Acknowledgements

First and foremost, I would like to give my sincerest thanks to my supervisor Prof. Frank Peters for giving me this masters opportunity, as well as for all the help and support he has provided me with over the last year. Thank you, Frank, for always finding time to discuss and offer advice about any aspect of my work, no matter how busy you were with your own work.

I would also like to thank Frank's former PhD student Dr. Kevin Shortiss, who worked with me in the office for the majority of this past year. You were good company and very helpful, providing me with many thoughts and suggestions about my masters project.

I would like to thank all the members of the Integrated Photonics Group. You made me feel like part of the team and it was always very interesting to learn what everyone was working on during the weekly meetings. I would also like to thank you for your ideas and advice regarding the analysis of PIC components.

I would also like to thank my family and friends for their support over the past year.

Finally, I would like to thank Science Foundation Ireland for providing funding for this project.

List of Acronyms

PIC ..... Photonic Integrated Circuit
IPG ..... Integrated Photonics Group
FFT ..... Fast Fourier Transform
FD ..... Finite Difference
FDM ..... Finite Difference Method
FEM..... Finite Element Method
BPM ..... Beam Propagation Method
FFT-BPM..... Fast Fourier Transform Beam Propagation Method
FD-BPM ..... Finite Difference Beam Propagation Method
SV-FD-BPM.... Semi-Vectorial Finite Difference Beam Propagation Method
TD-BPM..... Time Domain Beam Propagation Method
TE..... Transverse Electric
TM ..... Transverse Magnetic
SVEA ..... Slowly Varying Envelope Approximation
TBC ..... Transparent Boundary Condition
PML..... Perfectly Matched Layers
OIE ..... Overlap Integral Error
MME ..... Mode Mismatch Error
IQE ..... International Quantum Epitaxy

1 Introduction

This chapter will give a brief overview of what the motivation and aims of the project were, as well as give an introductory explanation of photonic integrated circuits, optical waveguides, and the methods used to analyse optical waveguides.

1.1 Motivation and Aims

Photonic integrated circuits (PICs) allow the integration of multiple optical devices on a single semiconductor chip. The goal of the past number of years has been to reduce the size of the optical devices, and thus the PICs, to improve efficiency and reduce costs while simultaneously improving the performance and capabilities of the PICs. Many of the photonic devices contain, or are connected by, curved optical waveguides. Therefore, as the sizes of optical devices decrease, allowing more of them to fit on a single PIC, bends of lower radii of curvature are needed to allow the devices to take up as little footprint as possible. However, as the radii of curvature of these curved optical waveguides decrease, performance worsens. The reason for this is the behaviour of the confined modes of the curved waveguide. When a waveguide transitions from a straight region to a bend, the modes of that waveguide shift towards the outside of the bend. This shift of the modes causes large amounts of loss at the straight, curved waveguide transition due to the mismatch of the fundamental modes. The mode shift also causes the tails of the fundamental mode on the outside of bend to become radiative, causing power to "leak" from the waveguide as the electromagnetic fields propagate around the bend. Unfortunately, as the radius of curvature of the bend decreases, the curvature increases, causing the modes to shift further to the outside of the bend, increasing the loss at the waveguide transition as well as the propagating loss around the bend. For the optical devices, and therefore the PICs, to decrease in size without causing a decrease in performance, new methods to reduce the loss of these smaller radii bends must be developed.

The aim of this thesis is therefore to improve the performance of these lower radii bends, allowing them to take up less space on a PIC. The analysis will focus on the improvement of the ridge waveguide bends fabricated by the Integrated Photonics Group (IPG) in the Tyndall National Institute.

Many advancements have already been made to improve the performance of optical waveguide bends. One such advancement is to make a deep etch in the waveguide [1]. This introduces a large refractive index contrast, causing the fundamental waveguide mode to become more laterally confined and causing less power to leak from the waveguide around the bend. Other methods developed to improve performance include widening the waveguide to provide higher mode confinement, offsetting the curved waveguide from the straight waveguide to improve overlap of the fundamental modes and therefore reduce transition loss [2], and bend matching where the bend is designed to end on an integer number of beat lengths for curved waveguides where the curvature causes multiple modes to be excited in the bend [3]. Another improvement in the performance of the bends was the introduction of a linear change in curvature as opposed to the standard constant

curvature (circular) bend [51]. The linear change in curvature greatly improved the transition loss at the straight-curved waveguide boundary as it allowed the fundamental mode to gradually move towards the outside of the bend.

This thesis will focus on using the linear change in curvature to improve the performance of the curved shallow and deep-etched ridge waveguide bends fabricated in Tyndall, by making the curvature profile of the bend partly or fully consist of a linear change in curvature. The aim is to make the bend's effective radius as small as possible without causing significant losses.

1.2 Optical Waveguides

Integrated photonic devices are based on light propagation along optical waveguides. An optical waveguide is a physical structure that guides electromagnetic waves in the optical spectrum. The origins of optical waveguides trace back to the 19th century when scientists such as Jean Colladon and John Tyndall demonstrated the guiding of light by a stream of water [4]. The operating phenomenon, total internal reflection, had previously been studied by Johannes Kepler in 1611 and mathematically defined by Snellius in 1621. Despite these observations and developments, the potential applications of optical waveguides beyond imaging were not realised until the mid-20th century when the development of the laser provided a coherent and collimated light source. This led to the advent of optical fibres – optical waveguide consisting of strands of glass that guide light and transmit information by modulating the electromagnetic carrier waves. Today, optical waveguides are widely used as the transmission medium in optical communications systems and as components of photonic integrated circuits.

Optical waveguides consist of a core region surrounded by a cladding or substrate region. The core region consists of a material with a higher refractive index material than that of the cladding. This causes light to be confined to the core by the principle of total internal reflection. This principle states that if light is incident on a refractive index boundary and the light is travelling from a region of higher refractive index, the light will be totally internally reflected if the light is incident at an angle to the normal of the boundary greater than the following critical angle [5]:

$$\theta_c = \sin^{-1}\left(\frac{n_2}{n_1}\right) \tag{1.1}$$

n_1 refers to the refractive index of the material the light is travelling from while n_2 refers to the refractive index of the material the light is travelling to. Figure 1.1 shows a diagram of a light ray traveling through an optical waveguide where the light ray is incident on the core cladding boundary at an angle that is greater than θ_c and thus is totally internally reflected.

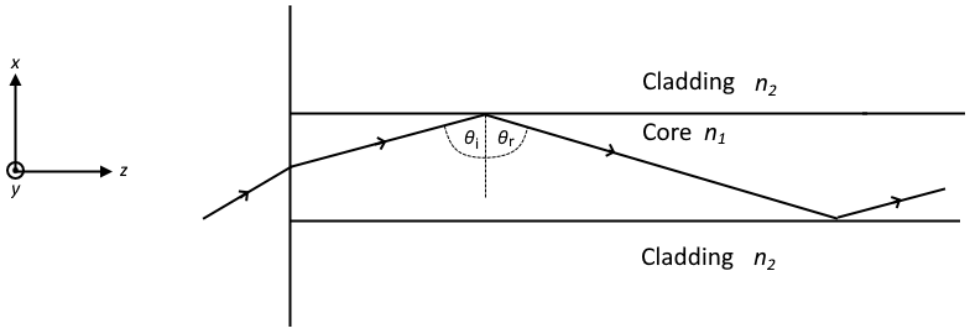

Figure 1.1: Light ray undergoing total internal reflection as it propagates through an optical waveguide.

The above shows how light is confined in the waveguide by total internal reflection as long as the light is incident at angles greater than the critical angle. However, not all light rays at arbitrary incident angles greater than the critical angle are able to propagate in the waveguide. Instead, light can only propagate in specific modes where each mode is associated with a discrete angle of propagation, as determined by electromagnetic wave analysis.

The formation of the modes can be well understood using the propagating ray through a waveguide [6]. Consider the two rays propagating in the $\hat{\boldsymbol{z}}$ direction at an inclination angle ϕ through the simple slab waveguide in Figure 1.2. Let the two rays belong to the same plane wave and let points *P* and *R* be on the same phase front. The light ray propagating from *P* to *Q* does not undergo any reflections, while the light ray propagating from *R* to *S* experiences two reflections. As points *Q* and *S* are on the same phase front, the product of the wavenumber and the optical path lengths *PQ* and *RS* should be equal or differ by an integer number of 2π to allow the phases of the two rays to match. However, when a ray experiences a reflection, it undergoes a phase shift Φ, known as the Goos-Hänchen shift [7]. Therefore, for the two rays to phase match, the following condition must hold:

$$(kn_1RS + 2\Phi) - kn_1PQ = 2m\pi \tag{1.2}$$

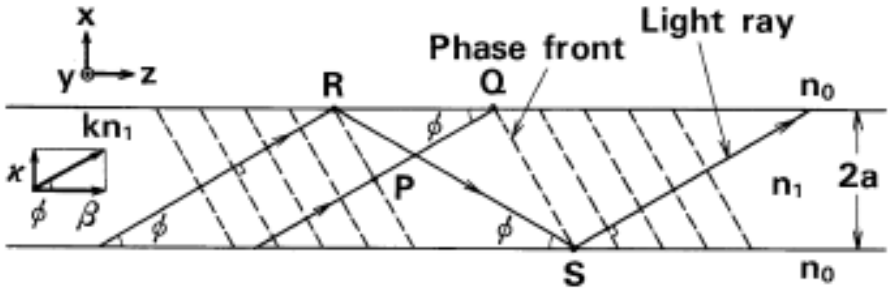

Figure 1.2: Light rays and their phase fronts [8].

The geometry of Figure 1.2 allows *RS* and *PQ* to be written in terms of the inclination angle ϕ and the waveguide width $2a$, while the phase shift Φ can be written in terms of ϕ using the reflection coefficient from electromagnetic wave theory [8]. This results in equation (1.2) giving rise to a transcendental equation for the solution of angle ϕ for different values

of m. The angles ϕ that satisfy the equation, and thus the phase matching condition, lead to optical field distributions that are known as modes, which arise due to the interference of light waves. Each mode has a corresponding propagation constant β, which is given by $\beta = kn_1 \cos\phi$, and the fundamental mode is the mode with the minimum angle ϕ. Figure 1.3 show the formations of the fundamental mode and the first higher order mode from the interference of the light rays in the slab waveguide. A waveguide can only support a finite number of modes as ϕ increases as the mode order increases. Eventually ϕ will reach a value where the incidence angle will become less than the critical angle at the waveguide boundary and total internal reflection no longer occurs.

The supported modes of a waveguide can also be understood using Maxwell's equations and electromagnetic boundary conditions [9].

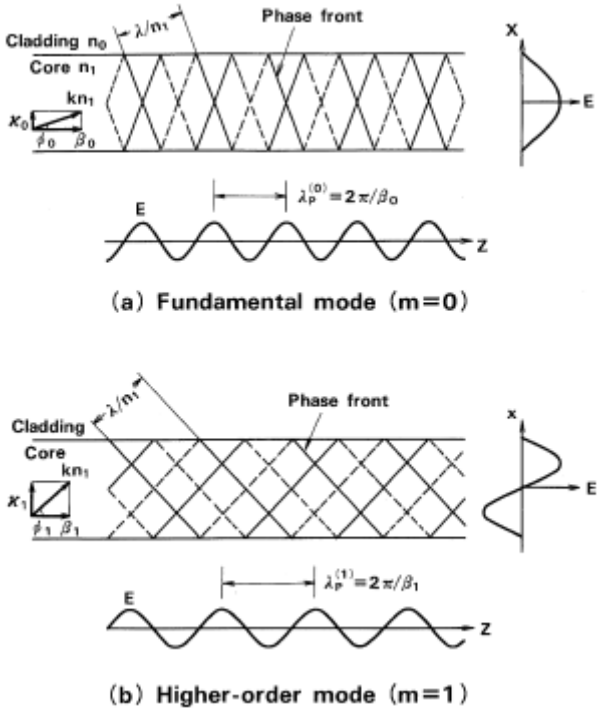

Figure 1.3: Formation of optical waveguide modes [8].

The shape of the supported modes depends on various factors including the geometry of the waveguide, the material properties, the wavelength of the light, and the direction in which the electromagnetic fields are polarised. Waveguides exist in a number of forms, some of which are shown in Figure 1.4. The simplest of these are the slab waveguide, where a layer of higher refractive index material is sandwiched between two layers of lower refractive index material giving optical confinement in one dimension, and the rectangular waveguide, where the higher index material is surrounded on all four sides by lower index material giving optical confinement in two dimensions. Rectangular waveguides and 2D channel waveguides are the most commonly used non-planar waveguides for PIC device applications [10]. Such channel waveguides include the ridge waveguide, the rib waveguide, the strip loaded waveguide, and the arrow waveguide, all of which can be seen in Figure 1.4. Ridge waveguides are advantageous as they allow for narrow waveguides with small bend

radii and therefore provide realisation of ultra-dense photonic circuits. Rib waveguides provide less horizontal confinement and therefore require larger bend radii. Meanwhile, strip-loaded waveguides provide horizontal confinement by having a narrower layer of lower refractive index material above the core which has the advantage of not needing to etch down into the core material in comparison with the rib waveguide [4]. One of the most well-known waveguide types is the circular waveguide which is utilised in optical fibre communications. The cores of these waveguides contain very thin strands of pure glass which are then surrounded by materials of lower refractive index. The refractive index can be constant throughout each material, making it a step index optical fibre, or can vary gradually, making it a graded index optical fibre. The fibre can also be designed to support one or multiple modes by varying the radius of the waveguide core. The different types of optical fibre are displayed in Figure 1.5. However, the analysis in this thesis will be on PIC components and will primarily focus on ridge and rib waveguides utilised in PICs.

The materials utilised in PICs depend on the functions to be integrated. The most commonly used materials are semiconductor materials such as Gallium Arsenide (GaAs) and Indium Phosphide (InP) which allow the operation of semiconductor lasers when optically or electrically pumped. The use of these materials therefore allows the integration of various active and passive components on the same chip [11]. As the different materials chosen have different refractive indices, and thus different refractive index contrasts between the guiding and cladding materials, the confinement and therefore shape of the supported modes are heavily influenced by the materials chosen. High contrast III – V semiconductor material systems are analysed in this thesis, which utilise materials such as InP, GaAs, and AlGaInAs. Lower refractive index contrast material systems are also used in PICs such as silica (SiO2) which is commonly used when coupling light with optical fibres. The refractive index contrast between the core and cladding is usually defined using the Δ parameter where $\Delta = (n_{core}^2 - {n^2}_{cladding})/2n_{core}^2$. For silica systems, this Δ parameter can be as low as 0.008. Meanwhile, for semiconductor materials such as InP and Si, this parameter can be as large as 0.45 at air boundaries. The Δ value is crucial to determining the number of supported modes of a waveguide, with a higher contrast allowing more modes [12]. The loss experienced during a waveguide bend also depends heavily on the index contrast, which will be seen later in the thesis. There are a wide array of other material systems used in PICs, such as SiON, $LiNbO_3$, and BCB, each used for different purposes. For example, SiON is an attractive material as its refractive index can be tuned over a wide range (from 1.45 (SiO_2) to 2.01 (Si_3N_4)), allowing it to be used in both low and high index contrast systems [13]. $LiNbO_3$ is regularly used in diffused waveguide systems where a high index confinement region is created by diffusion of dopants such as Titanium [4]. Due to the diffusion process, the refractive index varies gradually through the diffused region, with the change in refractive index proportional to the concentration of the impurities. The different material systems allow applications to be realised for various purposes across areas such as communications, optical sensing, and biophotonics.

The refractive index contrast of the materials also affects the suitability of the numerical methods used to analyse them, as the contrast in different material systems can vary by orders of magnitude. For the high contrast III – V semiconductor material systems analysed

in this thesis, the finite difference method (FDM) is utilised as it is one of the most effective methods for dealing with these material boundaries. In particular, a semi-vectorial FDM mode solver and a semi-vectorial finite difference beam propagation method (SV-FD-BPM) are used as the semi-vectorial method allows accurate analysis of the different modes (quasi-TE and quasi-TM) that become supported due to the sharp refractive index contrast. While the finite difference method should provide accurate analysis of the supported modes of most of the material systems and waveguide geometries mentioned, be they high index or low index contrast systems, different methods are more applicable to certain waveguide geometries. For example, the finite element method should allow easier and more accurate analysis of waveguides of mixed geometries such as ellipses and polygons. For waveguides with sharp refractive index changes in the propagation direction, a fully vectorial time domain finite difference method would be a more accurate method to deal with the reflection and scattering that occurs at these boundaries. This method would also allow accurate analysis of waveguide structures that have strong coupling between the quasi-TE and quasi-TM modes, such as polarisation couplers, the effect of which is ignored in semi-vectorial analysis [26].

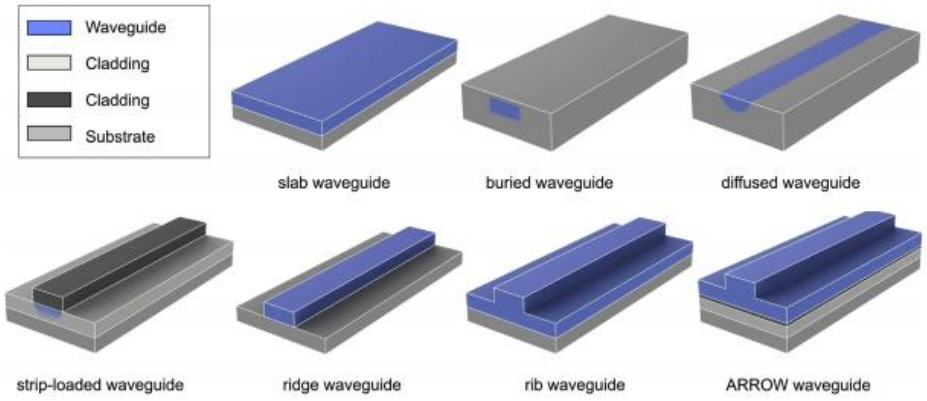

Figure 1.4: Examples of optical waveguides [14].

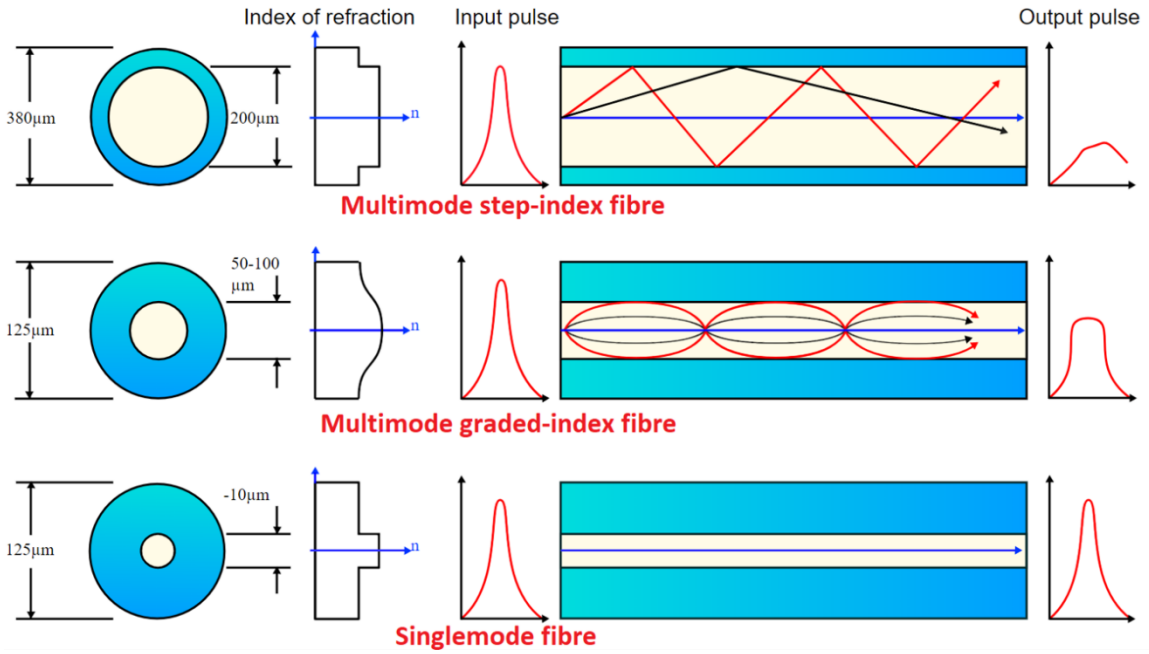

Figure 1.5: Optical fibres [15].

The main purpose of curved optical waveguides is to interconnect optical waveguide devices. Figure 1.6 gives an example of curved waveguides connecting two straight waveguides that are either at an angle to each other or offset from each other. The design of the waveguide bend must be carefully tailored to minimise the mode mismatch and propagation loss. In addition to connecting waveguides, curved optical waveguides are also used in the function of certain optical devices. For example, an optical ring resonator [16] consists of a set of waveguides where at least one is a closed loop or ring that is connected to an input waveguide and an output waveguide, examples of which are given by Figure 1.7. The device operates through optical coupling and constructive interference. The input and output waveguides are at a distance from the ring whereby the coupling length allows the light to transfer between the waveguides and the ring. The intensity of the light in the ring builds up over multiple round trips as the optical path length of the ring is designed to allow the light to interfere constructively inside the ring resonator. As different light wavelengths interfere constructively and destructively at different points along the ring, only certain wavelengths of light will allow the light to build up over multiple round trips and the resonator therefore functions as a wavelength filter.

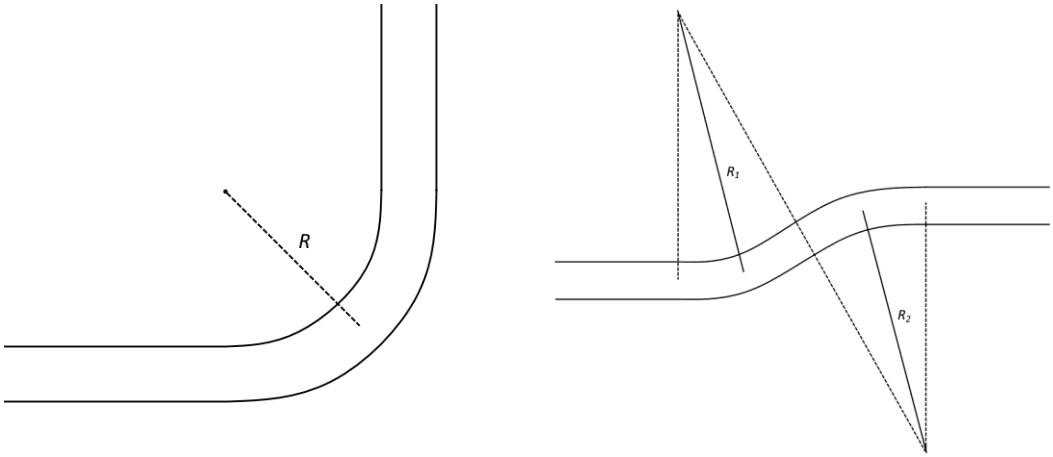

(a) 90° bend connecting two waveguides. (b) S-bend connecting two offset waveguides.

Figure 1.6: Examples of waveguide bends.

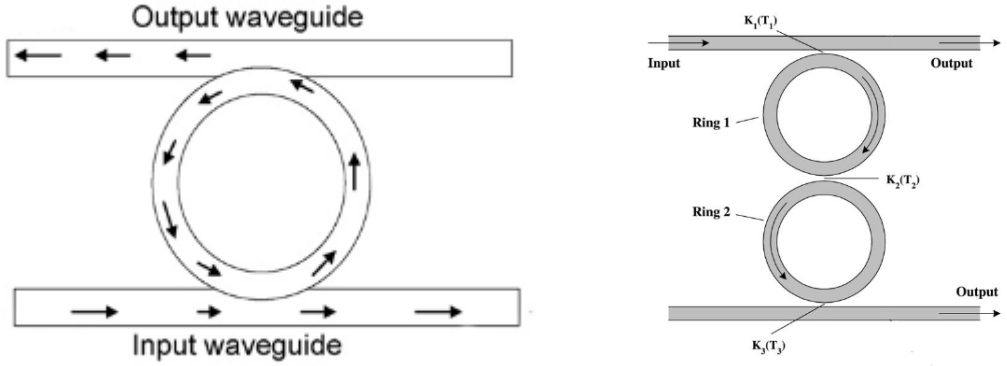

(a) Single ring resonator [17]. (b) Double ring resonator [18].

Figure 1.7: Ring resonators.

1.3 Methods of Analysing Optical Waveguides

In order to create and improve optical waveguide devices, methods of analysing the behaviour of light in optical waveguide structures have been developed. These consist of analytical methods for exact analysis of simpler optical waveguides and numerical methods for accurate analysis of the more complicated structures. The analytical methods focus on finding the effective refractive indices and mode profiles of the supported modes of an optical waveguide that is assumed to be invariant in the propagation direction. While the analytical methods provide an exact 1D solution to the slab waveguide, assumptions must be made to allow analysis of simple 2D structures, the rectangular waveguide for example, such as assuming the field to not exist in certain regions as well as neglecting derivatives of the relative permittivity. Meanwhile, the numerical methods do not need to make these assumptions and thus allow the 2D effective indices and mode profiles to be calculated more accurately. The numerical methods also allow analysis of more complicated structures and allow analysis of waveguide structures that vary in the propagation direction.

1.3.1 Analytical Methods

While analytical methods become less applicable as a waveguide becomes more complicated, they are easier to use and understand than the numerical methods. The simplest analytical method is that for analysing the wave equation for the 1D three-layer slab optical waveguide. The slab optical waveguide, which is shown in Figure 1.8, is a 1D structure consisting of three refractive index layers which extend infinitely in one transverse direction, the $\hat{\boldsymbol{y}}$ direction in Figure 1.8. The refractive index of the middle layer is higher than the refractive indices of the surrounding layers to support light confinement and the formation of optical waveguide modes.

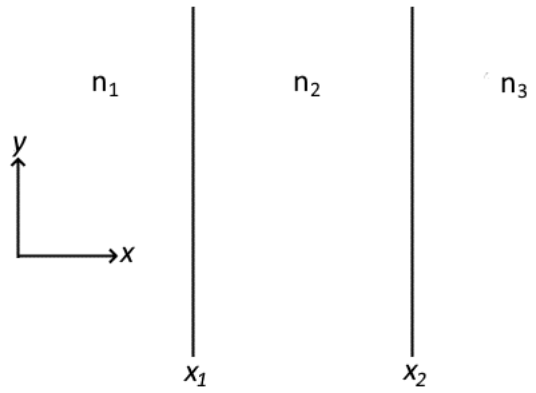

Figure 1.8: Three-layer slab waveguide.

The electromagnetic wave equation is a second order partial differential equation that describes the propagation of electromagnetic waves through a medium. The 1D Helmholtz wave equation for the electric field is given by equation (1.3) and is derived from Maxwell's equations by ignoring the derivative of the refractive index with respect to the transverse $\hat{\boldsymbol{x}}$ direction and, since the structure is uniform in the $\hat{\boldsymbol{y}}$ direction, letting the derivatives with respect to y equal 0. The analysis considers the time harmonic solution and therefore the field is assumed to oscillate at a single angular frequency, ω. The derivation of the wave equations from Maxwell's equations will be described in the next chapter.

$$\frac{d^2\mathbf{E}}{dx^2} + k_0^2\left(\varepsilon_r - n_{eff}^2\right)\mathbf{E} = 0 \tag{1.3}$$

In the above equation, n_{eff} is the effective refractive index of the mode and results from letting the derivatives with z, the propagation direction, equal $i\beta$, where β is the propagation constant and equal to $k_0 n_{eff}$, since the structure was assumed to be uniform in the propagation direction and the field was therefore assumed to take the form $E = E_0 \exp(i\beta z)$.

Two modes are found to propagate in the three-layer waveguide: the TE mode where the electric field is polarised in the $\hat{\boldsymbol{y}}$ direction and the magnetic field is polarised in the $\hat{\boldsymbol{x}}$ and $\hat{\boldsymbol{z}}$ directions, and the TM mode where the magnetic field is polarised in the $\hat{\boldsymbol{y}}$ direction and the electric field is polarised in the $\hat{\boldsymbol{x}}$ and $\hat{\boldsymbol{z}}$ directions. The polarisation of the field is important as the different polarisations cause different boundary conditions at the refractive index boundaries along the $\hat{\boldsymbol{x}}$ direction, as only the tangential components of the electric and magnetic fields are continuous at the boundary.

Consider the TE mode where the electric field is polarised in the $\hat{\boldsymbol{y}}$ direction. As the field should exponentially decrease in the first and third layers, the following ansatz is found to satisfy the wave equations if the middle layer begins and ends at $x_1 = 0$ and $x_2 = W$ [9]:

$$E_y(x) = A_1 \exp(\alpha_1 x), \qquad \alpha_1 = k_0\sqrt{n_{eff}^2 - n_1^2} \tag{1.4}$$

$$E_y(x) = A_2 \cos(\alpha_2 x + \gamma_1), \qquad \alpha_2 = k_0\sqrt{n_2^2 - n_{eff}^2} \tag{1.5}$$

$$E_y(x) = A_3 \exp\left(-\alpha_3(x - W)\right), \qquad \alpha_3 = k_0\sqrt{n_{eff}^2 - n_3^2} \tag{1.6}$$

From Maxwell's equations, the fields E_x, E_z and H_y are all found to equal 0 while the field H_x is equal to $-(\beta/\omega\mu_0)E_y$ and H_z is equal to $(-i/\omega\mu_0)\,\partial E_y/\partial x$. From the boundary conditions, E_y and H_z must be continuous at the refractive index boundaries x_1 and x_2. Applying the boundary conditions and manipulating the algebraic equations eventually results in the following equation, allowing the effective refractive indices to be solved by means of a numerical root finding method such as the bisection or secant method.

$$\alpha_2 W = -\tan^{-1}\left(\frac{\alpha_2}{\alpha_1}\right) - \tan^{-1}\left(\frac{\alpha_2}{\alpha_3}\right) + (q+1)\pi, \qquad q = 0, 1, 2 \ldots \tag{1.7}$$

The above method applies to one dimensional waveguides, i.e. the waveguide is assumed to extend infinitely in one transverse direction. As these waveguides do not exist in practice, methods had to be developed to analyse two dimensional waveguides, i.e. waveguides where refractive index boundaries exist in two transverse directions.

The simplest analytical method used to analyse the 2D waveguides is the effective index method [19]. The effective index method considers the 2D scalar wave equation given by equation (1.8), where derivatives of the refractive index with respect to the transverse directions are ignored.

$$\frac{\partial^2\phi(x,y)}{\partial x^2}+\frac{\partial^2\phi(x,y)}{\partial y^2}+k_0^2\left(\varepsilon_r-n_{eff}^2\right)\phi=0 \tag{1.8}$$

For the effective index method, it is assumed that separation of variables can be used to separate the field $\phi(x,y)$ into two functions $f(x)\cdot g(y)$. Substituting the two functions into the wave equation results in the following:

$$\frac{1}{f(x)}\frac{d^2f(x)}{dx^2}+\frac{1}{g(y)}\frac{d^2g(y)}{dy^2}+k_0^2\left(\varepsilon_r-n_{eff}^2\right)=0 \tag{1.9}$$

If the second and third terms are allowed to equal $k_0^2N^2(x)$, then the first and fourth terms will equal $-k_0^2N^2(x)$. This results in the following two independent equations:

$$\frac{d^2g(y)}{dy^2}+k_0^2\left(\varepsilon_r-N^2(x)\right)g(y)=0 \tag{1.10}$$

$$\frac{d^2f(x)}{dx^2}+k_0^2\left(N^2(x)-n_{eff}^2\right)f(x)=0 \tag{1.11}$$

The purpose of the effective index method is to therefore reduce the 2D waveguide to a number of 1D waveguides. Equation (1.10) is applied to each waveguide region along the y axis to find a number of $N(x)$ values and the $N(x)$ values are then used along the x axis for equation (1.11) to find the approximate effective refractive indices using, for example, the method for the three-layer slab waveguide. Figure 1.9 shows the application of the effective index method to a ridge waveguide.

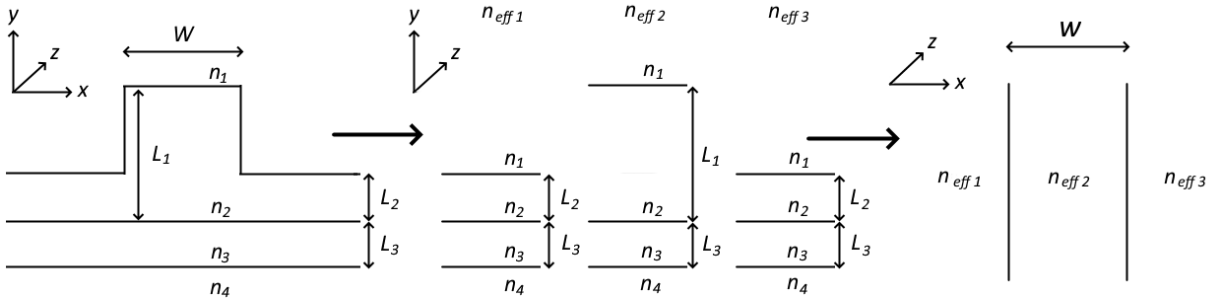

Figure 1.9: The effective index method [19].

While the effective index method is simple to implement, if the assumption that separation of variables can be applied to $\phi(x,y)$ is inaccurate, due to the waveguide structure or other reason, the accuracy of the method can become very poor.

The other major analytical method used to analyse 2D waveguides is the Marcatili method [20]. The Marcatili method focuses on rectangular waveguides consisting of a rectangular core, surrounded on all sides by the cladding. The field is only assumed to exist in the core and the rectangular cladding regions connected to the four sides of the rectangular core, i.e. the regions labelled with a refractive index in Figure 1.10. This simplifies the analysis and allows the fields to take a 2D ansatz in the same fashion as was taken for the three-layer slab waveguide. As the field is assumed to not exist in the regions outside the corners of the waveguide core, the Marcatili method is best used for rectangular waveguides where the field is strongly confined to the core region.

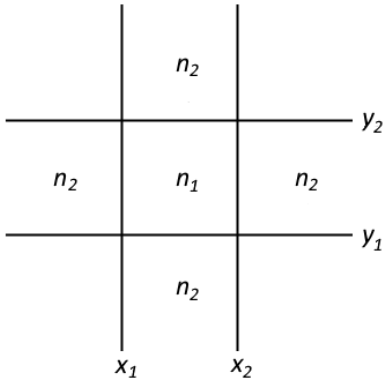

Figure 1.10: The Marcatili method.

1.3.2 Numerical Methods

Due to the inaccuracies of the analytical methods for analysing 2D waveguides, because of both the assumptions made and their inability to deal with propagating beams through optical waveguides with refractive index profiles that vary along the propagation direction, numerical methods have been developed to more accurately analyse the electromagnetic fields propagating through optical waveguides.

1.3.2.1 Calculating Modes of Propagation Direction Invariant Waveguides

For optical waveguides where the refractive index profile does not vary in the propagation direction, the waveguides can be analysed by considering the cross-section of the waveguide structure. As was done for the analytical methods, derivatives with respect to the propagation direction in the wave equation are let equal $i\beta$, where β is the mode propagation constant. There are then a number of numerical methods that can be used to analyse the wave equation to find the supported propagation constants and corresponding mode profiles. These include the finite element method (FEM) and the finite difference method (FDM).

The FEM solves the wave equation by subdividing the computational area into a number of smaller, simpler parts known as finite elements [21]. This method then approximates the solution of the wave equation in each element by adopting a simple form of function, for example, a polynomial. All of the element contributions to the system are assembled to form the functional. The functional consists of the field values at all the nodes and the boundary conditions at the peripheral nodes. The functional results in a system of linear equations, where the solutions of the equations give the field values to be obtained. The computational area can be discretised into a number of arbitrarily shaped elements, making this method particularly suited to solving modes of waveguides with geometries other than those made by connecting orthogonal sides, such as elliptical fibres and polygonal waveguides. Errors in the solutions can be easily reduced by using smaller sized elements.

Another numerical method used to analyse the supported modes of complicated waveguide structures, and the one utilised in this thesis, is the finite difference method. The FDM involves discretising the computational area into a number of points and then calculating the derivatives in the wave equation by the method of finite difference [22]. This leads to an eigenvalue matrix equation of the form $A\phi = \lambda\phi$, where the calculated eigenvalues result

in the effective refractive indices of the supported modes and the corresponding eigenvectors result in the mode's field distribution. The matrix is tridiagonal for 1D waveguides, which can be solved in a way that is numerically efficient. Although the matrix is no longer tridiagonal for 2D analysis, it is however sparse and structurally symmetric, allowing it to be solved relatively quickly with modern linear algebra software and computer processors. The application of the finite difference method to the wave equations is described in the next chapter. Like the FEM, the FDM also allows the analysis of complicated waveguide structures (as it can be implemented in various coordinate systems), provided enough computational points are used to minimise errors. The FDM is also particularly suited to analysing waveguides with high-step refractive index profiles and gradient refractive index profiles, making it a powerful solution for analysis of the high refractive index contrast waveguides discussed in this thesis.

Both the FDM and FEM can be implemented to analyse different variations of the wave equations. In Chapter 2, Maxwell's equations are used to derive the full vectorial versions of the wave equations for the electric and magnetic fields, which are given by equations (2.3) and (2.4). While the FEM and FDM can be implemented to analyse these equations directly, simplifications can be made to the wave equation in certain cases, allowing the wave equation to be analysed more efficiently. If the interaction between the two transversally polarised field components in the wave equations, which can be small, is ignored, the equations reduce to semi-vectorial forms. Unless a structure is specifically designed to induce coupling, such as polarisation couplers, the effect of the interaction terms is extremely weak and the semi-vectorial approximation is accurate, even in high index contrast waveguide structures [26]. It is therefore used to analyse the high index contrast structures in this thesis. Meanwhile, if the derivatives of the relative permittivity with respect to the transverse directions in the wave equations are ignored, the equations reduce to the same scalar form, ignoring any polarisation effects. Therefore, this method is only appropriate to analyse waveguides with very small index contrasts in both transverse directions.

The PIC platform analysed in this thesis consists of III – V semiconductor compounds such as InP and GaInAs. The composition and refractive index profile of the platform can be viewed in Table 4.1. The structure consists of a number of layers with sharp refractive index contrasts between many of the layers. An etch into the material creates further sharp refractive index contrast along the horizontal direction. The finite difference method is particularly suited to analyse this structure due to its ability to accurately calculate the derivatives at the refractive index boundaries.

1.3.2.2 Analysing Propagation Direction Variant Waveguides

PICs contain multiple components on a single chip. To analyse how light propagates through the different devices, several methods have also been developed. The most popular methods are the beam propagation methods (BPMs) and the finite-difference time-domain method (FD-TD). While BPMs can be used to find the confined modes of optical waveguides, their main advantage is their ability to analyse waveguide structures where the refractive index profile is not uniform in the propagation direction, as well as analyse the operation of

optical devices such as a power coupler and a multi-mode interferometer which operate by launching a field consisting of a superposition of the supported modes of the optical waveguide structure. Various BPMs have been developed, with the most commonly used being the fast Fourier transform BPM (FFT-BPM) [23] and the finite difference BPM (FD-BPM) [24].

The FFT-BPM was the original BPM implementation and had been widely used until the FD-BPM had been developed. The FD-BPM largely replaced the FFT-BPM as the FFT-BPM had several disadvantages due to the use of the FFT. These included a relatively long computation time, the requirement of equidistant computational point spacings, inferior boundary condition methods, the necessity of very small point spacing and propagation steps, its unsuitability for large index contrast waveguides, and the requirement of the number of transverse computational area points having to be a power of 2. Meanwhile, the FD-BPM is much more numerically efficient, the propagation step size can be made larger, and it can accurately deal with sharp refractive index contrast boundaries. Due to these differences, the FD-BPM is considered superior and thus a semi-vectorial implementation of it (SV-FD-BPM) was used to analyse the waveguides in this thesis. Its implementation will be described in the next chapter.

The previous methods mentioned to analyse the wave equations assume a steady state solution, i.e. the derivative with respect to time is replaced with $i\omega$. However, another method exists which directly solves the time-dependent Maxwell equations: the finite-difference time-domain method (FD-TD) [28]. It is a fully vectorial technique and can better deal with issues such as polarisation coupling and reflections along the propagation direction. However, the technique requires very small grid spacings and time steps, making the amount of memory and time required to analyse 3D optical waveguides very large and therefore it was not used to analyse optical waveguides in this thesis.

As this thesis analyses the propagation of light through curved waveguides, it is important to ensure that the analysis method is appropriate for this purpose. The next chapter will showcase how waveguide bends can be analysed by applying a conformal transformation to the semi-vectorial wave equations. The FD-BPM can easily be applied to the transformed equations, allowing the light propagation to be accurately analysed. As the curvature of the waveguide bends can vary along their length, the BPM is the most appropriate method to analyse how the field distribution alters as the light propagates through the varying curvature structures.

1.4 Thesis Structure

The thesis contains seven chapters. The first and current chapter gives an introduction to optical waveguides and the methods used to analyse them.

The second chapter derives the wave equations from Maxwell's equations and describes the implementation of the finite difference mode solver and the finite difference beam propagation method. Waveguides are analysed to show that the mode solver and BPM have been implemented correctly and a technique to improve wide-angle propagation is also described, implemented and tested.

The third chapter describes the method of analysing curved optical waveguides. The wave equations are altered using a conformal transformation and the finite difference method is again applied to the resulting wave equations. The FD-BPM is then tested on simple circular waveguides. The chapter also describes the curvature profiles of the curved waveguides analysed in this thesis.

The fourth chapter analyses curved shallow-etched ridge waveguides. 90 and 180 degree bends are analysed and the curvature profiles of the bends are altered in an attempt to reduce the bend loss.

The fifth chapter analyses curved deep-etched ridge waveguides. Different curvature profiles are again investigated and their performance is compared to that of the curved shallow-etched waveguides. The chapter also looks at the cause of the excitation of multiple modes in the waveguide bend and how these excitations can be prevented by using a linear change in curvature.

The sixth chapter investigates how best to combine shallow-etched waveguides with deep-etched bends. Many optical devices consist of, or contain, shallow-etched waveguides and this chapter aims to determine how best to connect them with deep-etched waveguide bends to take advantage of the lower loss offered by the deep-etched bends.

The last chapter outlines the conclusions that can be drawn from the thesis and describes what could be done or improved on in the future.

2 The 3D Finite Difference Beam Propagation Method

As described in Section 1.3, beam propagation methods are numerical techniques used to simulate the propagation of light along optical waveguide structures. The method utilized in this thesis is the three-dimensional semi-vectorial finite difference beam propagation method (3D-SV-FD-BPM), chosen as it allows accurate analysis of large refractive index contrast optical waveguides. This chapter involves the derivation of the method [24] and the mode solver [21] as well as describes the implementation of various modifications taken from different sources designed to improve the accuracy of the simulations, such as differing boundary conditions [36] [37] [39] and wide-angle propagation [41] [42]. The resulting mode solver and BPM equations were computationally implemented by the candidate and their implementation is also described in this chapter. Simulations from the computational implementation are discussed throughout the chapter to ensure the method was implemented correctly.

2.1 The Wave Equations

The vectorial wave equations can be derived from the following Maxwell's equations:

$$\mathbf{D} = \varepsilon\mathbf{E} \qquad \mathbf{B} = \mu\mathbf{H}$$

$$\boldsymbol{\nabla}\cdot\mathbf{D} = \rho \qquad \boldsymbol{\nabla}\cdot\mathbf{H} = 0$$

$$\boldsymbol{\nabla}\times\mathbf{E} = -\frac{\partial\mathbf{B}}{\partial t} \qquad \boldsymbol{\nabla}\times\mathbf{H} = \frac{\partial\mathbf{D}}{\partial t} + \mathbf{J}$$

$$\mathbf{J} = \sigma\mathbf{E} \qquad \boldsymbol{\nabla}\cdot\mathbf{J} = -\frac{\partial\rho}{\partial t}$$

The electric field is represented by $\mathbf{E}$, the electric flux density by $\mathbf{D}$, the magnetic field by $\mathbf{H}$, the magnetic flux density by $\mathbf{B}$, the current density by $\mathbf{J}$, the electric permittivity by ε, the magnetic permeability by μ, the charge density by ρ and the electric conductivity by σ. The waveguides analysed in this thesis are assumed to be passive and therefore $\mathbf{J}$ and ρ can be neglected. The electric permittivity consists of the relative permittivity ε_r multiplied by the permittivity of free space ε_0. The magnetic permeability consists of the relative permeability μ_r multiplied by the permeability of free space μ_0. This thesis will only analyse non-magnetic waveguides and therefore $\mu_r = 1$. The refractive index, n, of the waveguide material is assumed to be isotropic and uniform. As $n = \varepsilon_r^2$, the relative permittivity can be represented by a scalar function of position. Under these conditions, Maxwell's equations reduce to the following form:

$$\boldsymbol{\nabla}\cdot\varepsilon_r\mathbf{E} = 0 \qquad \boldsymbol{\nabla}\cdot\mathbf{H} = 0$$

$$\boldsymbol{\nabla}\times\mathbf{E} = -\mu_0\frac{\partial\mathbf{H}}{\partial t} \qquad \boldsymbol{\nabla}\times\mathbf{H} = \varepsilon_r\varepsilon_0\frac{\partial\mathbf{E}}{\partial t}$$

Assuming the fields oscillate at a singular angular frequency ω, $\mathbf{E}$ and $\mathbf{H}$ can be expressed in the following time harmonic form:

$$\mathbf{E}(x,y,z,t) = \mathrm{Re}[\mathbf{E}(x,y,z)\exp(-i\omega t)] \tag{2.1}$$

$$\mathbf{H}(x,y,z,t) = \mathrm{Re}[\mathbf{H}(x,y,z)\exp(-i\omega t)] \tag{2.2}$$

Substitution of these electromagnetic fields into Maxwell's equations allows the derivatives with respect to t to be replaced by $-i\omega$. This gives Maxwell's equations the following representation:

$$\boldsymbol{\nabla} \cdot \varepsilon_r \mathbf{E} = 0 \qquad \boldsymbol{\nabla} \cdot \mathbf{H} = 0$$

$$\boldsymbol{\nabla} \times \mathbf{E} = i\mu_0 \omega \mathbf{H} \qquad \boldsymbol{\nabla} \times \mathbf{H} = -i\varepsilon_r \varepsilon_0 \omega \mathbf{E}$$

Applying $\boldsymbol{\nabla} \times$ to the curl of $\mathbf{E}$ and substituting in the curl of $\mathbf{H}$ gives:

$$\boldsymbol{\nabla} \times (\boldsymbol{\nabla} \times \mathbf{E}) = k_0^2 \varepsilon_r \mathbf{E} \tag{2.3}$$

In the equation above, k_0 is the wave number in a vacuum and is given by $k_0 = \omega\sqrt{\varepsilon_0 \mu_0}$. Using the vector formula $\boldsymbol{\nabla} \times (\boldsymbol{\nabla} \times \mathbf{E}) = \boldsymbol{\nabla}(\boldsymbol{\nabla} \cdot \mathbf{E}) - \boldsymbol{\nabla}^2 \mathbf{E}$ and Maxwell's equation $\boldsymbol{\nabla} \cdot \varepsilon_r \mathbf{E} = \mathbf{0}$, equation (2.3) reduces to the vectorial wave equation for the electric field E:

$$\boldsymbol{\nabla}^2 \mathbf{E} + \boldsymbol{\nabla}\left(\frac{\boldsymbol{\nabla}\varepsilon_r}{\varepsilon_r} \cdot \mathbf{E}\right) + k_0^2 \varepsilon_r \mathbf{E} = 0 \tag{2.4}$$

Alternatively, applying $\boldsymbol{\nabla} \times$ to the curl of $\mathbf{H}$ and manipulating the equation using the previously used vector formula and Maxwell's equations leads to the following vectorial wave equation for the magnetic field $\mathbf{H}$:

$$\boldsymbol{\nabla}^2 \mathbf{H} + \frac{\boldsymbol{\nabla}\varepsilon_r}{\varepsilon_r} \times (\boldsymbol{\nabla} \times \mathbf{H}) + k_0^2 \varepsilon_r \mathbf{H} = 0 \tag{2.5}$$

In terms of components of the Cartesian coordinate system, the vectorial wave equation for the electric field can be expressed by the following three equations:

$$\frac{\partial^2 E_x}{\partial x^2} + \frac{\partial}{\partial x}\left(\frac{1}{\varepsilon_r}\frac{\partial \varepsilon_r}{\partial x} E_x\right) + \frac{\partial^2 E_x}{\partial y^2} + \frac{\partial}{\partial x}\left(\frac{1}{\varepsilon_r}\frac{\partial \varepsilon_r}{\partial y} E_y\right) + \frac{\partial^2 E_x}{\partial z^2} + \frac{\partial}{\partial x}\left(\frac{1}{\varepsilon_r}\frac{\partial \varepsilon_r}{\partial z} E_z\right) + k_0^2 \varepsilon_r E_x = 0 \tag{2.6}$$

$$\frac{\partial^2 E_y}{\partial x^2} + \frac{\partial}{\partial y}\left(\frac{1}{\varepsilon_r}\frac{\partial \varepsilon_r}{\partial x} E_x\right) + \frac{\partial^2 E_y}{\partial y^2} + \frac{\partial}{\partial y}\left(\frac{1}{\varepsilon_r}\frac{\partial \varepsilon_r}{\partial y} E_y\right) + \frac{\partial^2 E_y}{\partial z^2} + \frac{\partial}{\partial y}\left(\frac{1}{\varepsilon_r}\frac{\partial \varepsilon_r}{\partial z} E_z\right) + k_0^2 \varepsilon_r E_y = 0 \tag{2.7}$$

$$\frac{\partial^2 E_z}{\partial x^2} + \frac{\partial}{\partial z}\left(\frac{1}{\varepsilon_r}\frac{\partial \varepsilon_r}{\partial x} E_x\right) + \frac{\partial^2 E_z}{\partial y^2} + \frac{\partial}{\partial z}\left(\frac{1}{\varepsilon_r}\frac{\partial \varepsilon_r}{\partial y} E_y\right) + \frac{\partial^2 E_z}{\partial z^2} + \frac{\partial}{\partial z}\left(\frac{1}{\varepsilon_r}\frac{\partial \varepsilon_r}{\partial z} E_z\right) + k_0^2 \varepsilon_r E_z = 0 \tag{2.8}$$

Similarly, the vectorial wave equation for the magnetic field can be expressed by the following three equations in the Cartesian coordinate system:

$$\frac{\partial^2 H_x}{\partial x^2} + \frac{\partial^2 H_x}{\partial y^2} + \frac{1}{\varepsilon_r}\frac{\partial \varepsilon_r}{\partial y}\left(\frac{\partial H_y}{\partial x} - \frac{\partial H_x}{\partial y}\right) + \frac{\partial^2 H_x}{\partial z^2} - \frac{1}{\varepsilon_r}\frac{\partial \varepsilon_r}{\partial z}\left(\frac{\partial H_x}{\partial z} - \frac{\partial H_z}{\partial x}\right) + k_0^2 \varepsilon_r H_x = 0 \tag{2.9}$$

$$\frac{\partial^2 H_y}{\partial x^2} - \frac{1}{\varepsilon_r}\frac{\partial \varepsilon_r}{\partial x}\left(\frac{\partial H_y}{\partial x} - \frac{\partial H_x}{\partial y}\right) + \frac{\partial^2 H_y}{\partial y^2} + \frac{\partial^2 H_y}{\partial z^2} + \frac{1}{\varepsilon_r}\frac{\partial \varepsilon_r}{\partial z}\left(\frac{\partial H_z}{\partial y} - \frac{\partial H_y}{\partial z}\right) + k_0^2 \varepsilon_r H_y = 0 \tag{2.10}$$

$$\frac{\partial^2 H_z}{\partial x^2} + \frac{1}{\varepsilon_r}\frac{\partial \varepsilon_r}{\partial x}\left(\frac{\partial H_x}{\partial z} - \frac{\partial H_z}{\partial x}\right) + \frac{\partial^2 H_z}{\partial y^2} - \frac{1}{\varepsilon_r}\frac{\partial \varepsilon_r}{\partial y}\left(\frac{\partial H_z}{\partial y} - \frac{\partial H_y}{\partial z}\right) + \frac{\partial^2 H_z}{\partial z^2} + k_0^2 \varepsilon_r H_z = 0 \tag{2.11}$$

2.2 The 2D Finite Difference Mode Solver

If the waveguide is assumed to be uniform in the propagation direction, the $\hat{\boldsymbol{z}}$ direction, then the derivative of the electromagnetic field with respect to z is constant, such that $\frac{\partial}{\partial z} = i\beta$ [29]. β is the propagation constant and is the $\hat{\boldsymbol{z}}$ directed component of the wavenumber

$\boldsymbol{k}$. The ratio of β to the wave number in a vacuum, k_0, is known as the effective refractive index n_{eff}, $n_{eff} = \frac{\beta}{k_0}$. The physical meaning of the propagation constant is the phase rotation per unit propagation distance.

As electromagnetic fields propagate through optical waveguides, they take the shape of one of the waveguide's supported propagation modes. Each of these modes has a different propagation constant β and therefore a different effective refractive index n_{eff}. For the mode to be a supported non-radiating mode, the effective refractive index must have a value between that of the core of the waveguide and that of the surrounding material.

In order to use the beam propagation method, an initial field is required. This was usually generated by assuming the waveguide was invariant in the propagation direction and then using a 2D finite difference mode solver to find the fundamental mode and corresponding propagation constant. This section will describe how the mode solver was created by using the finite difference method on the wave equations [21].

As the waveguide is assumed to be invariant in the propagation direction, $\frac{\partial \varepsilon_r}{\partial z} = 0$. Substituting this and $\frac{\partial}{\partial z} = i\beta$ into the wave equations (2.6) – (2.11), the equations for the x and y components of the electromagnetic fields become:

$$\frac{\partial^2 E_x}{\partial x^2} + \frac{\partial}{\partial x}\left(\frac{1}{\varepsilon_r}\frac{\partial \varepsilon_r}{\partial x}E_x\right) + \frac{\partial^2 E_x}{\partial y^2} + \frac{\partial}{\partial x}\left(\frac{1}{\varepsilon_r}\frac{\partial \varepsilon_r}{\partial y}E_y\right) + k_0^2\left(\varepsilon_r - n_{eff}^2\right)E_x = 0 \qquad (2.12)$$

$$\frac{\partial^2 E_y}{\partial x^2} + \frac{\partial}{\partial y}\left(\frac{1}{\varepsilon_r}\frac{\partial \varepsilon_r}{\partial x}E_x\right) + \frac{\partial^2 E_y}{\partial y^2} + \frac{\partial}{\partial y}\left(\frac{1}{\varepsilon_r}\frac{\partial \varepsilon_r}{\partial y}E_y\right) + k_0^2\left(\varepsilon_r - n_{eff}^2\right)E_y = 0 \qquad (2.13)$$

$$\frac{\partial^2 H_x}{\partial x^2} + \frac{\partial^2 H_x}{\partial y^2} + \frac{1}{\varepsilon_r}\frac{\partial \varepsilon_r}{\partial y}\left(\frac{\partial H_y}{\partial x} - \frac{\partial H_x}{\partial y}\right) + k_0^2\left(\varepsilon_r - n_{eff}^2\right)H_x = 0 \qquad (2.14)$$

$$\frac{\partial^2 H_y}{\partial x^2} - \frac{1}{\varepsilon_r}\frac{\partial \varepsilon_r}{\partial x}\left(\frac{\partial H_y}{\partial x} - \frac{\partial H_x}{\partial y}\right) + \frac{\partial^2 H_y}{\partial y^2} + k_0^2\left(\varepsilon_r - n_{eff}^2\right)H_y = 0 \qquad (2.15)$$

For propagation through optical waveguides, the terms corresponding to the interaction between E_x and E_y, $\frac{\partial}{\partial x}\left(\frac{1}{\varepsilon_r}\frac{\partial \varepsilon_r}{\partial y}E_y\right)$ and $\frac{\partial}{\partial y}\left(\frac{1}{\varepsilon_r}\frac{\partial \varepsilon_r}{\partial x}E_x\right)$, and between H_x and H_y, $\frac{1}{\varepsilon_r}\frac{\partial \varepsilon_r}{\partial y}\frac{\partial H_y}{\partial x}$ and $\frac{1}{\varepsilon_r}\frac{\partial \varepsilon_r}{\partial x}\frac{\partial H_x}{\partial y}$, are usually quite small. Unless a structure is designed to induce coupling, such as polarization converters [25], the effect of these coupling terms is usually extremely weak and the semi-vectorial approximation is an excellent one, even in high index contrast structures such as semiconductor waveguides [26] [27]. Omitting them from the above vectorial wave equations decouples the wave equations and reduces them to semi-vectorial wave equations. This simplifies the analysis of these wave equations, allowing them to be solved in a way that is numerically efficient. The analysis can be further simplified by assuming the fields are polarized in a specific transverse direction. In the quasi-transverse electric (quasi-TE) mode analysis, the principal field component is assumed to be E_x or H_y, while in the quasi-transverse magnetic (quasi-TM) mode analysis, the principal field component is assumed to be E_y or H_x. The equations for the quasi-TE mode are therefore given by:

$$\frac{\partial^2 E_x}{\partial x^2} + \frac{\partial}{\partial x}\left(\frac{1}{\varepsilon_r}\frac{\partial \varepsilon_r}{\partial x}E_x\right) + \frac{\partial^2 E_x}{\partial y^2} + k_0^2\left(\varepsilon_r - n_{eff}^2\right)E_x = 0 \tag{2.16}$$

$$\varepsilon_r \frac{\partial}{\partial x}\left(\frac{1}{\varepsilon_r}\frac{\partial H_y}{\partial x}\right) + \frac{\partial^2 H_y}{\partial y^2} + k_0^2\left(\varepsilon_r - n_{eff}^2\right)H_y = 0 \tag{2.17}$$

Meanwhile, the equations for the quasi-TM mode are given by:

$$\frac{\partial^2 E_y}{\partial x^2} + \frac{\partial^2 E_y}{\partial y^2} + \frac{\partial}{\partial y}\left(\frac{1}{\varepsilon_r}\frac{\partial \varepsilon_r}{\partial y}E_y\right) + k_0^2\left(\varepsilon_r - n_{eff}^2\right)E_y = 0 \tag{2.18}$$

$$\frac{\partial^2 H_x}{\partial x^2} + \varepsilon_r \frac{\partial}{\partial y}\left(\frac{1}{\varepsilon_r}\frac{\partial H_x}{\partial y}\right) + k_0^2\left(\varepsilon_r - n_{eff}^2\right)H_x = 0 \tag{2.19}$$

2.2.1 Finite Difference Expressions of Wave Equations

The finite difference expressions for the semi-vectorial wave equations are derived by calculating the derivatives in the wave equation using the method of finite difference. Assume that a one-dimensional function $f(x)$ is continuous. Assume $f(x)$ has the values f_0, f_1 and f_2 at $x = 0, -h_1, h_2$ respectively. Let f_1 and f_2 be written as Taylor series expansions around $x = 0$:

$$f_1 = f(-h_1) = f(0) - \frac{h_1}{1!}\frac{df(0)}{dx} + \frac{h_1^2}{2!}\frac{d^2 f(0)}{dx^2} - \frac{h_1^3}{3!}\frac{d^3 f(0)}{dx^3} + O(h_1^4) \tag{2.20}$$

$$f_2 = f(h_2) = f(0) + \frac{h_2}{1!}\frac{df(0)}{dx} + \frac{h_2^2}{2!}\frac{d^2 f(0)}{dx^2} + \frac{h_2^3}{3!}\frac{d^3 f(0)}{dx^3} + O(h_2^4) \tag{2.21}$$

Subtracting f_1 from f_2 gives an expression for the first derivative along with the associated error, where h represents the point spacing if $h = h_1 = h_2$. If the spacing is not equal, the $O(h^3)$ term consists of an expression involving both h_1^3 and h_2^3.

$$f_2 - f_1 = (h_2 + h_1)\frac{df(0)}{dx} + \frac{(h_2^2 - h_1^2)}{2}\frac{d^2 f(0)}{dx^2} + O(h^3) \tag{2.22}$$

$$\frac{df(0)}{dx} = \frac{f_2 - f_1}{h_2 + h_1} - \frac{1}{2}(h_2 - h_1)\frac{d^2 f(0)}{dx^2} + O(h^2) \tag{2.23}$$

The error of the derivative is of the order $O(h^2)$ when the point spacing is equal and of the order $O(h)$ when the point spacing is unequal.

The second derivative of f about 0 is found in a similar manner and is given by:

$$\frac{d^2 f(0)}{dx^2} = \frac{2}{h_1 h_2}\frac{h_2 f_1 - (h_1 + h_2)f_0 + h_1 f_2}{h_1 + h_2} + O(h) \tag{2.24}$$

The error of the second derivative is $O(h)$, where h is an expression involving a linear combination of h_1 and h_2. However, the error reduces to $O(h^2)$ when $h = h_1 = h_2$.

From these derivative expressions, it is evident that it is preferable to use equidistant point discretisation when calculating derivatives by method of finite difference in order to reduce the size of the error term. However, to reduce computation time and memory, non-equidistant point discretisation is often used provided the difference in the point spacing is not made too large.

Applying the method of finite difference to the derivatives in the semi-vectorial wave equations (2.16) – (2.19) for the various component of the electromagnetic fields, the following finite difference expressions are obtained for the derivatives calculated at point (x_p, y_q) where A represents a component of the field, Δx_l and Δx_r represent the spacing to the left and right of a point along the $\hat{\boldsymbol{x}}$ axis, and Δy_d and Δy_u represent the spacing below and above a point along the $\hat{\boldsymbol{y}}$ axis:

$$\frac{\partial^2 A(x_p,y_q)}{\partial x^2} = \frac{2}{\Delta x_l(\Delta x_l+\Delta x_r)}A(x_{p-1},y_q) + \frac{2}{\Delta x_r(\Delta x_l+\Delta x_r)}A(x_{p+1},y_q) - \frac{2}{\Delta x_l \Delta x_r}A(x_p,y_q) \quad (2.25)$$

$$\frac{\partial^2 A(x_p,y_q)}{\partial y^2} = \frac{2}{\Delta y_d(\Delta y_d+\Delta y_u)}A(x_p,y_{q-1}) + \frac{2}{\Delta y_u(\Delta y_d+\Delta y_u)}A(x_p,y_{q+1}) - \frac{2}{\Delta y_d \Delta y_u}A(x_p,y_q) \quad (2.26)$$

$$\frac{\partial}{\partial x}\left(\frac{1}{\varepsilon_r}\frac{\partial \varepsilon_r}{\partial x}A(x_p,y_q)\right) = \frac{2}{\Delta x_l+\Delta x_r}\left[\frac{1}{\Delta x_r}\frac{\varepsilon_r(x_{p+1},y_q)-\varepsilon_r(x_p,y_q)}{\varepsilon_r(x_{p+1},y_q)+\varepsilon_r(x_p,y_q)}\Big(A(x_p,y_q)+A(x_{p+1},y_q)\Big) - \frac{1}{\Delta x_l}\frac{\varepsilon_r(x_p,y_q)-\varepsilon_r(x_{p-1},y_q)}{\varepsilon_r(x_p,y_q)+\varepsilon_r(x_{p-1},y_q)}\Big(A(x_p,y_q)+A(x_{p-1},y_q)\Big)\right] \quad (2.27)$$

$$\frac{\partial}{\partial y}\left(\frac{1}{\varepsilon_r}\frac{\partial \varepsilon_r}{\partial y}A(x_p,y_q)\right) = \frac{2}{\Delta y_d+\Delta y_u}\left[\frac{1}{\Delta y_u}\frac{\varepsilon_r(x_p,y_{q+1})-\varepsilon_r(x_p,y_q)}{\varepsilon_r(x_p,y_{q+1})+\varepsilon_r(x_p,y_q)}\Big(A(x_p,y_q)+A(x_p,y_{q+1})\Big) - \frac{1}{\Delta y_d}\frac{\varepsilon_r(x_p,y_q)-\varepsilon_r(x_p,y_{q-1})}{\varepsilon_r(x_p,y_q)+\varepsilon_r(x_p,y_{q-1})}\Big(A(x_p,y_q)+A(x_p,y_{q-1})\Big)\right] \quad (2.28)$$

Substituting these finite difference expressions into the wave equations results in a finite difference equation of the following form:

$$\alpha_l A_{p-1,q} + \alpha_r A_{p+1,q} + \alpha_d A_{p,q-1} + \alpha_u A_{p,q+1} + (\alpha_m + k_0^2 \varepsilon_r(p,q))A_{p,q} = \beta^2 A_{p,q} \quad (2.29)$$

The α coefficients depend on the mode and field analysed. In the quasi-TE mode with $A = E_x$:

$$\alpha_l = \frac{2}{\Delta x_l(\Delta x_l+\Delta x_r)}\frac{2\varepsilon_r(x_p,y_q)}{\varepsilon_r(x_p,y_q)+\varepsilon_r(x_{p-1},y_q)} \quad (2.30)$$

$$\alpha_r = \frac{2}{\Delta x_r(\Delta x_l+\Delta x_r)}\frac{2\varepsilon_r(x_p,y_q)}{\varepsilon_r(x_p,y_q)+\varepsilon_r(x_{p+1},y_q)} \quad (2.31)$$

$$\alpha_d = \frac{2}{\Delta y_d(\Delta y_d+\Delta y_u)} \quad (2.32)$$

$$\alpha_u = \frac{2}{\Delta y_u(\Delta y_d+\Delta y_u)} \quad (2.33)$$

$$\alpha_m = -\frac{4}{\Delta x_l \Delta x_r} + \alpha_l + \alpha_r - \alpha_d - \alpha_u \quad (2.34)$$

In the quasi-TE mode with $A = H_y$:

$$\alpha_l = \frac{2}{\Delta x_l(\Delta x_l+\Delta x_r)}\frac{2\varepsilon_r(x_{p-1},y_q)}{\varepsilon_r(x_p,y_q)+\varepsilon_r(x_{p-1},y_q)} \quad (2.35)$$

$$\alpha_r = \frac{2}{\Delta x_r(\Delta x_l+\Delta x_r)}\frac{2\varepsilon_r(x_{p+1},y_q)}{\varepsilon_r(x_p,y_q)+\varepsilon_r(x_{p+1},y_q)} \quad (2.36)$$

$$\alpha_d = \frac{2}{\Delta y_d(\Delta y_d+\Delta y_u)} \tag{2.37}$$

$$\alpha_u = \frac{2}{\Delta y_u(\Delta y_d+\Delta y_u)} \tag{2.38}$$

$$\alpha_m = -\alpha_l - \alpha_r - \alpha_d - \alpha_u \tag{2.39}$$

In the quasi-TM mode with $A = E_y$:

$$\alpha_l = \frac{2}{\Delta x_l(\Delta x_l+\Delta x_r)} \tag{2.40}$$

$$\alpha_r = \frac{2}{\Delta x_r(\Delta x_l+\Delta x_r)} \tag{2.41}$$

$$\alpha_d = \frac{2}{\Delta y_d(\Delta y_d+\Delta y_u)} \frac{2\varepsilon_r(x_p,y_{q-1})}{\varepsilon_r(x_p,y_q)+\varepsilon_r(x_p,y_{q-1})} \tag{2.42}$$

$$\alpha_u = \frac{2}{\Delta y_u(\Delta y_d+\Delta y_u)} \frac{2\varepsilon_r(x_p,y_{q+1})}{\varepsilon_r(x_p,y_q)+\varepsilon_r(x_p,y_{q+1})} \tag{2.43}$$

$$\alpha_m = -\frac{4}{\Delta y_d \Delta y_u} - \alpha_l - \alpha_r + \alpha_d + \alpha_u \tag{2.44}$$

In the quasi-TM mode with $A = H_x$:

$$\alpha_l = \frac{2}{\Delta x_l(\Delta x_l+\Delta x_r)} \tag{2.45}$$

$$\alpha_r = \frac{2}{\Delta x_r(\Delta x_l+\Delta x_r)} \tag{2.46}$$

$$\alpha_d = \frac{2}{\Delta y_d(\Delta y_d+\Delta y_u)} \frac{2\varepsilon_r(x_p,y_q)}{\varepsilon_r(x_p,y_q)+\varepsilon_r(x_p,y_{q-1})} \tag{2.47}$$

$$\alpha_u = \frac{2}{\Delta y_u(\Delta y_d+\Delta y_u)} \frac{2\varepsilon_r(x_p,y_q)}{\varepsilon_r(x_p,y_q)+\varepsilon_r(x_p,y_{q+1})} \tag{2.48}$$

$$\alpha_m = -\alpha_l - \alpha_r - \alpha_d - \alpha_u \tag{2.49}$$

Equation (2.29) is an eigenvalue matrix equation of the following form:

$$F\phi = \beta^2\phi \tag{2.50}$$

F represents the global matrix, ϕ represents the eigenvectors and β^2 represents the eigenvalues. Therefore, the propagation constants and corresponding field distributions can be found by solving the eigenvalue matrix equation. The global matrix F takes the form of a structurally symmetric sparse matrix, allowing it to be solved efficiently using a sparse matrix eigenvalue equation solver. The Armadillo C++ library was used for this purpose [30] [31]. Armadillo includes the ability to find a specified number of eigenvalues with the largest real part. This greatly sped up the computation as the effective refractive index of the fundamental mode always had the largest real part. For example, finding the fundamental mode of a waveguide where 250 x 250 discretisation points were used in the computation took approximately 30 seconds using two cores of an Intel Core i7-9700 processor.

2.2.2 Mode Solver Boundary Conditions

When programming the point mesh and global matrix, boundary conditions must be implemented on points at the edge of the computational window. The two different boundary conditions utilised for this purpose were the Derichlet condition and the Neumann condition [33].

According to the Derichlet condition, the field outside the computational area is set to zero.

$$\phi = 0 \tag{2.51}$$

According to the Neumann condition, the normal derivative of the field at the edge of the computational window is set to zero.

$$\frac{\partial \phi}{\partial n} = 0 \tag{2.52}$$

These boundary conditions can be implemented by considering a hypothetical point outside of the computational area. If, for example, this point is located to the left of the computational area at (x_{p-1}, y_q) while the point at (x_p, y_q) is at the edge of the computational area, the field at these points are related by:

$$\phi_{p-1,q} = \gamma \phi_{p,q} \tag{2.53}$$

γ is equal to zero in the case of Derichlet boundary conditions and γ is equal to one in the case of Neumann boundary conditions.

$$\gamma = \begin{cases} 0 & (\text{Dirichlet}) \\ 1 & (\text{Neumann}) \end{cases} \tag{2.54}$$

The finite difference expression given by equation (2.29) then changes to:

$$\alpha_r A_{p+1,q} + \alpha_d A_{p,q-1} + \alpha_u A_{p,q+1} + (\alpha_m{}' + k_0^2 \varepsilon_r(p,q)) A_{p,q} = \beta^2 A_{p,q} \tag{2.55}$$

with:

$$\alpha_m' = \alpha_m + \alpha_l \gamma \tag{2.56}$$

The same procedure is done for the boundaries at the other edges of the computational window.

2.2.3 Testing Mode Solver

The mode solver was tested to ensure it worked correctly for each mode and field polarisation. For this purpose, a simple square step index waveguide was analysed to easily observe if the field was continuous or discontinuous at refractive index boundaries for the different field polarisations. The width and height of the core are both 0.4 μm and the refractive indices of the core and cladding are 3.5 and 3.1693 respectively. This refractive index for the core is a typical refractive index for a semiconductor core waveguide material and the cladding refractive index is approximately that of InP which is again a typical material used in these structures. This is the same waveguide as was analysed in reference [32] to test their implementation of the semi-vectorial finite difference method. The cladding extends for 2 μm on each side of the core, giving the computational area a size of

$4.4\ \mu m \times 4.4\ \mu m$. The computational grid was divided into 251 x 251 points utilizing non-equidistant point discretisation. The minimum spacing between points close to the refractive index boundaries was $\sim 0.007\ \mu m$ and the maximum point spacing was $\sim 0.017\ \mu m$. Dirichlet boundary conditions were implemented in the simulation. The wavelength of the light analysed was 1.55 μm. This is the wavelength of the light analysed for all optical waveguides in this thesis, unless stated otherwise. A schematic of the waveguide is shown in Figure 2.1.

Figure 2.2 shows the calculated fundamental mode profiles for the polarised fields in both the quasi-TE and quasi-TM modes. Derived from the integral version of Maxwell's equations [34], certain conditions are imposed on the field either side of a material interface. If A_1 and A_2 are components of the electromagnetic field either side of a refractive index boundary, for the electric field, the conditions applied are: $\mathbf{n_{12}} \times (\mathbf{E_2} - \mathbf{E_1}) = 0$ and $(\mathbf{D_2} - \mathbf{D_1}) \cdot \mathbf{n_{12}} = \sigma_s$, where $\boldsymbol{n_{12}}$ is the normal vector from media 1 to media 2 and σ_s is the surface charge between the media. Meanwhile, for the magnetic field, the conditions applied are: $\mathbf{n_{12}} \times (\mathbf{H_2} - \mathbf{H_1}) = \mathbf{j_s}$ and $(\mathbf{B_2} - \mathbf{B_1}) \cdot \mathbf{n_{12}} = 0$, where $\mathbf{j_s}$ is the surface current density between the two media. As σ_s and $\mathbf{j_s}$ are both equal to zero, the following boundary conditions are applied to the polarised fields:

- Tangential components of the electric fields are continuous, $E_{1t} = E_{2t}$.
- Normal components of the electric flux densities are continuous, $D_{1n} = D_{2n}$ or $\varepsilon_{r1} E_{1n} = \varepsilon_{r2} E_{2n}$.
- Due to the assumption that the magnetic permeability is the same for both materials, both the tangential and normal components of the magnetic fields are continuous, $H_{1t} = H_{2t}, H_{1n} = H_{2n}$.

Figure 2.2 shows these conditions to hold, with E_x appearing discontinuous at the refractive index boundaries along the $\hat{\boldsymbol{x}}$ direction in the quasi-TE mode, and E_y appearing discontinuous at the refractive index boundaries along the $\hat{\boldsymbol{y}}$ direction in the quasi-TM mode. Meanwhile, H_x and H_y appear continuous at all refractive index boundaries.

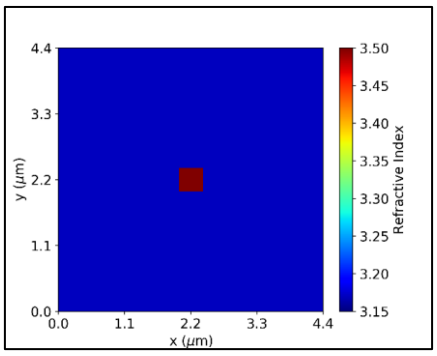

Figure 2.1: Refractive Index Profile of Rectangular Waveguide

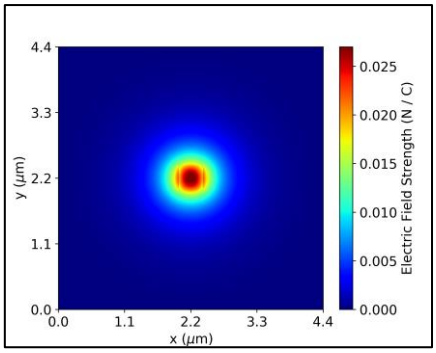

(a) E_x vs. x & y in the quasi-TE mode with $n_{eff} = 3.21682$

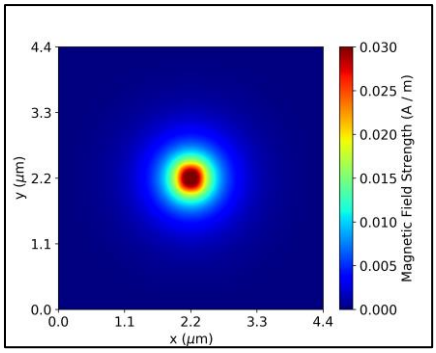

(b) H_y vs. x & y in the quasi-TE mode with $n_{eff} = 3.21682$

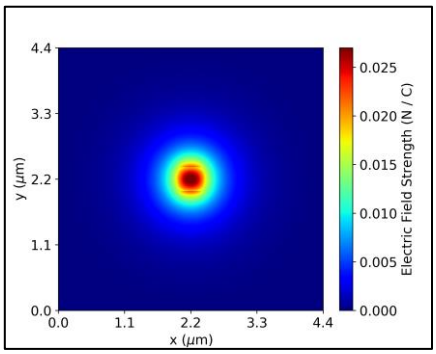

(a) E_y vs. x & y in the quasi-TM mode with $n_{eff} = 3.21682$

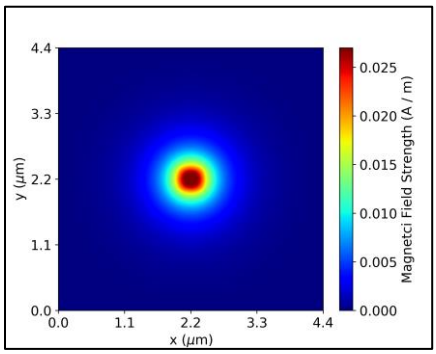

(b) H_x vs. x & y in the quasi-TM mode with $n_{eff} = 3.21682$

Figure 2.2: Fundamental electric and magnetic field profiles for the quasi-TE and quasi-TM modes.

The calculated effective refractive indices from the mode solver were 3.21682 for both the quasi-TE mode and the quasi-TM mode. These effective refractive indices were the same due to the square waveguide having the same properties along the $\hat{\boldsymbol{x}}$ and $\hat{\boldsymbol{y}}$ directions. In the analysis of reference [32], they got an effective refractive index of 3.2172 for both modes, however they used just 92 non-equidistant computational area points in each transverse direction and were therefore likely less accurate. To examine the accuracy of the simulations, the same simulation was done using different numbers of computational points and the calculated effective refractive indices were recorded. Figure 2.3 shows the results from the simulations involving the quasi-TM mode where the number of computational points along each direction varied from 51 to 251. The number of points close to the refractive index boundary was kept constant for each simulation, leaving the point spacing in this region at $\sim 0.007\ \mu m$, while the number of points in the other regions varied causing the point spacing to vary from $\sim 0.12\ \mu m$ with 51 computational points in both directions to $\sim 0.017\ \mu m$ with 251 computational points in both directions. The effective refractive index appears to converge to a value as the number of computational points increases. This is to be expected as the error in the finite difference approximations is of the order Δx when the point spacing is unequal and of the order Δx^2 when the point spacing is equal, as can be seen from equation (2.23).

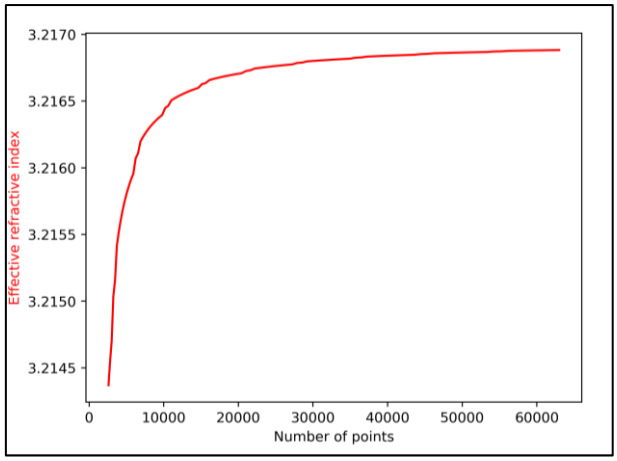

Figure 2.3: Calculated effective refractive index vs. number of points used in computation.

2.3 The 3D Semi-Vectorial Finite Difference Beam Propagation Method

For the beam propagation method, the waveguide is no longer assumed to be invariant in the propagation direction, and therefore the derivatives with respect to z must be calculated at each propagation point. Assuming there is no coupling between the differently polarised field components, this results in the following semi-vectorial wave equations for the quasi-TE mode as derived from equations (2.6) and (2.10):

$$\frac{\partial^2 E_x}{\partial x^2} + \frac{\partial}{\partial x}\left(\frac{1}{\varepsilon_r}\frac{\partial \varepsilon_r}{\partial x}E_x\right) + \frac{\partial^2 E_x}{\partial y^2} + \frac{\partial^2 E_x}{\partial z^2} + k_0^2 \varepsilon_r E_x = 0 \tag{2.57}$$

$$\varepsilon_r \frac{\partial}{\partial x}\left(\frac{1}{\varepsilon_r}\frac{\partial H_y}{\partial x}\right) + \frac{\partial^2 H_y}{\partial y^2} + \frac{\partial^2 H_y}{\partial z^2} + k_0^2 \varepsilon_r H_y = 0 \tag{2.58}$$

And for the quasi-TM mode, results in the following semi-vectorial wave equations as derived from equations (2.7) and (2.9):

$$\frac{\partial^2 E_y}{\partial x^2} + \frac{\partial^2 E_y}{\partial y^2} + \frac{\partial}{\partial y}\left(\frac{1}{\varepsilon_r}\frac{\partial \varepsilon_r}{\partial y}E_y\right) + \frac{\partial^2 E_y}{\partial z^2} + k_0^2 \varepsilon_r E_y = 0 \tag{2.59}$$

$$\frac{\partial^2 H_x}{\partial x^2} + \varepsilon_r \frac{\partial}{\partial y}\left(\frac{1}{\varepsilon_r}\frac{\partial H_x}{\partial y}\right) + \frac{\partial^2 H_x}{\partial z^2} + k_0^2 \varepsilon_r H_x = 0 \tag{2.60}$$

In the derivation of the magnetic fields above, the derivative of the relative permittivity with respect to z, $\partial\varepsilon_r/\partial z$, is assumed to be small and therefore the $\frac{1}{\varepsilon_r}\frac{\partial \varepsilon_r}{\partial z}\frac{\partial H}{\partial z}$ term is ignored.

The field components above can be expressed as the product of a complex field amplitude $\phi(x, y, z)$ and a propagation factor $\exp(ik_0 n_0 z)$, where n_0 is a reference index which is usually chosen to be that of the effective index of the propagating mode where possible. If the effective index is not known, the index of the cladding is usually used instead at the cost of lower accuracy. In this case, the wide angle Padé operators can be used to improve accuracy, where the choice of reference index has less impact on the calculation, as will be shown later in the chapter. For example, for E_x in the quasi-TE mode:

$$E_x(x, y, z) = \phi(x, y, z)\exp(ik_o n_o z) \tag{2.61}$$

Substituting this expression into equation (2.57) results in the following:

$$-2ik_0 n_0 \frac{\partial \phi}{\partial z} - \frac{\partial^2 \phi}{\partial z^2} = \frac{\partial^2 \phi}{\partial x^2} + \frac{\partial}{\partial x}\left(\frac{1}{\varepsilon_r}\frac{\partial \varepsilon_r}{\partial x}\phi\right) + \frac{\partial^2 \phi}{\partial y^2} + k_0^2(\varepsilon_r - n_0^2)\,\phi \tag{2.62}$$

2.3.1 Slowly Varying Envelope Approximation (SVEA)

If the wave is assumed to be paraxial, i.e. propagates at a very small angle to the $\hat{\boldsymbol{z}}$ direction, the slowly varying envelope approximation (SVEA) can be applied. According to the SVEA:

$$2k_o n_0 \left|\frac{\partial \phi}{\partial z}\right| \gg \left|\frac{\partial^2 \phi}{\partial z^2}\right| \tag{2.63}$$

This allows the following Fresnel equation for the E_x field in the quasi-TE mode to be obtained:

$$-2ik_0 n_0 \frac{\partial \phi}{\partial z} = \frac{\partial^2 \phi}{\partial x^2} + \frac{\partial}{\partial x}\left(\frac{1}{\varepsilon_r}\frac{\partial \varepsilon_r}{\partial x}\phi\right) + \frac{\partial^2 \phi}{\partial y^2} + k_0^2(\varepsilon_r - k_0^2 n_0^2)\phi \tag{2.64}$$

The same procedure is followed to find the Fresnel equations for the other fields.

2.3.2 Finite Difference Expressions of BPM Wave Equations

The right-hand side of equation (2.64) is the same as the left-hand side of equation (2.16), with ϕ replacing E_x and n_0 replacing n_{eff}. This means that the derivatives in the transverse directions may be approximated by the method of finite difference in the same fashion as was done for the mode solver. Discretising the right-hand side of equation (2.64) in this manner results in the following finite difference expression:

$$-2ik_0 n_0 \frac{\partial \phi}{\partial z} = \alpha_l \phi_{p-1,q} + \alpha_r \phi_{p+1,q} + \alpha_d \phi_{p,q-1} + \alpha_u \phi_{p,q+1} + (\alpha_m + k_0^2(\varepsilon_r(p,q) - n_0^2))\phi_{p,q} \tag{2.65}$$

The α coefficients are the same as those given by equations (2.30) to (2.49), depending on the mode and field analysed.

Next, equation (2.65) must be discretised with respect to the propagation direction, z. Applying the method of finite difference, the left-hand side of the equation is represented by:

$$-2ik_0 n_0 \frac{\phi_p^{k+1} - \phi_p^k}{\Delta z} \tag{2.66}$$

The superscript k refers to a point along the z propagation direction and Δz is the distance between propagation points.

The difference centre of equation (2.66), the left-hand side of equation (2.65), is midway between k and $k+1$ at $k+\frac{1}{2}$. Therefore, the difference centre of the right-hand side of equation (2.65) must also be at $k+\frac{1}{2}$. Discretisation of the propagation direction in this manner is known as the Crank-Nicholson scheme. To achieve this, the right-hand side is averaged at points k and $k+1$. This results in the following finite difference expression:

$$-2ik_0 n_0 \frac{\phi_p^{k+1} - \phi_p^k}{\Delta z} = \frac{1}{2}\left[\alpha_l^k \phi_{p-1,q}^k + \alpha_r^k \phi_{p+1,q}^k + \alpha_d^k \phi_{p,q-1}^k + \alpha_u^k \phi_{p,q+1}^k + (\alpha_m^k + k_0^2(\varepsilon_r^k(p,q) -\right.$$

$$n_0^2))\phi_{p,q}^k\Big] + \frac{1}{2}\Big[\alpha_l^{k+1}\phi_{p-1,q}^{k+1} + \alpha_r^{k+1}\phi_{p+1,q}^{k+1} + \alpha_d^{k+1}\phi_{p,q-1}^{k+1} + \alpha_u^{k+1}\phi_{p,q+1}^{k+1} + (\alpha_m^{k+1} + k_0^2(\varepsilon_r^{k+1}(p,q) - n_0^2))\phi_{p,q}^{k+1}\Big] \quad (2.67)$$

Rewriting the equation so that $k+1$ terms are put on the left-hand side and k terms are put on the right-hand side:

$$-\alpha_l^{k+1}\phi_{p-1,q}^{k+1} - \alpha_r^{k+1}\phi_{p+1,q}^{k+1} - \alpha_d^{k+1}\phi_{p,q-1}^{k+1} - \alpha_u^{k+1}\phi_{p,q+1}^{k+1} - \Big[\alpha_m^{k+1} + \frac{4ik_0n_0}{\Delta z} + k_0^2(\varepsilon_r^{k+1}(p,q) - n_0^2)\Big]\phi_{p,q}^{k+1} = \alpha_l^k\phi_{p-1,q}^k + \alpha_r^k\phi_{p+1,q}^k + \alpha_d^k\phi_{p,q-1}^k + \alpha_u^k\phi_{p,q+1}^k + \Big[\alpha_m^k - \frac{4ik_0n_0}{\Delta z} + k_0^2(\varepsilon_r^k(p,q) - n_0^2)\Big]\phi_{p,q}^k \quad (2.68)$$

As the field at point k is assumed to be known, equation (2.68) results in a structurally symmetric sparse matrix equation of the form $Ax = B$, to be solved at each propagation step. This equation was solved using the large sparse linear system of equations solver, Intel MKL PARDISO [35]. Intel MKL PARDISO was used as it included a parallel solver optimised for structurally symmetric sparse matrix equations and was also optimised for Intel processors.

2.3.3 Boundary Conditions

As applying the finite difference beam propagation method requires a finite computational area, boundary conditions must be implemented at the edge of the computational window. Without these boundary conditions, radiated waves would be reflected back into the waveguide at the computational boundary and would then interfere with the propagating fields. This would greatly reduce the accuracy of the BPM simulation and therefore these boundary conditions are required to supress the reflections at the boundary. Two different boundary conditions were used with this BPM, their use depending on the waveguide structure and the method used to analyse the waveguide.

2.3.3.1 Transparent Boundary Condition

The transparent boundary condition (TBC) [36] was developed by Hadley as a way to simulate a non-existent boundary, where radiation is allowed to escape the waveguide without appreciable reflection.

In the TBC, the field is assumed to be of the following form, with k_x representing the $\hat{\boldsymbol{x}}$ directed wave number and k_y representing the $\hat{\boldsymbol{y}}$ directed wave number:

$$\phi(x,y,z) = A(x,y,z)\exp(ik_x x)\exp(ik_y y) \quad (2.69)$$

At the waveguide boundary, the value of k_x or k_y (depending on the direction of the normal to the boundary) can be determined by using the boundary point and the point closest to that boundary point. For example, if the boundary is on the right-hand side in the $\hat{\boldsymbol{x}}$ direction at an arbitrary y and z location and the x axis is discretised into N points, the fields at the boundary point and at the point closest to the boundary point can be represented by $\phi_{N,q}^k$ and $\phi_{N-1,q}^k$, respectively, and are given by:

$$\phi_{N,q}^{k} = A(y,z)\exp(ik_x x_N) \tag{2.70}$$

$$\phi_{N-1,q}^{k} = A(y,z)\exp(ik_x x_{N-1}) \tag{2.71}$$

Dividing $\phi_{N,q}^{k}$ by $\phi_{N-1,q}^{k}$ gives the following expression for k_x:

$$k_x = -\frac{i}{x_N - x_{N-1}}\ln\left(\frac{\phi_{N,q}^{k}}{\phi_{N-1,q}^{k}}\right) \tag{2.72}$$

If a hypothetical point exists just outside the computational area at x_{N+1}, a distance Δx away from the boundary point where $\Delta x = x_{N+1} - x_N = x_N - x_{N-1}$, the field at this point can be expressed as:

$$\phi_{N+1,q}^{k} = A(y,z)\exp(ik_x x_{N+1}) \tag{2.73}$$

Dividing $\phi_{N+1,q}^{k}$ by $\phi_{N,q}^{k}$ gives the following expression for $\phi_{N+1,q}^{k}$:

$$\phi_{N+1,q}^{k} = \phi_{N,q}^{k}\exp(ik_x \Delta x) \tag{2.74}$$

Substituting in the value for k_x from equation (2.72) gives the following expression:

$$\phi_{N+1,q}^{k} = \frac{\phi_{N,q}^{k}}{\phi_{N-1,q}^{k}}\phi_{N,q}^{k} = \alpha_b \phi_{N,q}^{k} \tag{2.75}$$

However, as the wave travels rightward towards the boundary, this boundary condition is only sufficient to supress reflections at the boundary point if the real part of k_x is positive. If k_x is negative, this implies reflection occurs at the boundary, and therefore the sign of the real part of k_x must be switched to ensure the radiation escapes. If the sign of the real part of k_x is switched, the previously found field at the boundary point must be altered in accordance with this sign change as shown by equation (2.72).

Implementation of the boundary condition causes the finite difference equation (2.68) to take the following form at the right-hand boundary:

$$-\alpha_l^{k+1}\phi_{N-1,q}^{k+1} - \alpha_d^{k+1}\phi_{N,q-1}^{k+1} - \alpha_u^{k+1}\phi_{N,q+1}^{k+1} - \left[\alpha_m^{k+1} + \frac{4ik_0 n_0}{\Delta z} + \alpha_r^{k+1}\alpha_b + k_0^2(\varepsilon_r^{k+1}(N,q) - n_0^2)\right]\phi_{N,q}^{k+1} = \alpha_l^{k}\phi_{N-1,q}^{k} + \alpha_d^{k}\phi_{N,q-1}^{k} + \alpha_u^{k}\phi_{N,q+1}^{k} + \left[\alpha_m^{k} + \alpha_r^{k}\alpha_b - \frac{4ik_0 n_0}{\Delta z} + k_0^2(\varepsilon_r^{k}(N,q) - n_0^2)\right]\phi_{N,q}^{k} \tag{2.76}$$

The same procedure must be followed for points on the other boundaries, where the sign of k_x and k_y is flipped if necessary, to ensure radiation escapes at the boundary.

2.3.3.2 Perfectly Matched Layers

Another technique to supress reflections at the boundaries is Bérenger's perfectly matched layers (PMLs) [37] boundary condition. This technique involves placing layers with anisotropic conductivity at the edge of the computational area. This boundary condition requires additional memory and computation time but can be far more effective than the TBC for certain waveguide structures and especially for wide-angle propagation.

In this technique, the wave equation is mapped through an anisotropic complex transformation. The mapping produces a wave that is perfectly matched with the out-going waves in the original waveguide. If x',y' and z' were components of the original coordinate system, the coordinates are transformed as follows [39]:

$$x' \to x\left(1 + \frac{i\sigma_x}{\omega\varepsilon_0 n^2}\right) \tag{2.77}$$

$$y' \to y\left(1 + \frac{i\sigma_z}{\omega\varepsilon_0 n^2}\right) \tag{2.78}$$

$$z' \to z\left(1 + \frac{i\sigma_z}{\omega\varepsilon_0 n^2}\right) \tag{2.79}$$

σ_x, σ_y and σ_z are the anisotropic conductivities of the PML region. n is the refractive index of the PML region, which is assumed to be the same as that of the adjacent original computational region. The derivatives in the wave equations are replaced as shown below:

$$\frac{\partial}{\partial x'} \to \left(1 + \frac{i\sigma_x}{\omega\varepsilon_0 n^2}\right)^{-1} \frac{\partial}{\partial x} \tag{2.80}$$

$$\frac{\partial}{\partial y'} \to \left(1 + \frac{i\sigma_y}{\omega\varepsilon_0 n^2}\right)^{-1} \frac{\partial}{\partial y} \tag{2.81}$$

$$\frac{\partial}{\partial z'} \to \left(1 + \frac{i\sigma_z}{\omega\varepsilon_0 n^2}\right)^{-1} \frac{\partial}{\partial z} \tag{2.82}$$

As the refractive index is assumed to be constant across the PML boundary, if ϕ_1 is the field in the original region, ϕ_2 is the field in the PML region and $i = x, y, z$, the continuity equations require the following:

$$\phi_1 = \phi_2 \tag{2.83}$$

$$\left(1 + \frac{i\sigma_{i1}}{\omega\varepsilon_0 n^2}\right)^{-1} \frac{\partial\phi_1}{\partial i} = \left(1 + \frac{i\sigma_{i2}}{\omega\varepsilon_0 n^2}\right)^{-1} \frac{\partial\phi_2}{\partial i} \tag{2.84}$$

If R is the reflection coefficient at the boundary and the normal to the boundary is assumed to be in the $\hat{\boldsymbol{x}}$ direction, the field takes the following form in the non-PML region:

$$\phi_1 = \exp\left(ik_{x1}x + ik_{y1}y + ik_{z1}z\right) + R\exp\left(-ik_{x1}x + ik_{y1}y + ik_{z1}z\right) \tag{2.85}$$

If T is the transmission coefficient at the boundary, the field takes the following form in the PML region:

$$\phi_2 = T\exp\left(ik_{x2}x + ik_{y2}y + ik_{z2}z\right) \tag{2.86}$$

The k_{ij} wavenumbers above have been modified due to the coordinate transformation as follows:

$$k_{xj} = \left(1 + \frac{i\sigma_{xj}}{\omega\varepsilon_0 n^2}\right) nk_0 \sin\theta_j \cos\varphi_j \tag{2.87}$$

$$k_{yj} = \left(1 + \frac{i\sigma_{yj}}{\omega\varepsilon_0 n^2}\right) nk_0 \sin\theta_j \sin\varphi_j \tag{2.88}$$

$$k_{zj} = \left(1 + \frac{i\sigma_{zj}}{\omega\varepsilon_0 n^2}\right) nk_0 \cos\theta_j \tag{2.89}$$

The angles θ_j and φ_j are the polar and arizmuthal angles respectively on either side of the boundary in the spherical coordinate system, formed by the direction of the field incident on the boundary, as shown in Figure 2.4.

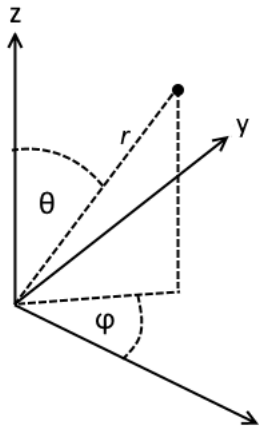

Figure 2.4: Coordinate system of propagating wave

If the field is assumed to be incident on the boundary at $x = 0$, utilising the boundary condition (2.83), each boundary condition of (2.84) leads to the following relationships:

$$i = z, \quad \cos\theta_1 = \cos\theta_2 \tag{2.90}$$

$$i = y, \quad \sin\theta_1 \sin\varphi_1 = \sin\theta_2 \sin\varphi_2 \tag{2.91}$$

$$i = x, \quad R = \frac{\sin\theta_1 \cos\varphi_1 - \sin\theta_2 \cos\varphi_2}{\sin\theta_2 \cos\varphi_2 + \sin\theta_1 \cos\varphi_2} \tag{2.92}$$

According to equations (2.90) and (2.91), $\theta_1 = \theta_2, \varphi_1 = \varphi_2$. This results in $R = 0$, meaning there is no reflection at the PML boundary no matter the angle the field is incident upon the boundary.

As the PML boundary is along the $\hat{\boldsymbol{x}}$ direction, σ_y and σ_z can be set to zero, giving the field the following form in the PML region:

$$\phi = \exp(ink_0(\sin\theta\cos\varphi\, x + \sin\theta\sin\varphi\, y + \cos\theta\, z)\exp\left(-\sigma_x n^{-1}\sin\theta\cos\varphi\sqrt{\mu_0/\varepsilon_0}x\right) \tag{2.93}$$

Therefore, the non-physical wave in the fictitious PML region matches perfectly with the physical wave in the real region adjacent to it and decays exponentially with the decay constant $\alpha_x = \sigma_x n^{-1}\sin\theta\cos\varphi\sqrt{\mu_0/\varepsilon_0}$. The same procedure is done for the PML outside the boundaries in the $\hat{\boldsymbol{y}}$ direction where the attenuation constant is instead given by $\alpha_y = \sigma_y n^{-1}\sin\theta\sin\varphi\sqrt{\mu_0/\varepsilon_0}$.

Implementation of the PML boundary condition causes the E_x wave equation in the quasi-TE mode to take the following form (after the application of the SVEA):

$$-2ik_0 n_0 \frac{\partial \phi}{\partial z} = q_x \frac{\partial}{\partial x}\left(q_x \frac{\partial \phi}{\partial x}\right) + q_x \frac{\partial}{\partial x}\left(\frac{q_x}{\varepsilon_r}\frac{\partial \varepsilon_r}{\partial x}\phi\right) + q_y \frac{\partial}{\partial y}\left(q_y \frac{\partial \phi}{\partial y}\right) + k_0^2(\varepsilon_r - n_0^2)\phi \quad (2.94)$$

The variables q_x and q_y are defined by:

$$q_x = \frac{1}{1+i\sigma_x/\omega\varepsilon_0 n^2}, \quad q_y = \frac{1}{1+i\sigma_y/\omega\varepsilon_0 n^2} \quad (2.95)$$

σ_x and σ_y are only set to a non-zero value in the PML regions outside boundaries in their respective directions. Meanwhile, σ_z has been set to 0 for all PML regions.

The resulting finite difference expression will take the same form as (2.68) with the α components modified to account for the q_x and q_y terms.

2.3.4 Testing 3D-SV-FD-BPM

To ensure the BPM was implemented correctly, a number of different propagating beams and waveguides were analysed. The first test was the propagation of a simple Gaussian beam in a uniform medium, which was sent propagating towards the computational boundary.

Assuming the field is polarized in the $\hat{\boldsymbol{x}}$ direction and propagates in the $\hat{\boldsymbol{r}}$ direction, the Gaussian shaped electric field takes the following initial form:

$$E(x, y, 0) = E_0 \exp\left(\frac{-\rho^2}{\omega_0^2}\right) \exp\left(i\left(k_x x + k_y y + k_z z\right)\right)\hat{\boldsymbol{x}} \quad (2.96)$$

$E_0 = E(0,0,0)$ is the initial field amplitude at the origin, ω_0 is the radial distance from the centre of the Gaussian where the field amplitude falls to $1/e$ of its value at the centre of the Gaussian, ρ is the radial distance from the centre of the Gaussian, and k_x, k_y and k_z are the wavenumbers in their respective directions and are given by:

$$k_x = nk_0 \sin\theta \cos\varphi \quad (2.97)$$

$$k_y = nk_0 \sin\theta \sin\varphi \quad (2.98)$$

$$k_z = nk_0 \cos\theta \quad (2.99)$$

To test the boundary conditions, the Gaussian was propagated at angles $\theta = 10°$ and $\varphi = 45°$ in a medium of uniform refractive index. If the boundary conditions are implemented correctly, the Gaussian should pass out of the computational region without appreciable reflection. The following parameters were used for the Gaussian beam: $E_0 = 1.2, \lambda = 1.55\ \mu m, \omega_0 = \lambda/2, n = 16$. A large refractive index value was used to prevent the beam radius growing too large as it propagated (Gaussian spreading) to allow the passage of the beam to be observed more easily. 201 equally spaced points were used in both the $\hat{\boldsymbol{x}}$ and $\hat{\boldsymbol{y}}$ directions giving a point spacing of 0.025 μm. Δz was equal to $0.1\ \mu m$. Although the Δz value is considerably greater than the transverse spacing, one of the advantages of the FD-BPM is to ability to use a relatively large propagation step, as the Crank-Nichelson scheme results in a very small error [40].

Figure 2.5 shows the propagation of the Gaussian beam with the implementation of the TBC. As can be seen from the graph, the beam passes through the computational area

without appreciable reflection. Figure 2.6 shows the propagation of the same Gaussian beam, this time with the implementation of the PML boundary condition. The PML region is not displayed in the graphs but extends for $L = 1\ \mu m$ beyond each boundary. The conductivities of the region are given by:

$$\sigma_x = \sigma_{max}\left(\frac{x - x_n}{L}\right)^2, \quad x \in [x_n, x_n + L] \tag{2.100}$$

$$\sigma_x = \sigma_{max}\left(\frac{x_1 - x}{L}\right)^2, \quad x \in [x_1 - L, x_1] \tag{2.101}$$

$$\sigma_y = \sigma_{max}\left(\frac{y - y_n}{L}\right)^2, \quad y \in [y_n, y_n + L] \tag{2.102}$$

$$\sigma_y = \sigma_{max}\left(\frac{y_1 - y}{L}\right)^2, \quad y \in [y_1 - L, y_1] \tag{2.103}$$

x_1, x_n, y_1, y_n represent the boundary points of the original non-PML region. $\sigma_{\max}$ must be tailored for each PML region to ensure the reflections are sufficiently surpessed. In this case, $\sigma_{\max} = 1.5\ \varepsilon_0 \omega$.

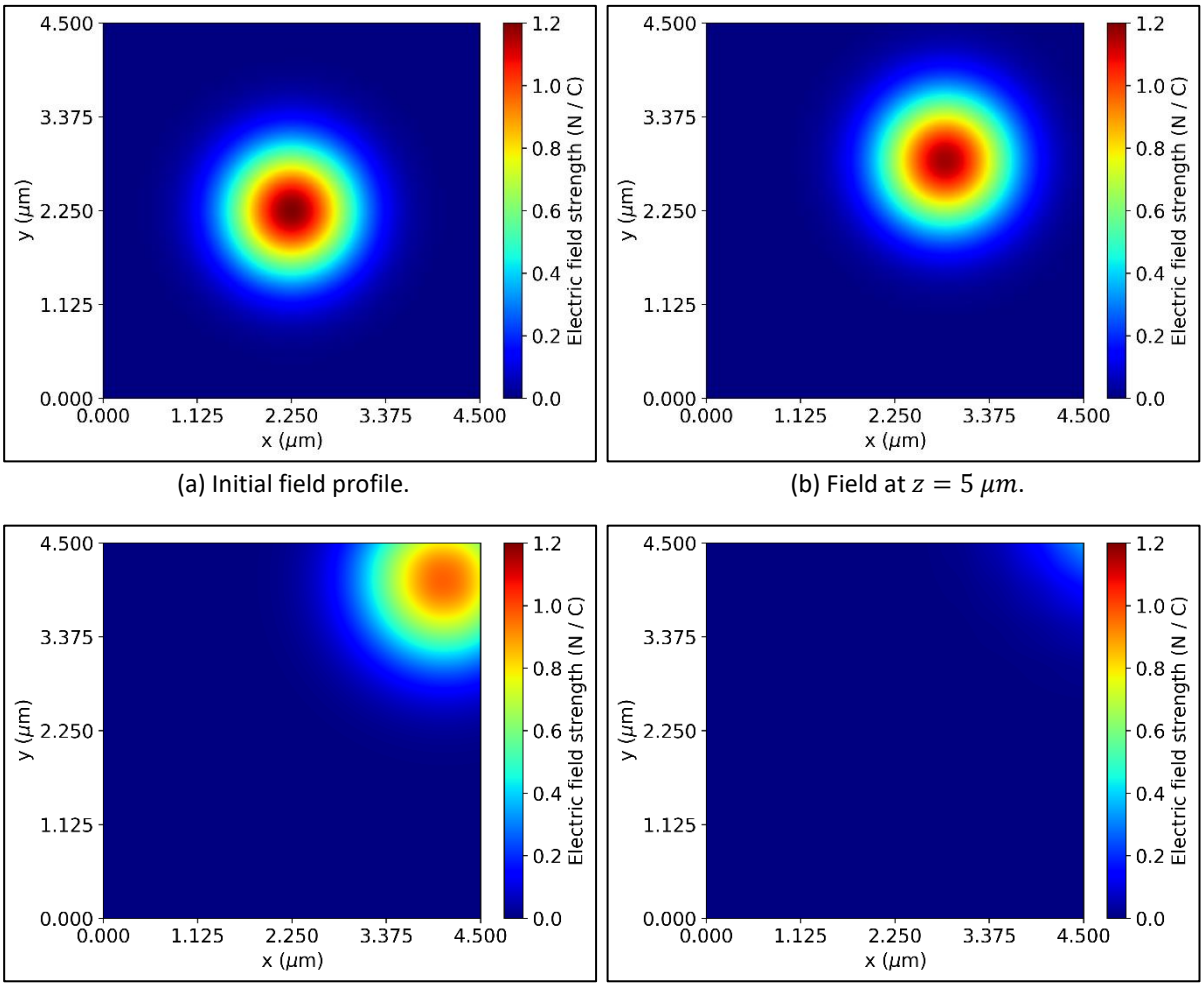

(a) Initial field profile.

(b) Field at $z = 5\ \mu m$.

(c) Field at $z = 15\ \mu m$.

(d) Field at $z = 25\ \mu m$.

Figure 2.5: Gaussian beam propagating through a uniform medium at angles $\theta = 10°$ and $\varphi = 45°$ with the TBC implemented.

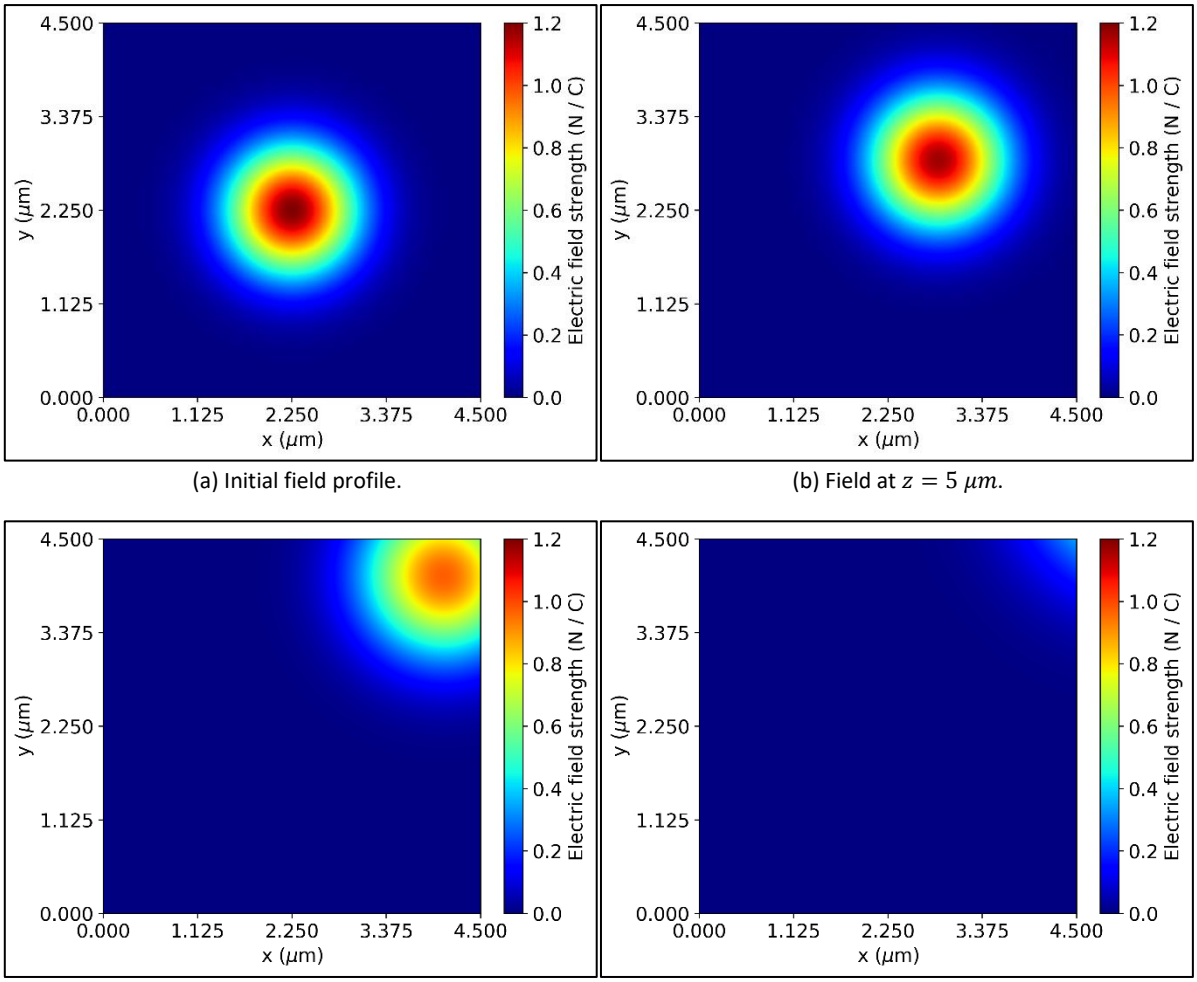

(a) Initial field profile.

(b) Field at $z = 5\ \mu m$.

(c) Field at $z = 15\ \mu m$.

(d) Field at $z = 25\ \mu m$.

Figure 2.6: Gaussian beam propagating through a uniform medium at angles $\theta = 10°$ and $\varphi = 45°$ with the PML implemented.

Figure 2.7 shows the fraction of power remaining in the computational area as the Gaussian propagates towards the boundary in the cases of both the TBC and PML. The graphs prove both boundary conditions to be effective with the TBC leaving slightly less power in the computational area than the PML after 100 μm in this case.

The BPM was then tested by propagating a Gaussian through the rectangular waveguide given by Figure 2.1. If the BPM is working correctly, the Gaussian would be expected to eventually take the shape of the fundamental mode as it propagates, as the waveguide only supports a single mode.

The Gaussian took the form of equation (2.96) with $\lambda = 1.55\ \mu m$, $E_0 = 0.03$, and $\omega_0 = \lambda/4$. 201 equally spaced points were used in both the $\hat{\boldsymbol{x}}$ and $\hat{\boldsymbol{y}}$ directions giving a point spacing of 0.022 μm. The Gaussian was propagated for 50 μm with 500 points used in the propagation direction giving a step size of $0.1\ \mu m$ in the $\hat{\boldsymbol{z}}$ direction. The shape of the Gaussian is given by Figure 2.8 (a) and, due to the lack of discontinuities in the magnetic fields, is assumed to represent the magnetic field H_y in the quasi-TE mode.

Figure 2.8 (b) shows the shape of the field after it has propagated $50\ \mu m$. The field has taken the form of the fundamental mode shown in Figure 2.2 (b). To further illustrate this, Figure 2.9 gives the overlap integral error (OIE) between the propagating Gaussian beam and the fundamental mode. The OIE is a sensitive measure of the deformation between two fields and is given by:

$$O_E = 1 - \frac{|\int_0^{Ly}\int_0^{Lx}\psi_1^*\psi_2\,dx\,dy|^2}{\int_0^{Ly}\int_0^{Lx}|\psi_1|^2\,dx\,dy\,\int_0^{Ly}\int_0^{Lx}|\psi_2|^2\,dx\,dy} \tag{2.104}$$

The OIE approaches 0 as the field propagates, showing that the initial Gaussian field takes the form of the fundamental mode.

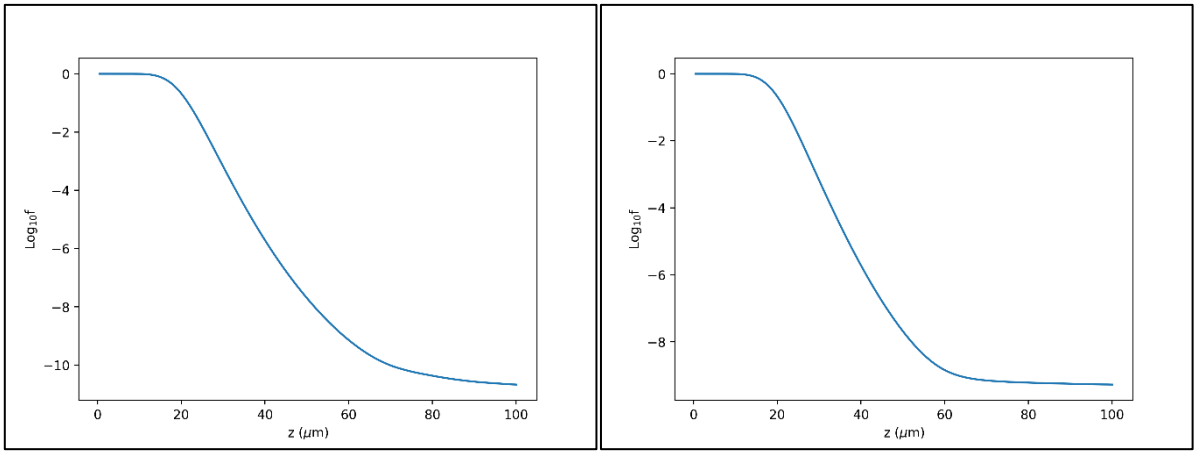

(a) TBC (b) PML

Figure 2.7: Log_{10} of the fraction of power remaining in the computational area as the Gaussian propagates.

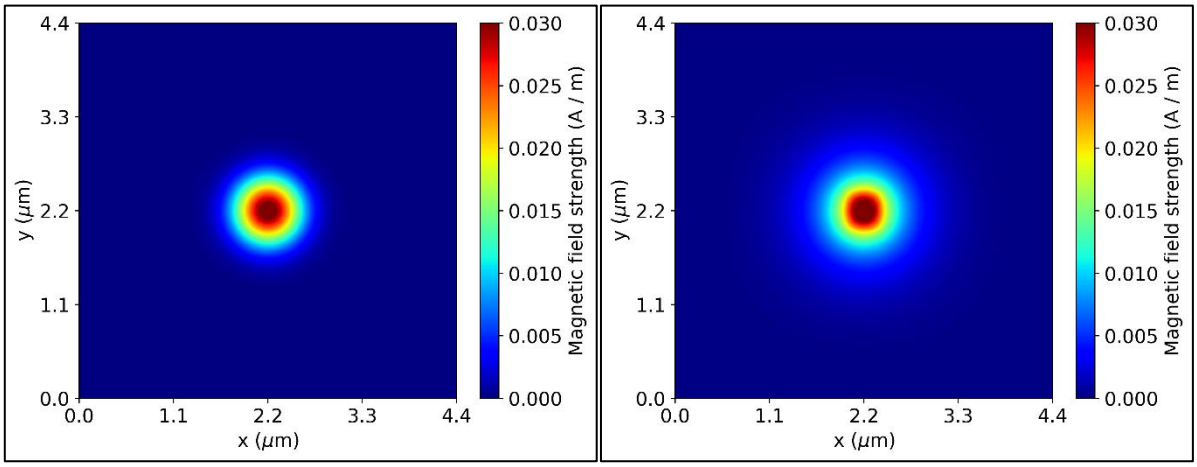

(a) Initial Gaussian. (b) Field at $z = 50\ \mu m$.

Figure 2.8: Initial and propagating form of Gaussian field assumed to be the magnetic field H_y in the quasi-TE mode as it propagates through a square waveguide.

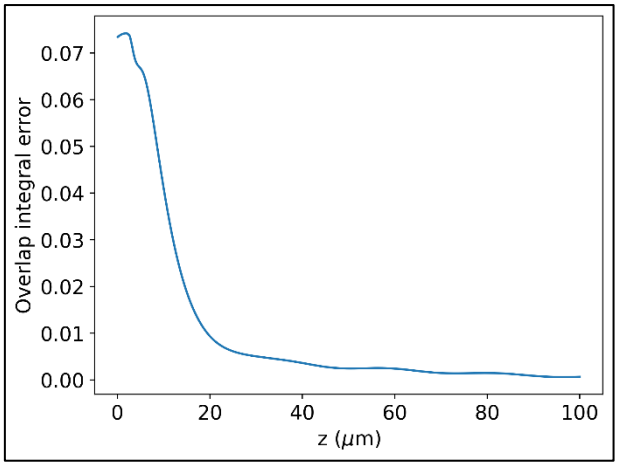

Figure 2.9: Overlap integral error between propagating Gaussian and the quasi-TE H_y fundamental mode of a rectangular waveguide.

To further test the boundary conditions, the Gaussian was propagated through the uniform medium along the z axis, causing it to spread due to diffraction. The analytical solution to the paraxial wave equation is known for this "Gaussian spreading" and is given by [38]:

$$E(x,y,z) = E_0 \frac{W_0}{W(z)} \exp\left(\frac{-(x^2+y^2)}{W^2(z)}\right) \exp\left(i\left(k_z z + k_z \frac{(x^2+y^2)}{2R(z)} + i\varphi(\mathrm{z})\right)\right)\hat{\boldsymbol{x}} \qquad (2.105)$$

In the above equation, $W(z)$ is known as the beam width and $W(z) = W_0\sqrt{1+\left(\frac{z}{z_0}\right)^2}$, W_0 is the waist radius, i.e. the beam width at $z = 0$ and equals $\frac{\lambda z_0}{n\pi}$, z_0 is the Rayleigh range, $R(z) = z\left[\left(1+\left(\frac{z_0}{z}\right)^2\right)\right]$, and $\varphi(z)$ is the phase retardation due to the Gouy Effect. As the analytical solution is known, the numerical computations can be compared with the analytical solution and the effectiveness of the boundary conditions can be further investigated. Figure 2.10 gives the Log_{10} of the fraction of power remaining in the computational area as the Gaussian propagates. The resulting curves appear very similar, suggesting the boundary conditions have successfully suppressed the reflections. Figure 2.11 gives the field distribution for both boundary conditions and the analytical solution at $z = 100\ \mu m$. The graphs appear to suggest that while the TBC allowed the radiation to pass outside the computational region, it was less successful at maintaining the shape of the propagating Gaussian. Meanwhile, the PML proved far more capable with this problem as the shape of the field closely resembled that of the analytical solution. The results suggest that the PML boundary conditions should be used when dealing with diffraction problems of this nature.

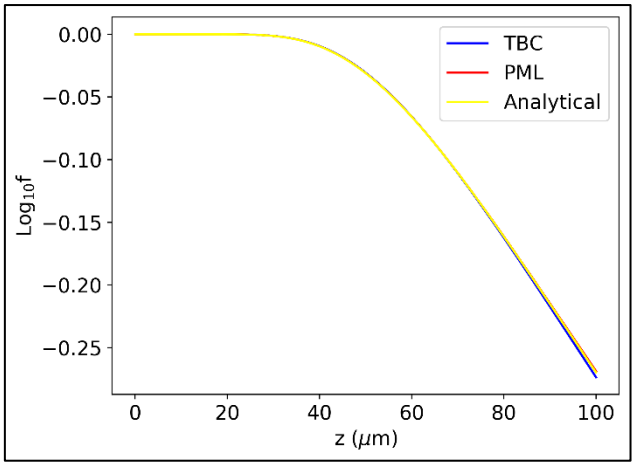

Figure 2.10: Log_{10} of the fraction of power remaining in the computational area as the Gaussian propagates for the TBC and PML boundary conditions and the analytical case.

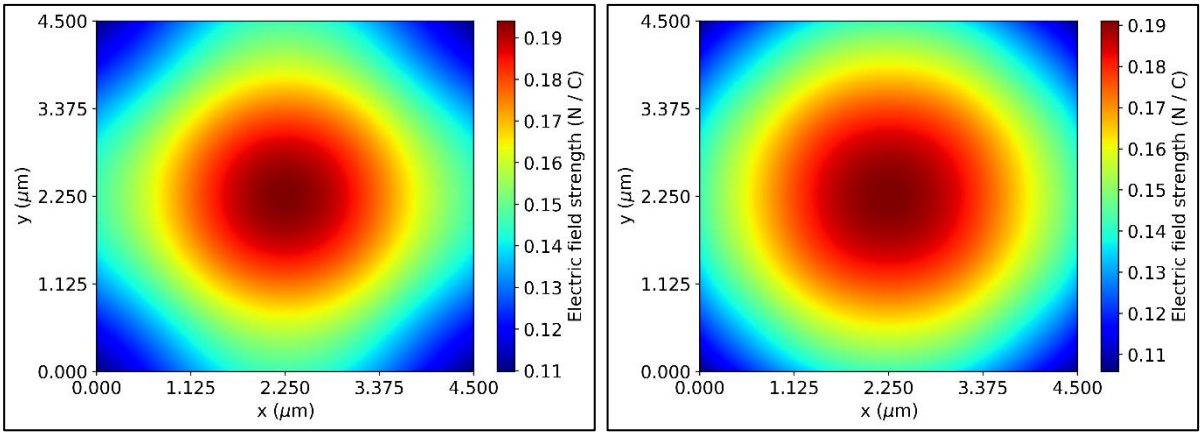

(a) TBC.

(b) PML.

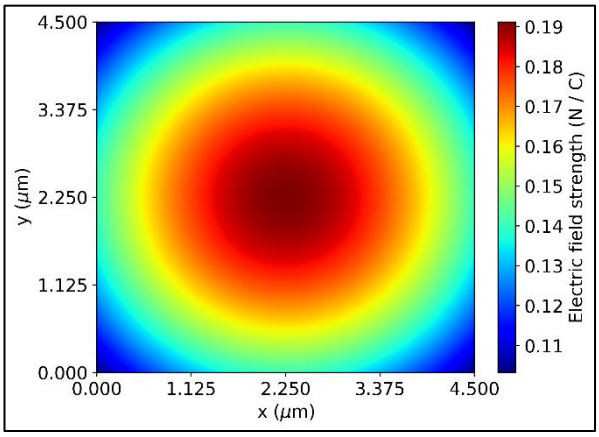

(b) Analytical solution.

Figure 2.11: Gaussian beam propagating along the z axis at $z = 100\ \mu m$ for the TBC and PML boundary conditions as well as the analytical solution.

2.4 Wide-Angle Propagation

Before this section, the BPM was based on the Fresnel wave equation, where the field was assumed to be propagating in primarily the $\hat{\boldsymbol{z}}$ direction. Here, wide-angle propagation is

implemented using Hadley's technique involving Padé approximant operators [41] and the multistep method [42].

2.4.1 Padé Approximant Operators

If the Fresnel approximation is not used, i.e. the second derivative with respect to z is not ignored, the wave equation takes the following form:

$$-2ik_0n_0\frac{\partial\phi}{\partial z}-\frac{\partial^2\phi}{\partial z^2}=P\phi \tag{2.106}$$

ϕ is the complex field amplitude from equation (2.61) and P is an operator which depends on the mode and field analysed. P takes the following forms:

$$P_{TE(E_x)}=\frac{\partial^2}{\partial x^2}+\frac{\partial}{\partial x}\left(\frac{1}{\varepsilon_r}\frac{\partial\varepsilon_r}{\partial x}\right)+\frac{\partial^2}{\partial y^2}+k_0^2(\varepsilon_r-n_0^2) \tag{2.107}$$

$$P_{TE(H_y)}=\varepsilon_r\frac{\partial}{\partial x}\left(\frac{1}{\varepsilon_r}\frac{\partial}{\partial x}\right)+\frac{\partial^2}{\partial y^2}+k_0^2(\varepsilon_r-n_0^2) \tag{2.108}$$

$$P_{TM(E_y)}=\frac{\partial^2}{\partial x^2}+\frac{\partial^2}{\partial y^2}+\frac{\partial}{\partial y}\left(\frac{1}{\varepsilon_r}\frac{\partial\varepsilon_r}{\partial y}\right)++k_0^2(\varepsilon_r-n_0^2) \tag{2.109}$$

$$P_{TM(H_x)}=\frac{\partial^2}{\partial x^2}+\varepsilon_r\frac{\partial}{\partial y}\left(\frac{1}{\varepsilon_r}\frac{\partial}{\partial y}\right)+k_0^2(\varepsilon_r-n_0^2) \tag{2.110}$$

Rewriting equation (2.106):

$$\frac{\partial}{\partial z}\left(1-\frac{i}{2k_0n_0}\frac{\partial}{\partial z}\right)\phi=\frac{iP}{2k_0n_0}\phi \tag{2.111}$$

Therefore:

$$\frac{\partial\phi}{\partial z}=\frac{iP/2k_0n_0}{1-(i/2k_0n_0)(\partial/\partial z)}\phi \tag{2.112}$$

Regarding the derivatives with respect to z in equation (2.112), a recurrence relation between the left and right hand side can be constructed as follows:

$$\left.\frac{\partial}{\partial z}\right|_n=\left.\frac{iP/2k_0n_0}{1-(i/2k_0n_0)(\partial/\partial z)}\right|_{n-1},\quad\left.\frac{\partial}{\partial z}\right|_0=0 \tag{2.113}$$

If n is considered to be the wide-angle order, the results for the first 6 orders of equation (2.113) are given below:

1. $n=1$ (Fresnel approximation)

$$\left.\frac{\partial}{\partial z}\right|_1=i\frac{P}{2k_0n_0} \tag{2.114}$$

2. $n=2$

$$\left.\frac{\partial}{\partial z}\right|_2=i\frac{P/2k_0n_0}{1+P/4k_0^2n_0^2} \tag{2.115}$$

3. $n=3$

$$\left.\frac{\partial}{\partial z}\right|_3=i\frac{P/2k_0n_0+P^2/8k_0^3n_0^3}{1+P/2k_0^2n_0^2} \tag{2.116}$$

4. $n = 4$

$$\left.\frac{\partial}{\partial z}\right|_4 = i\frac{P/2k_0n_0 + P^2/4k_0^3n_0^3}{1 + 3P/4k_0^2n_0^2 + P^2/16k_0^4n_0^4} \tag{2.117}$$

5. $n = 5$

$$\left.\frac{\partial}{\partial z}\right|_5 = i\frac{P/2k_0n_0 + 3P^2/8k_0^3n_0^3 + P^3/32k_0^5n_0^5}{1 + P/k_0^2n_0^2 + 3P^2/16k_0^4n_0^4} \tag{2.118}$$

6. $n = 6$

$$\left.\frac{\partial}{\partial z}\right|_6 = i\frac{P/2k_0n_0 + P^2/2k_0^3n_0^3 + 3P^3/32k_0^5n_0^5}{1 + 5P/4k_0^2n_0^2 + 3P^2/8k_0^4n_0^4 + P^3/64k_0^6n_0^6} \tag{2.119}$$

Therefore, the recurrence relation (2.113) can be reduced to an expression that only includes the components N and D which are both polynomials of the P operator:

$$\frac{\partial\phi}{\partial z} = i\frac{N}{D}\phi \tag{2.120}$$

The wide-angle orders correspond to the Padé operators as follows (the Padé order is of the form (A, B), where A is the degree of the P polynomial in N and B is the degree of the P polynomial in D):

Wide-angle order (n)	**Padé order**
1	(1, 0)
2	(1, 1)
3	(2, 1)
4	(2, 2)
5	(3, 2)
6	(3, 3)

Table 2.1: Wide-angle and Padé orders

2.4.2 Finite Difference Expressions Utilising Padé Approximant Operators

Differentiating equation (2.120) using the finite difference method and making both sides have the same difference centre results in the following finite difference expression:

$$\frac{1}{\Delta z}(\phi^{k+1} - \phi^k) = i\frac{N}{D}\frac{1}{2}(\phi^{k+1} + \phi^k) \tag{2.121}$$

Restructuring the equation allows it to take the following form:

$$\phi^{k+1} = \frac{D + i(\Delta z/2)N}{D - i(\Delta z/2)N}\phi^k \tag{2.122}$$

As the coefficients of the polynomials N and D are real, the equation can be written as:

$$\phi^{k+1} = \frac{D + i(\Delta z/2)N}{[D + i(\Delta z/2)N]^*}\phi^k = \frac{\sum_{i=0}^{m}\xi_i P^i}{\sum_{i=0}^{m}\xi_i^* P^i}\phi^k \tag{2.123}$$

The m in the sum refers to the largest power of P in N and D and is therefore equal to the larger of the A, B values in the (A, B) Padé order. The values ξ_i for each Padé order are as follows:

Padé order	ξ_0	ξ_1	ξ_2	ξ_3
(1, 0)	1	$\frac{i\Delta z}{4k_0 n_0}$	N/A	N/A
(1, 1)	1	$\frac{1}{4k_0^2 n_0^2}(1 + ik_0 n_0 \Delta z)$	N/A	N/A
(2, 1)	1	$\frac{1}{4k_0^2 n_0^2}(2 + ik_0 n_0 \Delta z)$	$\frac{i\Delta z}{16k_0^3 n_0^3}$	N/A
(2, 2)	1	$\frac{1}{4k_0^2 n_0^2}(3 + ik_0 n_0 \Delta z)$	$\frac{1}{16k_0^4 n_0^4}(1 + i2k_0 n_0 \Delta z)$	N/A
(3, 2)	1	$\frac{1}{4k_0^2 n_0^2}(4 + ik_0 n_0 \Delta z)$	$\frac{1}{16k_0^4 n_0^4}(3 + i3k_0 n_0 \Delta z)$	$\frac{i\Delta z}{64k_0^5 n_0^5}$
(3, 3)	1	$\frac{1}{4k_0^2 n_0^2}(5 + ik_0 n_0 \Delta z)$	$\frac{1}{16k_0^4 n_0^4}(6 + i4k_0 n_0 \Delta z)$	$\frac{1}{64k_0^6 n_0^6}(1 + i3k_0 n_0 \Delta z)$

Table 2.2: Coefficients of P^i for each Padé order

Therefore, the unknown field at ϕ^{k+1} can be found using equation (2.123).

2.4.3 Multistep Method

Due to equation (2.123) potentially containing P with powers greater than 1, the finite difference expression becomes more complicated and the subsequent matrix becomes less sparse as the Padé order increases. Fortunately, Hadley developed a method which simplifies the problem, the multistep method, originally created to keep the component matrix tridiagonal for his 2D analysis, as a tridiagonal matrix equation is much more numerically efficient to solve.

Consider the numerator on the right-hand side of equation (2.123). As ξ_0 always equals 1, the numerator is always written in the form $1 + \xi_1 P^1 + \xi_2 P^2 + \cdots + \xi_m P^m$. This allows the numerator to be factorised in the following form:

$$\sum_{i=0}^{m} \xi_i P^i = (1 + a_m P) \dots (1 + a_2 P)(1 + a_1 P) \tag{2.124}$$

The a coefficients can be found algebraically by relating them with the previously found ξ coefficients.

As the denominator of the right-hand side of equation (2.123) is just the complex conjugate of the numerator, it can be represented as:

$$\sum_{i=0}^{m} \xi_i^* P^i = (1 + a_m^* P) \dots (1 + a_2^* P)(1 + a_1^* P) \tag{2.125}$$

The field ϕ^{k+1} is therefore related to the field ϕ^k as follows:

$$\phi^{k+1} = \frac{(1+a_m P)\dots(1+a_2 P)(1+a_1 P)}{(1+a_m^* P)\dots(1+a_2^* P)(1+a_1^* P)} \phi^k \tag{2.126}$$

In order to solve the equation, it must first be rewritten as:

$$\frac{(1+a_m^* P)\dots(1+a_2^* P)}{(1+a_m P)\dots(1+a_2 P)} \phi^{k+1} = \frac{(1+a_1 P)}{(1+a_1^* P)} \phi^k \tag{2.127}$$

Allowing the left-hand side of the equation to be written as:

$$\frac{(1+a_m^*P)\ldots(1+a_2^*P)}{(1+a_mP)\ldots(1+a_2P)}\phi^{k+1} = \phi^{k+\frac{1}{m}} \tag{2.128}$$

Equation (2.127) can be represented by:

$$(1 + a_1^*P)\phi^{k+\frac{1}{m}} = (1 + a_1P)\phi^k \tag{2.129}$$

After applying the P operator, this equation takes the same form as equation (2.68), allowing it to be solved in the same manner as that of the Fresnel equation. Once $\phi^{k+\frac{1}{m}}$ has been found, the procedure is repeated with:

$$(1 + a_2^*P)\phi^{k+\frac{2}{m}} = (1 + a_2P)\phi^{k+\frac{1}{m}} \tag{2.130}$$

The procedure is repeated until ϕ^{k+1} is found with the final equation being:

$$(1 + a_m^*P)\phi^{k+1} = (1 + a_mP)\phi^{k+\frac{m-1}{m}} \tag{2.131}$$

Therefore, to find ϕ^{k+1} using Padé approximant operators, the Fresnel calculation must be done m times, m being the largest value of the (A, B) components of the Padé operator, with the a coefficient changing for each computation. For this reason, it only makes sense to use the (1, 1), (2, 2) and (3, 3) Padé orders as the computation time is practically no different to their (m, m-1) Padé order counterparts.

2.4.4 Testing Wide-Angle Propagation

To test that the wide-angle propagation was working correctly, a Gaussian beam was propagated with angles $\theta = 45°$ and $\varphi = 0°$ through free space. The Gaussian took the form of equation (2.96), with $E_0 = 1, \omega_0 = 2.828\ \mu m$ and $\lambda = 1.55\ \mu m$, and was initially centred at $x = 10\ \mu m, y = 0\ \mu m$. The computational area extended for 36 μm in the $\hat{\boldsymbol{x}}$ and $\hat{\boldsymbol{y}}$ directions and 301 points were used in both directions, giving a point spacing of $\Delta x = \Delta y = 0.12\ \mu m$. Meanwhile, the point spacing in the $\hat{\boldsymbol{z}}$ direction was $0.05\ \mu m$. Due to the large propagating angle with the $\hat{\boldsymbol{z}}$ direction, the simulation was expected to get more accurate as the Padé order increased.

As the Gaussian only propagates in the $x - z$ plane, Figure 2.12 shows the shape of the intensity of an x cross section through the peak of the field at $z = 10\ \mu m$ for different Padé orders. As the Padé order increases, the angle of propagation is seen to get closer to $45°$ as the field's centre gets closer to $x = 20\ \mu m$. The paraxial simulation also incorrectly preserves the shape of the Gaussian as it propagates. The shape of the field should spread out and become asymmetrical as it propagates due to the effect of diffraction [41], which is accurately reflected in the higher Padé order simulations.

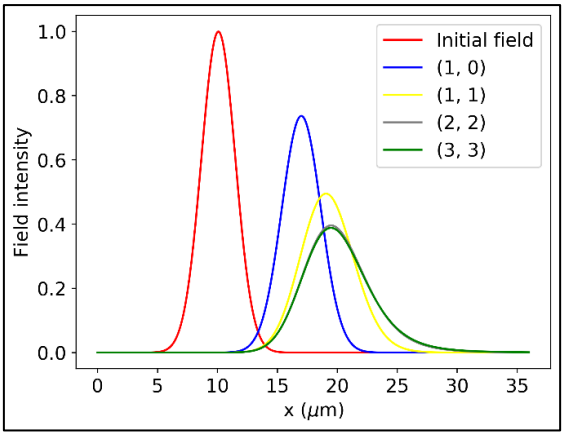

Figure 2.12: Field intensity at $z = 10\ \mu m$ after propagating through free space for different Padé orders.

According to various sources [43] [44], the use of Padé approximant operators should also significantly lessen the impact of the chosen reference refractive index on the accuracy of the beam propagation method. To verify this, a simple directional coupler was formed using two of the rectangular waveguides shown in Figure 2.1. The two waveguides were placed 0.6 μm apart as shown in Figure 2.13.

Only the left-hand waveguide was initially powered to observe the propagation distance when the power had completely transferred to the right-hand waveguide. This propagation distance is known as the coupling length. It is known that the coupling length of the directional coupler is related to the effective refractive indices of the even and odd modes of the directional coupler by the following equation [45], where n_{Eeff} is the effective index of the even mode and n_{Oeff} is the effective index of the odd mode:

$$L_C = \frac{\lambda}{2(n_{Eeff} - n_{Oeff})} \tag{2.132}$$

151 points were used in each transverse direction and the analysis was done on the E_x field in the quasi-TE mode. The found supported even and odd modes are given in Figure 2.14 and the found effective indices were 3.22581 and 3.20374 respectively. According to equation (2.132), this should give a coupling length of approximately 35.1 μm.

For the beam propagation simulation, the left-hand waveguide was initially powered and allowed to propagate for 100 μm with $\Delta z = 0.1\ \mu m$. The overlap integral error was found between the initial field and the propagating field at each propagation point, and the point where the error reached its maximum indicated the point where the power had completely transferred to the right-hand waveguide. Figure 2.15 shows the overlap integral error vs. propagating distance graph when the reference index was set to that of the even mode. The maximum error occurred at $z = 35.1\ \mu m$, which was the expected coupling length.

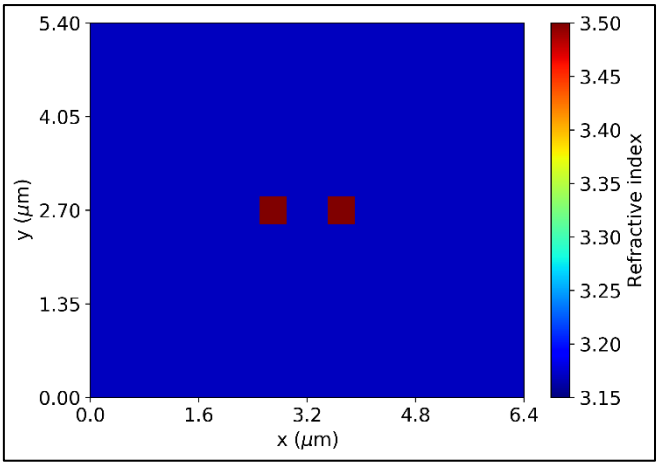

Figure 2.13: Directional coupler with two rectangular waveguides.

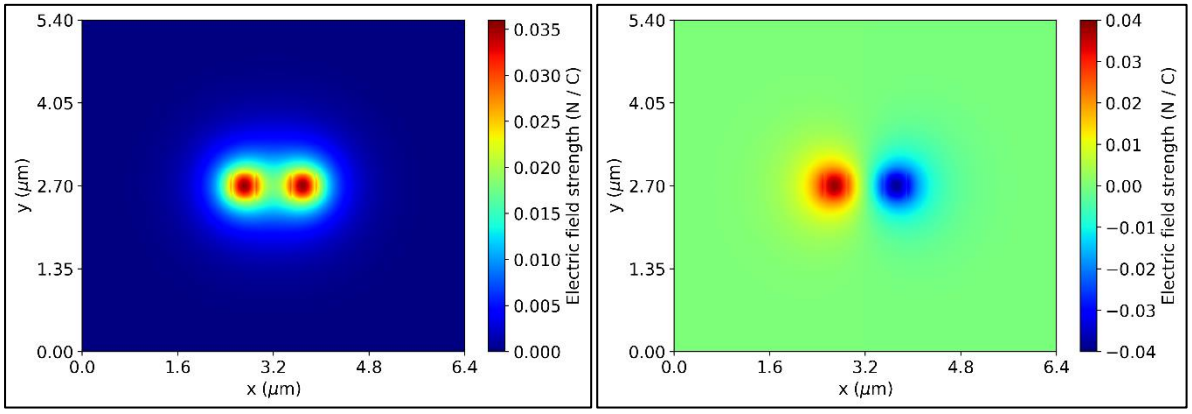

(a) Even mode. (b) Odd mode.

Figure 2.14: Even and odd modes of the directional coupler.

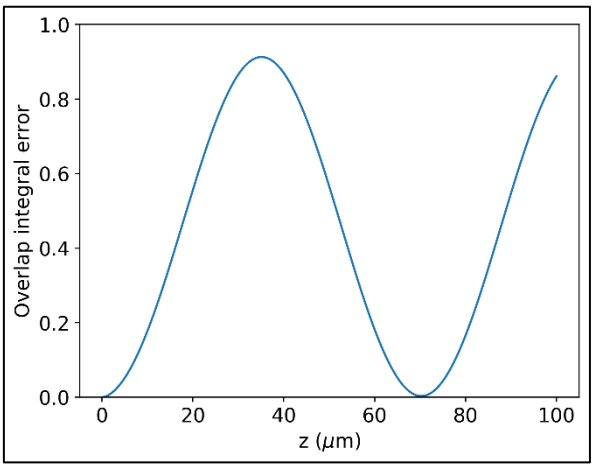

Figure 2.15: Overlap integral error vs. propagation distance through the directional coupler.

The reference index was then modified from this value and its impact on the coupling length was investigated for different Padé orders. Figure 2.16 displays the corresponding results and shows how the coupling length gets less sensitive to the reference refractive index as the Padé order increases. This is significant as a higher Padé order will give more accurate results when analysing multimode waveguides and waveguides with slowly radiating

evanescent modes, where the effective refractive indices of the different modes may be far apart, as will be the case for waveguides analysed later in the thesis.

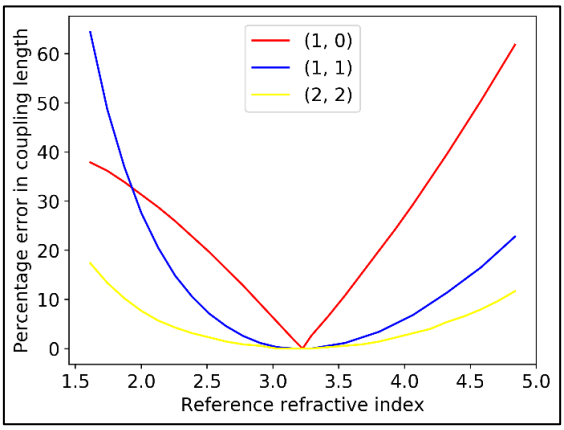

Figure 2.16: Percentage error in coupling length vs. reference refractive index for different Padé orders.

2.5 Conclusions

This chapter successfully derived the wave equations for the both the quasi-TE and quasi-TM modes as well as described the implementation of the finite difference method for both the mode solver and beam propagation method. The mode solver and beam propagation method were shown to be implemented correctly through examples and the Padé approximant operators were shown to improve wide-angle propagation.

The next chapters will use the mode solver and beam propagation method to analyse the behaviour of the electromagnetic fields through curved optical waveguides.

3 Curved Optical Waveguides

This chapter describes how semi-vectorial wave equations are analysed through a curved 3D waveguide. It also introduces the curvature profiles of the waveguides analysed in this thesis.

3.1 The Wave Equations in the Cylindrical Coordinate System

Assuming a field propagates initially in the $\hat{\boldsymbol{z}}$ direction through a straight waveguide and then transitions to a curved waveguide, with the waveguide bending in the (x, z) plane, the $\hat{\boldsymbol{x}}$ directed field in the straight waveguide in the cartesian coordinate system immediately becomes the $\hat{\boldsymbol{r}}$ directed field in the curved waveguide in the cylindrical coordinate system, as shown in Figure 3.1. Meanwhile, the propagation direction becomes the $\hat{\boldsymbol{\varphi}}$ direction.

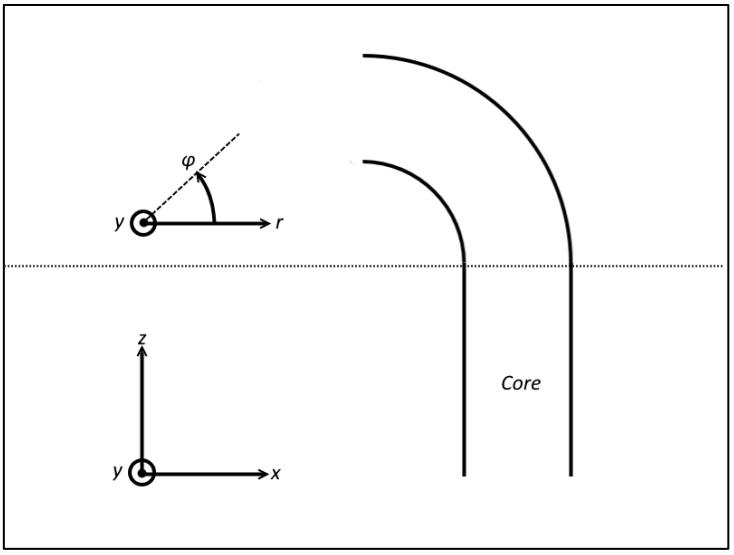

Figure 3.1: Change of coordinate system from straight to curved waveguide.

In the cylindrical coordinate system, the vectorial equation for the electric field (2.4) results in the following two equations for the transverse components of the electric field [46]:

$$\frac{\partial^2 E_r}{\partial r^2}+\frac{1}{r}\frac{\partial E_r}{\partial r}+\frac{1}{r^2}\frac{\partial^2 E_r}{\partial \varphi^2}+\frac{\partial^2 E_r}{\partial y^2}+\frac{\partial}{\partial r}\left(\frac{1}{\varepsilon_r}\frac{\partial \varepsilon_r}{\partial r}E_r\right)+\frac{\partial}{\partial r}\left(\frac{1}{\varepsilon_r r}\frac{\partial \varepsilon_r}{\partial \varphi}E_\varphi\right)+\frac{\partial}{\partial r}\left(\frac{1}{\varepsilon_r}\frac{\partial \varepsilon_r}{\partial y}E_y\right)+k_0^2\varepsilon_r E_r=0 \quad (3.1)$$

$$\frac{\partial^2 E_y}{\partial r^2}+\frac{1}{r}\frac{\partial E_y}{\partial r}+\frac{1}{r^2}\frac{\partial^2 E_y}{\partial \varphi^2}+\frac{\partial^2 E_y}{\partial y^2}+\frac{\partial}{\partial y}\left(\frac{1}{\varepsilon_r}\frac{\partial \varepsilon_r}{\partial r}E_r\right)+\frac{\partial}{\partial y}\left(\frac{1}{\varepsilon_r r}\frac{\partial \varepsilon_r}{\partial \varphi}E_\varphi\right)+\frac{\partial}{\partial y}\left(\frac{1}{\varepsilon_r}\frac{\partial \varepsilon_r}{\partial y}E_y\right)+k_0^2\varepsilon_r E_y=0 \quad (3.2)$$

Similarly, the vectorial equation for the magnetic field (2.5) results in the following two equations for the transverse components of the magnetic field:

$$\frac{\partial^2 H_r}{\partial r^2}+\frac{1}{r}\frac{\partial H_r}{\partial r}+\frac{1}{r^2}\frac{\partial^2 H_r}{\partial \varphi^2}+\frac{\partial^2 H_r}{\partial y^2}+\frac{1}{\varepsilon_r r^2}\frac{\partial \varepsilon_r}{\partial \varphi}\left(\frac{\partial(rH_\varphi)}{\partial r}-\frac{\partial H_r}{\partial \varphi}\right)-\frac{1}{\varepsilon_r}\frac{\partial \varepsilon_r}{\partial y}\left(\frac{\partial H_r}{\partial y}-\frac{\partial H_y}{\partial r}\right)+k_0^2\varepsilon_r H_r=0 \quad (3.3)$$

$$\frac{\partial^2 H_y}{\partial r^2}+\frac{1}{r}\frac{\partial H_y}{\partial r}+\frac{1}{r^2}\frac{\partial^2 H_y}{\partial \varphi^2}+\frac{\partial^2 H_y}{\partial y^2}+\frac{1}{\varepsilon_r}\frac{\partial \varepsilon_r}{\partial r}\left(\frac{\partial H_r}{\partial y}-\frac{\partial H_y}{\partial r}\right)-\frac{1}{\varepsilon_r r}\frac{\partial \varepsilon_r}{\partial \varphi}\left(\frac{1}{r}\frac{\partial H_y}{\partial \varphi}-\frac{\partial H_\varphi}{\partial y}\right)+k_0^2\varepsilon_r H_y=0 \quad (3.4)$$

The refractive index profile is assumed to vary slowly in the $\hat{\boldsymbol{\varphi}}$ direction, i.e. $\partial\varepsilon_r/\partial\varphi \approx 0$. In the semi-vectorial formulation, the coupling between the different transverse directions is also assumed to be small and is therefore neglected. In the quasi-TE mode, E_r and H_y are

the principal field components and their wave equations take the following semi-vectorial forms in the cylindrical coordinate system:

$$\frac{\partial^2 E_r}{\partial r^2}+\frac{1}{r}\frac{\partial E_r}{\partial r}+\frac{1}{r^2}\frac{\partial^2 E_r}{\partial \varphi^2}+\frac{\partial^2 E_r}{\partial y^2}+\frac{\partial}{\partial r}\left(\frac{1}{\varepsilon_r}\frac{\partial \varepsilon_r}{\partial r}E_r\right)+k_0^2\varepsilon_r E_r=0 \tag{3.5}$$

$$\frac{\partial^2 H_y}{\partial r^2}+\frac{1}{r}\frac{\partial H_y}{\partial r}+\frac{1}{r^2}\frac{\partial^2 H_y}{\partial \varphi^2}+\frac{\partial^2 H_y}{\partial y^2}-\frac{1}{\varepsilon_r}\frac{\partial \varepsilon_r}{\partial r}\frac{\partial H_y}{\partial r}+k_0^2\varepsilon_r H_y=0 \tag{3.6}$$

In the quasi-TM mode, E_y and H_r are the principal field components and their wave equations take the following semi-vectorial forms in the cylindrical coordinate system:

$$\frac{\partial^2 E_y}{\partial r^2}+\frac{1}{r}\frac{\partial E_y}{\partial r}+\frac{1}{r^2}\frac{\partial^2 E_y}{\partial \varphi^2}+\frac{\partial^2 E_y}{\partial y^2}+\frac{\partial}{\partial y}\left(\frac{1}{\varepsilon_r}\frac{\partial \varepsilon_r}{\partial y}E_y\right)+k_0^2\varepsilon_r E_y=0 \tag{3.7}$$

$$\frac{\partial^2 H_r}{\partial r^2}+\frac{1}{r}\frac{\partial H_r}{\partial r}+\frac{1}{r^2}\frac{\partial^2 H_r}{\partial \varphi^2}+\frac{\partial^2 H_r}{\partial y^2}-\frac{1}{\varepsilon_r}\frac{\partial \varepsilon_r}{\partial y}\frac{\partial H_r}{\partial y}+k_0^2\varepsilon_r H_r=0 \tag{3.8}$$

3.2 Conformal Transformation Approach to Analysing Curved Waveguides

The conformal transformation approach to analysing curved waveguides was introduced by Heiblum and Harris [47], and was originally used to analyse the 2D scalar wave equation. A conformal transformation is an angle preserving transformation [48] and Heiblum and Harris' method used a conformal transformation to map the curved waveguide structure onto an equivalent straight waveguide structure, as shown in Figure 3.2. The effect is to simplify the wave equations and allow them to be analysed by methods such as the finite-difference beam propagation method.

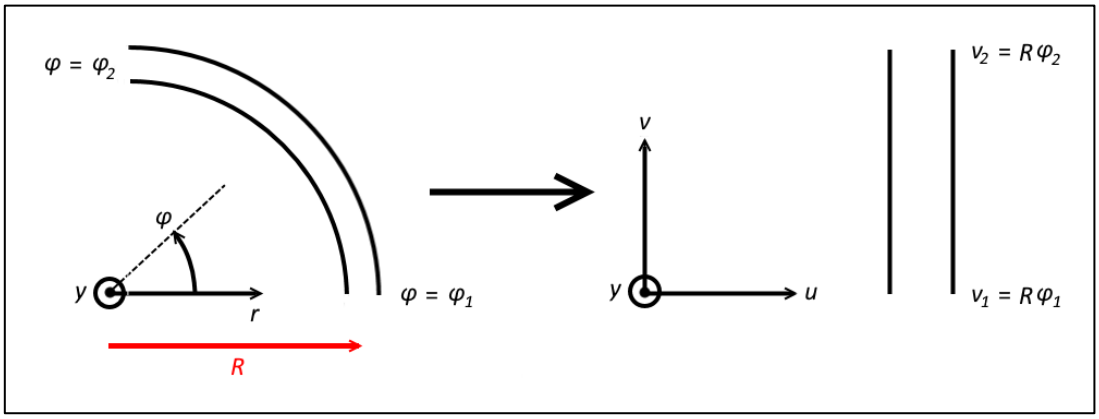

Figure 3.2: Waveguide structure before and after conformal transformation.

Assuming the path of the centre of the waveguide along the $\hat{\boldsymbol{\varphi}}$ direction in Figure 3.1 describes that of a segment of a circle of radius R, the circular region in the (r,φ) plane can be mapped to a rectangular region in the complex (u,v) plane. The coordinate transformation is represented by $W=u+iv=f(Z)=f(r\exp(i\varphi))$. To analyse the wave equations in the (u,v) plane, the following transformation is used [47]:

$$W=R\ln\frac{Z}{R} \tag{3.9}$$

Splitting W into real and complex components gives the following expressions for u and v:

$$u = R \ln \frac{r}{R} \tag{3.10}$$

$$v = R\varphi \tag{3.11}$$

Next, the derivatives in the wave equations with respect to r and φ must be replaced with derivatives with respect to u and v using $r = R\exp(u/R)$ and $\varphi = v/R$ as follows:

$$\frac{\partial f}{\partial r} = \frac{\partial f}{\partial u}\frac{\partial u}{\partial r} = \frac{R}{r}\frac{\partial f}{\partial u} = \exp\left(-\frac{u}{R}\right)\frac{\partial f}{\partial u} \tag{3.12}$$

$$\frac{\partial f}{\partial \varphi} = \frac{\partial f}{\partial v}\frac{\partial v}{\partial \varphi} = R\frac{\partial f}{\partial v} \tag{3.13}$$

Substituting these derivatives into the wave equations results in the following expressions for the semi-vectorial wave equations in the quasi-TE mode:

$$\frac{\partial^2 E_u}{\partial u^2} + \frac{\partial^2 E_u}{\partial v^2} + \exp\left(\frac{2u}{R}\right)\frac{\partial^2 E_u}{\partial y^2} + \exp\left(\frac{u}{R}\right)\frac{\partial}{\partial u}\left(\frac{1}{\varepsilon_r \exp\left(u/R\right)}\frac{\partial \varepsilon_r}{\partial u}E_u\right) + k_0^2 \varepsilon_r \exp\left(\frac{2u}{R}\right)E_u = 0 \tag{3.14}$$

$$\frac{\partial^2 H_y}{\partial u^2} + \frac{\partial^2 H_y}{\partial v^2} + \exp\left(\frac{2u}{R}\right)\frac{\partial^2 H_y}{\partial y^2} - \frac{1}{\varepsilon_r}\frac{\partial \varepsilon_r}{\partial u}\frac{\partial H_y}{\partial u} + k_0^2 \varepsilon_r \exp\left(\frac{2u}{R}\right)H_y = 0 \tag{3.15}$$

And the following semi-vectorial wave equations in the quasi-TM mode:

$$\frac{\partial^2 E_y}{\partial u^2} + \frac{\partial^2 E_y}{\partial v^2} + \exp\left(\frac{2u}{R}\right)\frac{\partial^2 E_y}{\partial y^2} + \exp\left(\frac{2u}{R}\right)\frac{\partial}{\partial y}\left(\frac{1}{\varepsilon_r}\frac{\partial \varepsilon_r}{\partial y}E_y\right) + k_0^2 \varepsilon_r \exp\left(\frac{2u}{R}\right)E_y = 0 \tag{3.16}$$

$$\frac{\partial^2 H_u}{\partial u^2} + \frac{\partial^2 H_u}{\partial v^2} + \exp\left(\frac{2u}{R}\right)\frac{\partial^2 H_u}{\partial y^2} - \exp\left(\frac{2u}{R}\right)\frac{1}{\varepsilon_r}\frac{\partial \varepsilon_r}{\partial y}\frac{\partial H_u}{\partial y} + k_0^2 \varepsilon_r \exp\left(\frac{2u}{R}\right)H_u = 0 \tag{3.17}$$

3.2.1 Finding Supported Modes of a Circular Waveguide

To find the supported modes of a circular region of the waveguide, the waveguide is assumed to be invariant in the $\hat{v}$ direction and therefore the derivative with respect to v can be replaced with $i\beta$ where $\beta = k_0 n_{eff}$ is the propagation constant, analogous to what was done for the modes in the original straight waveguide. This has the following effect on the semi-vectorial equations in the quasi-TE mode:

$$\frac{\partial^2 E_u}{\partial u^2} + \exp\left(\frac{2u}{R}\right)\frac{\partial^2 E_u}{\partial y^2} + \exp\left(\frac{u}{R}\right)\frac{\partial}{\partial u}\left(\frac{1}{\varepsilon_r \exp\left(u/R\right)}\frac{\partial \varepsilon_r}{\partial u}E_u\right) + k_0^2\left(\varepsilon_r \exp\left(\frac{2u}{R}\right) - n_{eff}^2\right)E_u = 0 \tag{3.18}$$

$$\frac{\partial^2 H_y}{\partial u^2} + \exp\left(\frac{2u}{R}\right)\frac{\partial^2 H_y}{\partial y^2} - \frac{1}{\varepsilon_r}\frac{\partial \varepsilon_r}{\partial u}\frac{\partial H_y}{\partial u} + k_0^2\left(\varepsilon_r \exp\left(\frac{2u}{R}\right) - n_{eff}^2\right)H_y = 0 \tag{3.19}$$

And the following effect on the semi-vectorial wave equations in the quasi-TM mode:

$$\frac{\partial^2 E_y}{\partial u^2} + \exp\left(\frac{2u}{R}\right)\frac{\partial^2 E_y}{\partial y^2} + \exp\left(\frac{2u}{R}\right)\frac{\partial}{\partial y}\left(\frac{1}{\varepsilon_r}\frac{\partial \varepsilon_r}{\partial y}E_y\right) + k_0^2\left(\varepsilon_r \exp\left(\frac{2u}{R}\right) - n_{eff}^2\right)E_y = 0 \tag{3.20}$$

$$\frac{\partial^2 H_u}{\partial u^2} + \exp\left(\frac{2u}{R}\right)\frac{\partial^2 H_u}{\partial y^2} - \exp\left(\frac{2u}{R}\right)\frac{1}{\varepsilon_r}\frac{\partial \varepsilon_r}{\partial y}\frac{\partial H_u}{\partial y} + k_0^2\left(\varepsilon_r \exp\left(\frac{2u}{R}\right) - n_{eff}^2\right)H_u = 0 \tag{3.21}$$

The above equations correspond to equations (2.16) - (2.19) in the original straight waveguide and can be analysed in the same way with the result being an eigenvalue matrix equation to be solved, with the eigenvalues giving the propagation constants and the corresponding eigenvectors giving the mode profiles.

3.2.2 Beam Propagation Method Through a Curved Waveguide

As was done for the beam propagation method in the straight waveguide, the field components above can once again be expressed as the product of a complex field amplitude $\phi(u, y, v)$ and a propagation factor $\exp(ik_0 n_0 v)$, where n_0 is a reference index which is chosen to be as close as possible to the effective index of the propagating mode. For example, for H_y in the quasi-TE mode:

$$H_y(u, y, v) = \phi(u, y, v) \exp(ik_0 n_0 v) \tag{3.22}$$

Substituting this expression into equation (3.15) results in the following:

$$-2ik_0 n_0 \frac{\partial \phi}{\partial v} - \frac{\partial^2 \phi}{\partial v^2} = \frac{\partial^2 \phi}{\partial u^2} + \exp\left(\frac{2u}{R}\right)\frac{\partial^2 \phi}{\partial y^2} - \frac{1}{\varepsilon_r}\frac{\partial \varepsilon_r}{\partial u}\frac{\partial \phi}{\partial u} + k_0^2\left(\varepsilon_r \exp\left(\frac{2u}{R}\right) - n_0^2\right)\phi \tag{3.23}$$

From here, the same approach can be applied to this wave equation as carried out in section 2.3. The wave equations in the (u, y, v) coordinate system (3.14) - (3.17) are very similar to the original wave equations in the straight waveguide's (x, y, z) coordinate system with just extra factors of $\exp(2u/R)$ appearing for the curved waveguide. This means that the finite difference method, boundary conditions and Padé approximant operators can all also be easily applied to the wave equations in the (u, y, v) coordinate system.

3.3 Effect of Curvature on Supported Modes and the Propagating field

In the original straight waveguide, if the derivative of the relative permittivity with respect to the transverse directions is neglected, equations (2.6) to (2.11) would reduce to the same equation, known as the scalar equation:

$$\frac{\partial^2 \psi}{\partial x^2} + \frac{\partial^2 \psi}{\partial z^2} + \frac{\partial^2 \psi}{\partial y^2} + k_0^2 \varepsilon_r \psi = 0 \tag{3.24}$$

Correspondingly, in the (u, y, v) coordinate system of the curved waveguide, if the derivative of the relative permittivity with respect to the transverse directions is neglected, equations (3.14) to (3.21) would reduce to the following scalar equation:

$$\frac{\partial^2 \psi}{\partial u^2} + \frac{\partial^2 \psi}{\partial v^2} + \exp\left(\frac{2u}{R}\right)\frac{\partial^2 \psi}{\partial y^2} + k_0^2 \varepsilon_r \exp\left(\frac{2u}{R}\right)\psi = 0 \tag{3.25}$$

In the (u, y, v) coordinate system, with the absence of a derivative of the relative permittivity with respect to a transverse direction, the conformal mapping has the effect of multiplying the original refractive index profile by $\exp(u/R)$. Figure 3.3 displays this transformation of the refractive index for the square waveguide analysed in chapter 2, for a radius of curvature of $20\ \mu m$. This transformation will clearly cause the fundamental mode

to shift towards the outside of the bend, as the refractive index exponentially increases from the inside of the bend to the outside of the bend. The amount of shift however is dependent on the radius of curvature, with the mode shifting further as the radius of curvature decreases.

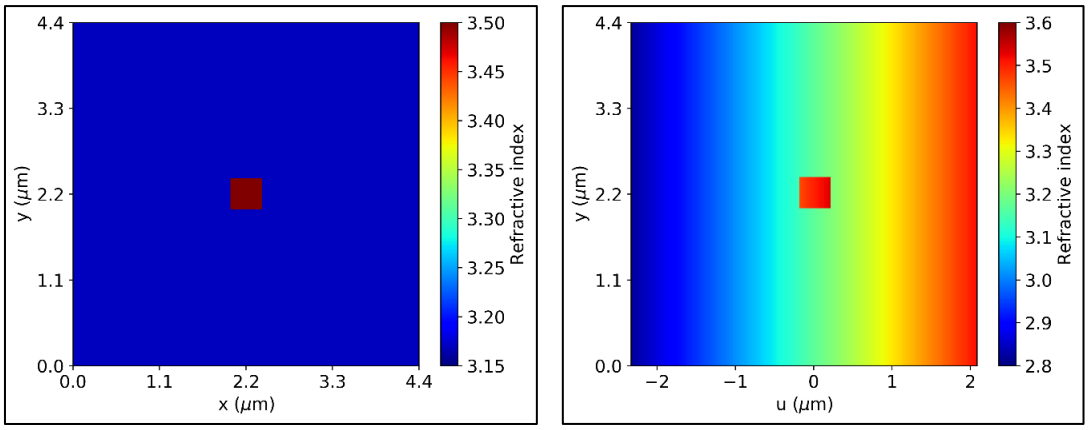

(a) Straight waveguide (b) Circular waveguide

Figure 3.3: Transformation of the refractive index profile of a square waveguide from the straight waveguide in the (x, y) plane to the circular waveguide in the (u, y) plane, according to the conformal mapping of the scalar wave equation for a radius of $20\ \mu m$.

However, while the above transformation to the refractive index is true for the scalar wave equation and the semi-vectorial wave equations in the quasi-TM mode, care must be taken when applying the conformal transformation to the semi-vectorial wave equations (3.14) and (3.15) in the quasi-TE mode. The presence of the $\partial \varepsilon_r / \partial u$ terms in these equations means the refractive index cannot simply be multiplied by $\exp(u/R)$ as this would lead to errors at the refractive index boundaries along the $\hat{\boldsymbol{u}}$ direction.

3.3.1 Effect of Curvature on Supported Semi-Vectorial Modes

Figure 3.4 shows the effect of the curvature on the fundamental mode fields for both the quasi-TE and quasi-TM modes of the square waveguide, with a relatively large radius of curvature of $150\ \mu m$. The modes were computed in the (u, y) plane and the coordinates were then transformed back to the (r, y) plane. The corresponding modes in the straight waveguide can be seen in Figure 2.2. For the curved waveguide modes, the horizontal axis has been replaced with $\rho = r - R$, where R is the radius of curvature, to allow for a clearer representation of the axis. The computations were done using an 8.4 X 6.4 micron grid but only the area close to the core is plotted to allow the shift of the mode profiles to be seen more clearly. The centre of the waveguide is shown by a dashed white line to also allow the shift to be seen more clearly. 351 grid points were used along the $\hat{\boldsymbol{\rho}}$ direction and 251 points were used along the $\hat{\boldsymbol{y}}$ direction. Neumann boundary conditions were implemented. In each case, the field shifts slightly towards the outside of the bend, with the electric fields also maintaining the discontinuities at the refractive index boundaries. Figure 3.5 displays the electric fields as they approach the edge of the computational area on the outside of the bend. For both modes, the fields appear to decay to zero away from the centre of the waveguide and then actually become slightly negative as they approach the right-hand side of the computational window. This suggests that the modes have become slightly radiative

at this radius of curvature as the boundary conditions implemented are insufficient to deal with the tails of the field.

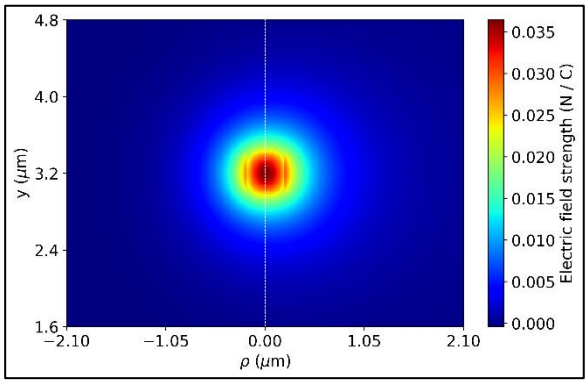

(a) E_r in the quasi-TE mode

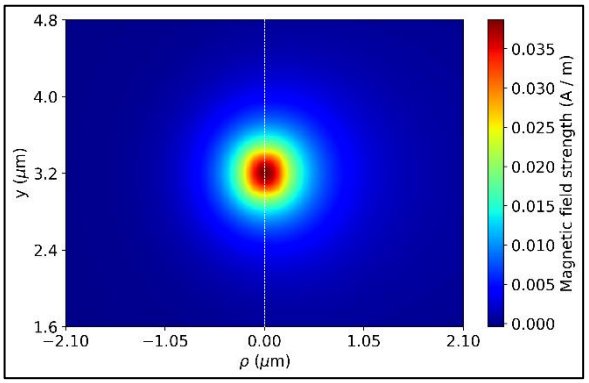

(b) H_y in the quasi-TE mode

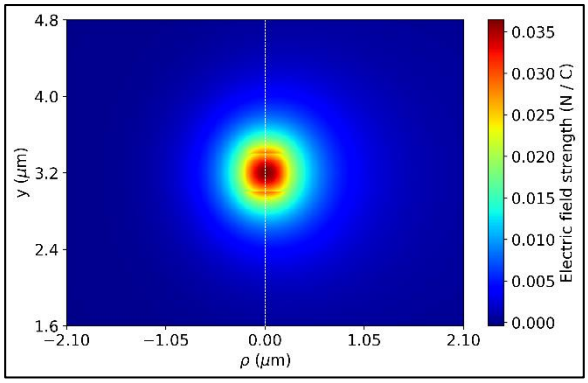

(c) E_y in the quasi-TE mode

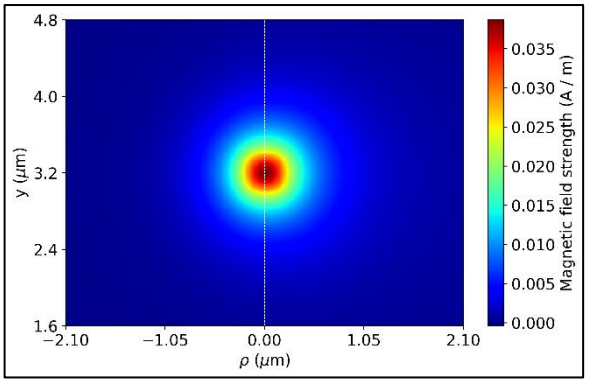

(d) H_r in the quasi-TM mode

Figure 3.4: Shifts in the fundamental mode fields of the quasi-TE and quasi-TM modes at a radius of curvature of $150\ \mu m$. The quasi-TE mode has an effective refractive index of 3.21770 and the quasi-TM mode has an effective refractive index of 3.21768.

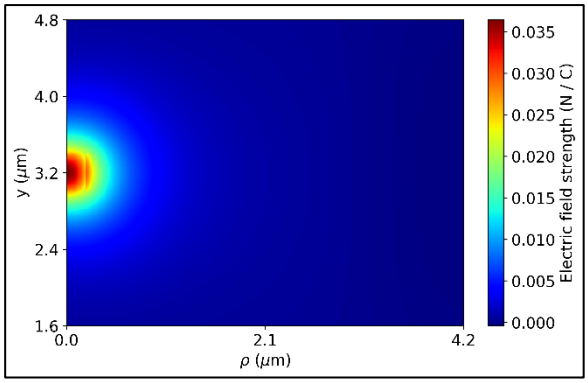

(a) E_r in the quasi-TE mode

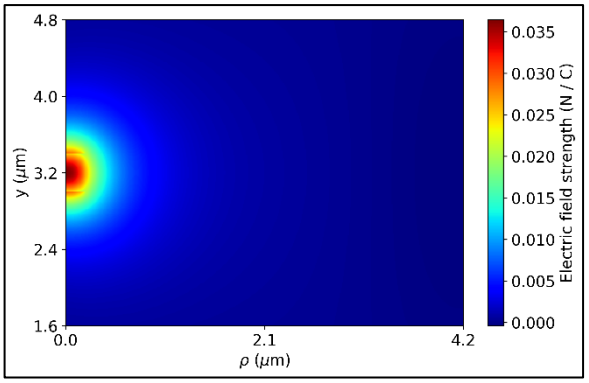

(b) E_y in the quasi-TE mode

Figure 3.5: Fundamental mode electric fields for the 150 μm radius circular rectangular waveguides in the quasi-TE mode as the fields approach the computational boundary on the outside of the bend.

Meanwhile, Figure 3.6 shows the mode profiles of the square waveguide for a radius of curvature of $75\ \mu m$. A white line has again been drawn through the centre of the plot to better display the shifting of the mode profile. At this radius of curvature, the amplitudes of the fields appear to oscillate as they approach the right-hand computational boundary. This suggests that the mode profiles have become lossy [49], and are therefore known as “leaky”

modes as they radiate away their power as they propagate around the bend. The ability of the mode solver to accurately analyse these leaky modes is insufficient due to the simplicity of the implemented Dirichlet or Neumann boundary conditions, and the oscillating part of the mode profile can vary substantially depending on the width of the computational area allocated to the outside of the waveguide bend. To analyse how the shape of the fundamental mode is altered by the curvature in such waveguides correctly, the beam propagation method must be used which utilises the more powerful TBC and PML boundary conditions.

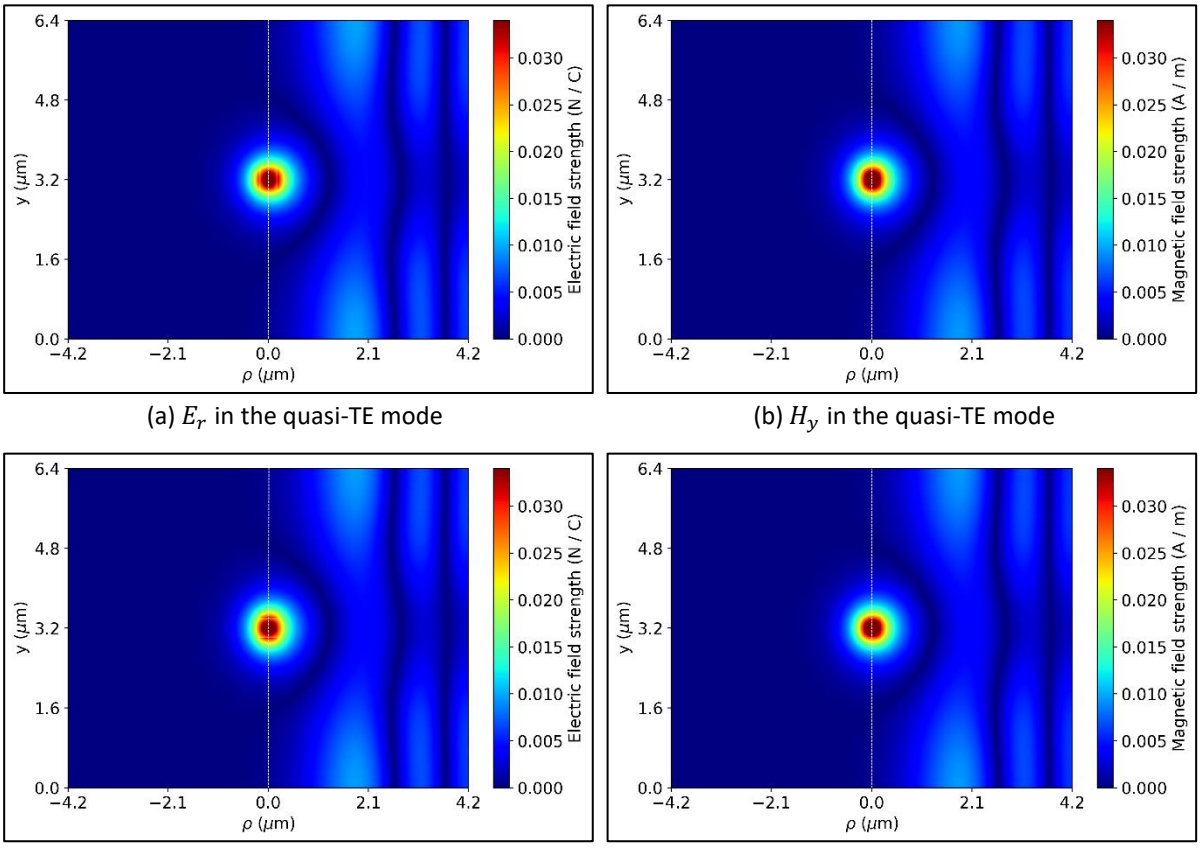

(a) E_r in the quasi-TE mode

(b) H_y in the quasi-TE mode

(c) E_y in the quasi-TM mode

(d) H_r in the quasi-TE mode

Figure 3.6: Shifts in the fundamental fields of the quasi-TE and quasi-TM modes at a radius of curvature of $75\ \mu m$.

3.3.2 Effect of Curvature on the Propagating Fundamental Mode

When the transition from a straight waveguide to a circular waveguide and then back to a straight waveguide is analysed using the beam propagation method, the fundamental mode of the straight waveguide is expected to transition to the shape of the fundamental curved waveguide mode at the straight-curved waveguide boundary. Loss would occur at both straight-curved waveguide boundaries due to the mismatch of fundamental modes. The loss due to the transition between modes can be measured using the overlap integral method, and is given by:

$$T_L = -10\log_{10}(1 - O_E)\ dB \tag{3.26}$$

In the above equation, O_E represents the overlap integral error, given by equation (2.104), and is computed using the propagating field in the curved waveguide and the initially

propagated field in the straight waveguide, i.e. the fundamental mode field of the straight waveguide. The mode mismatch loss from the bend can be measured once the propagating field has transitioned back to the straight waveguide and can be computed as follows:

$$M_L = -10\log_{10}(1 - M_E)\ dB \tag{3.27}$$

M_E is known as the mode mismatch error and is given by:

$$M_E = 1 - \frac{\left|\int \phi_0 \phi^*\, dx\, dy\right|^2}{\left|\int |\phi_0|^2\, dx\, dy\right|^2} \tag{3.28}$$

ϕ_0 refers to the field in the initial straight waveguide and ϕ refers to the field in the straight waveguide after the bend.

The fundamental mode fields in both the quasi-TE and quasi-TM modes of the square waveguide were propagated through a 90° circular bend with a radius of $150\ \mu m$. The waveguide was initially straight for approximately 30 μm, then turned through 90°, then set to straight again for approximately 90 μm. The same number of transverse points were used in the computation as were used for the computation of the curved waveguide modes. Figure 3.7 shows a top-down view of the propagating fields through the y centre of the waveguide. The horizontal ρ axis shows the x distance from the centre of the waveguide for the straight regions and the r distance from the centre of the waveguide for the curved regions. The vertical z axis shows the propagation distance for the field through the centre of the waveguide. Dashed black lines have been drawn on the H_y graph in the quasi-TE mode and the E_y and H_r graphs in the quasi-TM mode to indicate the edges of the waveguide. They have not been drawn on the E_r graph in the quasi-TE mode as discontinuities can already be observed at the refractive index boundaries. The field is seen to shift slightly towards the outside of the bend at the straight-curved waveguide boundary, and then shift back to the centre at the curved-straight waveguide boundary. In the bend, the tails of the field on the outside of the bend are observed to have a non-zero value at the edge of computational region, showing that the shifted fundamental mode has become a leaky mode and thus the field loses a small amount of power as it propagates around the bend.

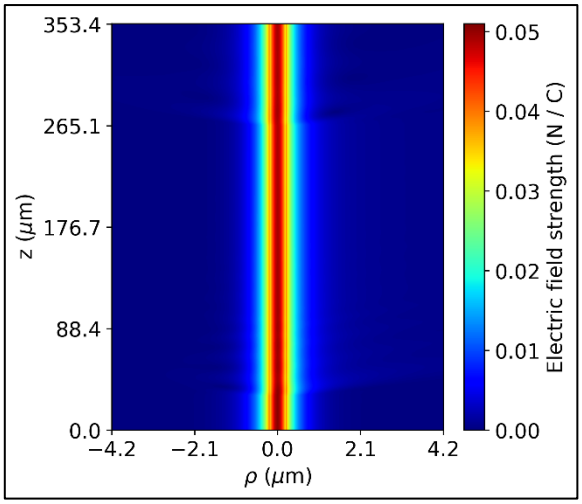

(a) E_r in the quasi-TE mode.

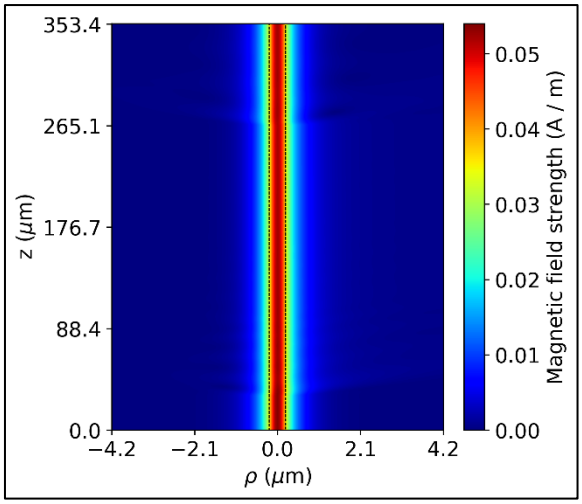

(b) H_y in the quasi-TM mode.

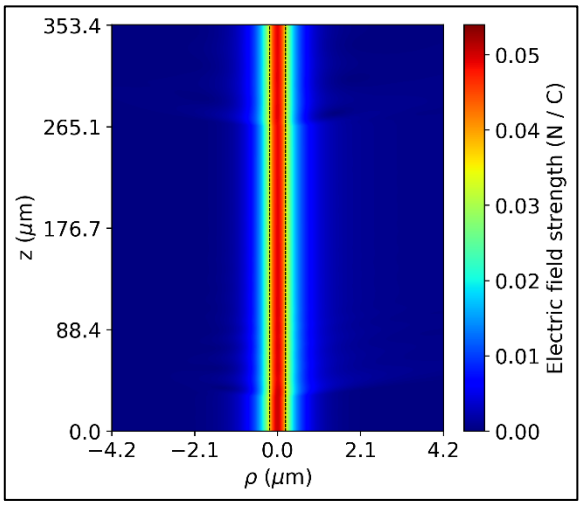

(c) E_y in the quasi-TM mode.

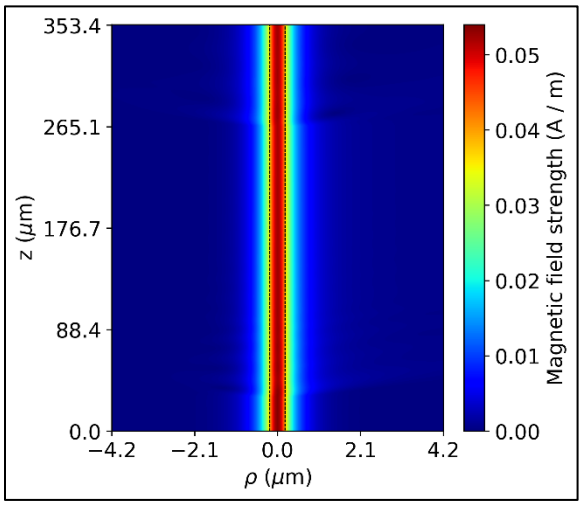

(d) H_r in the quasi-TM mode.

Figure 3.7: Evolution of the fields at the y centre of the waveguide as they propagate through the straight-curved-straight square waveguide structure.

Figure 3.8 shows the shape of the transverse cross section of the fields once they have propagated 45° through the bend. The fields are seen to have slightly shifted towards the outside of the bends to take the forms of the curved waveguide modes given by Figure 3.4. This is made easier to see by Figure 3.9 which shows a zoomed in view of the shifted fundamental mode E_r field from Figure 3.4 and the propagating E_r field 45° through the bend. To further show this numerically, the evolution of the overlap integral error between the propagating fields and the initially propagated fundamental mode fields of the straight waveguide is represented by the blue curves in Figure 3.10. The s parameter on the horizontal axis defines the propagating distance through the centre of the waveguide. For each propagating field, the overlap integral error is seen to rise sharply after entering the curve before settling at a constant value as it propagates around the circular bend. It then falls back to 0 as it propagates through the exit straight waveguide. The constant value found while propagating through the waveguide bend occurs when the field has taken the form of the fundamental mode of the circular waveguide, and should therefore equal the overlap integral error between the corresponding fundamental modes in Figure 2.2 and

Figure 3.4. The calculated overlap integral errors between these modes found using the mode solver were as follows: 0.0106 for E_r in the quasi-TE mode, 0.0096 for H_y in the quasi-TE mode, 0.0100 for E_y in the quasi-TM mode, and 0.0096 for H_r in the quasi-TM mode. These values are represented by the dashed red lines in Figure 3.10, showing that the overlap integral error between the modes from the BPM was slightly larger in each case, suggesting the curved waveguide modes had become leaky and were therefore inaccurately found by the mode solver.

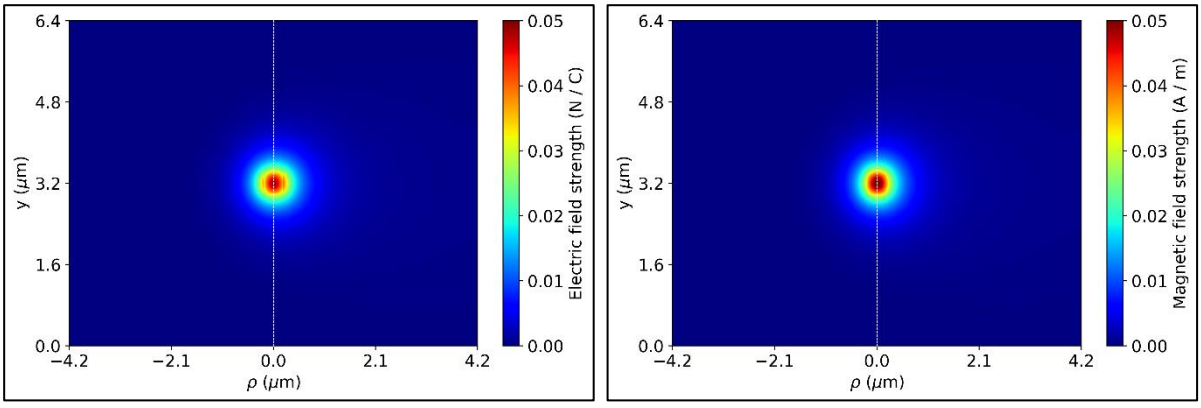

(a) E_r in the quasi-TE mode.

(b) H_y in the quasi-TE mode.

(c) E_y in the quasi-TM mode.

(d) H_r in the quasi-TM mode.

Figure 3.8: Transverse field profiles after propagating 45° through a circular square waveguide with a radius of curvature of 150 μm.

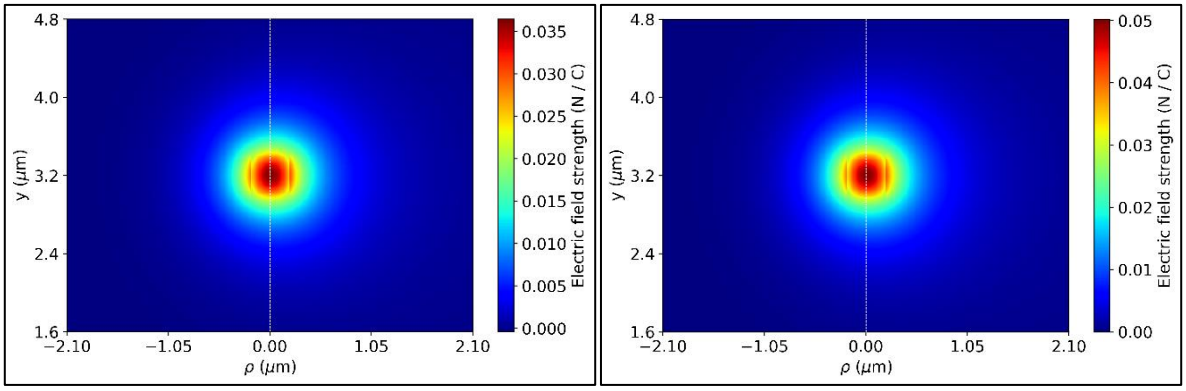

(a) Shifted fundamental mode.

(b) Propagating field 45° through bend.

Figure 3.9: Comparison of the shifted fundamental mode E_x field with the propagating E_x field at 45° through a circular square waveguide bend with a radius of curvature of 150 μm.

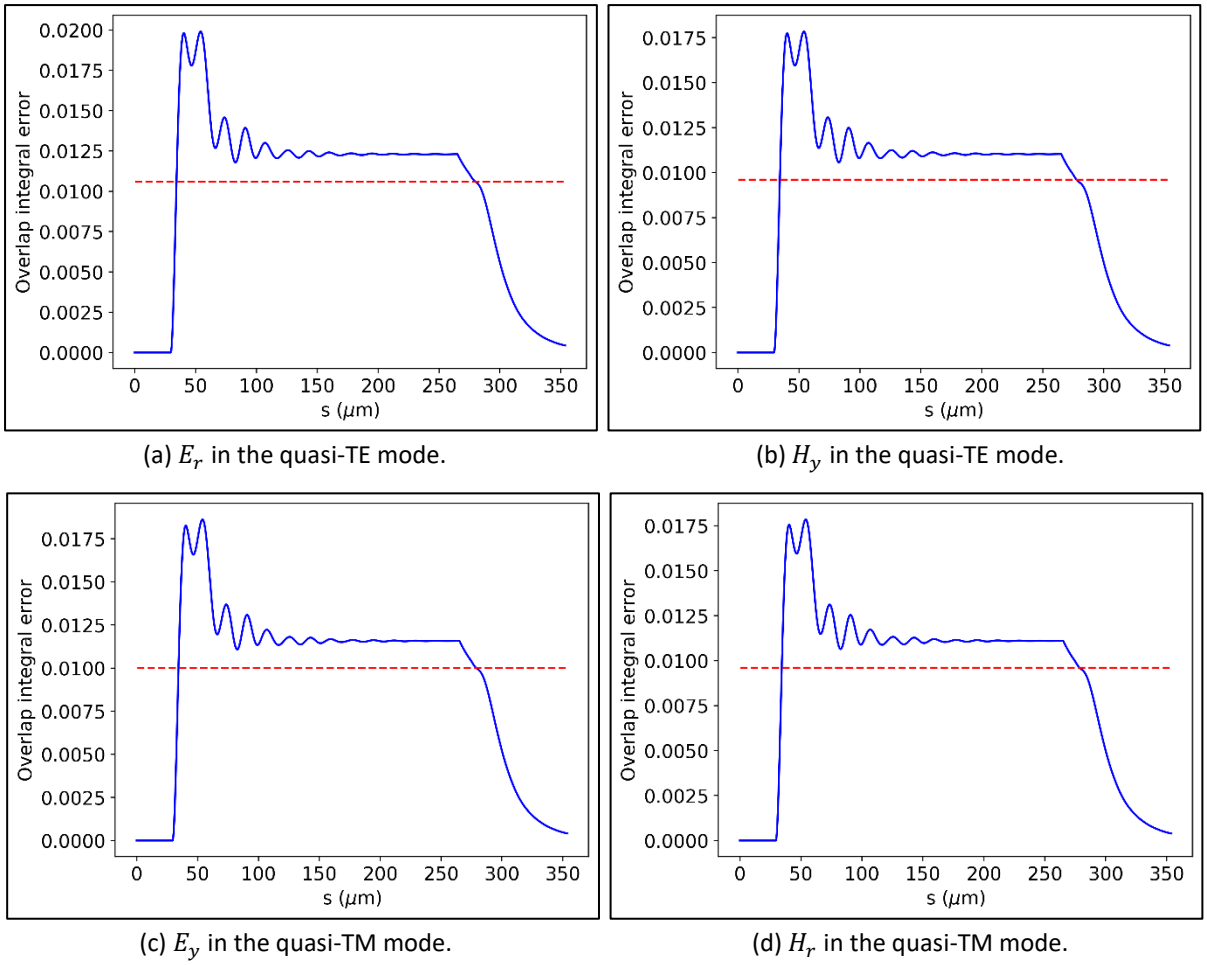

(a) E_r in the quasi-TE mode.

(b) H_y in the quasi-TE mode.

(c) E_y in the quasi-TM mode.

(d) H_r in the quasi-TM mode.

Figure 3.10**:** Overlap integral error between the propagating fields and the fundamental mode fields of the square waveguide.

Figure 3.11 shows the mode mismatch error between the propagating fields and the fundamental mode fields of the straight waveguide. Whereas the overlap integral error just accounts for the deformation of the mode profile, the mode mismatch error also accounts for the loss of the mode as it propagates. The mode mismatch error graphs show that the fundamental mode fields of the curved waveguide have become leaky, as the mode mismatch error continues to increase over the propagating distance where the overlap integral error had become constant, indicating that the curved waveguide modes had become lossy.

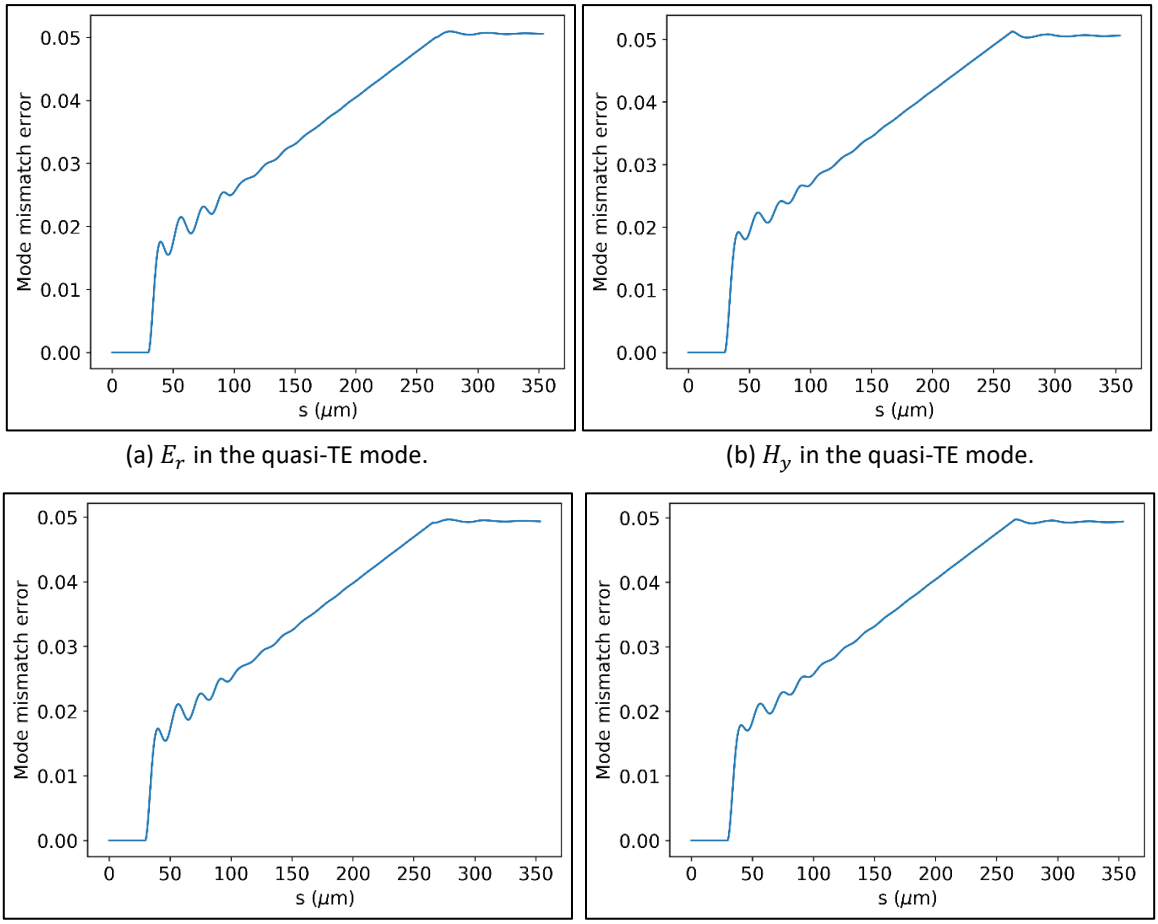

(a) E_r in the quasi-TE mode.

(b) H_y in the quasi-TE mode.

(c) E_y in the quasi-TM mode.

(d) H_x in the quasi-TM mode.

Figure 3.11: Mode mismatch error between the propagating fields and the fundamental fields of the square waveguide.

3.4 Curvature Profiles

So far, this chapter has only dealt with circular waveguides where the radius of curvature is constant. This section will describe the other curvature profiles which will be analysed in this thesis. The first is the linearly changing curvature profile, where the curvature linearly increases for half of the bend and then linearly decreases for the other half of the bend. The second is the trapezoidal curvature profile, where the curvature linearly increases to some maximum curvature for a certain fraction of the bend, then stays as this maximum curvature for the next portion of the bend before linearly decreasing for the rest of the bend. The three curvature profiles can be seen in Figure 3.12. When analysing a non-constant curvature waveguide using the FD-BPM, a conformal transformation is made to update the curvature at each propagation step.

Euler's method of natural equations [50] allows the path of a bend to be described using the curvature of the bend along its path length. This requires, firstly, the evaluation of an integral which gives the angle a tangent to the curve at a point makes with the tangent to the curve at the start of the curve. The bend is then described by evaluating another pair of integrals which gives a parametric representation of the bend based on the relative axes. All three curvature profiles can be parameterised in this manner [51] [52].

Let the centre of a waveguide describe a path s as the waveguide follows a bend in the (x, z) plane. Assume the curvature κ of the bend varies along s. If a tangent to the curve s is drawn at point s_1, it will intersect the z axis with an angle ϕ_1, the bending angle, as shown in Figure 3.13. If the curve s intersects the z axis at point s_0 along its path length, the angle ϕ_1 can be calculated using the curve's curvature κ as follows:

$$\phi_1 = \int_{s_0}^{s_1} \kappa(s)\, ds \tag{3.29}$$

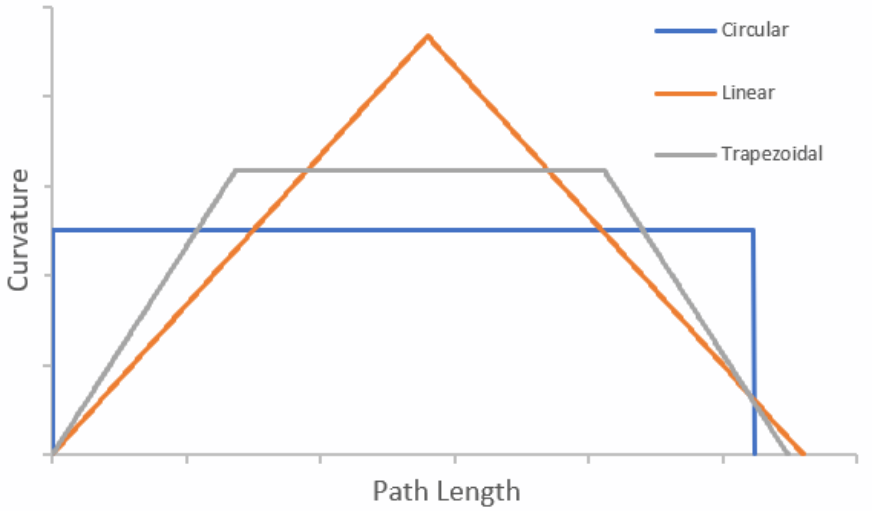

Figure 3.12: Circular, liner and trapezoidal curvature profiles.

The bend occurs in the (x, z) plane and will therefore be parameterised using x and z. Let ds be an infinitesimally small length of the bend s. ds extends for length dx along the negative $\hat{\boldsymbol{x}}$ direction and dz along the $\hat{\boldsymbol{z}}$ direction and the lengths are related by $ds^2 = dx^2 + dz^2$. If ϕ is the angle ds makes with the z axis, dx and dz can be individually expressed by:

$$dx = -\sin\phi\, ds \tag{3.30}$$

$$dz = \cos\phi\, ds \tag{3.31}$$

The parametric representation of the bend in the (x, z) coordinate system at point s_1 along the path length can therefore be found by integrating both sides of the above equations:

$$x(s_1 - s_0) = -\int_{s_0}^{s_1} \sin\phi(s)\ ds \tag{3.32}$$

$$z(s_1 - s_0) = \int_{s_0}^{s_1} \cos\phi(s)\ ds \tag{3.33}$$

Therefore, to parameterise the bend in the (x, z) coordinate system, ϕ must first be calculated at each point along s using equation (3.29), and then equations (3.32) and (3.33) are used to find the x and z parameterisation at each point along s.

In the case of the circular waveguide, the curvature is constant along the bend and, assuming the s_0 point is at $(0, 0)$ in the (x, z) coordinate system, equation (3.29) is simply expressed as $\phi_1 = \kappa s_1$. $x(s_1)$ and $z(s_1)$ are therefore given by:

$$x(s_1) = -\int_0^{s_1} \sin(\kappa s)\ ds = -\frac{1}{\kappa}(1 - \cos(\kappa s_1)) \tag{3.34}$$

$$z(s_1) = \int_0^{s_1} \cos(\kappa s)\ ds = \frac{1}{\kappa}\sin(\kappa s_1) \tag{3.35}$$

As $\kappa = 1/R$, where R is the radius of curvature, the parametric representation of the circular bend is simply given by:

$$x_C(s_1) = -R\left(1 - \cos\left(\frac{s_1}{R}\right)\right) \tag{3.36}$$

$$z_C(s_1) = R\sin\left(\frac{s_1}{R}\right) \tag{3.37}$$

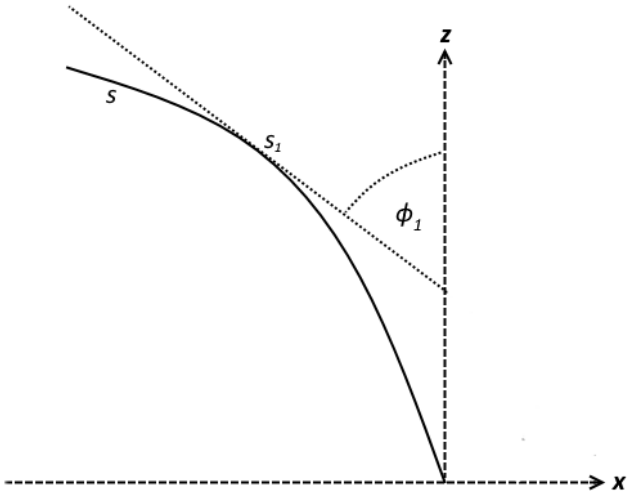

Figure 3.13: Tangent of curve s at point s_1 intersecting z axis with angle ϕ_1.

3.4.1 Linearly Changing Curvature Bend

In this curvature profile, the curvature is set to linearly change with s. If the bend is designed to have a total path length L, the curvature is designed to linearly increase for the first half of the path length and then linearly decrease for the second half of the path length. If m_l is the slope of the change in curvature with s, $\kappa(s)$ is represented by:

$$\kappa(s) = \begin{cases} m_l s & 0 \le s \le \frac{\mathrm{L}}{2} \\ m_l(L - s) & \frac{\mathrm{L}}{2} < s \le L \end{cases} \tag{3.38}$$

The linearly changing curvature bend is designed to have the same end point as that of a circular waveguide that turns through an angle φ with radius R. It is therefore necessary to set L and m_l to values that will achieve this. A relationship between φ, L, and m_l can be found using equation (3.29):

$$\frac{\varphi}{2} = \int_0^{\frac{L}{2}} m_l s\ ds = \frac{m_l L^2}{8} \tag{3.39}$$

To find the relationship between R, L, and m_l, the x and z parameterisation of the linearly changing curvature bend must be constructed and then be allowed to equate to the x and z parameterisation of the circular bend at $s = L$.

According to equation (3.29), in each region the bending angle at s is given by:

$$\phi(s) = \begin{cases} \frac{m_l s^2}{2} & 0 \leq s \leq \frac{\mathrm{L}}{2} \\ m_l L s - \frac{m_l L^2}{4} - \frac{m_l s^2}{2} & \frac{\mathrm{L}}{2} < s \leq L \end{cases} \tag{3.40}$$

According to equations (3.32) and (3.33), the parametrisation of the linearly changing curvature bend is therefore given by:

$$x(s_1) = \begin{cases} -\int_0^{s_1} \sin\left(\frac{m_l s^2}{2}\right) ds & 0 \leq s_1 \leq \frac{L}{2} \\ -\int_0^{\frac{L}{2}} \sin\left(\frac{m_l s^2}{2}\right) ds - \int_{\frac{L}{2}}^{s_1} \sin\left(m_l L s - \frac{m_l s^2}{2} - \frac{m_l L^2}{4}\right) ds & \frac{L}{2} < s_1 \leq L \end{cases} \tag{3.41}$$

$$z(s_1) = \begin{cases} \int_0^{s_1} \cos\left(\frac{m_l s^2}{2}\right) ds & 0 \leq s_1 \leq \frac{L}{2} \\ \int_0^{\frac{L}{2}} \cos\left(\frac{m_l s^2}{2}\right) ds + \int_{\frac{L}{2}}^{s_1} \cos\left(m_l L s - \frac{m_l s^2}{2} - \frac{m_l L^2}{4}\right) ds & \frac{L}{2} < s_1 \leq L \end{cases} \tag{3.42}$$

The integrals in the equations above can be written in terms of the Fresnel integrals [53]. The Fresnel integrals are defined through the following integral representations:

$$C(x) = \int_0^x \cos\frac{\pi t^2}{2}\, dt \tag{3.43}$$

$$S(x) = \int_0^x \sin\frac{\pi t^2}{2}\, dt \tag{3.44}$$

Using the above Fresnel integrals, the integrals in equations (3.41) and (3.42) can be evaluated using the following formulae:

$$\int_{s_0}^{s_1} \cos(as^2)\, ds = \sqrt{\frac{\pi}{2a}}\, C\left(\sqrt{\frac{2a}{\pi}}\, s\right)\Big|_{s_0}^{s_1} \tag{3.45}$$

$$\int_{s_0}^{s_1} \sin(as^2)\, ds = \sqrt{\frac{\pi}{2a}}\, S\left(\sqrt{\frac{2a}{\pi}}\, s\right)\Big|_{s_0}^{s_1} \tag{3.46}$$

$$\int_{s_0}^{s_1} \cos(as^2 + 2bs + c)\, ds = \sqrt{\frac{\pi}{2a}}\left[\cos\left(\frac{b^2 - ac}{a}\right) C\left(\sqrt{\frac{2}{a\pi}}(as + b)\right) + \sin\left(\frac{b^2 - ac}{a}\right) S\left(\sqrt{\frac{2}{a\pi}}(as + b)\right)\right]\Big|_{s_0}^{s_1} \tag{3.47}$$

$$\int_{s_0}^{s_1} \sin(as^2 + 2bs + c)\, ds = \sqrt{\frac{\pi}{2a}}\left[\cos\left(\frac{b^2 - ac}{a}\right) S\left(\sqrt{\frac{2}{a\pi}}(as + b)\right) - \sin\left(\frac{b^2 - ac}{a}\right) C\left(\sqrt{\frac{2}{a\pi}}(as + b)\right)\right]\Big|_{s_0}^{s_1} \tag{3.48}$$

Using the above formulae, the x and z parameterisation at point $s = s_1$ is given by:

$$x_L(s_1) = -\sqrt{\frac{\pi}{m_l}} S\left(\sqrt{\frac{m_l}{\pi}} s_1\right) \qquad 0 \le s_1 \le \frac{L}{2} \qquad (3.49)$$

$$x_L(s_1) = -\sqrt{\frac{\pi}{m_l}}\left[S\left(\sqrt{\frac{m_l}{\pi}}\frac{L}{2}\right) - \cos\left(\frac{m_l L^2}{4}\right)\left[S\left(\sqrt{\frac{m_l}{\pi}}(s-L)\right) + S\left(\sqrt{\frac{m_l}{\pi}}\frac{L}{2}\right)\right] + \sin\left(\frac{m_l L^2}{4}\right)\left[C\left(\sqrt{\frac{m_l}{\pi}}(s-L)\right) + C\left(\sqrt{\frac{m_l}{\pi}}\frac{L}{2}\right)\right]\right] \qquad \frac{L}{2} < s_1 \le L \qquad (3.50)$$

$$z_L(s_1) = \sqrt{\frac{\pi}{m_l}} C\left(\sqrt{\frac{m_l}{\pi}} s_1\right) \qquad 0 \le s_1 \le \frac{L}{2} \qquad (3.51)$$

$$z_L(s_1) = \sqrt{\frac{\pi}{m_l}}\left[C\left(\sqrt{\frac{m_l}{\pi}}\frac{L}{2}\right) + \cos\left(\frac{m_l L^2}{4}\right)\left[C\left(\sqrt{\frac{m_l}{\pi}}(s-L)\right) + C\left(\sqrt{\frac{m_l}{\pi}}\frac{L}{2}\right)\right] + \sin\left(\frac{m_l L^2}{4}\right)\left[S\left(\sqrt{\frac{m_l}{\pi}}(s-L)\right) + S\left(\sqrt{\frac{m_l}{\pi}}\frac{L}{2}\right)\right]\right] \qquad \frac{L}{2} < s_1 \le L \qquad (3.52)$$

As the linearly changing curvature bend must end at the same point as that of a circular bend of a certain radius of curvature R (R is known as the effective radius of curvature) and path length $L_C = R\varphi$:

$$x_C(L_C) = x_L(L) \qquad (3.53)$$

$$z_C(L_C) = z_L(L) \qquad (3.54)$$

Applying equations (3.53) and (3.39) results in the following expression for m_l in terms of R and φ:

$$m_l = \frac{\pi}{R^2(1-\cos(\varphi))^2}\left[S\left(\sqrt{\frac{\varphi}{\pi}}\right)(1-\cos(\varphi)) + C\left(\sqrt{\frac{\varphi}{\pi}}\right)\sin(\varphi)\right]^2 \qquad (3.55)$$

And substituting m_l into equation (3.39) allows L to be expressed in terms of R and φ:

$$L = 2R(1-\cos(\varphi))\sqrt{\frac{\varphi}{\pi}}\left[S\left(\sqrt{\frac{\varphi}{\pi}}\right)(1-\cos(\varphi)) + C\left(\sqrt{\frac{\varphi}{\pi}}\right)\sin(\varphi)\right]^{-1} \qquad (3.56)$$

As the maximum curvature $\kappa_l = \kappa(L/2) = m_l L/2$:

$$\kappa_l = \frac{\sqrt{\pi\varphi}}{R(1-\cos(\varphi))}\left[S\left(\sqrt{\frac{\varphi}{\pi}}\right)(1-\cos(\varphi)) + C\left(\sqrt{\frac{\varphi}{\pi}}\right)\sin(\varphi)\right] \qquad (3.57)$$

3.4.2 Trapezoidal Curvature Bend

In a trapezoidal curvature bend, the curvature increases linearly for some fraction of the path length of the bend until it reaches a certain value. The curvature then stays at this constant value for another fraction of the path length of the bend, before decreasing linearly for the rest of the bend. This makes the shape of the curvature profile represent a trapezoid, as can be seen in Figure 3.12.

If m_l is the slope of the change in curvature with s, k_t is the maximum curvature reached, σ is the path length of the linearly increasing curvature section, $v - \sigma$ is the path length of the constant curvature section, and L is the total path length of the bend, $\kappa(s)$ is represented by:

$$k(s) = m_l s \qquad 0 \leq s \leq \sigma \qquad (3.58)$$

$$k(s) = k_t \qquad \sigma < s \leq v \qquad (3.59)$$

$$k(s) = m_l(L - s) \qquad v < s \leq L \qquad (3.60)$$

The curvature profile is designed so that the path length traversed while the curvature is linearly increasing is equal to the path length traversed while the curvature is linearly decreasing, i.e. $\sigma = L - v$. If $\sigma = 0$, the curvature profile reduces to the circular case as the curvature is constant around the full bend. If $\sigma = L/2$, the curvature profile reduces to the linearly changing curvature case. The curvature profile must be continuous at σ and v, and this is the case as long as:

$$\sigma = \frac{k_t}{m_l} \qquad (3.61)$$

As was the case for the linearly changing curvature profile, the bend is designed to give the same endpoints as a circular waveguide of an equivalent radius of curvature, R, that turns through an angle φ. m_l, k_t and L must be set to achieve this for values σ and v set to some fraction of the total path length. Equation (3.29) gives the relationship between m_l, k_t, L and φ. The integral only needs to be evaluated from 0 to $L/2$ due to the symmetry in the curvature profile:

$$\int_0^{\sigma} m_l s \, ds + \int_{\sigma}^{\frac{L}{2}} k_t \, ds = \frac{\varphi}{2} \qquad (3.62)$$

$$\frac{m_l \sigma^2}{2} + \frac{k_t L}{2} - k_t \sigma = \frac{\varphi}{2} \qquad (3.63)$$

To find the relationship between R, L, m_l and k_t, the x and z parameterisation of the trapezoidal curvature bend must be constructed and then be allowed to equate to the x and z parameterisation of the circular bend at $s = L$.

According to equation (3.29), in each region the bending angle at s is given by:

$$\phi(s) = \frac{m_l s^2}{2} \qquad 0 \leq s \leq \sigma \qquad (3.64)$$

$$\phi(s) = k_t s - \frac{k_t^2}{2m_l} \qquad \sigma < s \leq v \qquad (3.65)$$

$$\phi(s) = -\frac{k_t^2}{m_l} + k_t L - \frac{m_l s^2}{2} - \frac{m_l L^2}{2} + m_l L s \qquad v < s \leq L \qquad (3.66)$$

According to equations (3.32) and (3.33), the x and z parameterisation at s_1 is given by:

$$x(s_1) = -\int_0^{s_1} \sin\left(\frac{m_l s^2}{2}\right) ds \qquad 0 \leq s_1 \leq \sigma \qquad (3.67)$$

$$x(s_1) = -\int_0^{\sigma} \sin\left(\frac{m_l s^2}{2}\right)\, ds - \int_{\sigma}^{s_1} \sin\left(k_t s - \frac{k_t^2}{2m_l}\right)\, ds \qquad \sigma \le s_1 \le v \qquad (3.68)$$

$$x(s_1) = -\int_0^{\sigma} \sin\left(\frac{m_l s^2}{2}\right)\, ds - \int_{\sigma}^{v} \sin\left(k_t s - \frac{k_t^2}{2m_l}\right) ds \; - \int_{v}^{s_1} \sin\left(-\frac{m_l s^2}{2} + m_l L s - \frac{m_l L^2}{2} + k_t L - \frac{k_t^2}{m_l}\right)\, ds \qquad v < s_1 \le L \qquad (3.69)$$

$$z(s_1) = \int_0^{s_1} \cos\left(\frac{m_l s^2}{2}\right)\, ds \qquad 0 \le s_1 \le \sigma \qquad (3.70)$$

$$z(s_1) = \int_0^{\sigma} \cos\left(\frac{m_l s^2}{2}\right)\, ds + \int_{\sigma}^{s_1} \cos\left(k_t s - \frac{k_t^2}{2m_l}\right)\, ds \qquad \sigma \le s_1 \le v \qquad (3.71)$$

$$z(s_1) = \int_0^{\sigma} \cos\left(\frac{m_l s^2}{2}\right)\, ds + \int_{\sigma}^{v} \cos\left(k_t s - \frac{k_t^2}{2m_l}\right) ds \; + \int_{v}^{s_1} \cos\left(-\frac{m_l s^2}{2} + m_l L s - \frac{m_l L^2}{2} + k_t L - \frac{k_t^2}{m_l}\right)\, ds \qquad v < s_1 \le L \qquad (3.72)$$

The integrals in equations (3.67) to (3.72) can be evaluated using the Fresnel integrals in the following manner:

$$\int_0^{s_1} \cos\left(\frac{m_l s^2}{2}\right)\, ds = \sqrt{\frac{\pi}{m_l}}\, C\left(\sqrt{\frac{m_l}{\pi}}\, s_1\right) \qquad (3.73)$$

$$\int_0^{s_1} \sin\left(\frac{m_l s^2}{2}\right)\, ds = \sqrt{\frac{\pi}{m_l}}\, S\left(\sqrt{\frac{m_l}{\pi}}\, s_1\right) \qquad (3.74)$$

$$\int_{\sigma}^{s_1} \cos\left(k_t s - \frac{k_t^2}{2m_l}\right)\, ds = \frac{2}{k_t} \sin\left(\frac{1}{2}\left(k_t s_1 - \frac{k_t^2}{m_l}\right)\right) \cos\left(\frac{k_t s_1}{2}\right) \qquad (3.75)$$

$$\int_{\sigma}^{s_1} \sin\left(k_t s - \frac{k_t^2}{2m_l}\right)\, ds = \frac{2}{k_t} \sin\left(\frac{1}{2}\left(k_t s_1 - \frac{k_t^2}{m_l}\right)\right) \sin\left(\frac{k_t s_1}{2}\right) \qquad (3.76)$$

$$\int_{v}^{s_1} \cos\left(-\frac{m_l s^2}{2} + m_l L s - \frac{m_l L^2}{2} + k_t L - \frac{k_t^2}{m_l}\right)\, ds = \sqrt{\frac{\pi}{m_l}} \cos\left(k_t L - \frac{k_t^2}{m_l}\right)\left[C\left(\sqrt{\frac{m_l}{\pi}}(s_1 - L)\right) + C\left(\frac{k_t}{\sqrt{m_l \pi}}\right)\right] + \sqrt{\frac{\pi}{m_l}} \sin\left(k_t L - \frac{k_t^2}{m_l}\right)\left[S\left(\sqrt{\frac{m_l}{\pi}}(s_1 - L)\right) + S\left(\frac{k_t}{\sqrt{m_l \pi}}\right)\right] \qquad (3.77)$$

$$\int_{v}^{s_1} \sin\left(-\frac{m_l s^2}{2} + m_l L s - \frac{m_l L^2}{2} + k_t L - \frac{k_t^2}{m_l}\right)\, ds = \sqrt{\frac{\pi}{m_l}} \sin\left(k_t L - \frac{k_t^2}{m_l}\right)\left[C\left(\sqrt{\frac{m_l}{\pi}}(s_1 - L)\right) + C\left(\frac{k_t}{\sqrt{m_l \pi}}\right)\right] - \sqrt{\frac{\pi}{m_l}} \cos\left(k_t L - \frac{k_t^2}{m_l}\right)\left[S\left(\sqrt{\frac{m_l}{\pi}}(s_1 - L)\right) + S\left(\frac{k_t}{\sqrt{m_l \pi}}\right)\right] \qquad (3.78)$$

The trapezoidal bend is therefore parameterised as follows:

$$x_T(s_1) = -\sqrt{\frac{\pi}{m_l}} S\left(\sqrt{\frac{m_l}{\pi}} s_1\right) \qquad 0 \le s_1 \le \sigma \quad (3.79)$$

$$x_T(s_1) = -\left(\sqrt{\frac{\pi}{m_l}} S\left(\frac{k_t}{\sqrt{\pi m_l}}\right) + \frac{2}{k_t}\sin\left(\frac{1}{2}\left(k_t s_1 - \frac{k_t^2}{m_l}\right)\right)\sin\left(\frac{k_t s_1}{2}\right)\right) \qquad \sigma < s_1 \le v \quad (3.80)$$

$$\begin{aligned} x_T(s_1) = -\Bigg\{ & \sqrt{\frac{\pi}{m_l}} S\left(\frac{k_t}{\sqrt{\pi m_l}}\right) + \frac{2}{k_t}\sin\left(\frac{1}{2}\left(k_t L - \frac{2k_t^2}{m_l}\right)\right)\sin\left(\frac{1}{2}\left(k_t L - \frac{k_t^2}{m_l}\right)\right) + \\ & \sqrt{\frac{\pi}{m_l}}\sin\left(k_t L - \frac{k_t^2}{m_l}\right)\left[C\left(\sqrt{\frac{m_l}{\pi}}(s_1 - L)\right) + C\left(\frac{k_t}{\sqrt{m_l \pi}}\right)\right] - \\ & \sqrt{\frac{\pi}{m_l}}\cos\left(k_t L - \frac{k_t^2}{m_l}\right)\left[S\left(\sqrt{\frac{m_l}{\pi}}(s_1 - L)\right) + S\left(\frac{k_t}{\sqrt{m_l \pi}}\right)\right]\Bigg\} \qquad v < s_1 \le L \end{aligned} \quad (3.81)$$

$$z_T(s_1) = \sqrt{\frac{\pi}{m_l}} C\left(\sqrt{\frac{m_l}{\pi}} s_1\right) \qquad 0 \le s_1 \le \sigma \quad (3.82)$$

$$z_T(s_1) = \sqrt{\frac{\pi}{m_l}} C\left(\frac{k_t}{\sqrt{\pi m_l}}\right) + \frac{2}{k_t}\sin\left(\frac{1}{2}\left(k_t s_1 - \frac{k_t^2}{m_l}\right)\right)\cos\left(\frac{k_t s_1}{2}\right) \qquad \sigma < s_1 \le v \quad (3.83)$$

$$\begin{aligned} z_T(s_1) = & \sqrt{\frac{\pi}{m_l}} C\left(\frac{k_t}{\sqrt{\pi m_l}}\right) + \frac{2}{k_t}\sin\left(\frac{1}{2}\left(k_t L - \frac{2k_t^2}{m_l}\right)\right)\cos\left(\frac{1}{2}\left(k_t L - \frac{k_t^2}{m_l}\right)\right) + \\ & \sqrt{\frac{\pi}{m_l}}\cos\left(k_t L - \frac{k_t^2}{m_l}\right)\left[C\left(\sqrt{\frac{m_l}{\pi}}(s_1 - L)\right) + C\left(\frac{k_t}{\sqrt{m_l \pi}}\right)\right] + \\ & \sqrt{\frac{\pi}{m_l}}\sin\left(k_t L - \frac{k_t^2}{m_l}\right)\left[S\left(\sqrt{\frac{m_l}{\pi}}(s_1 - L)\right) + S\left(\frac{k_t}{\sqrt{m_l \pi}}\right)\right] \qquad v < s_1 \le L \end{aligned} \quad (3.84)$$

Let f be the fraction of the path length of the bend devoted to linearly increasing curvature:

$$f = \frac{\sigma}{L} = \frac{k_t}{m_l L} \quad (3.85)$$

As the trapezoidal curvature bend must end at the same point as that of a circular bend with an effective radius of curvature R and path length $L_C = R\varphi$:

$$x_T(L) = x_C(L_C) \quad (3.86)$$

$$z_T(L) = z_C(L_C) \quad (3.87)$$

Utilising equations (3.61), (3.63), (3.85), and (3.86) leads to the following expression for m_l in terms of f, φ and R:

$$\begin{aligned} m_l = \frac{1}{R^2(1-\cos(\varphi))^2}\Bigg\{ & \sqrt{\pi}\, S\left(\sqrt{\frac{f\varphi}{\pi(1-f)}}\right) + 2\sqrt{\frac{1-f}{\varphi f}}\sin\left(\frac{\varphi}{2}\left(\frac{1-2f}{1-f}\right)\right)\sin\left(\frac{\varphi}{2}\right) + \\ & \sqrt{\pi}\sin(\varphi)\left[C\left(\sqrt{\frac{f\varphi}{\pi(1-f)}}\right)\right] - \sqrt{\pi}\cos(\varphi)\left[S\left(\sqrt{\frac{f\varphi}{\pi(1-f)}}\right)\right]\Bigg\}^2 \end{aligned} \quad (3.88)$$

Equations (3.61), (3.63), and (3.85) then allow k_t and L to be expressed in terms of m_l, f, and φ:

$$k_t = \sqrt{\frac{\varphi m_l f}{(1-f)}} \tag{3.89}$$

$$L = \sqrt{\frac{\varphi}{m_l f(1-f)}} \tag{3.90}$$

The parameterisation of the bend in the (x, z) coordinate system also allows a cross section of the waveguide and the propagating field to be plotted easily in plotting software. For example, Figure 3.14 and Figure 3.15 show the y cross section through the centre of the square waveguide (Figure 2.1) and the propagating H_y field, respectively, in the cases of the circular and linearly changing curvature bends, for an effective radius of curvature of $10\ \mu m$. This graphical representation of the bend makes it easy to see how the fundamental mode shifts towards the outside of the bend and then 'leaks' as it propagates around the bend.

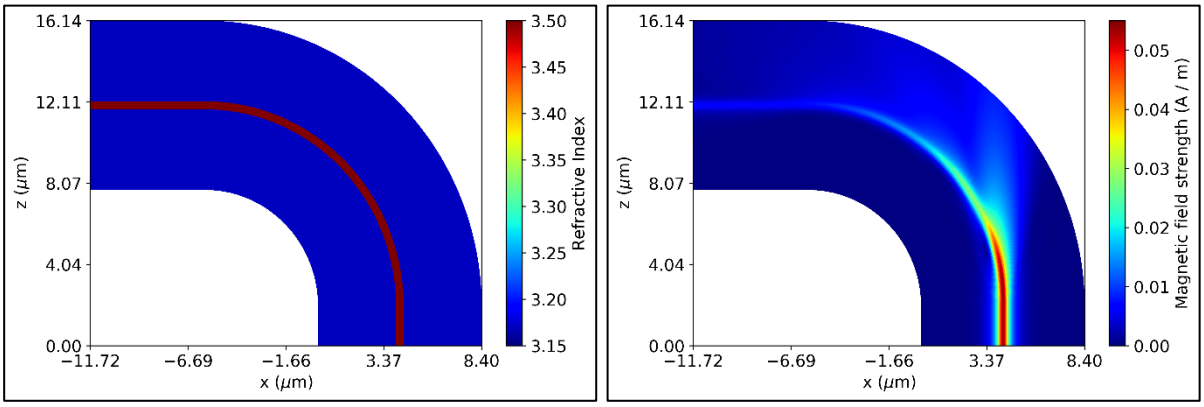

Figure 3.14: y cross section of the square waveguide and propagating H_y field in the quasi-TE mode through a 90° circular bend.

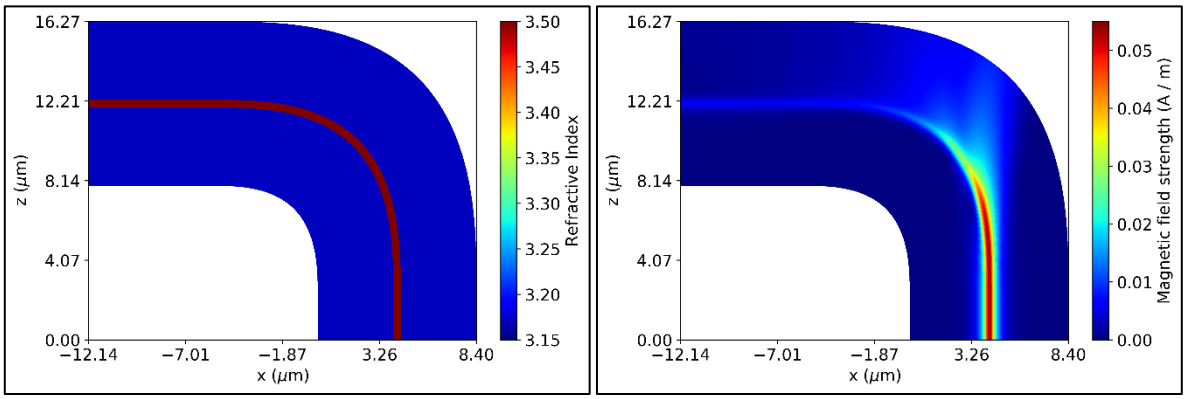

Figure 3.15: y cross section of the square waveguide and propagating H_y field in the quasi-TE mode through a 90° linearly changing curvature bend.

3.5 Conclusions

This chapter introduced the method of analysing curved optical waveguides by conformal transformation. Both the mode solver and beam propagation method were shown to work correctly with the transformed curved waveguide structures. The curvature profiles of the waveguide bends were also introduced and explained in this chapter.

The next chapters will analyse the propagation of light through curved shallow-etched and deep-etched ridge optical waveguides.

4 Analysis of the Curved Shallow-Etched Ridge Waveguide

This chapter will focus on the analysis of curved shallow-etched ridge optical waveguides. These waveguides are regularly used in photonic integrated circuits and, in this chapter, an effort will be made to reduce the loss of a curve in the shallow-etched waveguide by utilising different curvature profiles.

4.1 The Shallow-Etched Ridge Waveguide

The shallow-etched waveguide analysed in this chapter is based on a standard $1550\ nm$ commercial laser material from International Quantum Epitaxy (IQE). This material is commonly used in the PICs fabricated by the integrated photonics group in the Tyndall National Institute. Although shallow-etched waveguide bends were used in the past, bends are now generally made using a deeper etch after they were found to produce much better performance at far smaller radii of curvature. This chapter therefore aims to confirm the inferiority of the shallow-etched bend in comparison to the deeper etch bend, which will be analysed later in this thesis, and also attempts to better understand why this is the case. It will also aim to observe if changing the curvature profile of the shallow-etched bend can lead to better performance.

Table 4.1 shows the material and refractive index profile of the 16 layer IQE material which will be shallow etched. The width of the ridge waveguide after the etch is 2.5 μm and the shallow etch depth is approximately $1.85\ \mu m$, stopping before reaching the quantum well region given by layers 8 to 5.

Layer Number	Material	Thickness (μm)	Refractive Index
16	$GaIn_{(0.53)}As$	0.2	3.5112
15	$GaIn_{(0.71)}As_{(0.62)}P$	0.05	3.29429
14	InP	0.1	3.1673
13	InP	1.5	3.1673
12	$GaIn_{(0.85)}As_{(0.33)}P$	0.02	3.18055
11	InP	0.05	3.1673
10	$[Al_{(0.9)}Ga]In_{(0.53)}As$	0.06	3.22444
9	$[Al_{(0.72\ to\ 0.9)}Ga]In_{(0.53)}As$	0.06	3.2725
8	$[Al_{(0.440\ )}Ga]In_{(0.49)}As$	0.01	3.36103
7 × 5	$[Al_{(0.24\ )}Ga]In_{(0.71)}As$	0.006	3.44344
6 × 5	$[Al_{(0.440\ )}Ga]In_{(0.49)}As$	0.01	3.36103
5	$[Al_{(0.9\ to\ 0.72\ )}Ga]In_{(0.53)}As$	0.06	3.22444
4	$[Al_{(0.9\ )}Ga]In_{(0.53)}As$	0.06	3.22444
3	$[Al_{(0.86\ to\ 0.9\ )}Ga]In_{(0.53)}As$	0.01	3.2347
2	InP	0.5	3.1673
1	InP	0.3	3.1673

Table 4.1: Composition and refractive index profile of IQE wafer.

Due to the small thicknesses of some layers, and especially those comprising of the quantum well region, a very large number of computational area points would have to be used to analyse the shallow-etched waveguide accurately using the mode solver and beam

propagation method, requiring a significant amount of memory and time to run simulations. Therefore, to reduce the number of points needed for the computation, thin layers of the material were combined into a bulk material, and the refractive index set to one which would maintain the shape of the fundamental mode profile. Table 4.2 shows the refractive indices and thicknesses of the layers of the reduced bulk material. If n_i is the refractive index and T_i is the thickness of an IQE layer used in the combination of N IQE layers to form the bulk material layer, the refractive index of the combined bulk material layer n_{CL} was initially set as follows, where T_{CL} is the thickness of the bulk material layer which is the sum of the thicknesses of the individual IQE layers:

$$n_{CL} = \sum_{i=1}^{N} n_i \left(\frac{T_i}{T_{CL}}\right) \tag{4.1}$$

However, to improve the selection of the refractive indices of the layers, 1D mode simulations were made on the original waveguide and the reduced bulk material waveguide, as 1D calculations allow much faster computations and therefore more computational area points could be used. 1D simulations assumed the waveguides to extend infinitely along the horizontal and allowed the fundamental mode profiles of the waveguides along the $\hat{\boldsymbol{y}}$ direction to be calculated. The OIE was then calculated between the two fundamental mode fields and the refractive indices of the bulk material regions were then altered until the OIE between the fundamental mode fields was minimised. The analysis was done for the TE mode, which assumes the electric field to be polarised in the $\hat{\boldsymbol{x}}$ direction. 4000 computational points were used for the computations, giving a point spacing of approximately 0.002 microns. The refractive index values given by Table 4.2 were those resulting in the minimum OIE between the fields of approximately 1.07×10^{-5} and Figure 4.1 shows the fundamental mode E_x fields calculated for the original waveguide and the reduced bulk waveguide for this minimum OIE value. The calculated effective refractive indices were 3.19633 for the original waveguide and 3.19644 for the reduced bulk material waveguide.

Layer Number	**IQE Wafer Layers**	**Thickness (μm)**	**Refractive Index**
8	16	0.2	3.5112
7	15	0.05	3.29429
6	13, 14	1.6	3.1673
5	11, 12	0.07	3.168
4	9, 10	0.12	3.25
3	5 × 6, 5× 7, 8	0.09	3.387
2	3, 4, 5	0.13	3.229
1	1, 2	0.8	3.1673

Table 4.2: Refractive index profile of bulk material waveguide.

Figure 4.2 shows the refractive index profile of the analysed bulk material shallow-etched waveguide. The shallow etch was made through the top three layers, giving an etch depth of 1.85 μm. The etch causes the waveguide to be surrounded by air, with a refractive index of 1. The substrate, with the same refractive index as layer 1, extended for 3.7 μm to allow the shape of the fundamental modes to be calculated accurately.

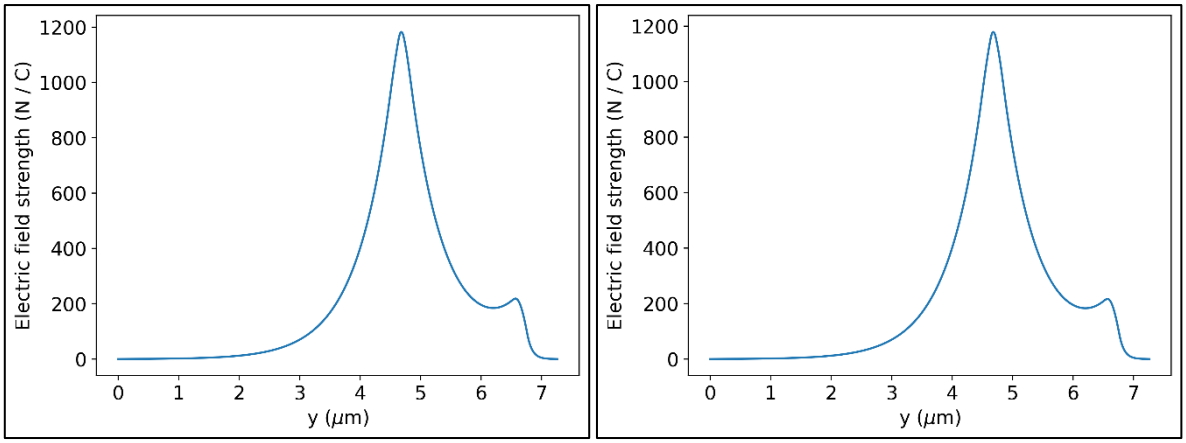

(a) Original waveguide. (b) Bulk material waveguide.

Figure 4.1: 1D TE fundamental mode E_x profiles for the original waveguide and the reduced bulk material waveguide.

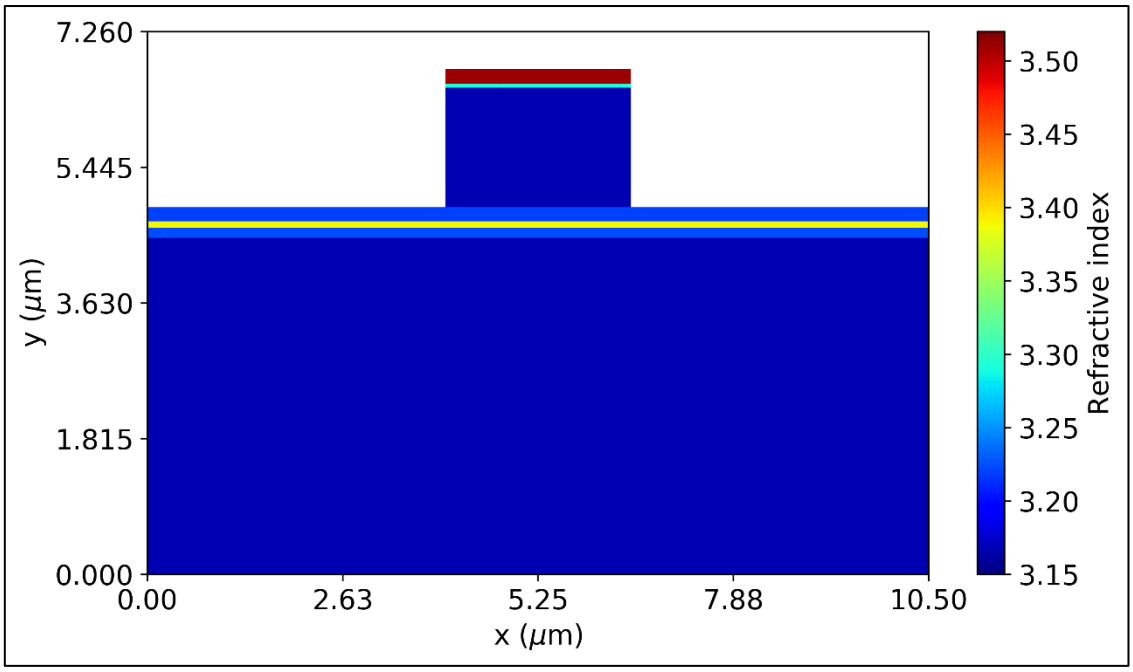

Figure 4.2: Refractive index profile of analysed shallow-etched waveguide.

Figure 4.3 shows the calculated fundamental mode field distributions for both the quasi-TE and quasi-TM modes of the shallow-etched waveguide. 250 computational grid points were used in each transverse direction, with a grid spacing reducing to $0.01\ \mu m$ close to refractive index boundaries. The effective refractive index of the quasi-TE mode is 3.1851 and the effective refractive index of the quasi-TM mode is 3.1817. The E_x and H_y field distributions appear very similar, with the largest amount of power confined in the bulk material representation of the quantum well region. As this etch is not deep enough to penetrate this region, the refractive index profile of the region is constant along the $\hat{x}$ direction. This means the electromagnetic fields are continuous across the region for both the E_x and H_y fields, making the electromagnetic field profiles appear similar. For the E_y field distribution, multiple discontinuities can be seen in the field along the $\hat{y}$ direction, due the many layers with different refractive indices. Note however that there should be more as the quantum well region layers of different refractive indices have been combined to form the bulk

material. Also note that there appears to be another small peak in the field at the top of the waveguide for both fields in the quasi-TE mode, whereas the field amplitude in the quasi-TM mode gradually reduces as it approaches the top of the waveguide. This can be seen more clearly in Figure 4.4, which shows a 1D y slice of the magnetic fields at $x = 5.25\ \mu m$.

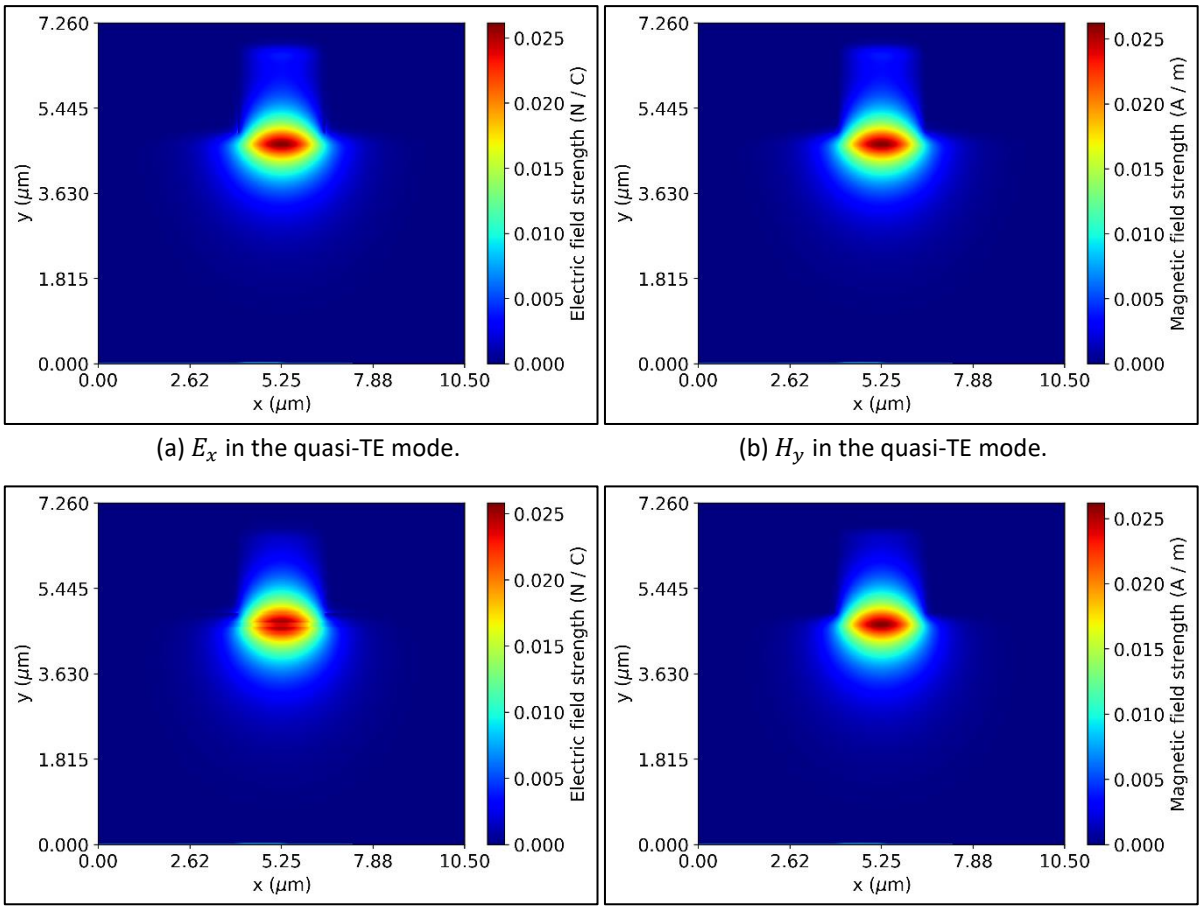

(a) E_x in the quasi-TE mode.

(b) H_y in the quasi-TE mode.

(c) E_y in the quasi-TM mode.

(d) H_x in the quasi-TM mode.

Figure 4.3: Fundamental mode field distributions of the quasi-TE and quasi-TM modes for the shallow-etched waveguide.

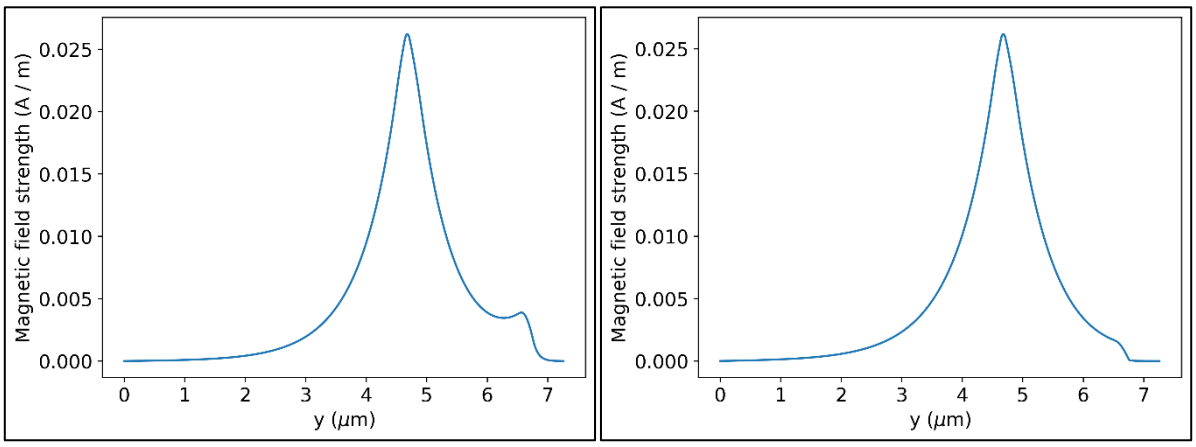

(a) H_y vs. y at $x = 5.25\ \mu m$ in the quasi-TE mode.

(b) H_x vs. y at $x = 5.25\ \mu m$ in the quasi-TM mode.

Figure 4.4: y cross section of the magnetic field in the quasi-TE and quasi-TM modes at $x = 5.25\ \mu m$ for the shallow-etched waveguide.

4.2 The Curved Shallow-Etched Ridge Waveguide

This section will analyse the behaviour and loss of the fields as they propagate through a curved shallow-etched waveguide. $90°$ and $180°$ waveguide bends will be analysed as these bends are regularly used in PICs.

4.2.1 Shallow-Etched Ridge Waveguide with a 90° Bend

Figure 4.5 to Figure 4.8 show the electromagnetic fields in both the quasi-TE and quasi-TM modes before, during, and after a $90°$ circular bend with a radius of curvature of $400\ \mu m$. For these computations, the computational area was extended for an extra $1\ \mu m$ in each transverse direction to achieve a more accurate representation of the propagating field, as the field was expected to shift upon entering the curved waveguide region. 250 computational points were used in each transverse direction and the TBC was implemented at the computational boundaries. The fields were propagated using the $(1, 1)$ Padé order. The horizontal ρ axis represents the x distance from the centre of the waveguide when in the straight waveguide and represents the radial distance from the centre of the waveguide when in the curved waveguide.

Each propagating field behaves in the same manner: they shift towards the outside of the bend once entering the circular region, then gradually lose power as they propagate around the waveguide bend, and then shift back to the centre of the waveguide upon exiting the bend. Note, however, that the field profiles shown in the exit straight waveguide were calculated approximately 235 μm after the bend, and at this propagation distance, excited radiation modes in the shallow-etched waveguide have not yet completely radiated away, causing an asymmetrical appearance of the field either side of the ridge. The behaviour of the propagating fields is made further apparent by Figure 4.9, which shows a cross section of the fields, at y where the initial field amplitude was maximum, as the fields propagate. From the graphs, the fields in the quasi-TM mode appear to be slightly less lossy than the fields in the quasi-TE mode. To confirm this, Figure 4.10 and Figure 4.11 show the mode mismatch error (MME) and overlap integral error (OIE), respectively, between the input fundamental mode of the straight waveguide and the propagating field, for both fields in the quasi-TE and quasi-TM modes. The MME graphs show that the MME after the bend is practically identical for both propagating fields in an individual mode, but it is approximately 0.1 lower for the fields in the quasi-TM mode compared to those in the quasi-TE mode. Interestingly, the OIE graphs appear to show the OIE reach a constant value of approximately 0.1 as the fields in the quasi-TM mode propagate around the circular bend, while the value of the OIE appears to oscillate between approximately 0.13 and 0.14 for the fields in the quasi-TE mode. After the bend, the OIE tends to 0 as the propagating field takes the shape of the fundamental mode, but it has not yet reached 0 at the final propagation distance as the excited radiation modes of the shallow-etched waveguide have not yet fully radiated away at this propagation distance.

The slight oscillations in the OIE for the fields in the quasi-TE mode, as they propagate through the circular bend, suggest an amount of mode beating. Figure 4.12 shows the E_x propagating field at two propagation points: one where the OIE is at a minimum in its oscillation at 420 μm and the other where the OIE is at a maximum in its oscillation at 450

μm. The graphs show how the amount of power confined at the top of the waveguide oscillates as the field propagates. This suggests beating with a waveguide mode that is confined at the top of the waveguide. As the shallow-etched waveguide is single mode, the mode solver was run on the original straight waveguide to discover if there were any radiation modes which could be beating with the fundamental mode when shifted in the curved waveguide. A number of radiation modes were found to exist with much of their mode profile inhabiting the top of the waveguide. Figure 4.13 (a) shows an example of one such mode. Figure 4.13 (b) shows the mode to be relatively slowly radiating, requiring hundreds of microns before losing most of its power while propagating through the straight waveguide. These radiation modes suggest the shifted fundamental mode was beating with this shifted radiation mode or modes as it propagated around the bend, causing the OIE to oscillate. These radiation modes possibly contributed to the larger MME observed by the propagating fields in the quasi-TE mode, as the quasi-TM mode did not contain such radiation modes.

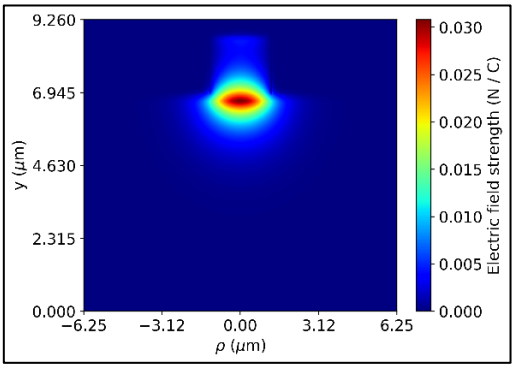

(a) Initial E_x in the straight waveguide.

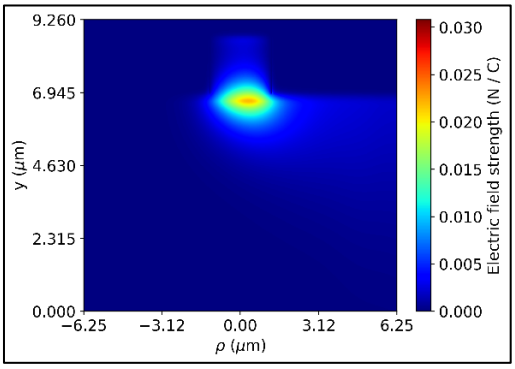

(b) E_r at 45° through the waveguide bend.

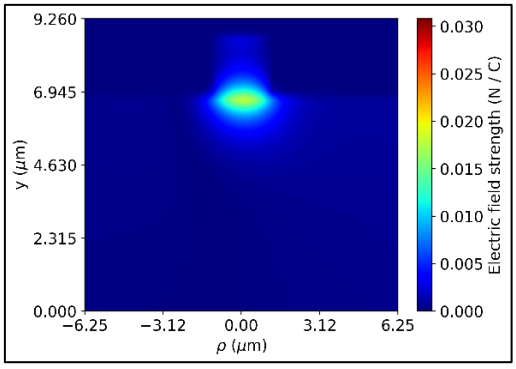

(c) E_x in the exit straight waveguide.

Figure 4.5: The electric field in the quasi-TE mode before, during, and after a 90° circular shallow-etched ridge waveguide bend with a radius of curvature of $400\ \mu m$.

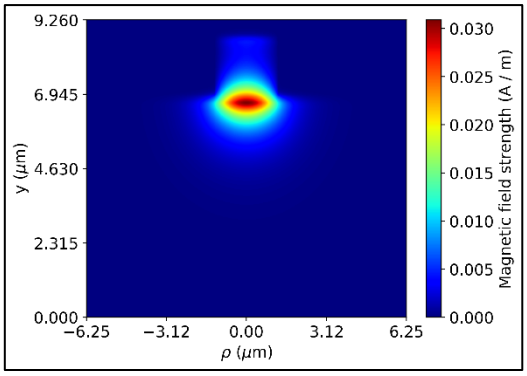

(a) Initial H_y in the straight waveguide.

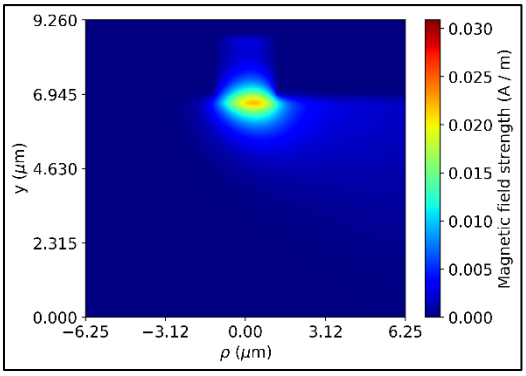

(b) H_y at 45° though the waveguide bend.

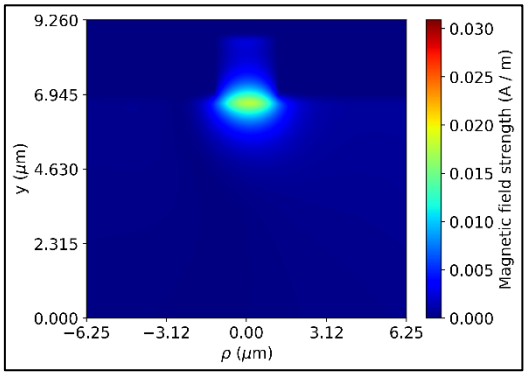

(c) H_y in the exit straight waveguide.

Figure 4.6: The magnetic field in the quasi-TE mode before, during and after a $90°$ circular shallow-etched ridge waveguide bend with a radius of curvature of $400\ \mu m$.

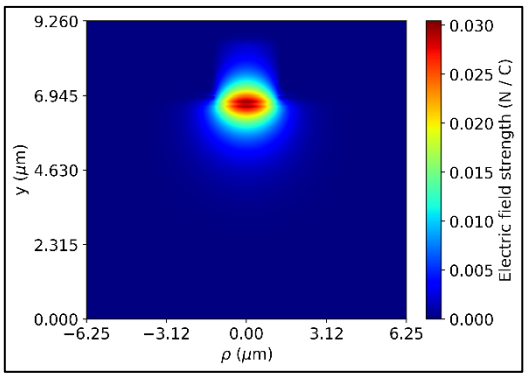

(a) Initial E_y in the straight waveguide.

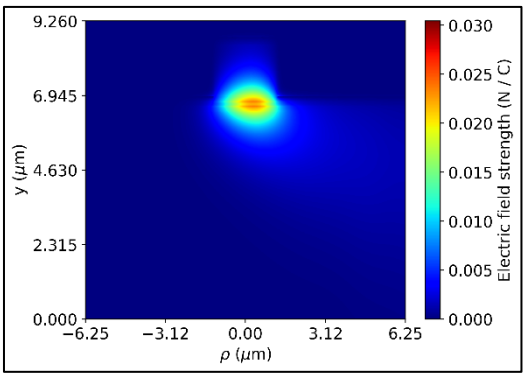

(b) E_y at 45° through the waveguide bend.

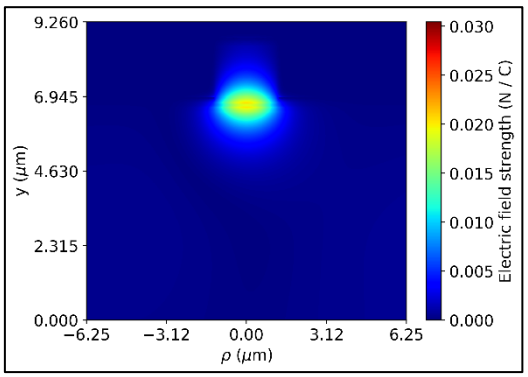

(c) E_y in the exit straight waveguide.

Figure 4.7: The electric field in the quasi-TM mode before, during and after a $90°$ circular shallow-etched ridge waveguide bend with a radius of curvature of $400\ \mu m$.

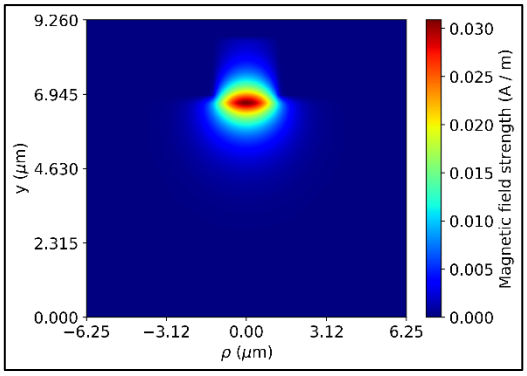

(a) Initial H_x in the straight waveguide.

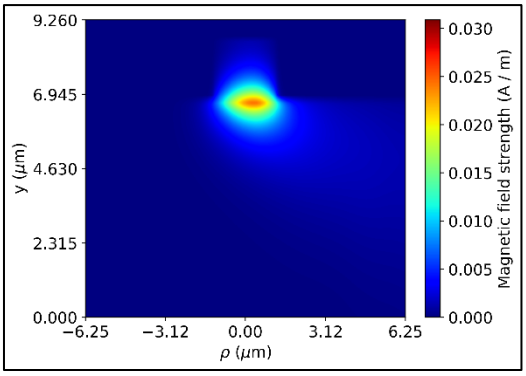

(b) H_r at 45° though the waveguide bend.

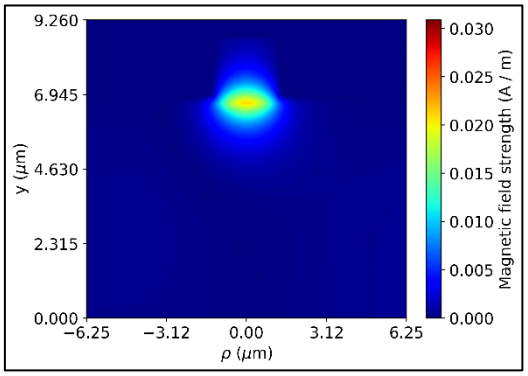

(c) H_x in the exit straight waveguide.

Figure 4.8: The magnetic field in the quasi-TM mode before, during and after a 90° circular bend with a radius of curvature of 400 μm in a shallow-etched ridge waveguide.

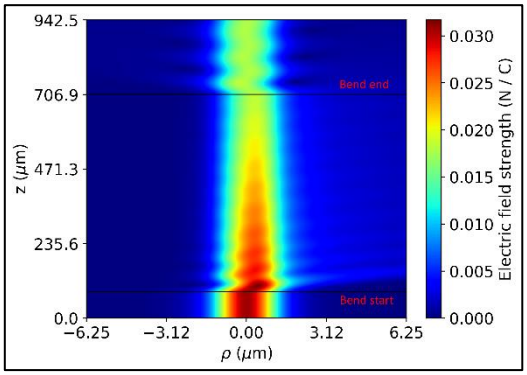

(a) E_x in the quasi-TE mode.

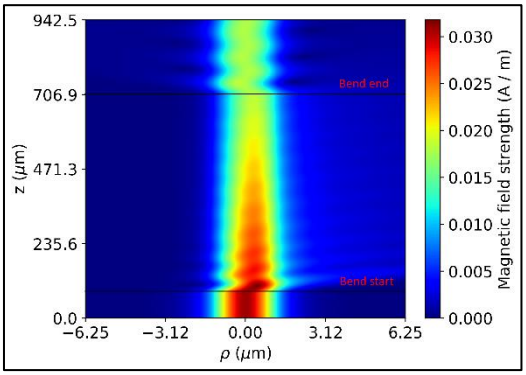

(b) H_y in the quasi-TE mode.

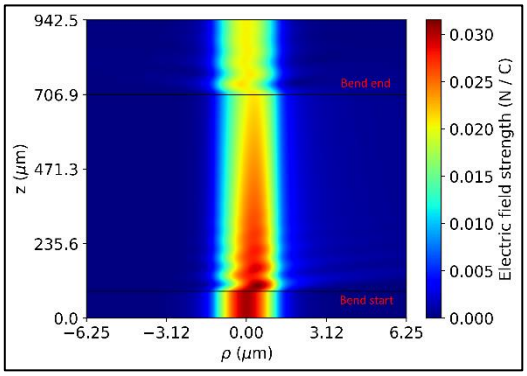

(c) E_y in the quasi-TM mode.

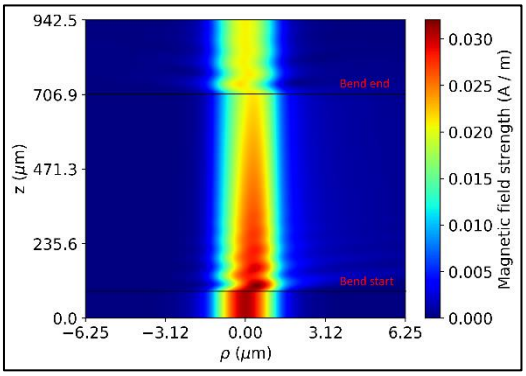

(d) H_x in the quasi-TM mode.

Figure 4.9: Cross section of the fields, at y through the peak of the initial field, as they propagate through the 90° circular shallow-etched waveguide bend with $R = 400\ \mu m$.

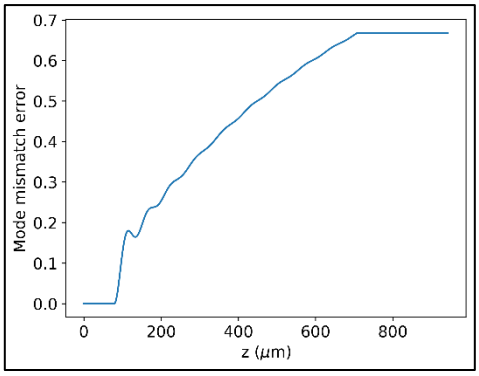

(a) E_x in the quasi-TE mode.

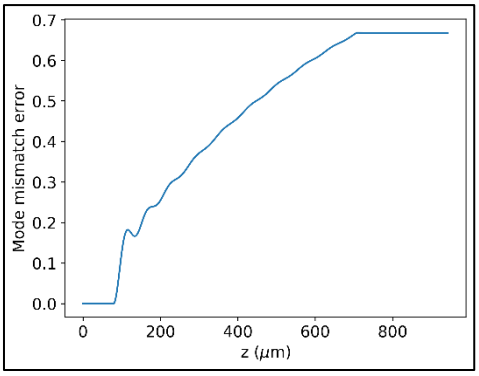

(b) H_y in the quasi-TE mode.

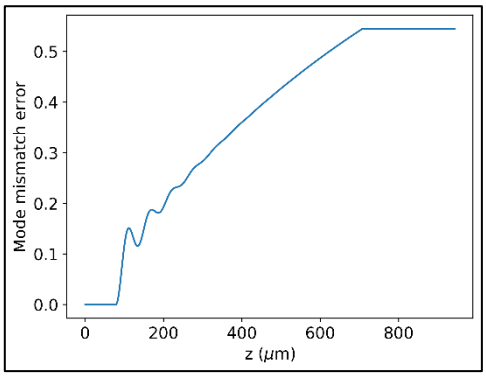

(c) E_y in the quasi-TM mode.

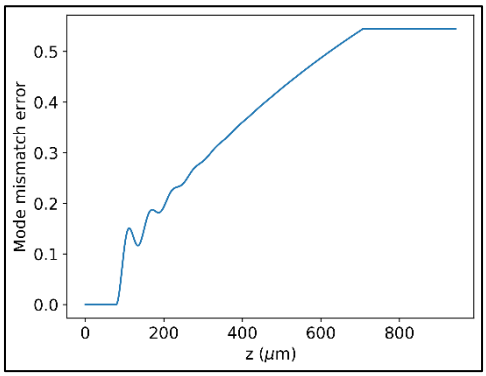

(d) H_x in the quasi-TM mode.

Figure 4.10: Mode mismatch error as each field propagates through the $90°$ circular bend shallow-etched waveguide with $R = 400\ \mu m$.

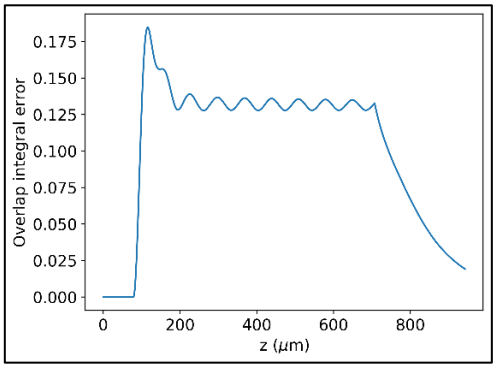

(a) E_x in the quasi-TE mode.

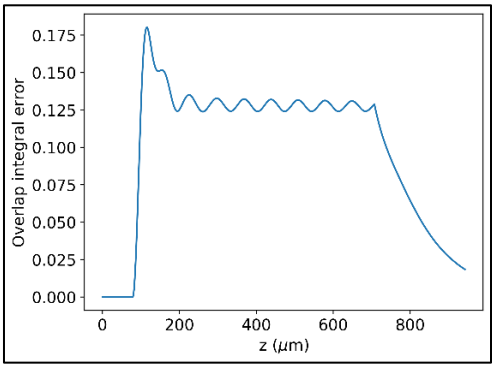

(b) H_y in the quasi-TE mode.

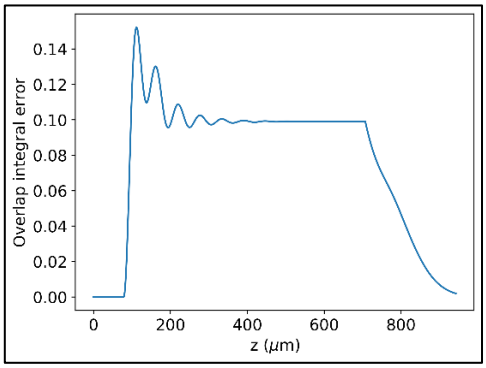

(c) E_y in the quasi-TM mode.

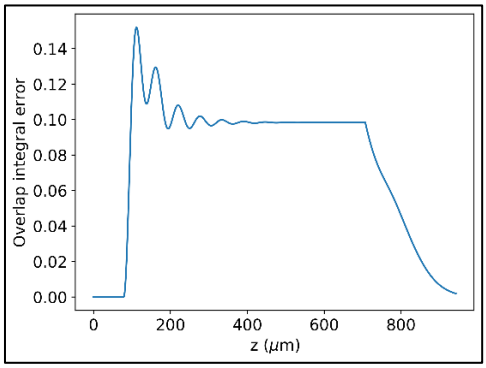

(d) H_x in the quasi-TM mode.

Figure 4.11: Overlap integral error as each field propagates through the $90°$ circular shallow-etched waveguide bend with $R = 400\ \mu m$.

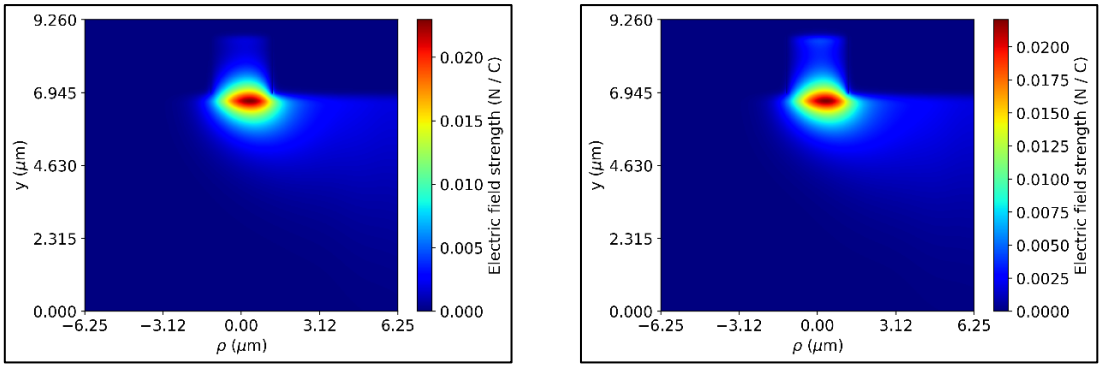

(a) E_y at minimum in OIE. (b) E_y at maximum in OIE.

Figure 4.12: E_y in the quasi-TE mode at a minimum and maximum in the overlap integral error while propagating through the 90° circular shallow-etched waveguide.

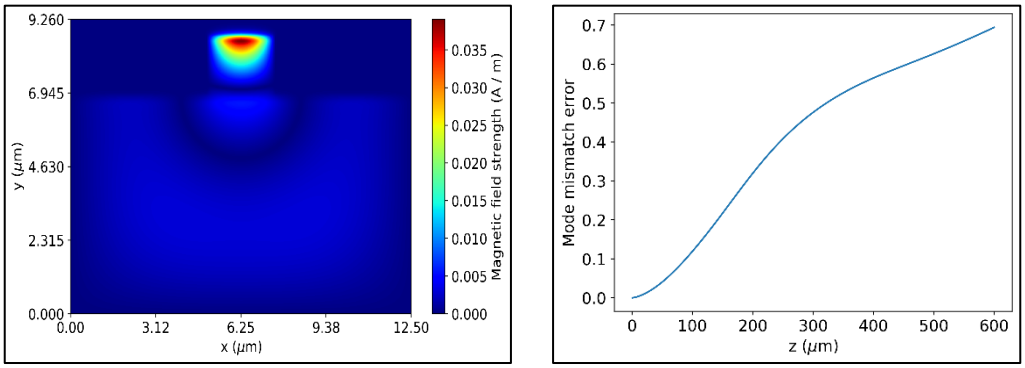

(a) Radiation mode of effective index 3.16396. (b) MME as radiation mode propagates.

Figure 4.13: Radiation mode field distribution of shallow-etched waveguide and MME as it propagates.

The simulations through the 90° bend were then repeated using a linear change of curvature. The bend was designed to have the same end point as the previously analysed circular bend, meaning the linearly changing curvature bend had an effective radius of curvature of 400 μm. The same computational parameters as those used for the circular bend were used for the linearly changing curvature bend. Figure 4.14 shows the propagated E_x field before, during, and after the 90° bend, in the quasi-TE mode. At the 45° point, the field appears to be shifted further to the outside of the bend than that of the corresponding circular waveguide at an angle of 45°. After the bend, when the field has shifted back to the centre of the waveguide, the mode has appeared to have lost more of its power than that in the corresponding circular waveguide. The same behaviour is observed for the propagated H_y, E_y and H_x fields. Figure 4.15 shows a cross section of the E_x field in the quasi-TE mode and the E_y field in the quasi-TM mode, at y where the initial field amplitude was maximum, as the fields propagate. In each case, as the curvature linearly increases, the fields appear to move further and further towards the outside of the bend. As the fields approach the 45° mark, the curvature appears to reach a point where substantial power leaks from the waveguide, especially for the quasi-TE mode. Then, after 45° through the bend, the curvature linearly decreases, causing the fields to move back towards the centre of the waveguide. Like the circular waveguide, for both the quasi-TE and quasi-TM modes, the graph for the propagated magnetic field appears practically identical to the graph for the propagated electric field and is therefore omitted in this case.

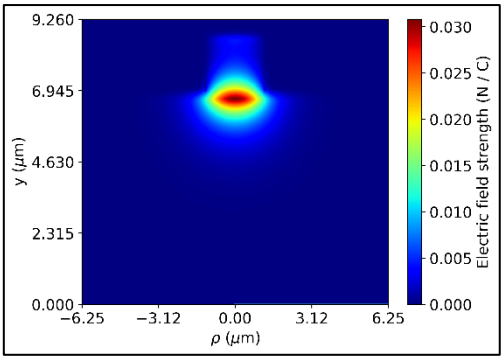

(a) Initial E_x in the straight waveguide.

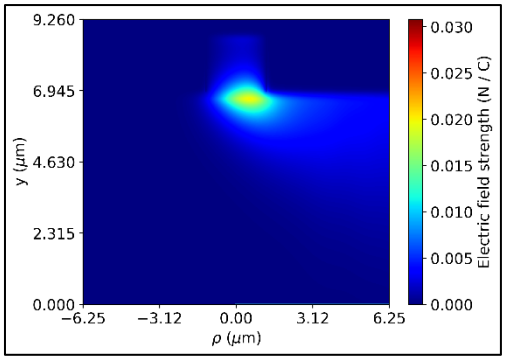

(b) E_r at 45° through the waveguide bend.

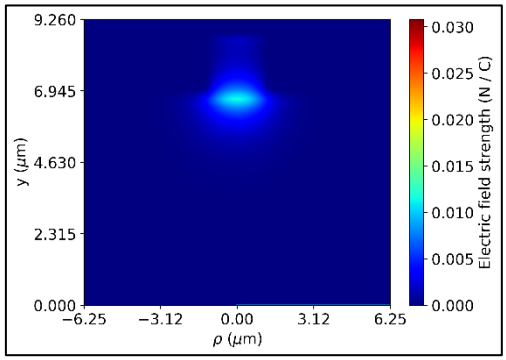

(c) E_x in the exit straight waveguide.

Figure 4.14: E_x in the quasi-TE mode before, during and after a 90° linearly changing curvature shallow-etched ridge waveguide bend with an effective radius of curvature of $400\ \mu m$.

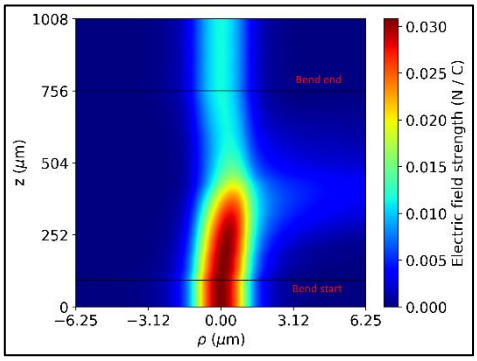

(a) E_x in the quasi-TE mode.

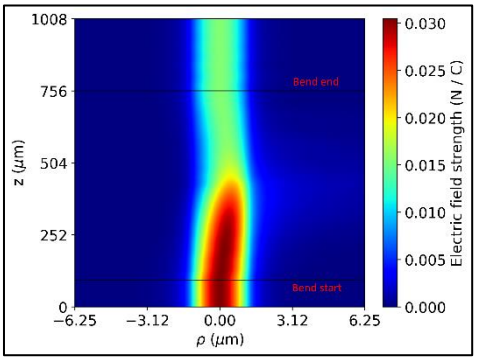

(b) E_y in the quasi-TM mode.

Figure 4.15: Cross section of the fields, at y where the initial field was maximum, as they propagate through a 90° linearly changing curvature shallow-etched waveguide bend with $R_{eff} = 400\ \mu m$.

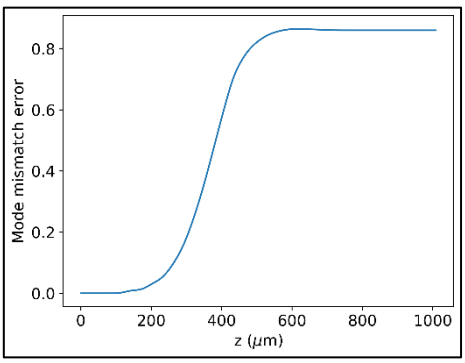

(a) E_x in the quasi-TE mode.

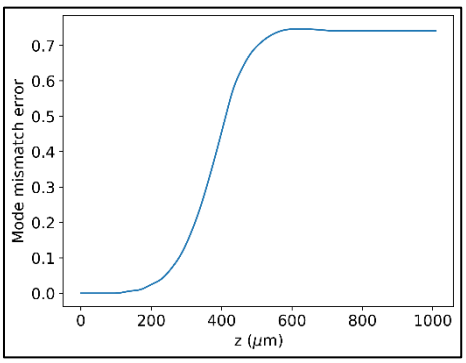

(b) E_y in the quasi-TM mode.

Figure 4.16: Mode mismatch error as each field propagates through the 90° linearly changing curvature shallow-etched waveguide bend with $R_{eff} = 400\ \mu m$.

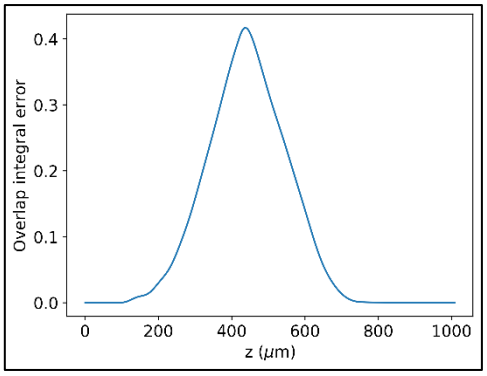

(a) E_x in the quasi-TE mode.

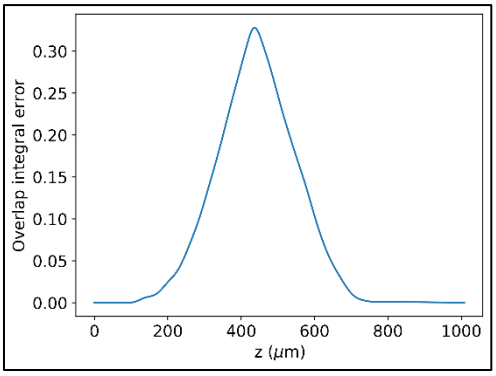

(b) E_y in the quasi-TM mode.

Figure 4.17: Overlap integral error as each field propagates through the $90°$ linearly changing curvature shallow-etched waveguide bend with $R_{eff} = 400\ \mu m$.

Figure 4.16 and Figure 4.17 show the MME and OIE respectively between the initially propagated fundamental mode field and the propagating field for the electric field in both the quasi-TE and quasi-TM modes. The MME is seen to rise smoothly as the fields propagate through the linearly increasing curvature part of the bend. The MME is then observed to stop rising as the curvature of the bend begins to linearly decrease, causing the field to shift back towards the centre of the waveguide. Meanwhile, in both cases, the OIE rises steadily until the maximum curvature is reached where it then decreases steadily as the field again takes the shape of the initially propagated field. In contrast to the MME and OIE graphs observed for the circular waveguide, no oscillations are observed in the MME and OIE graphs for the linearly changing curvature waveguide. This is because the linear change in curvature removes the sharp transition between the straight and curved waveguides which occurs in the circular waveguide. This causes the shape of the field at each propagation point through the bend to be very close to the shape of the fundamental mode of the curved waveguide at the next propagation step. This results in primarily the excitation of the fundamental mode of the curved waveguide, causing very little excitation of the radiation modes. The transition loss observed in the linearly changing curvature waveguide is therefore minimal.

Unfortunately, the MME observed after the linearly changing curvature bend is far higher than that observed for the circular bend, for both the quasi-TE and quasi-TM modes. According to equation (3.57), the maximum curvature reached is 1.87 times the curvature of the circular waveguide of the equivalent radius of curvature. Figure 4.15 shows that most of the power leaks from the waveguide when the curvature of the waveguide is in the region of this maximum curvature. This suggests that although the linear change in curvature removes the sharp transition at the straight-curved waveguide interface, the propagating field loses much more power from the maximum curvature region of the linearly changing curvature waveguide than the propagating field through the circular waveguide loses from both the straight-curved waveguide transitions and the constant curvature of the bend.

Interestingly, the MME for the E_x field in the quasi-TE mode is higher than that for the E_y field in the quasi-TM mode after the linearly changing curvature bend, in agreement with what was observed for the circular bend. However, the higher MME in this case cannot be

attributed to the excitation of shifted radiation modes, as the linear change in curvature should prevent these radiation modes from being excited.

The linearly changing curvature bend was then replaced with a trapezoidal curvature bend with the same equivalent radius of curvature of 400 μm. The bend was designed for half the path length to consist of linearly changing curvature and the other half to consist of circular curvature. This gives the fraction of the path length consisting of linearly increasing curvature, f in equation (3.85), a value of 0.25. The same computational parameters were used for this bend as were used in for the circular and linearly changing curvature bends.

Figure 4.18 gives the cross section of the propagating electric fields for both the quasi-TE and quasi-TM modes. The fields behave as expected from the previous bends, with the fields slowly moving towards the outside of the bend during the linearly increasing curvature section of the waveguide, and then remaining at the outside of the bend and losing power as they propagate through the circular region. Again, more power appears to leak in the quasi-TE mode than the quasi-TM mode. Figure 4.19 shows the MME between the propagating field and the initially propagated field. The MME appears to increase until the curvature of the waveguide begins to linearly decrease, as observed in the linearly changing curvature waveguide. The MME after the bend is between that of the circular bend and the linearly changing curvature bend at approximately 0.78 for the quasi-TE mode and 0.66 for the quasi-TM mode. The overlap integral error graph in Figure 4.20 appears to have almost a trapezoidal shape. This is due to the shape of the field profile shifting as it propagates through the linearly changing curvature regions, and then taking a constant shape as it propagates through the circular regions.

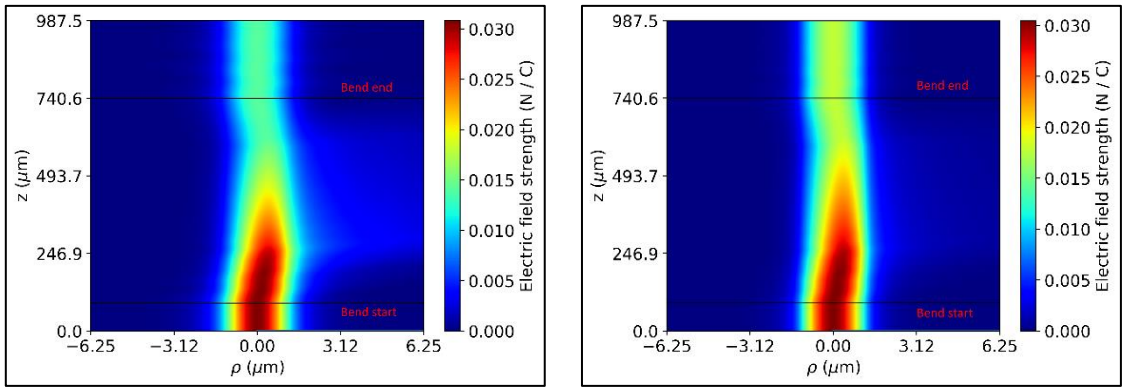

(a) E_x in the quasi-TE mode. (b) E_y in the quasi-TM mode.

Figure 4.18: Cross section of the fields, at y through the peak of the initial field, as they propagate through the 90° trapezoidal curvature bend shallow-etched waveguide with $f = 0.25$ and $R_{eff} = 400\ \mu m$.

The MME results from the bends analysed appear to suggest that, for the 90° bend, the best approach is the simple circular curvature bend. The reduction in transition loss offered by the linear curvature bend is inconsequential in comparison to extra propagating loss suffered due to the larger maximum curvature reached. To verify this, and to investigate if it holds for bends of different effective radii of curvature, Figure 4.21 gives a graph of the mode mismatch error for different radii of curvature and different linear curvature fractions for the magnetic field in both the quasi-TE and quasi-TM modes. The graphs confirm that

the mode mismatch error increases with decreasing radius of curvature and increasing linear curvature fraction. Therefore, the bend profile with the least loss is the circular curvature bend. The graphs also show that less loss is observed for fields propagated in the quasi-TM mode for every effective radius of curvature and linear curvature fraction. To make shallow-etched bends without significant losses, the graphs suggest that the effective radius of curvature should be kept above approximately $500\ \mu m$ for the circular waveguide and above $650\ \mu m$ for the linearly changing curvature waveguide.

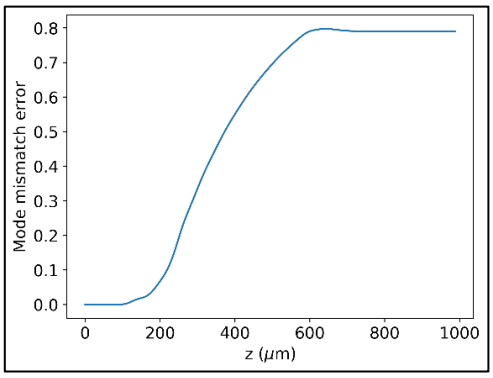

(a) E_x in the quasi-TE mode.

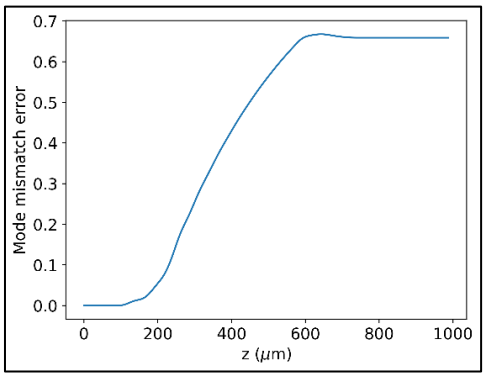

(b) E_y in the quasi-TM mode.

Figure 4.19: Mode mismatch error as each field propagates through the $90°$ trapezoidal curvature bend shallow-etched waveguide with $f = 0.25$ and $R_{eff} = 400\ \mu m$.

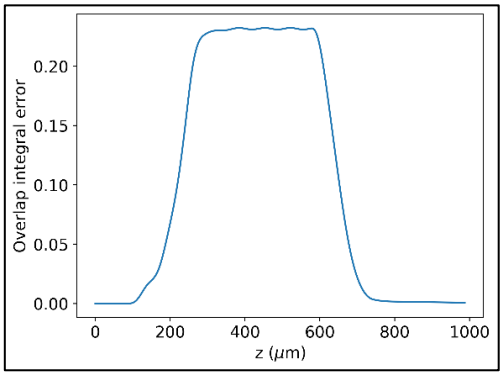

(a) E_x in the quasi-TE mode.

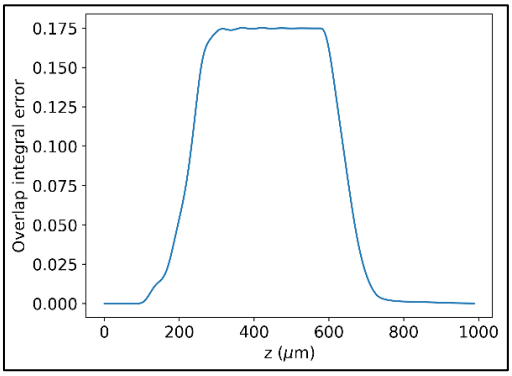

(b) E_y in the quasi-TM mode.

Figure 4.20: Overlap integral error as each field propagates through the $90°$ trapezoidal curvature bend shallow-etched waveguide with $f = 0.25$ and $R_{eff} = 400\ \mu m$.

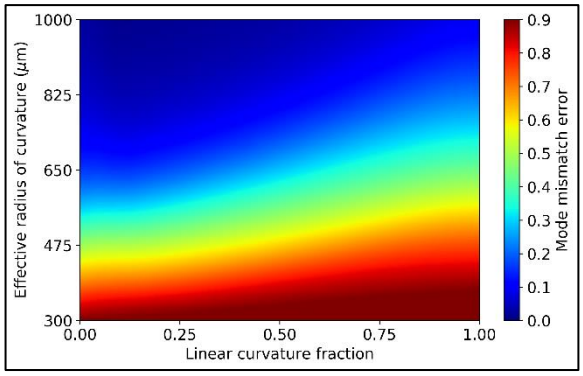

(a) H_y in the quasi-TE mode.

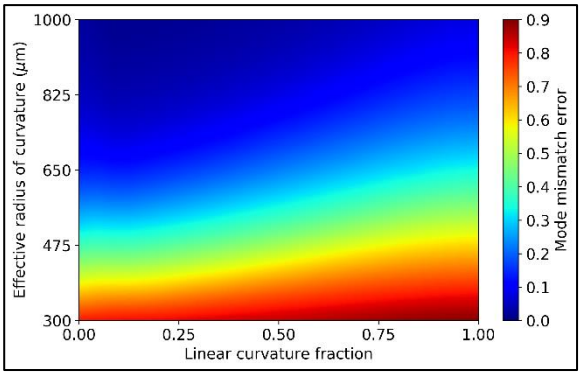

(b) H_x in the quasi-TM mode.

Figure 4.21: Mode mismatch error vs. effective radius of curvature and the fraction of the path length consisting of linearly changing curvature for the 90° bend.

4.2.2 Shallow-Etched Ridge Waveguide with a 180° Bend

Following on from the $90°$ bend analysis, the same procedure was used to find the best curvature profile for the 180° bend. Different results could be expected for the 180° bend, as the maximum curvature reached is smaller than that reached for the 90° bend in the cases of the linearly changing curvature and trapezoidal curvature profiles. For example, for the linear curvature waveguide, according to equation (3.57), the maximum curvature reached is 1.3768 times the curvature of a circular waveguide with the same effective radius of curvature. This is much lower than that of the 90° bend waveguide with 1.87 times the circular curvature.

Figure 4.22 gives the cross section of the fields, at y through the peak of the initial field, as they propagate through a circular bend with a radius of curvature of 500 μm. This is larger than the 400 μm radius bend analysed for the 90° bend as a 180° bend produces more loss than a 90° bend with the same radius of curvature, due to the longer path length of the bend. The field of course behaves in the same manner as for the 90° circular bend, immediately shifting towards the outside of the bend at the straight-waveguide boundary and then losing power as it propagates through the circular bend. Figure 4.23 again shows the quasi-TM mode to perform better than the quasi-TE mode. And Figure 4.24 again shows how the bend causes shifted slow radiating mode(s) to be exited in the quasi-TE mode, however, this time it is easier to see the oscillations in the OIE dampen as the field propagates through the bend, showing that the power leaks substantially from the excited radiation mode(s).

Next, Figure 4.25 shows the cross section of the field, at y through the peak of the initial field, as it propagates through a linearly changing curvature bend with an effective radius of curvature of 500 μm. The field moves slowly towards the outside of the bend as the curvature linearly increases and then back to the centre of the waveguide as the curvature linearly decreases. In contrast to the 90° bend, the power does not leak substantially in the region of the waveguide close to the maximum curvature. Figure 4.26 shows the MME between the propagating fields and the initially propagated fundamental mode fields. In this case however, the MME after the bend appears to be slightly less than that of the corresponding circular bend, suggesting a linear change of curvature is of benefit to the 180° bend.

Figure 4.28 shows the cross section of the field as it propagates through a trapezoidal curvature bend with half the path length designated for linearly changing curvature and with an effective radius of curvature of 500 μm. For both the quasi-TE and quasi-TM modes, the field transitions smoothly to the fundamental mode of the circular region and loses most of its power while propagating through this circular region. The MME graphs show the MME to be less than both the circular and linearly changing curvature bends, suggesting a trapezoidal curvature profile is preferred to minimise loss.

Although the bend appears to have the least amount of loss for the half linearly changing curvature, half circular bend, it is important to check if any other fraction of linearly changing curvature would reduce the loss further. It is also important to see if the observation holds for other radii of curvature. Figure 4.31 therefore gives the MME after the

bend for different radii and linearly changing curvature fractions, for the magnetic field in both the quasi-TE and quasi-TM modes. The graphs suggest that the MME is minimised when the graph is approximately half linearly changing curvature, half circular curvature, but the reduction in MME by designing the bend in this way appears to be relatively small. The linear curvature fraction where the MME is minimum also appears to vary depending on the effective radius of curvature. For example, Figure 4.32 more clearly shows the MME for the quasi-TE mode at effective radii of curvature of approximately 530 μm and 730 μm. When $R_{eff} = 530\ \mu m$, the minimum appears to be at a linear curvature fraction of 0.45 and the difference between the maximum and minimum MME is 0.06. Meanwhile, when $R_{eff} = 730\ \mu m$, the minimum appears to be at a linear curvature fraction of 0.35 and the difference between the maximum and minimum MME is 0.05. As the effective radius of curvature is lowered from 1000 μm to 300 μm, the linear curvature fraction where the MME is minimum appears to gradually shift from approximately 0.33 to 0.5. However, the difference between maximum and minimum MME remains relatively low at all effective radii of curvature.

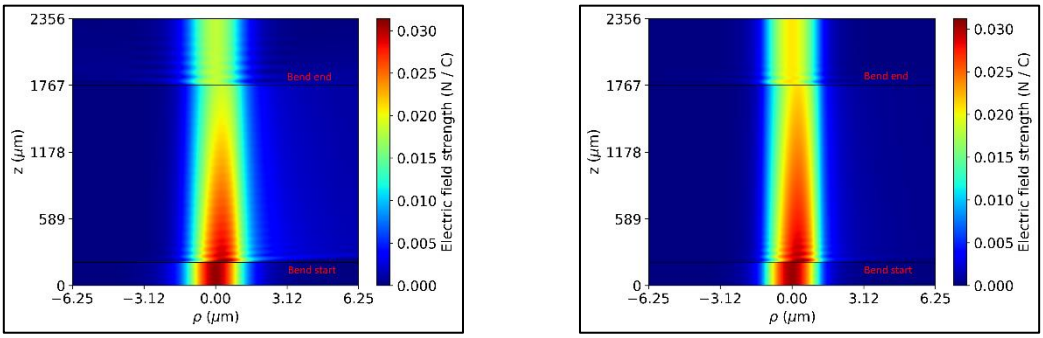

(a) E_x in the quasi-TE mode. (b) E_y in the quasi-TM mode.

Figure 4.22: Cross section of the fields, at y through the peak of the initial field, as they propagate through the $180°$ circular shallow-etched waveguide bend with $R = 500\ \mu m$.

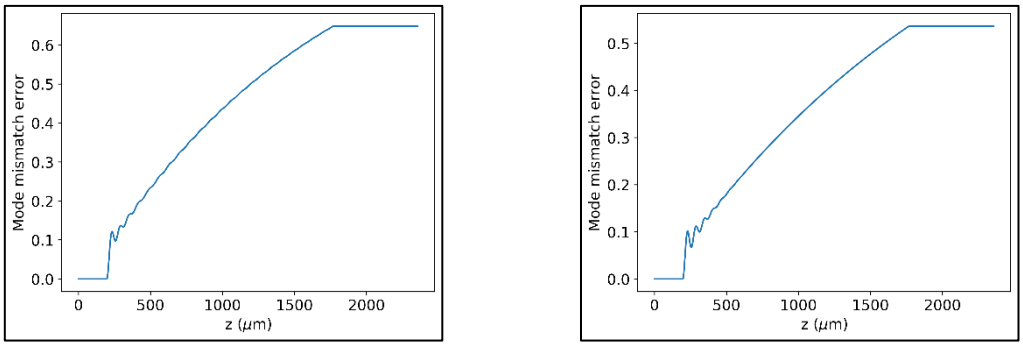

(a) E_x in the quasi-TE mode. (b) E_y in the quasi-TM mode.

Figure 4.23: Mode mismatch error as each field propagates through the $180°$ circular shallow-etched waveguide bend with $R = 500\ \mu m$.

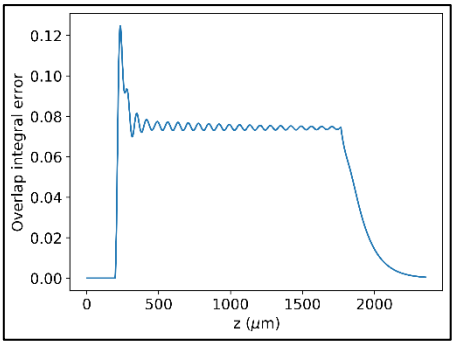

(a) E_x in the quasi-TE mode.

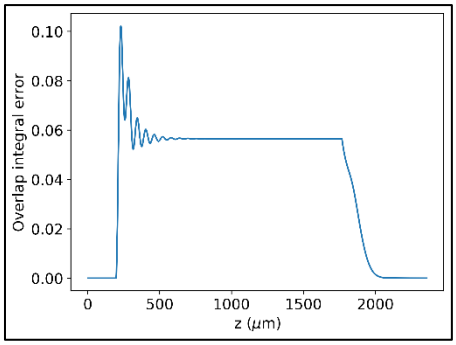

(b) E_y in the quasi-TM mode.

Figure 4.24: Overlap integral error as each field propagates through the 180° circular shallow-etched waveguide bend with $R = 500\ \mu m$.

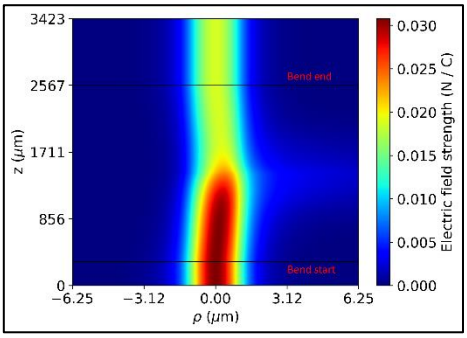

(a) E_x in the quasi-TE mode.

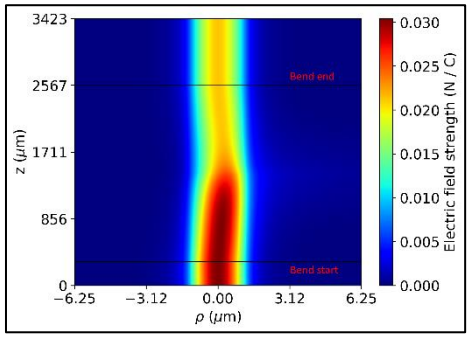

(b) E_y in the quasi-TM mode.

Figure 4.25: Cross section of the fields, at y through the peak of the initial field, as they propagate through the 180° linearly changing curvature shallow-etched waveguide bend with $R_{eff} = 500\ \mu m$.

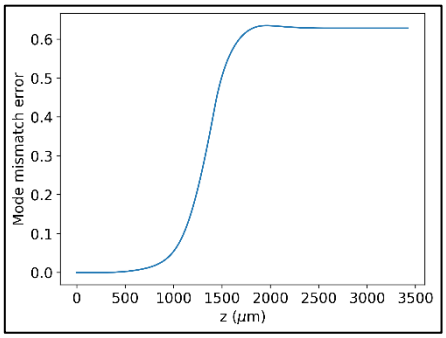

(a) E_x in the quasi-TE mode.

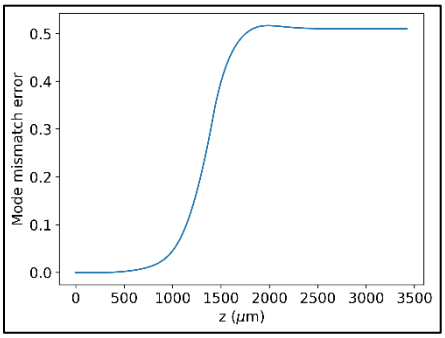

(b) E_y in the quasi-TM mode.

Figure 4.26: Mode mismatch error as each field propagates through the 180° linearly changing curvature shallow-etched waveguide bend with $R_{eff} = 500\ \mu m$.

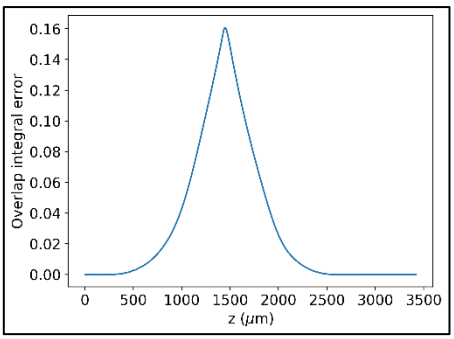

(a) E_x in the quasi-TE mode.

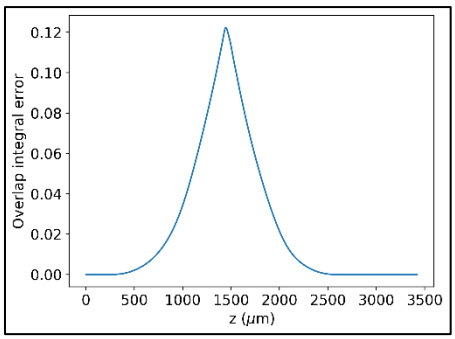

(b) E_y in the quasi-TM mode.

Figure 4.27: Overlap integral error as each field propagates through the 180° linearly changing curvature shallow-etched waveguide bend with $R_{eff} = 500\ \mu m$.

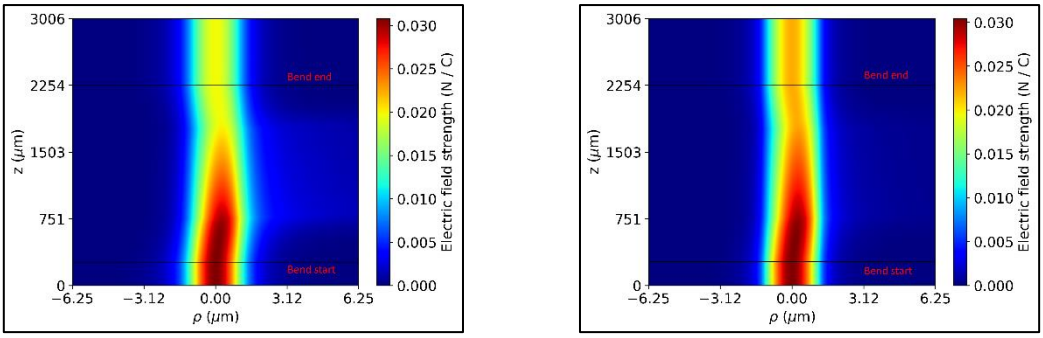

(a) E_x in the quasi-TE mode. (b) E_y in the quasi-TM mode.

Figure 4.28: Cross section of the fields, at y through the peak of the initial field, as they propagate through the 180° trapezoidal shallow-etched waveguide bend with $R_{eff} = 500\ \mu m$.

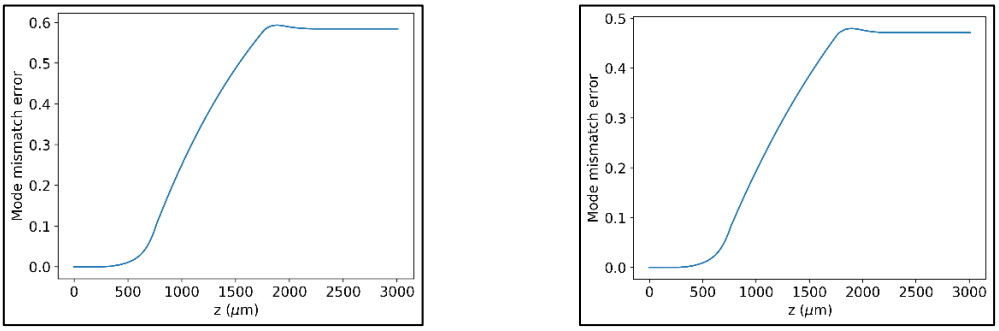

(a) E_x in the quasi-TE mode. (b) E_y in the quasi-TM mode.

Figure 4.29: Mode mismatch error as each field propagates through the 180° trapezoidal shallow-etched waveguide bend with $R_{eff} = 500\ \mu m$.

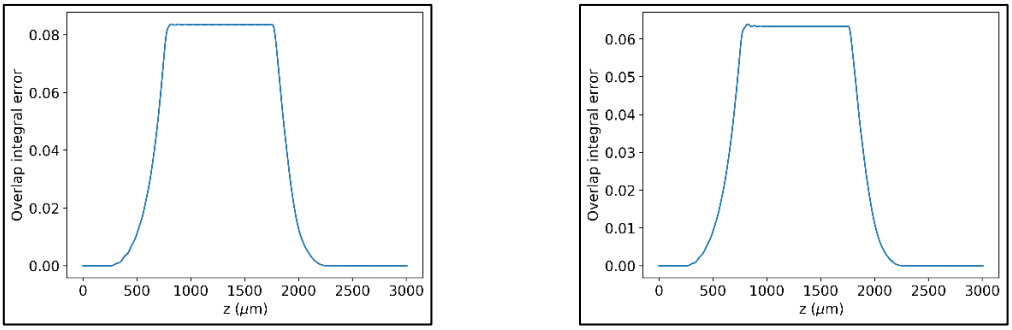

(a) E_x in the quasi-TE mode. (b) E_y in the quasi-TM mode.

Figure 4.30: Overlap integral error as each field propagates through the 180° trapezoidal shallow-etched waveguide bend with $R_{eff} = 500\ \mu m$.

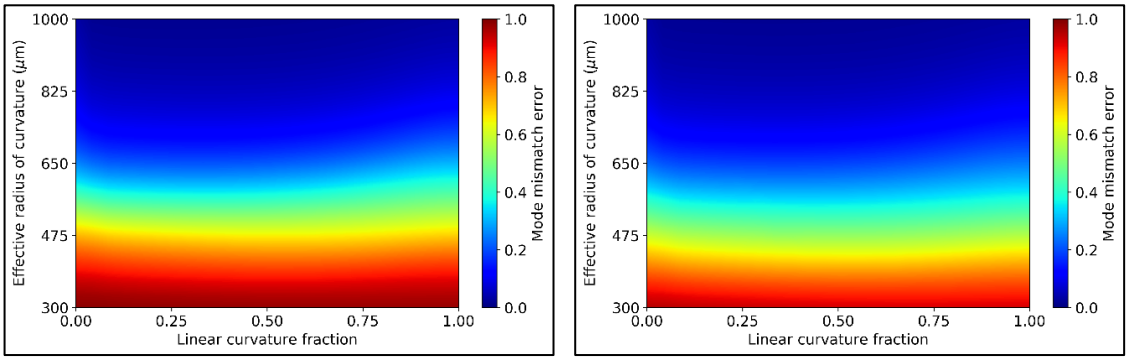

(a) H_y in the quasi-TE mode. (b) H_x in the quasi-TM mode.

Figure 4.31: Mode mismatch error vs. effective radius of curvature and the fraction of the path length consisting of linearly changing curvature for the 180° shallow-etched bend.

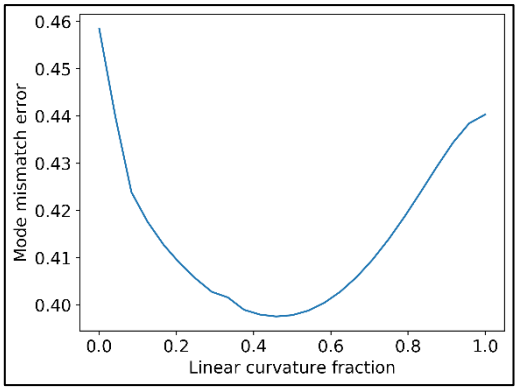

(a) $R_{eff} = 530\ \mu m$.

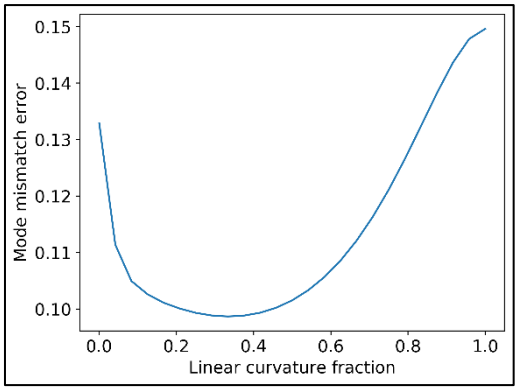

(b) $R_{eff} = 730\ \mu m$.

Figure 4.32: Change of mode mismatch error with linear curvature fraction for a constant effective radius of curvature for the 180° shallow-etched bend.

4.3 Effect of Waveguide Width and Shallow Etch Depth on Curved Waveguide Loss

The effect of changing the width and shallow etch depth of the waveguide were investigated to observe if the bend loss could be reduced. Increasing the width of the waveguide has previously be shown to reduce the bend loss of curved waveguides as the fundamental mode becomes more confined [54].

4.3.1 The Effect of Waveguide Width on Curved Waveguide Loss

The width of the shallow-etched waveguide was varied to observe the effect it would have on loss from the waveguide bend. This is also important as the waveguide width can sometimes vary from approximately 2.4 μm to 2.6 μm during fabrication if designed to be 2.5 μm, for example. The shallow-etched waveguide refractive index profile is the same as the one analysed in the previous section. Figure 4.33 gives the mode mismatch error between the initially propagated magnetic field in the quasi-TM mode and the field after a 180° bend, for both a circular waveguide and a linear changing curvature waveguide with effective radii of curvature of 500 μm, where the waveguide width was varied from 2 μm to 3 μm. The same computational parameters were again used for this computation as the computations in the previous section. The graphs show that the MME decreases considerably with increasing waveguide width in both cases. As the width of the original waveguide was 2.5 μm, increasing the width to $3\ \mu m$ would give a decrease in the MME of approximately 0.12 from 0.52 to 0.4 for the circular waveguide and a decrease of approximately 0.14 from 0.5 to 0.36 for the linearly changing curvature waveguide. Waveguide widths beyond $3\ \mu m$ were not included as the waveguide becomes multimode in the quasi-TM mode beyond this width. Meanwhile, the shallow-etched waveguide becomes multimode at a waveguide width of approximately 2.8 μm in the quasi-TE mode.

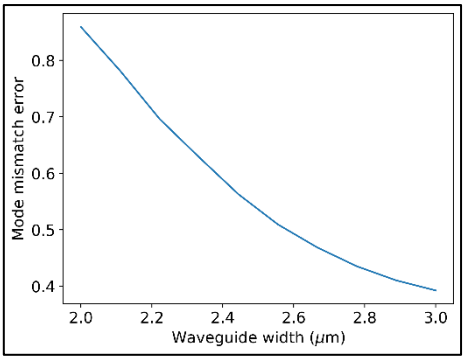

(a) Circular Waveguide.

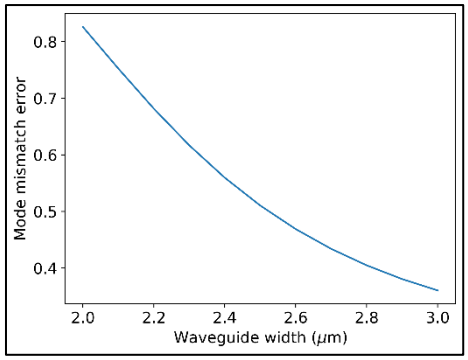

(b) Linearly changing curvature waveguide.

Figure 4.33: Effect of waveguide width on mode mismatch error after a 180° bend for H_x in the quasi-TM mode.

Figure 4.34 gives the H_x field profiles in the quasi-TM mode through the straight waveguide for waveguide widths of $2\ \mu m$, $2.5\ \mu m$, and $3\ \mu m$ and offers an insight into why the varying waveguide width has such an impact on the bend loss. The decreasing waveguide width causes more of the field distribution to be pushed down from the region above the etch to the region below the etch. Numerically, for the $2\ \mu m$ width, 19% of the total power is confined to the region above the etch, compared to 23.4% for the $2.5\ \mu m$ width and 26% for the $3\ \mu m$ waveguide width. The decreasing waveguide width therefore allows more power to leak from the waveguide during the bend, as less of the field distribution is now confined by the sharp refractive index contrast between the waveguide material and air.

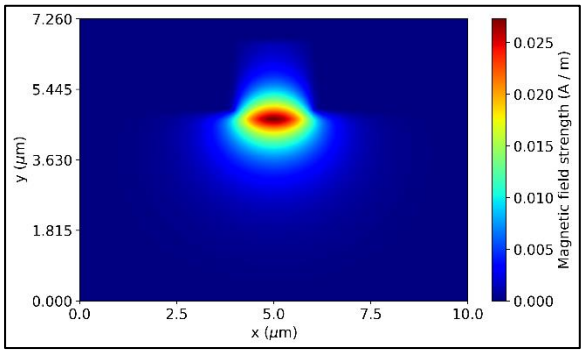

(a) 2 μm waveguide width.

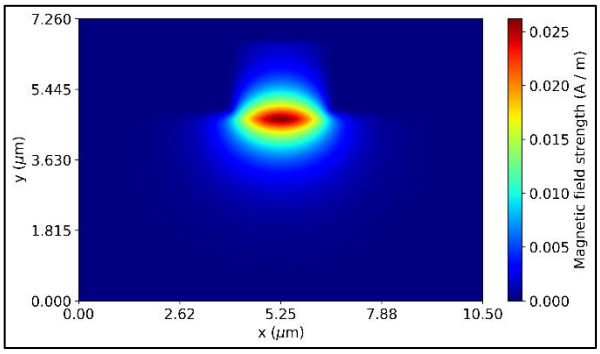

(b) 2.5 μm waveguide width.

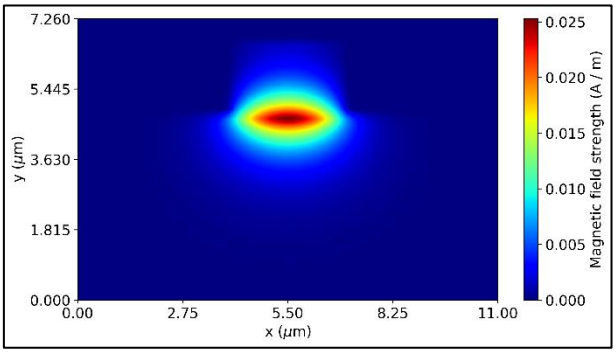

(c) 3 μm waveguide width.

Figure 4.34: H_x field profiles in the quasi-TM mode for the shallow-etched waveguide of various widths.

4.3.2 The Effect of Etch Depth on Curved Waveguide Loss

The effect of altering the shallow etch depth on the curved waveguide loss was investigated. Although typically designed for a depth of 1.85 μm, the actual etch depth can vary slightly during fabrication. The effect on the loss was investigated for etch depths from 1.75 μm to 1.95 μm.

Figure 4.35 shows graphs of the mode mismatch error between the initially propagated field and the field after 180° circular and linearly changing curvature bends with effective radii of 500 μm, as the etch depth varies, for the magnetic field in both the quasi-TE and quasi-TM modes. The MME varies significantly within this etch depth range, becoming smaller as the etch depth increases.

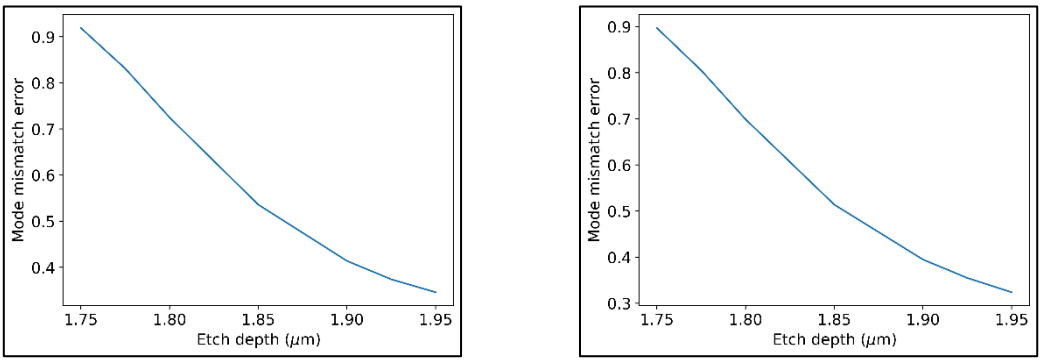

(a) Circular Waveguide. (b) Linearly changing curvature waveguide.

Figure 4.35: Effect of etch depth on mode mismatch error after a 180° bend for H_x in the quasi-TM mode.

The reason for these results is again primarily due to how much power is confined within the etch. This is clearly seen in Figure 4.36, which shows the H_x field profile in the quasi-TM mode for etch depths of $1.75\ \mu m$, $1.85\ \mu m$, and $1.95\ \mu m$. The deeper the etch, the more power is confined by the sharp refractive index change, and the less power escapes from under the etch during the bend. At etch depths greater than 1.95 μm, the etch approaches the quantum well region and would therefore be considered a deep etch.

4.4 Conclusions

Curved shallow-etched ridge waveguides of various curvature profiles were analysed in an attempt to reduce the bend loss. Modifying the curvature profile of the bend only slightly improved the bend performance, as the shallow etch allowed the fundamental mode to easily shift and leak power from the bend regardless of the curvature profile. Large effective radii of curvature bends were therefore still needed to allow low loss shallow-etched bends. Slightly increasing the width and etch depth of the waveguide were shown to have a far greater impact on reducing the bend loss.

The next chapter will analyse curved deep-etched ridge waveguides, where the higher mode confinement may cause the different curvature profiles to have a better impact on the curved waveguide loss.

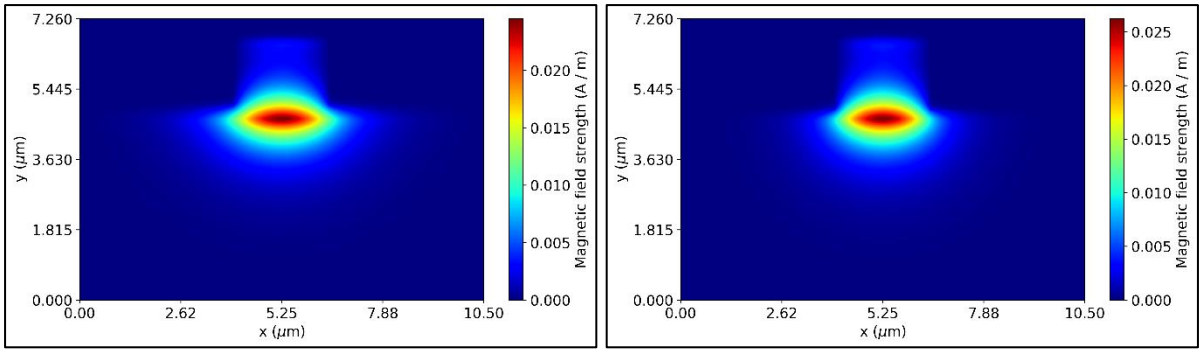

(a) 1.75 μm etch depth.

(b) 1.85 μm etch depth.

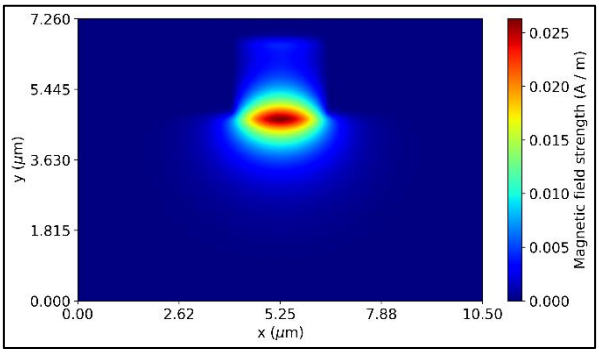

(c) 1.95 μm etch depth.

Figure 4.36: H_x field profiles in the quasi-TM mode for the shallow-etched waveguide of various etch depths.

5 Analysis of the Curved Deep-Etched Ridge Waveguide

This chapter will focus on the analysis of deep-etched ridge optical waveguides. The waveguide structure is equivalent to the waveguide analysed in the previous chapter, with the etch depth now penetrating through the quantum well region. This deep etch causes greater lateral confinement of the waveguide's fundamental mode, leading to differing behaviour of the propagating field through a bend in the waveguide to that through the curved shallow-etched waveguide.

5.1 The Deep-Etched Ridge Waveguide

The waveguide analysed is again based on the standard 1550 nm commercial laser material from IQE. After the material was deeply etched in the fabrication process at Tyndall, much less loss was observed after a bend in the waveguide, and much lower radii bends could be used relative to those used for the shallow-etched waveguide. This chapter therefore aims to show and understand the superior performance of the deep-etched bends and also investigate if the performance of the bend could be improved by varying the curvature profile of the bend.

The material and refractive index structure of the original waveguide and simplified bulk material waveguide are again given by Table 4.1 and Table 4.2 respectively. The depth of the deep etch is 2.96 μm, which is the etch depth of the deep etch used by the IPG in Tyndall, and this depth causes the etch to extend approximately 0.8 μm beyond the quantum well region. Figure 5.1 shows the refractive index profile of the bulk material deep-etched waveguide.

Figure 5.2 shows the calculated fundamental mode field distributions for both the quasi-TE and quasi-TM modes of the deep-etched waveguide. 250 computational grid points were used in each transverse direction, with a grid spacing of 0.01 μm used close to refractive index boundaries. Dirichlet boundary conditions were used for the computation. The effective refractive index of the quasi-TE mode is 3.18164 and the effective refractive index of the quasi-TM mode is 3.17941. The fields appear very similar to those computed for the shallow-etched waveguide in Figure 4.3, with the difference being that the fields through the quantum well region are now more confined in the $\hat{\boldsymbol{x}}$ direction due to the deep etch through the quantum well region causing a large refractive index contrast between the waveguide material and air.

The properties of the different fields are also clearly evident for the deep-etched waveguide, i.e. the E_x field is discontinuous at refractive index boundaries along the $\hat{\boldsymbol{x}}$ direction, the E_y field is discontinuous at refractive index boundaries along the $\hat{\boldsymbol{y}}$ direction, and the magnetic fields are continuous at all refractive index boundaries. In the case of all the fields, a small amount of the fields distribution still exists in the substrate region below the deep etch. In the case of the fields in the quasi-TE mode, a small second peak is again observed at the top of the waveguide.

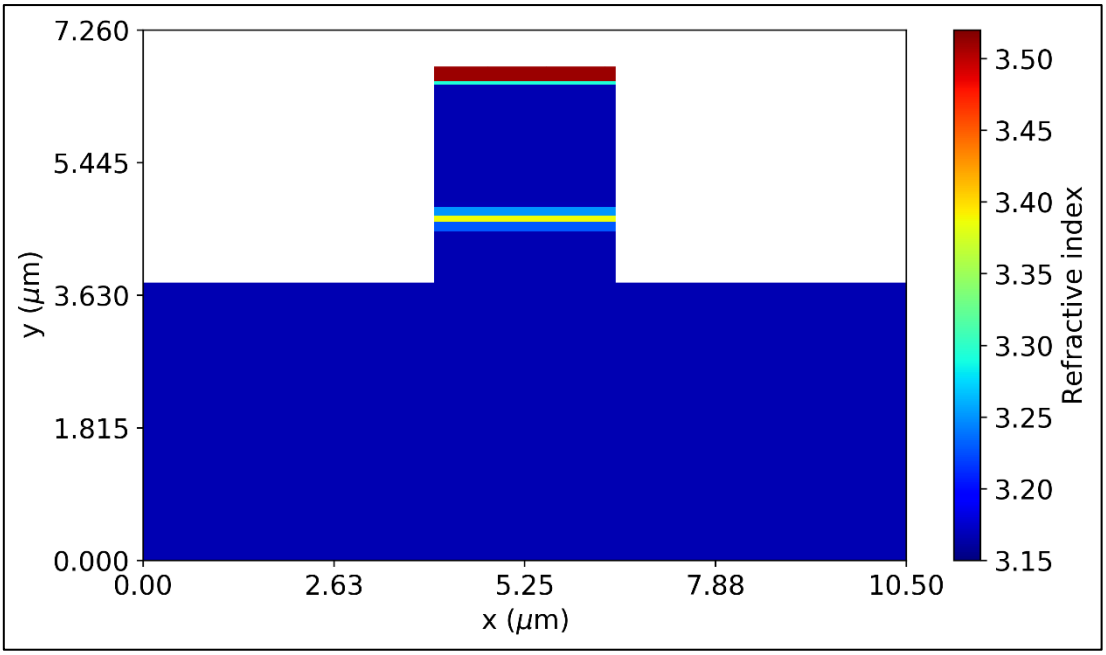

Figure 5.1: Refractive index profile of the deep-etched waveguide.

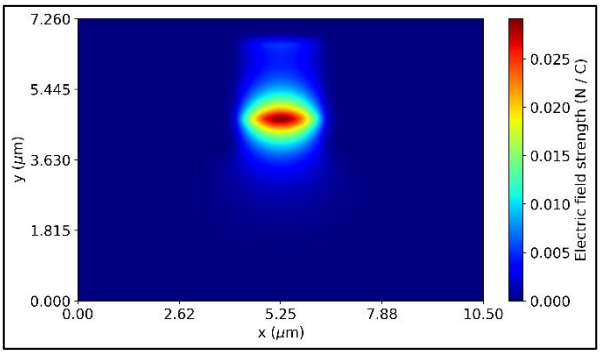

(a) E_x in the quasi-TE mode.

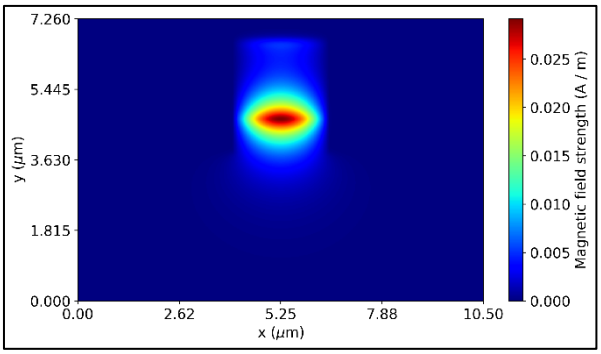

(b) H_y in the quasi-TE mode.

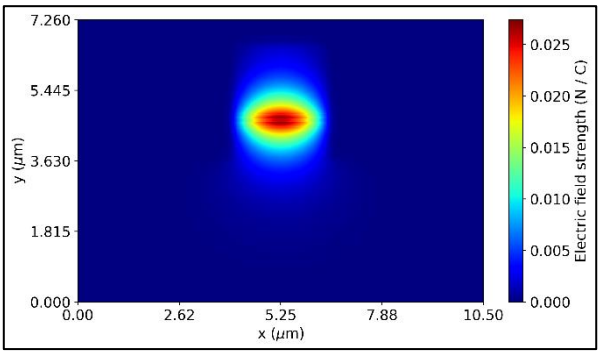

(c) E_y in the quasi-TM mode.

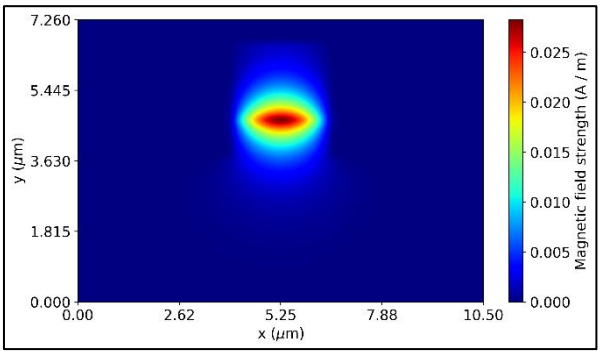

(d) H_x in the quasi-TM mode.

Figure 5.2: Fundamental mode field distributions of the quasi-TE and quasi-TM modes for the deep-etched waveguide.

5.2 The Curved Deep-Etched Ridge Waveguide

This section will analyse the behaviour and loss of the fields as they propagate through a curved deep-etched waveguide. This analysis will again focus on 90° and 180° bends.

5.2.1 Deep-Etched Ridge Waveguide with a 90° Bend

5.2.1.1 Circular Bend

Figure 5.3 and Figure 5.4 show the propagating electric fields in the quasi-TE mode and quasi-TM mode, respectively, before, during, and after a 90° circular bend with a radius of curvature of 100 μm. 350 computational points were used in each transverse direction, including a PML region which extended for approximately 2 μm beyond the original computational boundaries. The propagation step size was 0.1 μm and the fields were propagated using the (2, 2) Padé order. The field within the PML region was not included in the graphs. These computational parameters were used for all BPM simulations done in this chapter, unless stated otherwise.

Figure 5.3 (b) and (c) show the electric field in the quasi-TE mode at angles 44.2° and 51.9° through the bend. Although the angles only differ by $8.7°$, the field distributions are quite different, with the field at $\varphi = 44.2°$ shifted towards the outside of the bend, and the field at $\varphi = 51.9°$ appearing to be located far closer to the centre of the waveguide. This changing shape of the field profile suggests the excitation of multiple modes on entry to the circular waveguide, which then beat together as the field propagates. This is made further evident by Figure 5.5 (a) which shows the cross section of the field, at y through the peak of the initial field, as it propagates. The field appears to repeatedly shift towards and away from the outside of the bend as it propagates through the waveguide. Figure 5.3 (d) shows the field 59 μm after the bend. The field had exited the bend as a superposition of curved waveguide modes causing multiple radiation modes to be excited in the exit straight waveguide. At this propagation distance, the field is deformed from the shape of the straight fundamental mode field suggesting the radiation modes are still beating, which in turn suggests the radiation modes are slowly radiating. The same behaviour is observed for the propagating field in the quasi-TM mode, with the field beating between modes as it propagates through the bend.

Figure 5.6 shows the mode mismatch error between the propagating field and the initially propagated straight waveguide fundamental mode field for both the quasi-TE and quasi-TM modes. The MME oscillates as the fields propagate through the circular waveguide due to the excitation of the multiple modes which have different effective refractive indices. The MME values at the peaks and troughs also increase as the fields propagate due to the power slowly escaping under the deep etch due to the excitation of the leaky shifted fundamental mode and the shifted radiation mode(s). If the bend is designed to end on one of these troughs, the excitation of the fundamental straight waveguide mode can be maximised, leading to lower loss. The design of a waveguide bend in this manner is known as a matched bend and this method was applied to high index contrast waveguides in the University of Notre Dame [3]. In their analysis, two bend modes were excited and the bend was designed to end where the two excited modes had identical phases which caused the original field to be reproduced. This would correspond to ending the bend on a trough of Figure 5.6. The

path length of the bend was therefore designed to be an integer number of the beat length between the two modes, with the beat length given by:

$$L_B = \frac{\lambda}{n_1 - n_2} \tag{5.1}$$

n_1 and n_2 refer to the effective refractive indices of the bend modes. Returning to Figure 5.6, the rate of MME oscillation with propagating distance is slightly smaller for the quasi-TM mode, causing the quasi-TM mode to perform worse at this radius of curvature, as the MME is approximately midway between a peak and a trough when the bend ends for the quasi-TM mode, while the MME is close to a trough when the bend ends for the quasi-TE mode. However, the MME at a peak or trough is larger for the quasi-TM mode than the corresponding peak or trough for the quasi-TE mode. This suggests the propagation loss is higher for the fields in the quasi-TM mode than the quasi-TE mode, opposite to what was true for the shallow-etched waveguide.

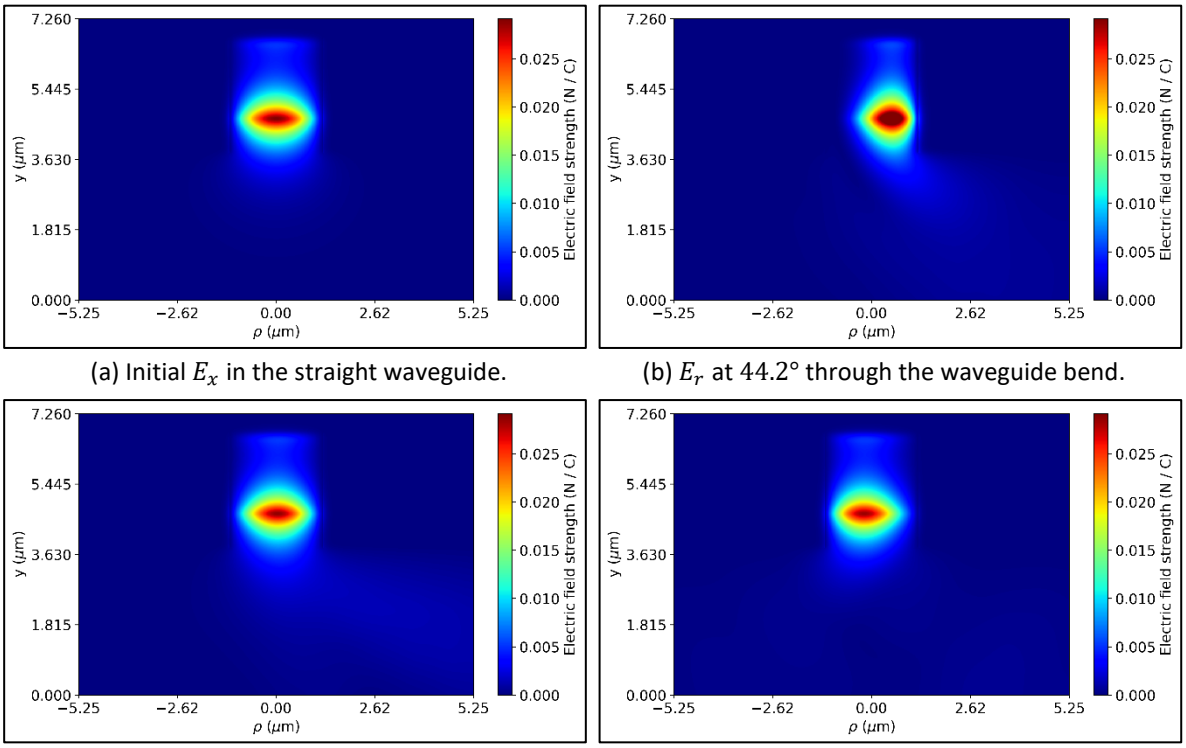

(a) Initial E_x in the straight waveguide.

(b) E_r at $44.2°$ through the waveguide bend.

(c) E_r at $52.9°$ through the waveguide bend.

(c) E_x $59\ \mu m$ after the bend.

Figure 5.3: The electric field in the quasi-TE mode before, during and after a $90°$ circular deep-etched ridge waveguide bend with a radius of curvature of $100\ \mu m$.

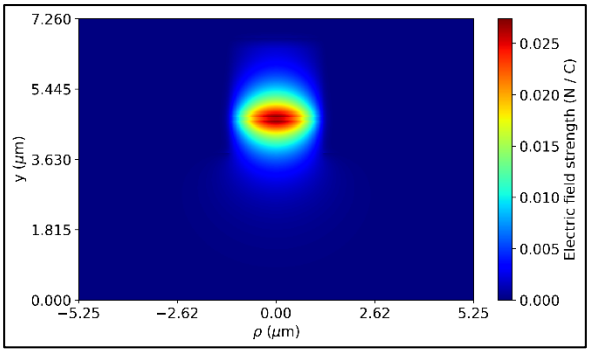

(a) Initial E_y in the straight waveguide.

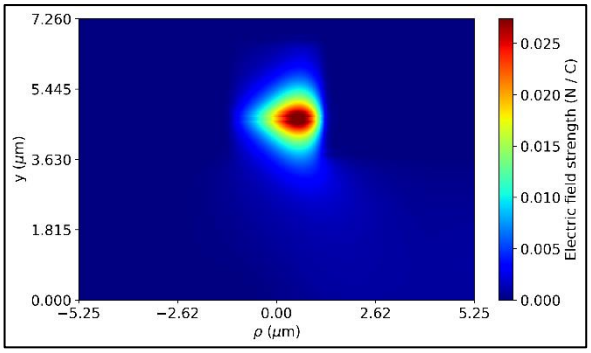

(b) E_y at 47.5° through the waveguide bend.

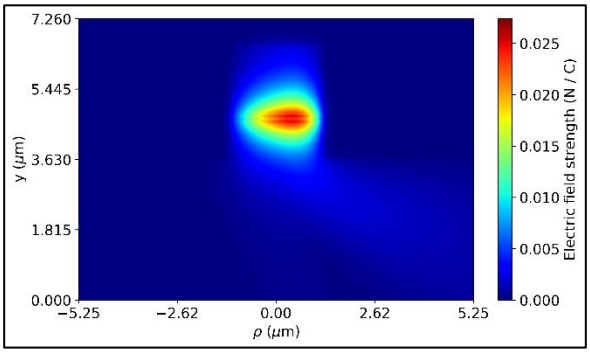

(c) E_y at 56.8° through the waveguide bend.

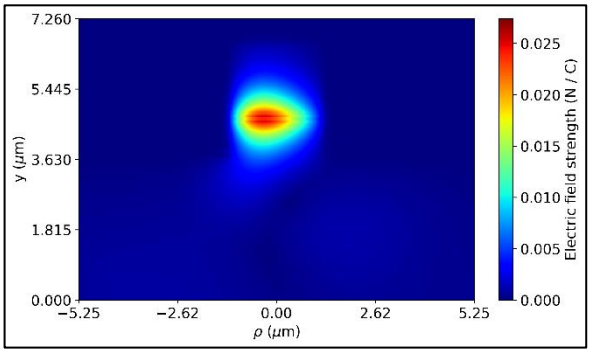

(c) E_y 59 μm after the bend.

Figure 5.4: The electric field in the quasi-TM mode before, during and after a 90° circular deep-etched ridge waveguide bend with a radius of curvature of 100 μm.

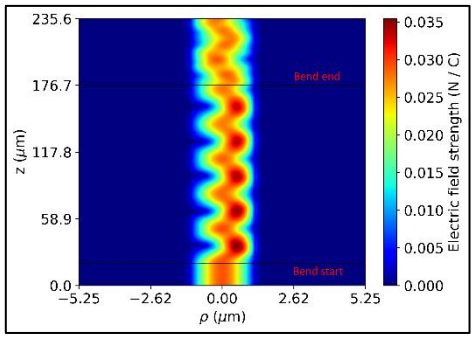

(a) E_x in the quasi-TE mode.

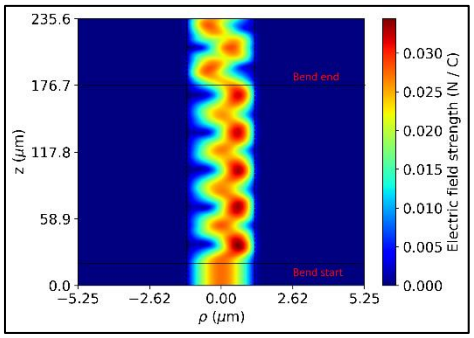

(b) E_y in the quasi-TM mode.

Figure 5.5: Cross section of the field, at y through the peak of the initial field, as it propagates through the 90° circular deep-etched waveguide bend with $R = 100\ \mu m$.

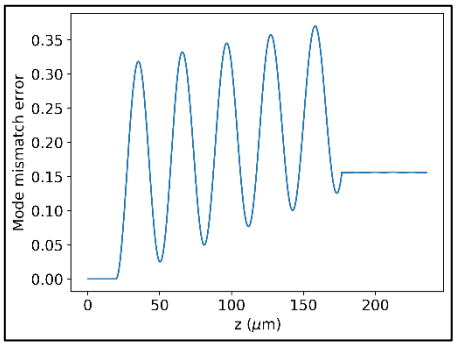

(a) E_x in the quasi-TE mode.

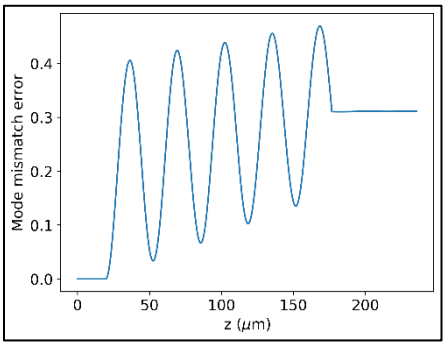

(b) E_y in the quasi-TM mode.

Figure 5.6: Mode mismatch error as each field propagates through the 90° circular deep-etched waveguide bend with $R = 100\ \mu m$.

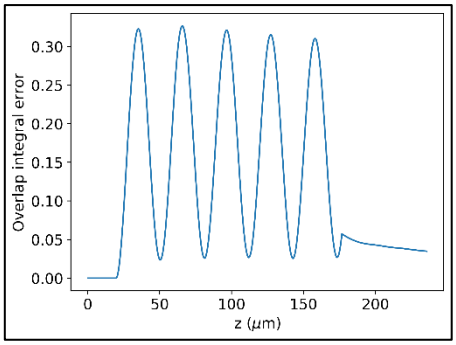

(a) E_x in the quasi-TE mode.

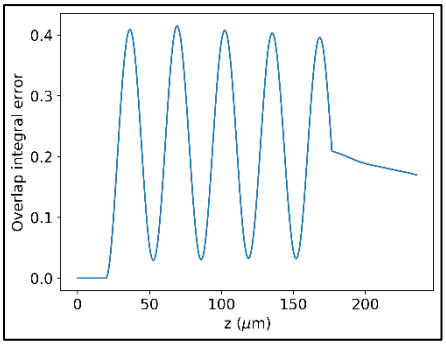

(b) E_y in the quasi-TM mode.

Figure 5.7: Overlap integral error as each field propagates through the $90°$ circular deep-etched waveguide bend with $R = 100\ \mu m$.

Meanwhile, Figure 5.7 shows the overlap integral error between the propagating field and the initially propagated field. In contrast to the MME graph, the OIE values at the peaks and troughs do not rise as the field propagates as the OIE does not take into account the loss of the field. The OIE however does slowly decrease after exiting the bend, as the excited straight waveguide radiation modes slowly lose their power.

To confirm these oscillations in the MME and OIE are due to the excitation of shifted slowly radiating higher order mode(s), Figure 5.8 shows the two quasi-TE radiation modes of the straight waveguide with the largest fraction of their field distribution confined in the waveguide above the deep etch, before and after they have propagated through a straight waveguide of length 400 μm. The first field is shown to be very slowly radiating, propagating for hundreds of microns while losing very little power. The second radiation mode field, while being far more radiative than the first field, would still be considered slowly radiating as it requires a couple of hundred microns to lose most of its power. This is shown numerically by Figure 5.9 where the MME is shown for both propagating fields.

Meanwhile, unlike the quasi-TE mode, the quasi-TM mode does not contain a radiation mode where the field distribution is primarily contained in the top of the waveguide, as was also observed in the case of the shallow-etched waveguide. It does however contain a radiation mode with 2 peaks in the $\hat{x}$ direction, very similar to the radiation mode found in the quasi-TE mode. The radiation mode field before and after propagating through a straight waveguide is given by Figure 5.10 and the MME is given by Figure 5.11. The MME is observed to progress very similarly to the MME for the corresponding radiation mode in the quasi-TE mode.

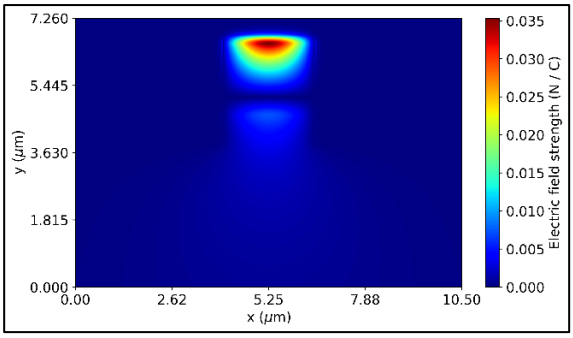

(a) Quasi-TE E_x radiation mode at $z = 0$.

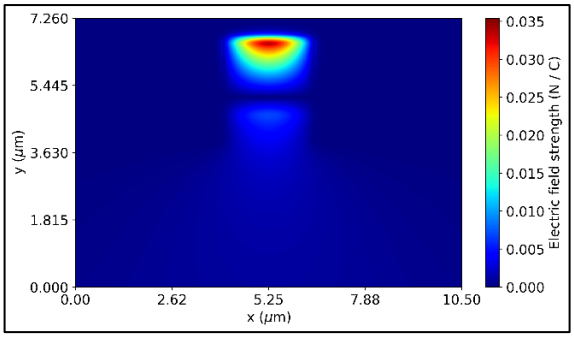

(b) Quasi-TE E_x radiation mode at $z = 400\ \mu m$.

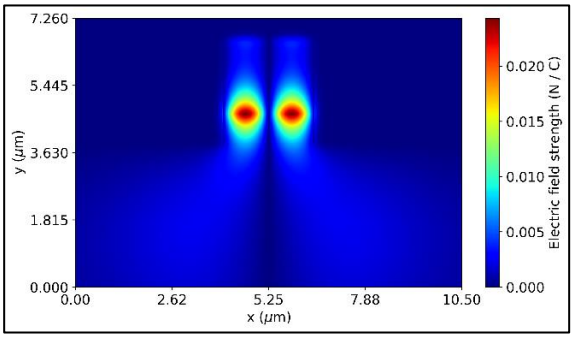

(c) Quasi-TE E_x radiation mode at $z = 0$.

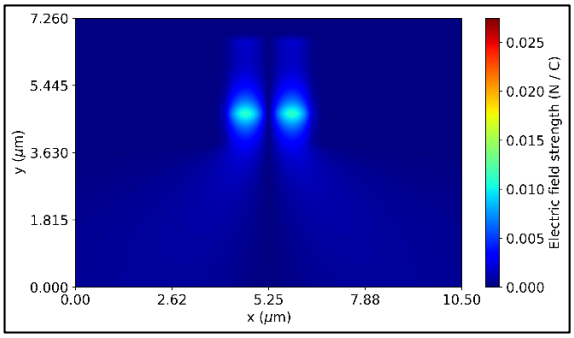

(d) Quasi-TE E_x radiation mode at $z = 400\ \mu m$.

Figure 5.8: Two propagating radiation modes through the straight deep-etched waveguide in the quasi-TE mode. The first has an effective index of 3.16404 and the second has an effective index of 3.13681.

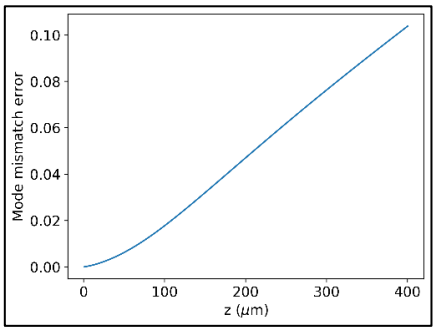

(a) Mode with $n_{eff} = 3.16404$.

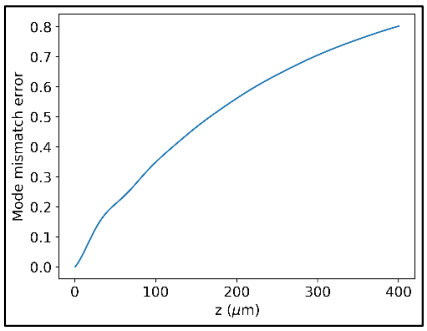

(b) Mode with $n_{eff} = 3.13681$.

Figure 5.9: Mode mismatch error as the radiation modes propagate through the straight deep-etched waveguide in the quasi-TE mode.

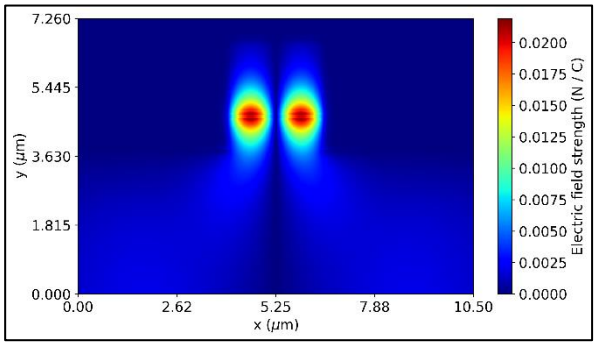

(a) Quasi-TM E_y radiation mode at $z = 0$.

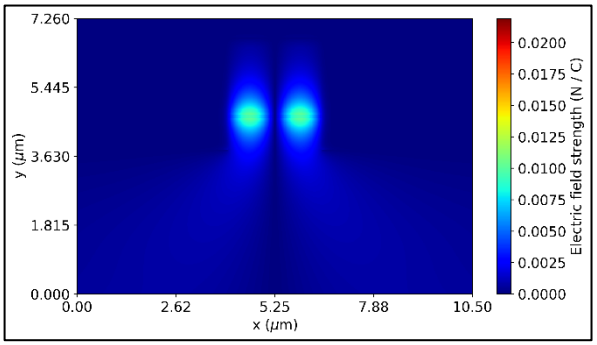

(b) Quasi-TM E_y radiation mode at $z = 400\ \mu m$.

Figure 5.10: Propagating radiation mode through the straight deep-etched waveguide in the quasi-TM mode with an effective index of 3.14001.

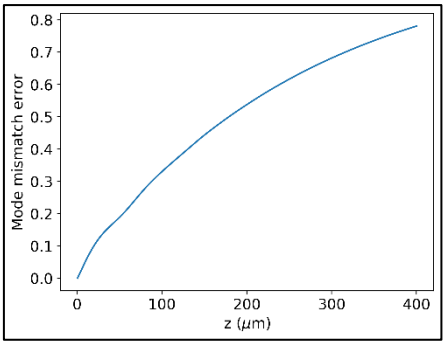

Figure 5.11: Mode mismatch error as the radiation mode propagates through the straight deep-etched waveguide in the quasi-TM mode with an effective index of 3.14001.

The radiation modes in the curved waveguide consist of shifted versions of these modes, meaning that although these modes would be excited in the curved waveguide structure, assuming the shifted radiation modes are still slowly radiating, much of the power is not lost during the bend, allowing the superposition of the curved waveguide fundamental mode and radiation modes to excite the fundamental mode of the straight waveguide at the end of the bend. As the mode beating manifests by the field moving towards and away from the outside of the bend, it likely occurs primarily due the excitation of the shifted fundamental mode and the shifted radiation mode which has 2 peaks in the $\hat{x}$ direction. Using the mode solver on the circular deep-etched waveguide with a radius of curvature of 100 μm, the shifted version of the modes can be found and are given by Figure 5.12. Although the field distribution inside the waveguide above the deep etch should be accurate, note that the tail regions of the fields are inaccurate due to the insufficiencies of the boundary conditions. Beating between these two modes is likely what is observed as the field propagates through the circular bend. To confirm this, the beat length of the modes can be approximately calculated according to equation (5.1) and compared to the propagating distance between successive peaks or troughs in Figure 5.6. The calculated effective refractive indices of the two modes in the quasi-TE mode were 3.18784 and 3.13808 respectively. This gives a beat length of approximately 31.15 μm. Meanwhile, from Figure 5.6, the average distance between two troughs is approximately 31.1 μm. The closeness of these results confirms the mode beating occurring in the propagating field is between the two modes. Also note that less of the field distribution appears to be confined to the region above the deep etch for the shifted fundamental mode in the quasi-TM mode than for the shifted fundamental mode in the quasi-TE mode. This would cause the propagation loss from the shifted fundamental mode to be higher for the quasi-TM mode which would explain the larger MME between the fields before and after the bend for the quasi-TM mode.

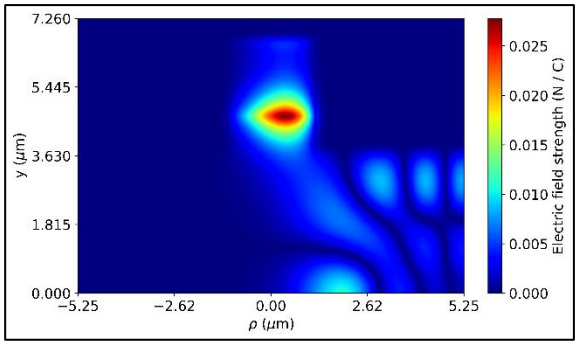

(a) Quasi-TE E_r shifted fundamental mode.

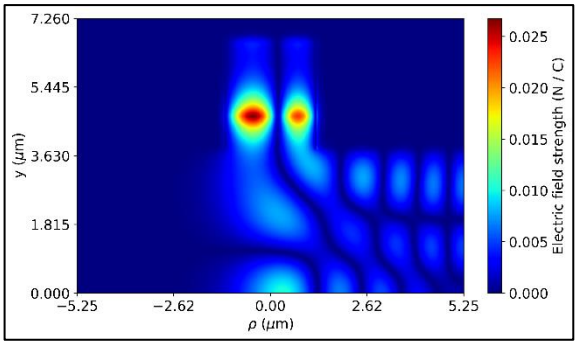

(b) Quasi-TE E_r shifted radiation mode.

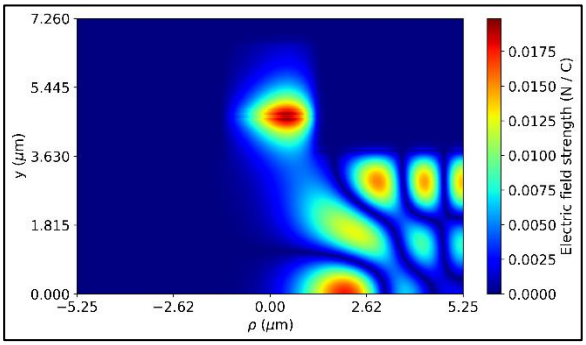

(c) Quasi-TM E_y shifted fundamental mode.

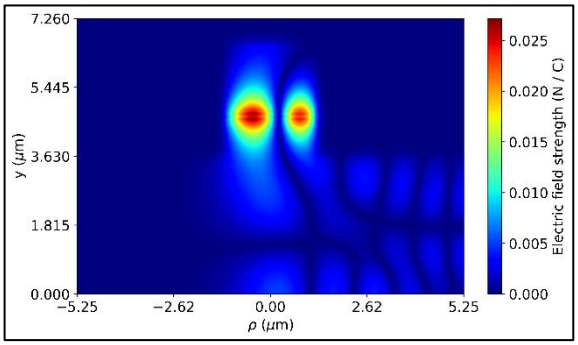

(d) Quasi-TM E_y shifted radiation mode.

Figure 5.12: Modes in a circular deep-etched waveguide with a radius of curvature of 100 μm.

5.2.1.2 Linearly Changing Curvature Bend

As the circular curvature results in the excitation of curved radiation modes, a linear change in curvature can be introduced to prevent these modes from being excited, as the shape of the field should be very similar to the shaped of the curved fundamental mode at each propagation step. The field should slowly move towards the outside of the bend as the curvature linearly increases and then move back towards the centre of the waveguide as the curvature linearly decreases. This should prevent the field exiting the bend as a superposition of the curved waveguide modes. This means the mode mismatch error between the field before and after the bend should be almost entirely dependent on the propagation loss of the shifted fundamental mode and not on the shape of the field exiting the bend.

Figure 5.13 and Figure 5.14 show the electric field in the quasi-TE mode and quasi-TM mode, respectively, before, during, and after the linearly changing curvature 90° bend with an effective radius of curvature of 100 μm. In both cases, the field is observed to have shifted towards the outside of the bend midway through the bend and then shifted back to the centre of the waveguide after the bend. Figure 5.15 shows the fields to have shifted slowly to the outside of the bend and then back again. Small horizontal oscillations in the field suggest that there were small excitations of shifted radiation modes but were far less significant than for the circular waveguide.

The MME and OIE between the initially propagated field and the propagating field are given by Figure 5.16 and Figure 5.17 respectively. The final MME of approximately 0.13 in the quasi-TE mode is slightly smaller than the MME for the corresponding circular waveguide which was approximately 0.16, while the final MME of approximately 0.175 in the quasi-TM

mode is much smaller than the MME for the corresponding circular waveguide which was approximately 0.31. The small oscillations in the MME and OIE again suggest slight excitations of the curved waveguide radiation modes.

The advantage of the linearly changing curvature is that the propagating field should always be close to the shape of the fundamental mode of the straight waveguide when leaving the curved waveguide, due to little excitation of shifted radiation modes. This means that most of the field leaving the bend will take the shape of the fundamental mode of the straight waveguide. On the other hand, for the circular waveguide, the amount of the field leaving the bend that will take the shape of the fundamental mode of the straight waveguide is entirely dependent on the superposition of the fundamental mode and the radiation modes when leaving the waveguide bend. This means a small change in radius of curvature could cause a large change in MME for the circular curvature but the MME should change little for the linearly changing curvature waveguide. This is shown in Figure 5.18 where the MME after the bend is compared for the circular and linearly changing curvature bends as effective radius increases. Above 50 μm, as the effective radius increases, the MME is observed to steadily decrease for the linearly changing curvature waveguide while the MME is observed to largely oscillate while decreasing for the circular curvature. The MME curve for the linearly changing curvature also approximately passes through the minima of the MME for the circular curvature, meaning it is always beneficial to use linear curvature at effective radii greater than 50 μm. It also means that the extra propagating loss from the longer path length and larger maximum curvature has negligible contribution to the MME in comparison to the circular curvature. Below an effective radius of 50 μm, the MME again appears to oscillate for the linearly changing curvature waveguide, suggesting excitations of higher order modes, which will be investigated later in the chapter.

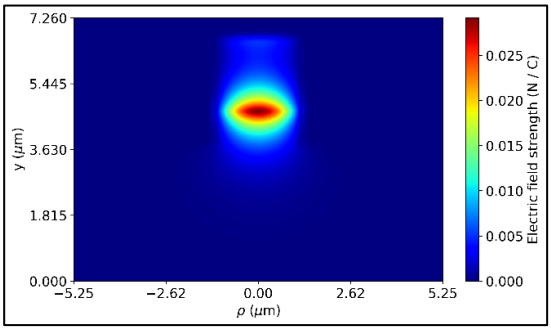

(a) Initial E_x in the straight waveguide.

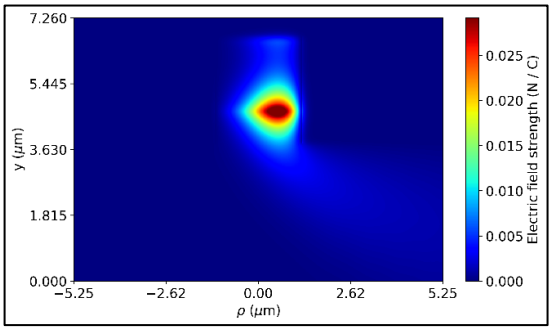

(b) E_r halfway through the waveguide bend.

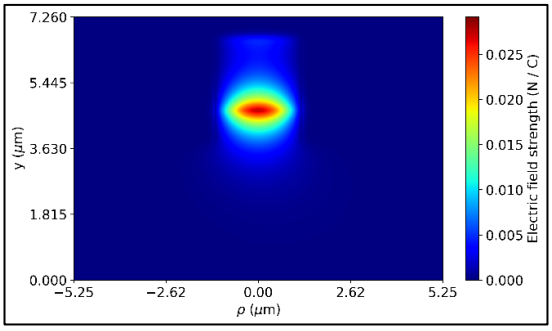

(c) E_x 62.5 μm after the waveguide bend.

Figure 5.13: The electric field in the quasi-TE mode before, during, and after a $90°$ linearly changing curvature deep-etched ridge waveguide bend with an effective radius of curvature of $100\ \mu m$.

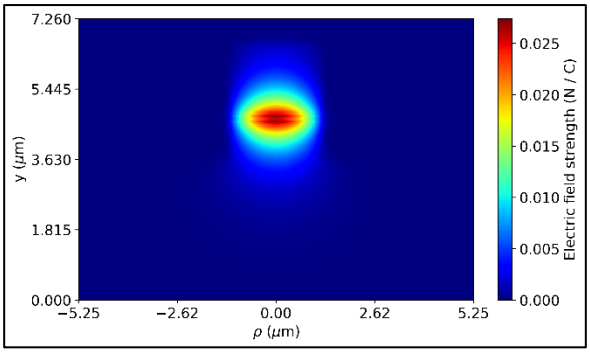

(a) Initial E_y in the straight waveguide.

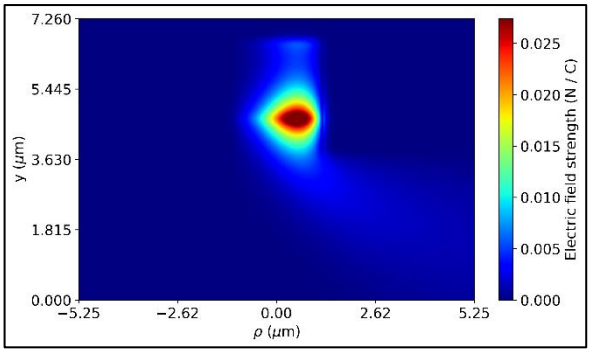

(b) E_y halfway through the waveguide bend.

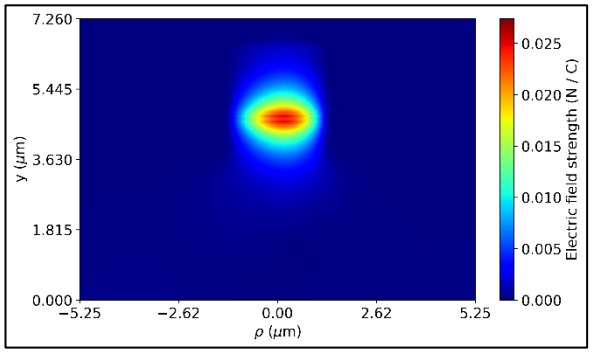

(c) E_y 62.5 μm after the waveguide bend.

Figure 5.14: The electric field in the quasi-TM mode before, during, and after a 90° linearly changing curvature deep-etched ridge waveguide bend with an effective radius of curvature of 100 μm.

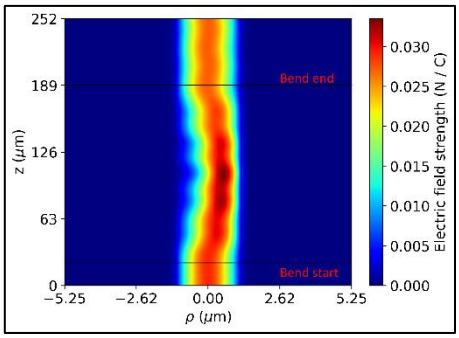

(a) E_x in the quasi-TE mode.

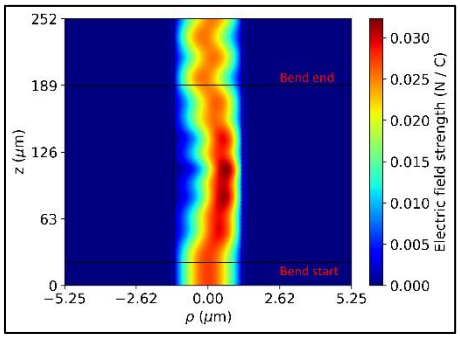

(b) E_y in the quasi-TM mode.

Figure 5.15: Cross section of the fields, at y through the peak of the initial field, as the fields propagate through the 90° linearly changing curvature deep-etched ridge waveguide bend with $R_{eff} = 100\ \mu m$.

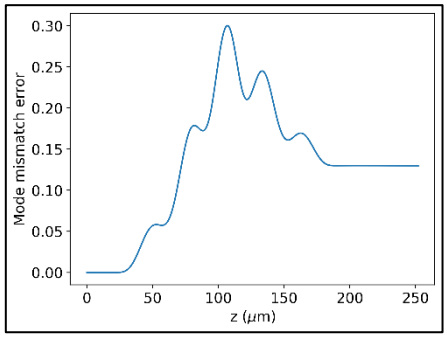

(a) E_x in the quasi-TE mode.

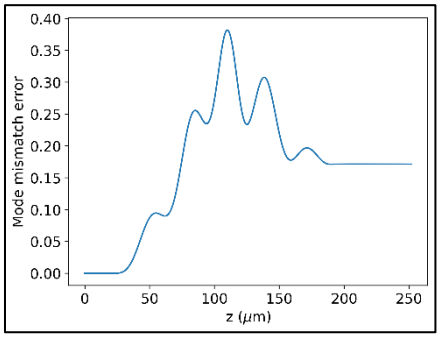

(b) E_y in the quasi-TM mode.

Figure 5.16: Mode mismatch error as each field propagates through the 90° linearly changing curvature deep-etched ridge waveguide bend with $R_{eff} = 100\ \mu m$.

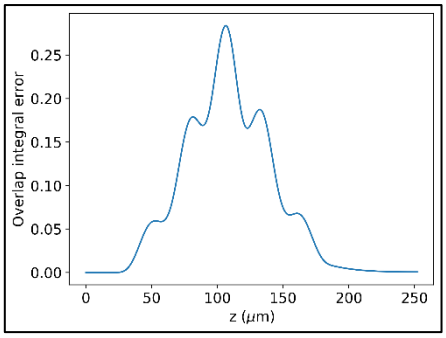

(a) E_x in the quasi-TE mode.

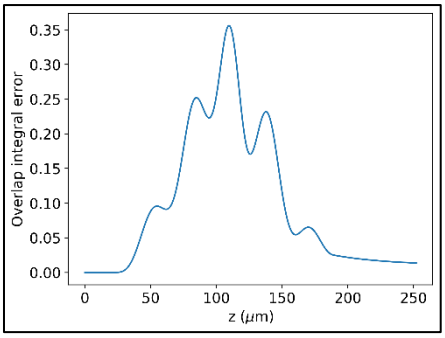

(b) E_y in the quasi-TM mode.

Figure 5.17: Overlap integral error as each field propagates through the 90° linearly changing curvature deep-etched ridge waveguide bend with $R_{eff} = 100\ \mu m$.

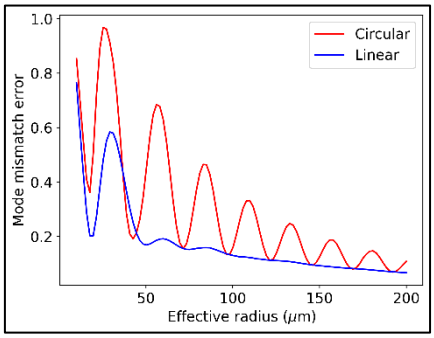

Figure 5.18: Mode mismatch error as radius increases for the 90° circular and linearly changing curvature deep-etched ridge waveguide bends for the electric field in the quasi-TE mode.

5.2.1.3 Trapezoidal Curvature Bend

The above results show that the linear change of curvature reduces the loss of the waveguide bend. It will now be investigated if the loss can be reduced further by mixing the circular curvature and linearly changing curvature for the trapezoidal curvature profile. If the linearly changing curvature portion of the bend sufficiently suppresses the excitations of the shifted radiation modes, lower propagating loss may be achieved due to the shorter path length of the bend and the smaller maximum curvature reached, relative to the linearly changing curvature bend.

Again using the example of the bend with an effective radius of curvature of 100 μm, Figure 5.19 gives the cross section of the electric fields, at y through the peak of the initial field, as they propagate through the trapezoidal waveguide bend for both the quasi-TE and quasi-TM modes. The bend was designed for half the path length to consist of linearly changing curvature and half the path length to consist of circular curvature. Although the first quarter of the bend path length consists of linearly increasing curvature, the field still appears to beat slightly between the shifted fundamental mode and shifted radiation modes in the circular section. This suggests the linearly changing curvature section did not completely supress the excitations of the shifted radiation modes, but still considerably reduced them in comparison to the circular waveguide. This is confirmed by Figure 5.20 and Figure 5.21, where the oscillations in the MME and OIE still show the excitation of higher order radiation modes. The linearly decreasing curvature part of the bend still causes primarily the fundamental mode of the straight waveguide to be excited at the end of the bend and the MME at the end of the bend is very similar to that of the linearly changing curvature waveguide at approximately 0.125 for the quasi-TE mode and 0.17 for the quasi-TM mode.

For effective radii below 50 μm, both the circular and linearly changing curvature bends caused oscillations in the MME due to excitations of higher order modes. However, for the linearly changing curvature bend, there appeared an effective radius of approximately 20 μm where the MME was minimised and gave a low value of approximately 0.2. To check if a trapezoidal curvature waveguide with a certain linear curvature fraction could reduce this MME further, Figure 5.22 gives a plot of the MME between the field before the bend and after the bend as the effective radius of curvature and linear curvature fraction increase. The plots show that this MME is minimum for the linearly changing curvature waveguide at an effective radius of 18.75 μm for the quasi-TE mode and an effective radius of 19.5 μm for the quasi-TM mode. If the waveguide is designed to have a different effective radius of curvature, the MME will be minimum for trapezoidal waveguides with different linear curvature fractions. For example, for the quasi-TE mode, if the effective radius of curvature is 30 μm, the MME is minimised at approximately $f = 0.75$, and if the effective radius of curvature is 60 μm, the MME is minimised at approximately $f = 0.5$.

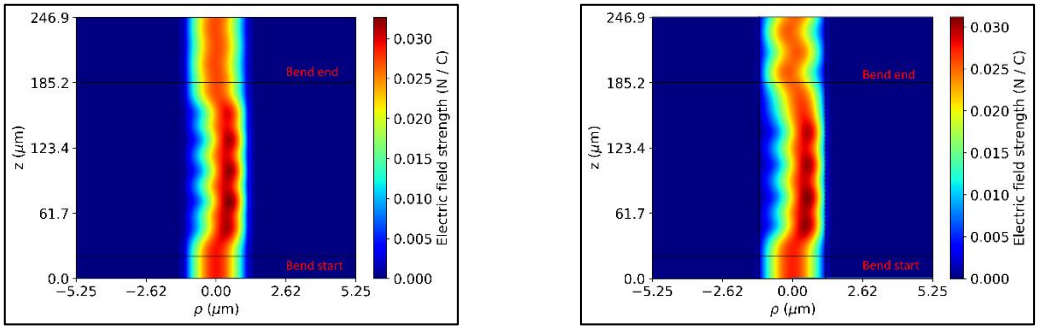

(a) E_x in the quasi-TE mode. (b) E_y in the quasi-TM mode.

Figure 5.19: Cross section of the fields, at y through the peak of the initial fields, as they propagate through the 90° trapezoidal curvature deep-etched ridge waveguide bend with $R_{eff} = 100\ \mu m$.

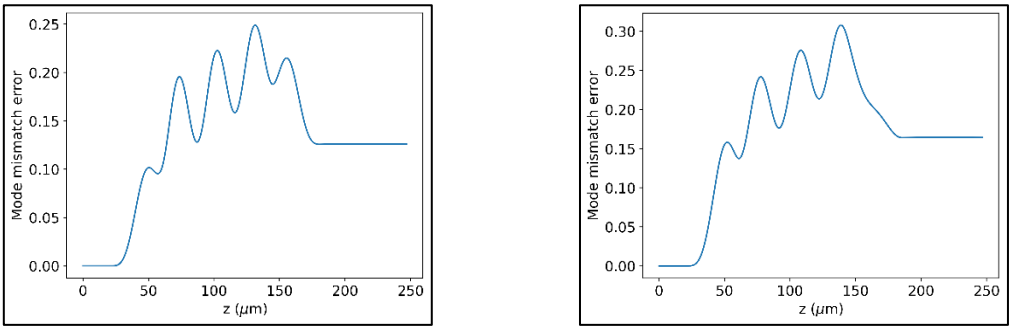

(a) E_x in the quasi-TE mode. (b) E_y in the quasi-TM mode.

Figure 5.20: Mode mismatch error as each field propagates through the 90° trapezoidal curvature deep-etched ridge waveguide bend with $R_{eff} = 100\ \mu m$.

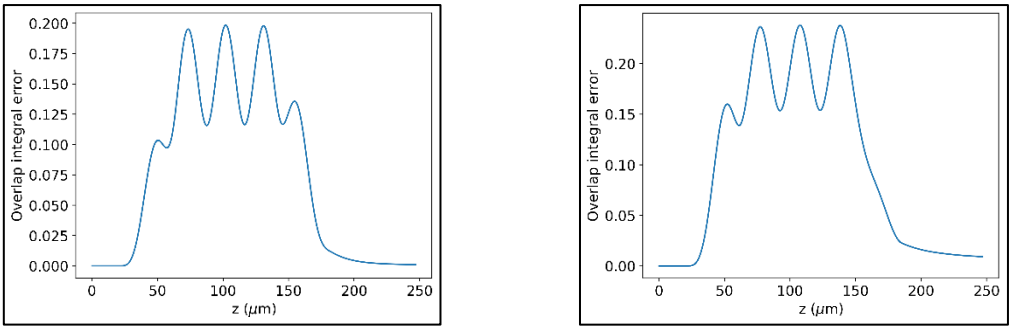

(a) E_x in the quasi-TE mode. (b) E_y in the quasi-TM mode.

Figure 5.21: Overlap integral error as each field propagates through the 90° trapezoidal curvature deep-etched ridge waveguide bend with $R_{eff} = 100\ \mu m$.

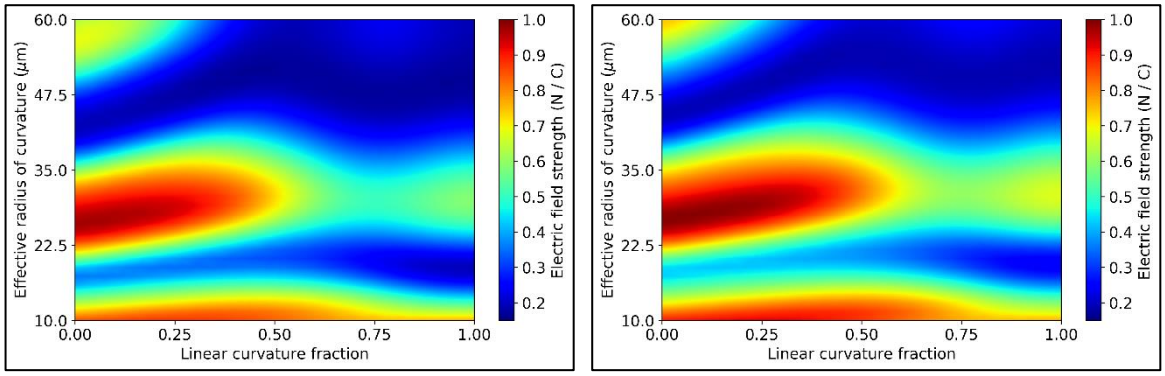

(a) E_x in the quasi-TE mode. (b) E_y in the quasi-TM mode.

Figure 5.22: Mode mismatch error vs. effective radius of curvature and the fraction of the path length consisting of linearly changing curvature for the 90° deep-etched bend.

5.2.2 Deep-Etched Ridge Waveguide with a 180° Bend

The previous analysis was repeated for the 180° bend. Due to the larger maximum curvature reached, smaller curvature slope, and larger fractional path length change for the linearly changing curvature and trapezoidal curvature 180° bends in comparison to the 90° bends, different results for the best curvature profile for each effective radius of curvature would be expected.

5.2.2.1 Circular Bend

Figure 5.23 shows the cross section of the electric fields, at y through the peak of the initial field, as they propagate through the circular 180° waveguide with a radius of curvature of 100 μm. The fields of course behave in the same way as for the 90° circular waveguide except that the bend now has double the path length. The input field is observed to excite the shifted fundamental mode and the shifted radiation modes which then beat as the light propagates through the circular region. This is confirmed by the presence of the oscillations in the MME and OIE plots given by Figure 5.24 and Figure 5.25 respectively. At this particular radius of curvature, the loss is much higher for the quasi-TM mode in comparison to the quasi-TE mode, both due to the higher propagation loss for the quasi-TM mode in general and the field exiting the bend when the MME was at a peak in its oscillation.

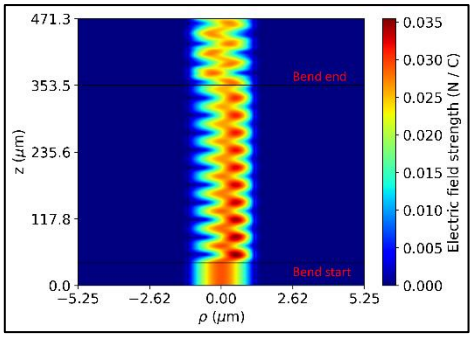

(a) E_x in the quasi-TE mode.

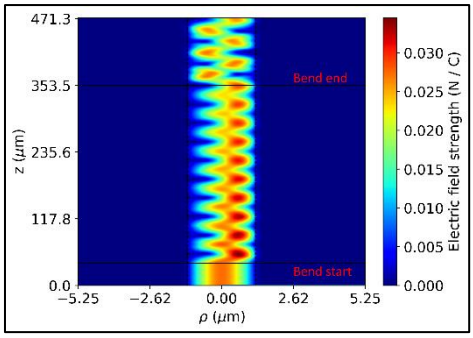

(b) E_y in the quasi-TM mode.

Figure 5.23: Cross section of the fields, at y through the peak of the initial field, as they propagate through the $180°$ circular deep-etched waveguide bend with $R = 100\ \mu m$.

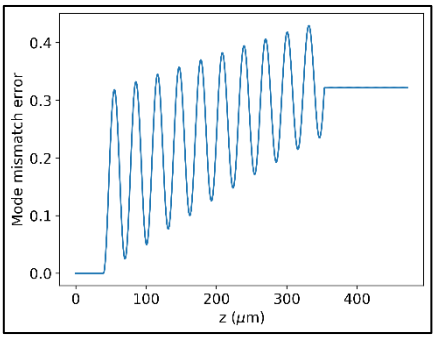

(a) E_x in the quasi-TE mode.

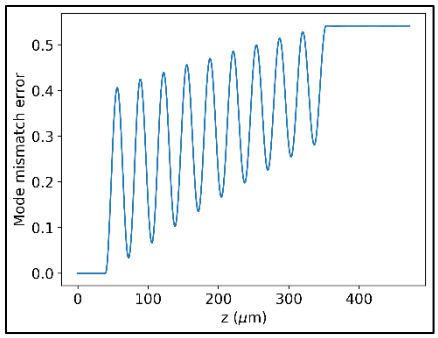

(b) E_y in the quasi-TM mode.

Figure 5.24: Mode mismatch error as each field propagates through the $180°$ circular deep-etched waveguide bend with $R = 100\ \mu m$.

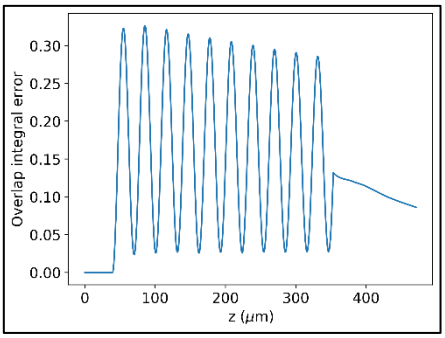

(a) E_x in the quasi-TE mode.

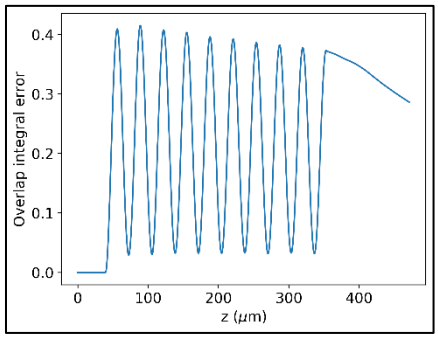

(b) E_y in the quasi-TM mode.

Figure 5.25: Overlap integral error as each field propagates through the $180°$ circular deep-etched waveguide bend with $R = 100\ \mu m$.

5.2.2.2 Linearly Changing Curvature Bend

Figure 5.26 shows the cross section of the fields, at y through the peak of the initial fields, as they propagate through the linearly changing curvature waveguide. The fields appear to shift towards the outside of the bend much more smoothly than what was observed for the 90° linearly changing curvature bend, with just slight transverse oscillations in the field suggesting very little higher order mode excitations. This is confirmed by Figure 5.27 and Figure 5.28 which show very slight oscillations in the MME and OIE. The oscillations are noticeably larger for the quasi-TM mode, again suggesting larger excitations of the shifted radiation modes due to a larger mismatch error between the input field and the curved fundamental mode.

For both the quasi-TE and quasi-TM modes, the final MME is considerably lower for the linearly changing curvature bend than for the circular bend. Although the path length of the linearly changing curvature bend is approximately 45% longer than that of the circular bend, the ability of the curvature profile to suppress higher order mode excitations makes it far more effective at reducing loss. To investigate if this result holds for all effective radii, Figure 5.29 shows a graph of the MME between the propagating electric field in the quasi-TE mode before and after both the circular and linearly changing curvature bends, as the effective radius increases. The graph shows the linearly changing curvature to be far superior to the circular curvature for effective radii greater than approximately 40 μm. The improvement made by the linear curvature is shown to be even greater than that made for the 90° bend, as the MME curve for the linearly changing curvature is below that made by the oscillation minima of the circular MME plot. This is despite the fact that the path length for the linearly changing curvature is approximately 45% longer than that of the circular curvature for the 180° bend, in comparison to just 7% longer for the 90° bend. However, the maximum curvature reached by the linearly changing curvature is approximately 38% larger than the circular curvature for the 180° bend, in comparison to 87% larger for the 90° bend. Due to the longer path length and smaller maximum curvature, the slope of the change in curvature with path length is also much smaller for the linearly changing curvature 180° bend, with it being approximate 0.27 times the value of the slope for the 90° bend. This suggests the loss caused by the higher order mode excitations is much more significant than the propagating loss from the shifted fundamental mode.

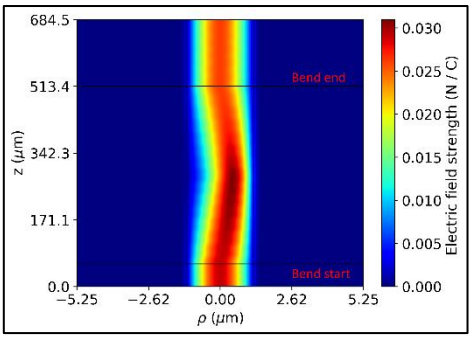

(a) E_x in the quasi-TE mode.

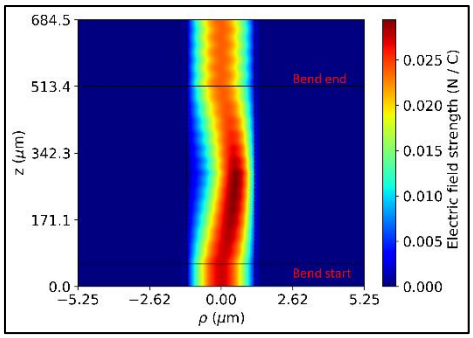

(b) E_y in the quasi-TM mode.

Figure 5.26: Cross section of the fields, at y through the peak of the initial field, as they propagate through the 180° linearly changing curvature deep-etched waveguide bend with $R_{eff} = 100\ \mu m$.

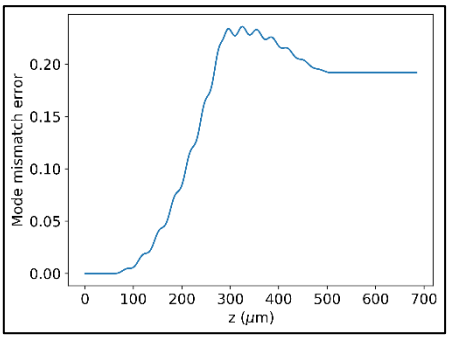

(a) E_x in the quasi-TE mode.

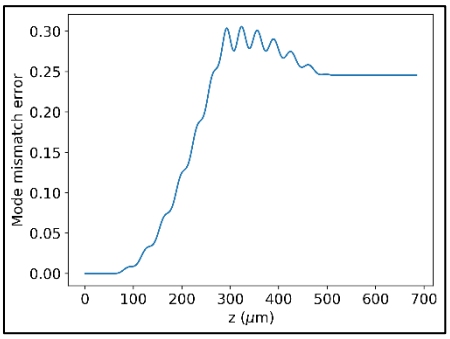

(b) E_y in the quasi-TM mode.

Figure 5.27: Mode mismatch error as each field propagates through the 180° linearly changing curvature deep-etched waveguide bend with $R_{eff} = 100\ \mu m$.

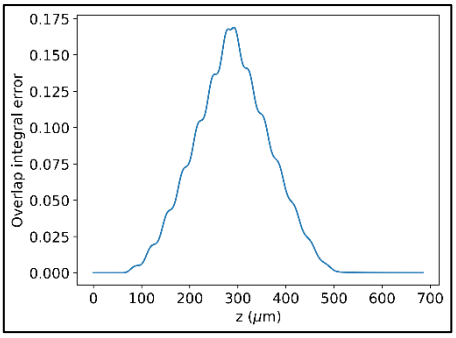

(a) E_x in the quasi-TE mode.

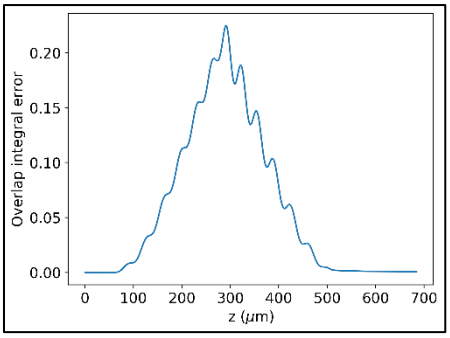

(b) E_y in the quasi-TM mode.

Figure 5.28: Overlap integral error as each field propagates through the 180° linearly changing curvature deep-etched waveguide bend with $R_{eff} = 100\ \mu m$.

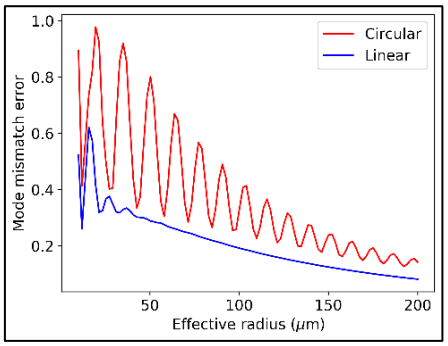

Figure 5.29: Mode mismatch error as radius increases for the circular and linearly changing curvature 180° deep-etched waveguide bend for propagation in the quasi-TE mode.

5.2.2.3 Trapezoidal Curvature Bend

Figure 5.30 shows the cross section of the electric fields, at y through the peak of the initial field, as they propagate through the trapezoidal curvature waveguide where half the path length consists of linearly changing curvature and the effective radius of curvature is 100 μm. Figure 5.31 and Figure 5.32 shows the MME and OIE between the originally propagated fields and the propagating fields, respectively. The three figures show little higher order mode excitations for the quasi-TE mode with the field propagating through the circular region with very little mode beating, which is supported by the presence of only small oscillations in the MME and OIE graphs. The curvature profile for the quasi-TM mode is less successful at suppressing the excitation of radiation modes, with visible mode beating occurring as the field propagates through the circular region. The MME after the bend is slightly larger than what was observed for the linearly changing curvature bend with the same effective radius of curvature, suggesting the linearly changing curvature bend to be superior at this effective radius of curvature.

Below an effective radius of approximately 50 μm, Figure 5.29 showed the linearly changing curvature MME to oscillate as the curve failed to prevent the excitation of higher order modes. To investigate if a trapezoidal curvature waveguide could be used to reduce the loss, Figure 5.33 shows a colour plot of the MME for different linear curvature fractions and effective radii of curvature between 10 and 60 μm for the electric fields in the quasi-TE and quasi-TM modes. The results appear to be very similar for the different modes, with the differing locations of the maxima and minima only becoming noticeable as the effective

radius increases. As these maxima and minima appear primarily due to beating between the excited shifted fundamental mode and the higher order mode in the bend, equation (5.1) suggests that the effective refractive index difference between the shifted fundamental mode and the higher order mode must be very similar for both the quasi-TE and quasi-TM modes. The shift becoming more evident as the radius increases is likely due to the longer path length of the larger radii bends causing more power transitions between the shifted fundamental mode and the higher order mode to occur and therefore a larger difference in the mode loss at the end of the bend will accumulate between the quasi-TE and quasi-TM modes. Both the graphs show the MME to be greatly reduced as long as the linear curvature fraction is greater than approximately 0.5. The MME can be slightly reduced further by using a linear curvature fraction between 0.5 and 1 where the minimum depends on the effective radius of curvature. The graphs also show a minimum to exist at an effective radius of curvature of approximately 12 μm which slightly decreases as the linear curvature fraction increases. Although the linear curvature fails to prevent excitations of radiative modes at this effective radius, the superposition of modes exiting the bend ends up closely resembling the shape of the fundamental mode of the straight waveguide, resulting in the low MME.

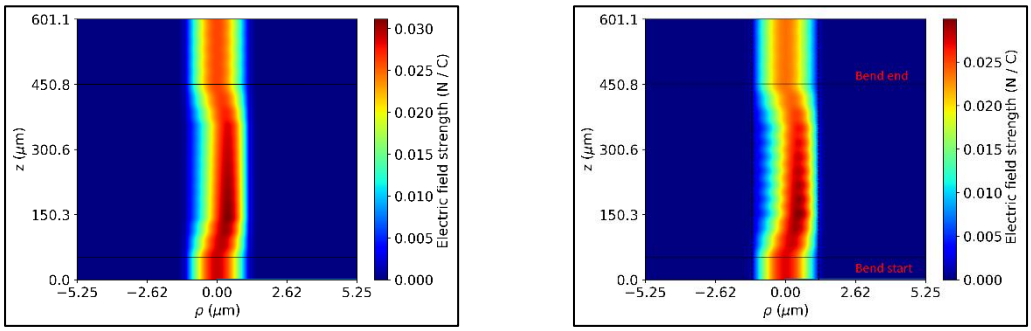

(a) E_x in the quasi-TE mode. (b) E_y in the quasi-TM mode.

Figure 5.30: Cross section of the fields, at y through the peak of the initial field, as they propagate through the $180°$ trapezoidal curvature deep-etched waveguide bend with $R_{eff} = 100\ \mu m$.

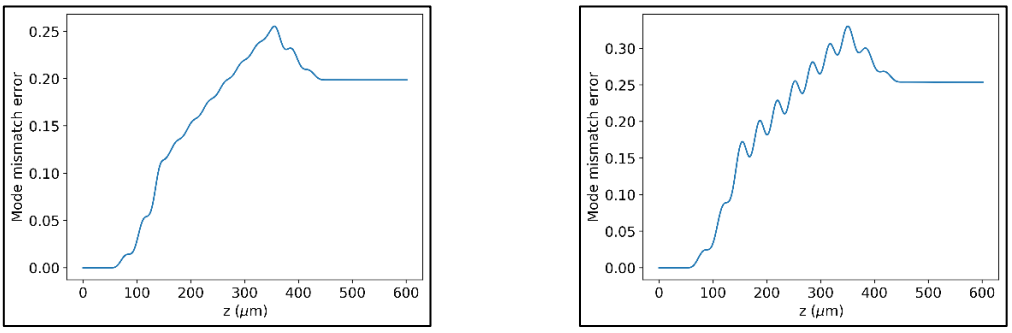

(a) E_x in the quasi-TE mode. (b) E_y in the quasi-TM mode.

Figure 5.31: Mode mismatch error as each field propagates through the $180°$ trapezoidal curvature deep-etched waveguide bend with $R_{eff} = 100\ \mu m$.

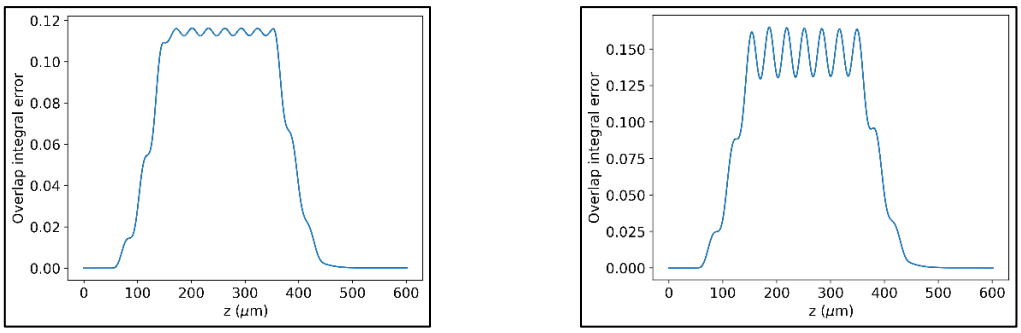

(a) E_x in the quasi-TE mode. (b) E_y in the quasi-TM mode.

Figure 5.32: Overlap integral error as each field propagates through the 180° trapezoidal curvature deep-etched waveguide bend with $R_{eff} = 100\ \mu m$.

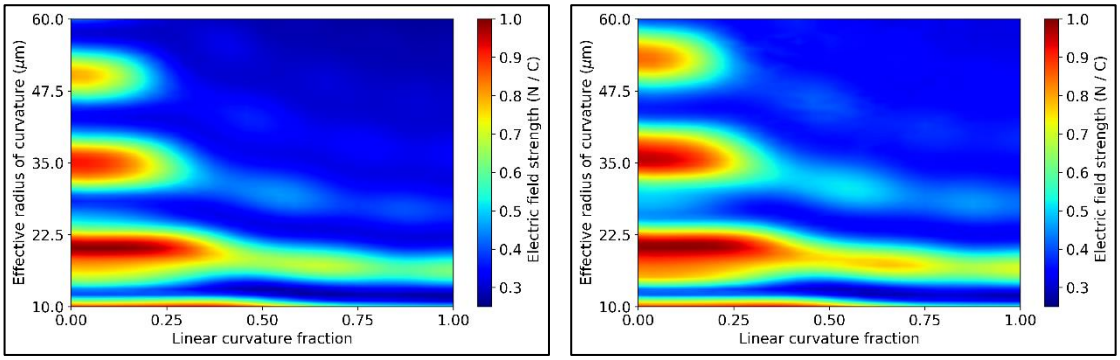

(a) E_x in the quasi-TE mode. (b) E_y in the quasi-TM mode.

Figure 5.33: Mode mismatch error vs. effective radius of curvature and the fraction of the path length consisting of linearly changing curvature for the 180° deep-etched bend.

5.3 The Effect of Waveguide Width and Etch Depth on Curved Deep-Etched Waveguide Loss

This section will investigate the effect of the deep etch depth and waveguide width on the loss of the curved waveguide.

5.3.1 The Effect of the Waveguide Width on Curved Deep-Etched Waveguide Loss

The width of the deep-etched waveguide was varied to observe the effect it would have on the loss from the curved waveguide. Changing the width of the waveguide could cause better suppression of higher order modes for certain trapezoidal curvature profiles. It could also change the beat length of the shifted fundamental mode and excited radiation mode(s) causing different effective radii of curvature where the mode mismatch error would be at a minimum.

Figure 5.34 gives the MME between the initially propagated electric field in the quasi-TE mode and the field after a 180° bend for both the circular and linearly changing curvature waveguides with an effective radius of curvature of 100 μm, where the waveguide width was increased from 2 μm to 3 μm. Oscillations in the MME are observed for the circular bend, suggesting the changing width alters the beat length between the shifted fundamental mode and the excited radiation mode(s). The oscillations grow in amplitude as the width is increased further. Meanwhile, the MME appears to decrease as the waveguide

width increases for the linearly changing curvature. As the linear change in curvature successfully suppresses the excitations of higher order modes at this effective radius of curvature, the MME decreasing as the waveguide width increases is indicative of the widening waveguide allowing more of the fields distribution to be confined in the waveguide above the deep etch. This causes less power to leak under the etch during the waveguide bend. This is supported by Figure 5.35 which shows the field distributions for waveguide widths 2, 2.5, and 3 microns.

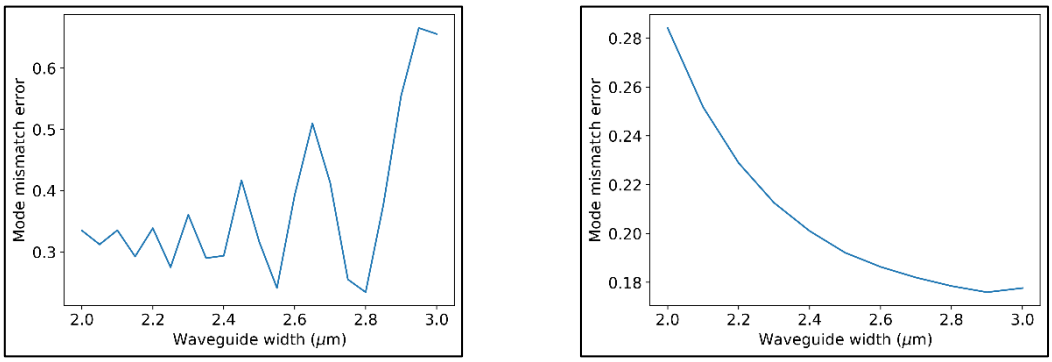

(a) Circular Waveguide. (b) Linearly changing curvature waveguide.

Figure 5.34: Effect of waveguide width on mode mismatch error after a 180° deep-etched bend with $R_{eff} = 100\ \mu m$ for E_x in the quasi-TE mode.

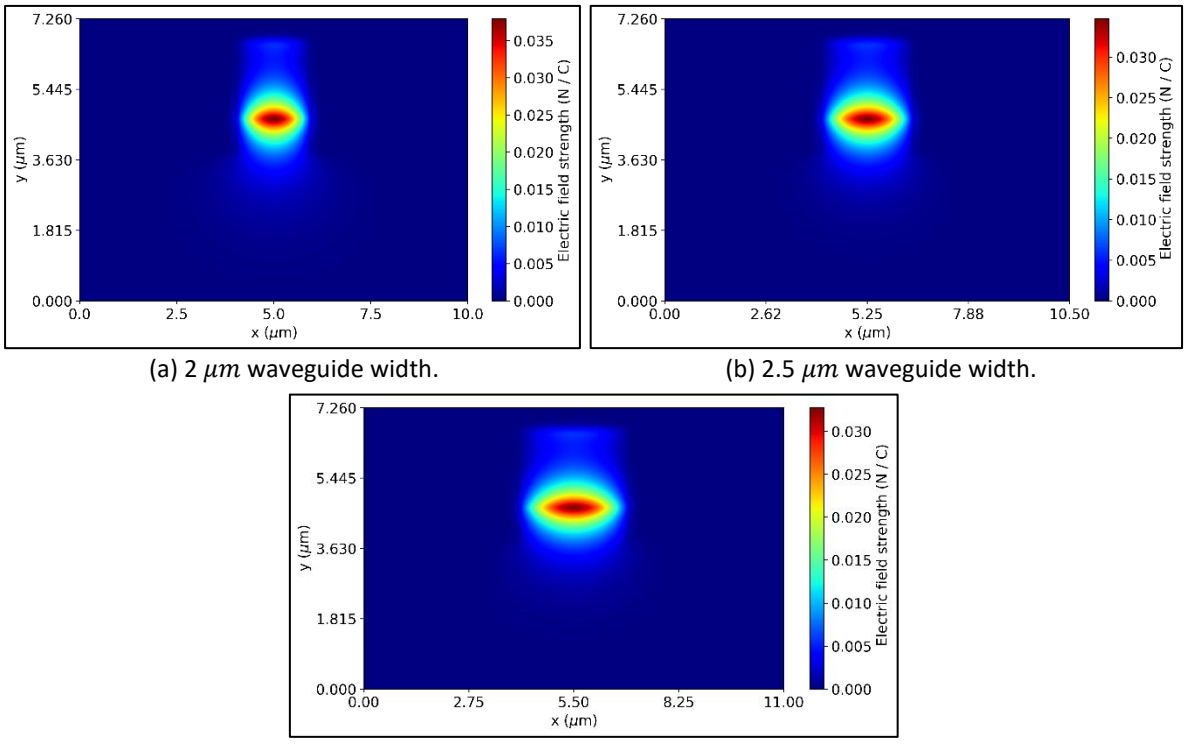

(a) 2 μm waveguide width. (b) 2.5 μm waveguide width.

(c) 3 μm waveguide width.

Figure 5.35: E_x field profiles in the quasi-TE mode for the deep-etched waveguide of various waveguide widths.

As the varying width causes the MME to oscillate for the circular deep-etched waveguide at an effective radius of 100 μm, the varying width should also cause the MME to oscillate for the linearly changing curvature deep-etched bend when the effective radius is small and radiation modes are significantly excited. To show this, Figure 5.36 gives the MME as width

increases for linearly changing curvature 180° waveguide bends with effective radii of curvature of 12 μm and 17 μm. These effective radii of curvature were selected as they were where the MME was at a minimum and maximum, respectively, in Figure 5.33. The results are interesting with the MME curve for the 12 μm taking a parabolic shape with the minimum close to the original 2.5 μm width. There is also only a small change in the maximum MME of 0.31 and the minimum MME of 0.263. This makes sense as the MME for this effective radius of curvature was at a minimum for the original 2.5 μm and changing the width of the waveguide should cause the beat length to change, causing the MME minimum to change. However, for the 17 μm bend, the MME increases greatly as the width increases, from 0.31 at a width of 2 μm to 0.88 at a width of 3 μm. This suggests the effective radius where the MME is minimum may only change slightly with waveguide width, but the amplitude of the MME oscillations increases greatly as the width increases. This suggests the linear change in curvature is better able to suppress the higher order mode oscillations at smaller waveguide widths. To prove this, Figure 5.37 shows how the MME changes with the effective radius for the 180° linearly changing curvature deep-etched waveguide bend for waveguide widths 2 and 3 microns. The excitations are significantly suppressed for the 2 μm waveguide widths as the MME oscillations are far smaller than what was observed for the 2.5 μm waveguide width. The MME also still remains relatively low even at a maximum in the MME oscillation with a value of 0.39 at an effective radius of curvature of approximately 15 μm. Meanwhile, the MME oscillations for the 3 μm are far larger, showing significant excitations of higher order modes. Although the narrower waveguide better prevents the excitations of higher order modes, it also must be noted that it has larger propagation loss due to the narrower width confining less of the field distribution above the deep etch. This leads to certain effective radii of curvature where a wider waveguide performs better. An effective radius of 60 μm is example of this from Figure 5.37.

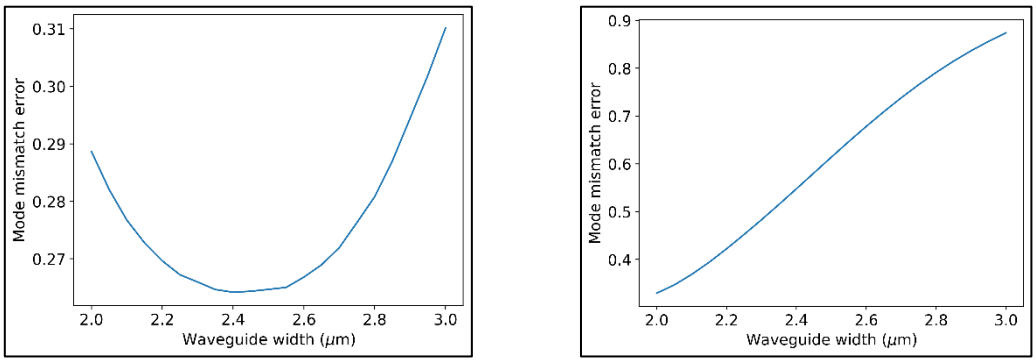

(a) Effective radius of 12 μm.

(b) Effective radius of 17 μm.

Figure 5.36: Effect of waveguide width on mode mismatch error after a 180° deep-etched linearly changing curvature bend for E_x in the quasi-TE mode.

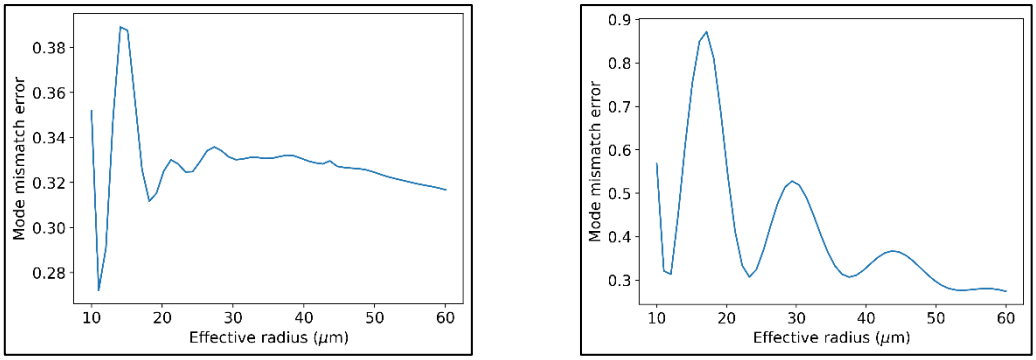

(a) Waveguide width of 2 μm. (b) Waveguide width of 3 μm.

Figure 5.37: Mode mismatch error after a 180° deep-etched linearly changing curvature bend of different effective radii and waveguide widths for E_x in the quasi-TE mode.

5.3.2 The Effect of the Etch Depth on Curved Deep-Etched Waveguide Loss

The depth of the deep etch was varied to investigate the effect it would have on the curved deep-etched waveguide loss. The etch depth used previously in the chapter was 2.96 μm. The etch depth was therefore varied between 2.46 μm and 4.46 μm to observe if the loss could be improved.

Figure 5.38 gives the MME between the initially propagated electric field in the quasi-TE mode and the field after a 180° bend for both the circular and linearly changing curvature waveguides with an effective radius of curvature of 100 μm, where the etch depth was increased from 2.46 μm to 4.46 μm. The waveguide width was set to 2.5 μm. As the etch depth is increased, the MME falls sharply until the etch depth reaches approximately 3 μm. Beyond this depth, the MME appears to flatten. The MME falls sharply initially simply due to the field distribution, which is primarily contained in the region containing the bulk material representation of the quantum wells, becoming more strongly confined by the sharp refractive index contrast between the waveguide material and air. This is shown in Figure 5.39 which gives the field distributions for etch depths of 2.5, 3, and 4 microns.

When the field propagates through the bend, lower loss is therefore observed as etch depth increases, as less power can leak from under the deep etch. As the etch depth is increased further, it has less effect on the loss as very little power escapes in this manner once a certain etch depth is reached, which in this case is approximately 4 μm. Beyond this etch depth, the MME flattens to approximately 0.175 for this particular circular waveguide and practically 0 for the linearly changing curvature waveguide. The zero MME for the linearly changing curvature waveguide and the non-zero MME for the circular waveguide suggest very little loss occurs due to power leakage beyond this etch depth, and the MME is primarily impacted by the superposition of modes entering the exit straight waveguide from the curved waveguide.

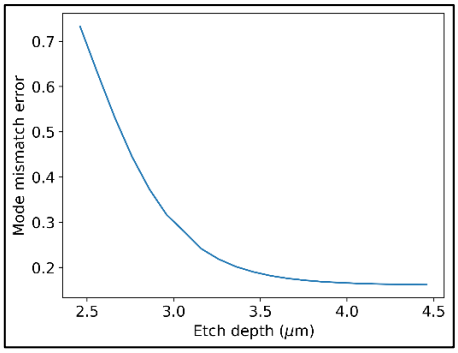

(a) Circular Waveguide.

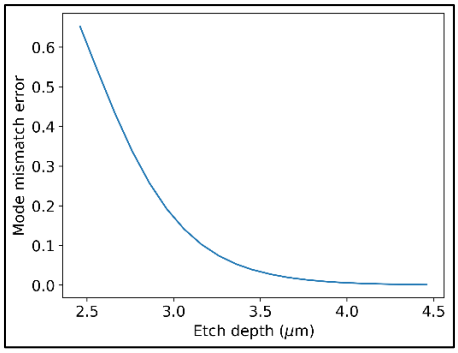

(b) Linearly changing curvature waveguide.

Figure 5.38: Effect of etch depth on mode mismatch error for E_x in the quasi-TE mode after a 180° deep-etched bend with an effective radius of curvature of 100 μm.

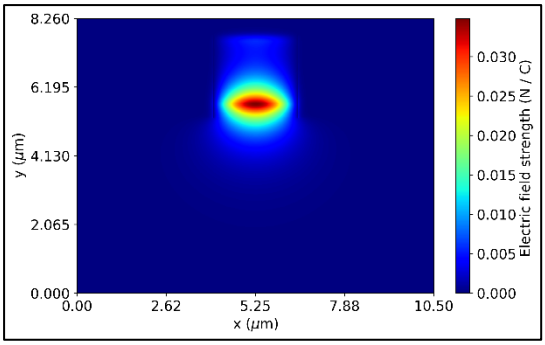

(a) 2.5 μm etch depth.

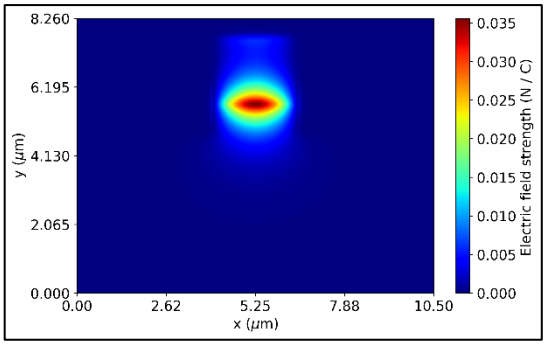

(b) 3 μm etch depth.

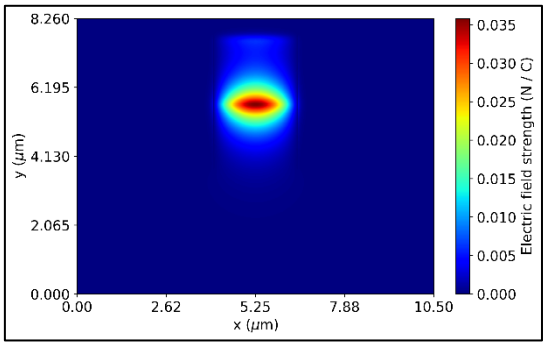

(c) 4 μm etch depth.

Figure 5.39: E_x field profiles in the quasi-TE mode for the deep-etched waveguide of various etch depths.

The lack of noticeable oscillations in the MME for the circular waveguide means varying the deep etch depth likely has very little impact on the effective radii where the MME peaks and troughs occur. This is because the shapes of the fundamental mode and the radiation modes where much of the field distribution is above the etch change very little as the deep etch depth is increased beyond 3 μm. This is confirmed by Figure 5.40 which shows the OIE between the initially propagated field and the field after the bend as the etch depth increases, for both the circular and linearly changing curvature waveguides. The OIE oscillates only slightly between a depth of 2.5 and 3 microns and then approaches a constant value as the etch depth is increased further. Meanwhile, the OIE always remains low for the linearly changing curvature waveguide as the higher order mode excitations are always sufficiently suppressed at this effective radius of curvature.

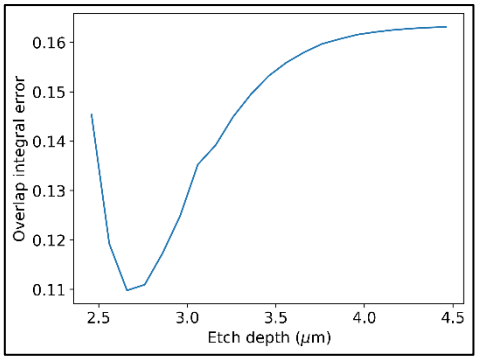

(a) Circular Waveguide.

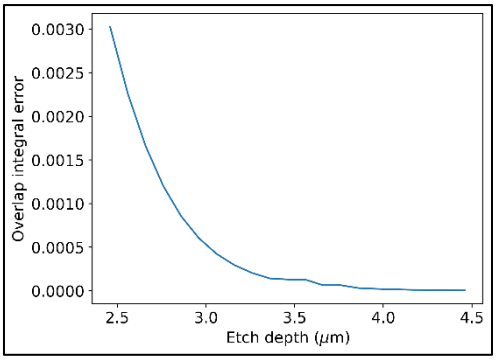

(b) Linearly changing curvature waveguide.

Figure 5.40: Effect of etch depth on overlap integral error for E_x in the quasi-TE mode after a 180° deep-etched bend with an effective radius of curvature of 100 μm.

5.4 Investigating the Cause of Higher Order Mode Excitations in Linearly Changing Curvature Waveguides

The previous section shows the linear changing curvature and trapezoidal curvature to reduce the deep-etched bend loss by preventing significant excitations of shifted higher order modes. This is effective down to a certain radius of curvature, under which the higher order modes are significantly excited. This section aims to better understand what causes these higher order mode excitations at lower radii of curvature.

The curvature profile of the linearly changing curvature and trapezoidal curvature is characterised based on the path length, the maximum curvature reached, and the slope of the change in curvature of the linear section with path length. As the effective radius of curvature decreases, the path length decreases and the maximum curvature increases, causing the slope of the change in curvature with path length to increase. This section will investigate the impact of the maximum curvature reached and the slope of the curvature change with path length on the higher order mode excitations.

To show the excitation of higher order modes, the amount of excitation of the shifted fundamental mode can be analysed. This is done by calculating the shifted fundamental mode using the mode solver at the maximum curvature that is reached at the end of the linearly increasing curvature section. The fundamental mode of the straight waveguide is then propagated through the curved waveguide and, when the maximum curvature is reached, the overlap integral error is calculated between the propagating field at that point and the calculated fundamental mode at the maximum curvature. If the overlap integral error is low, the fundamental mode has been significantly excited and thus excitations of curved radiation modes are low. If the overlap integral error is high, significant excitations of shifted radiation modes have taken place. Unfortunately, due to the inability of the mode solver to accurately calculate the fundamental mode of the shifted waveguide due it being a leaky mode, the deep etch is assumed to be infinite to prevent the fundamental mode from becoming leaky. From the previous section, this should still be accurate as the deep etch depth should not noticeably affect the beat length and therefore the excitations of the shifted fundamental modes from the original deep etch depth of approximately 3 μm. Figure 5.41 shows the refractive index profile of the infinite deep-etched waveguide as well

as the calculated curved fundamental mode electric field profile for a linearly changing curvature 90° waveguide bend with an effective radius of curvature of 100 μm when the curvature has reached its maximum.

To prove that multiple modes are excited in the linearly changing curvature region at small effective radii, Figure 5.42 shows the OIE between the propagating field when the waveguide has reached the maximum curvature and the calculated curved fundamental mode at maximum curvature for effective radii between 20 and 200 μm. The OIE increases as the effective radius decreases, showing that more excitations of higher order modes occur as the radius decreases.

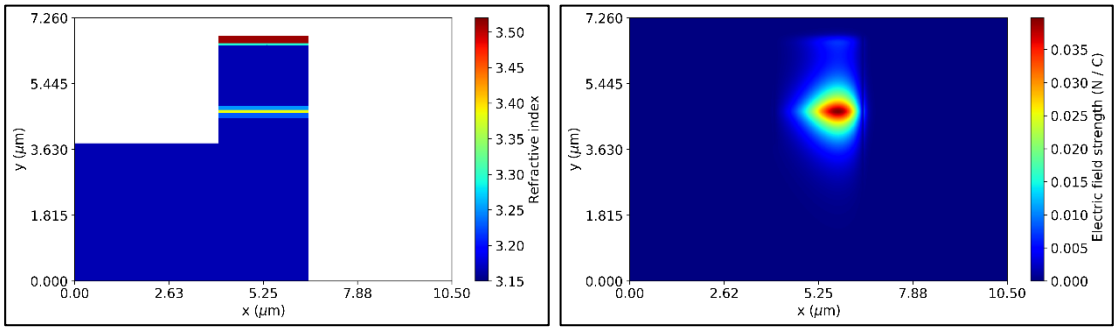

(a) Refractive index profile. (b) E_x field.

Figure 5.41: Refractive index profile and curved fundamental mode when the curvature was maximum for the electric field in the quasi-TE mode for a linearly changing curvature 90° deep-etched bend with an effective radius of 100 μm.

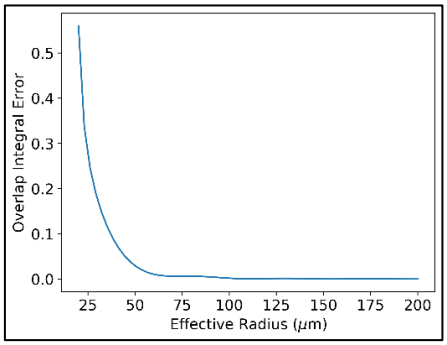

Figure 5.42: Change in the overlap integral error between the propagating field at maximum curvature and the calculated fundamental mode field at maximum curvature with effective radius for the electric field in the quasi-TE mode for a 90° linearly changing curvature deep-etched bend.

Due to the higher order mode excitations occurring as the effective radius decreases, the impact of the maximum curvature reached and the curvature change with path length must be investigated to determine their individual contributions. To investigate the impact of the maximum curvature reached, the 90° linearly changing curvature bend with an effective radius of 100 μm was initially selected. The electric field was propagated through the bend and when the field reached where the curvature was maximum, the OIE was calculated between the propagating field and the curved fundamental mode field at this maximum curvature. The angle turned through by the bend and the linear curvature fraction were then varied to allow a different maximum curvature to be reached, with the effective radius changed to keep the slope of the curvature with path length constant. The procedure was then repeated for multiple waveguide bends. Figure 5.43 shows the different maximum

curvatures reached for the constant slope as well as the calculated OIE between the propagating field and the curved fundamental mode field at maximum curvature for different maximum curvatures with the same curvature-path length slope. The OIE was observed to oscillate as the maximum curvature increased, with the amplitudes of the oscillations decreasing as the curvature increased. This indicated that the excited radiation modes were beating with the shifted fundamental mode, with the oscillation amplitudes decreasing as the excited radiation modes leak more strongly with propagating distance. As a line through the centre of the OIE oscillations does not increase with the increasing maximum curvature, the excitations of the radiation modes do not depend on the maximum curvature reached.

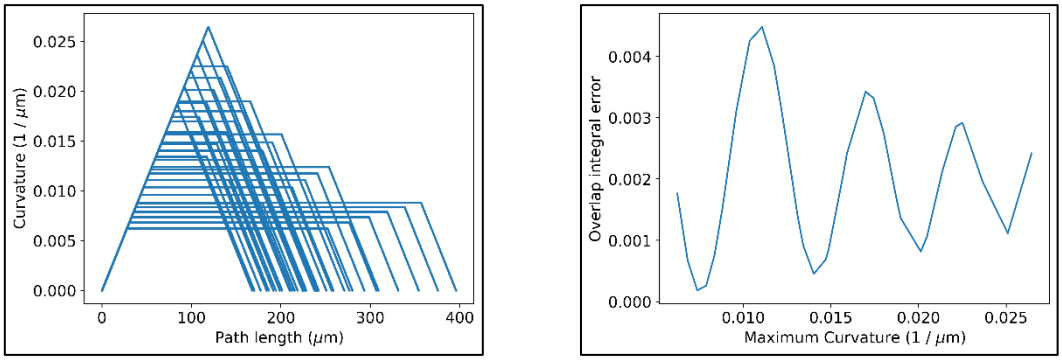

(a) Curvature profile. (b) Overlap integral error.

Figure 5.43: Curvature profiles and the overlap integral error for trapezoidal bends with the same linear curvature slope and different maximum curvatures reached.

This suggests the excitations of the radiation modes depend entirely on the slope of the curvature change with path length. To prove this, the above procedure was repeated, using the same initial effective radius of curvature of 100 μm, this time with the maximum curvature remaining constant and slope varying. Figure 5.44 shows a graph of the curvature profiles of the different bends as well as the overlap integral error between the propagating field and the curved fundamental mode field at maximum curvature. The OIE is shown to oscillate, with the amplitude of the oscillations growing larger as the slope of the curvature with path length is increased. This slope is clearly the cause of the higher order mode excitations in the curved deep-etched waveguide.

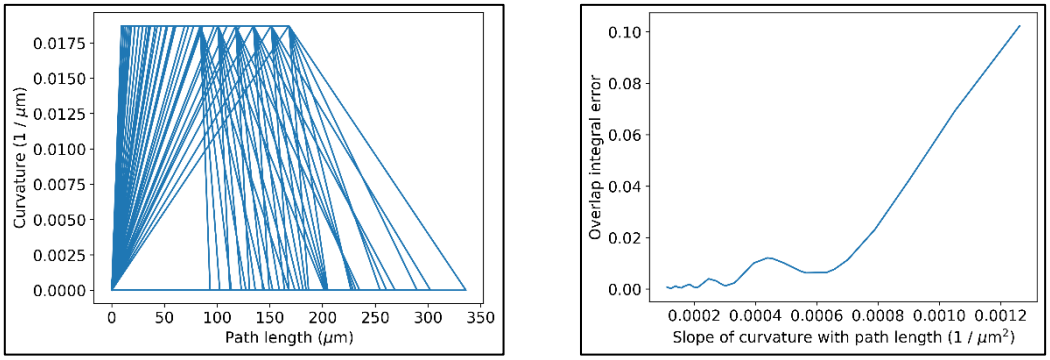

(a) Curvature profile. (b) Overlap integral error.

Figure 5.44: Curvature profiles and the overlap integral error for trapezoidal bends with the same maximum curvature and different linear curvature slopes.

5.5 Conclusions

Curved deep-etched ridge waveguides of various curvature profiles were analysed in an attempt to reduce the bend loss. Bends with a linearly changing curvature component were shown to greatly reduce the curved waveguide loss in most cases due to their ability to suppress excitations of higher order modes. The effect of the width of the waveguide and the deep etch depth on the loss was also investigated. The width of the waveguide was shown to greatly affect the ability of the linear change in curvature to supress higher order mode excitations, and while the deep etch depth had little effect on these higher order mode excitations, the deeper etch was shown to greatly reduce propagation losses. The cause of the excitations of higher order modes in the linearly changing curvature deep-etched waveguides was investigated, with the excitations of the modes found to be dependent on the slope of the change in curvature.

The next chapter will analyse devices where shallow-etched waveguides are connected by deep-etched bends to take advantage of the lower bend loss offered by the deep-etched bends.

6 Shallow-Etched Waveguides Connected by Deep-Etched Bends

Many of the PIC devices fabricated in Tyndall consist of, or contain, waveguides with a shallow etch. Therefore, to allow the devices to be connected by small radii bends, a deep-etched waveguide bend must be used. This chapter will therefore aim to find the best method and location to make the shallow etch-deep etch transition to achieve the lowest loss from the transitions and the bend. Note that the accuracy of some of the BPM simulations in this chapter may be slightly reduced at the shallow etch - deep etch transitions as the $\partial\varepsilon_r/\partial z = 0$ approximation used to omit the coupling between the transverse and propagation directions in the derivation of the semi-vectorial wave equations in chapter two will no longer be valid. A vectorial FDTD simulation would be a superior method to analyse the behaviour and reflection of the fields for these sharper waveguide transitions.

6.1 The Transition Between the Shallow-Etched and Deep-Etched Waveguides

When the propagating field transitions from the shallow-etched waveguide to the deep-etched waveguide, loss will occur due to the mismatch between the fundamental mode fields of both waveguides. The shallow-etched and deep-etched waveguides analysed for the transition have the same properties as those analysed in the previous chapters: the material composition is given by Table 4.1, the bulk material representation of the waveguide is given by Table 4.2, the width of the waveguide is 2.5 μm, the etch depth for the shallow etch is 1.85 μm, and the etch depth for the deep etch is 2.96 μm. The fundamental mode fields for both waveguides can be seen back in Figure 4.3 and Figure 5.2.

To investigate the transition between the waveguides, the fundamental mode magnetic fields in the quasi-TE and quasi-TM modes were firstly launched into the shallow-etched waveguide. After a propagating distance of 100 μm, the waveguide was made deep etched, and after a further propagating distance of 1700 μm, the waveguide was again made shallow etched for a further 200 μm. The long deep-etched waveguide length was used to allow the excited slowly radiating higher order modes to lose their power. 251 computational points were used in the transverse directions and a propagation step of 0.1 μm was used. The (2, 2) Padé order was implemented, along with PML boundary conditions. These computational parameters were used for the other simulations done in this chapter, unless stated otherwise.

Figure 6.1 gives the $x - z$ cross section of the propagating fields at y where the initial fields were maximum. The graph shows the fields to narrow upon entering the deep-etched section. Small oscillations occur initially due to the excitation of radiation modes, but the oscillations are observed to lessen as the field propagates through the deep-etched waveguide as the radiation modes lose their power, especially in the case of the quasi-TM mode. At the transition back to the shallow-etched waveguide, the propagating field again takes the shape of the initially propagated field. To further examine the behaviour of the fields, Figure 6.2 and Figure 6.3 show the mode mismatch error and overlap integral error between the initially propagated fundamental mode fields of the shallow-etched waveguide

and the propagating fields. When the propagating fields enter the deep-etched region, both the MME and OIE are observed to immediately rise and then oscillate rapidly. The rapid oscillations are due to the excitation of the multiple higher order radiation modes in the deep-etched region. As the fields propagate further through the region, the rapid oscillations fade as the higher order modes lose their power. This causes the MME and OIE to approach a constant value for the quasi-TM mode as the field propagates through the deep-etched region, but for the quasi-TE mode, oscillations still occur as the field propagates, with the amplitude of the oscillations slightly decreasing with propagating distance. These oscillations are due to the fundamental mode beating with the very slowly radiating higher order mode which was analysed in Figure 5.8. This radiation mode is not present in the quasi-TM mode which explains the lack of oscillations in the MME and OIE. After the waveguide transitions back to being shallow etched, the MME is approximately 0.15 for the quasi-TE mode and 0.09 for the quasi-TM mode, showing the loss resulting from the waveguide transitions.

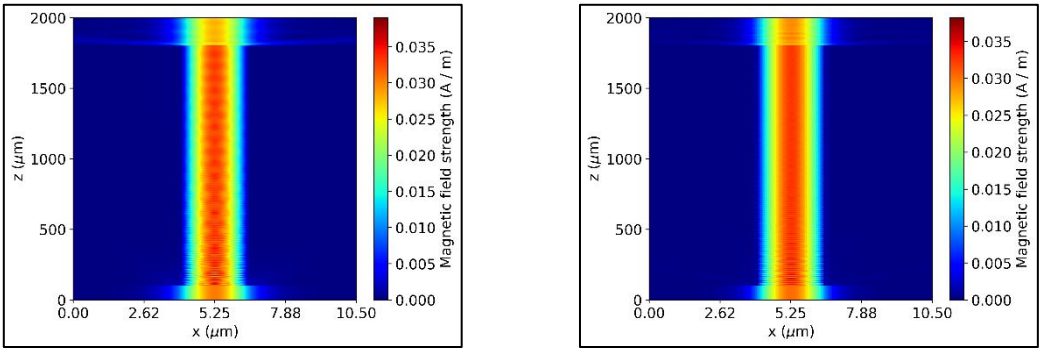

(a) H_y in the quasi-TE mode. (b) H_x in the quasi-TM mode.

Figure 6.1: Cross section of the magnetic fields, at y where the initial field was maximum, as the fields propagate through the shallow to deep and deep to shallow etch waveguide transitions.

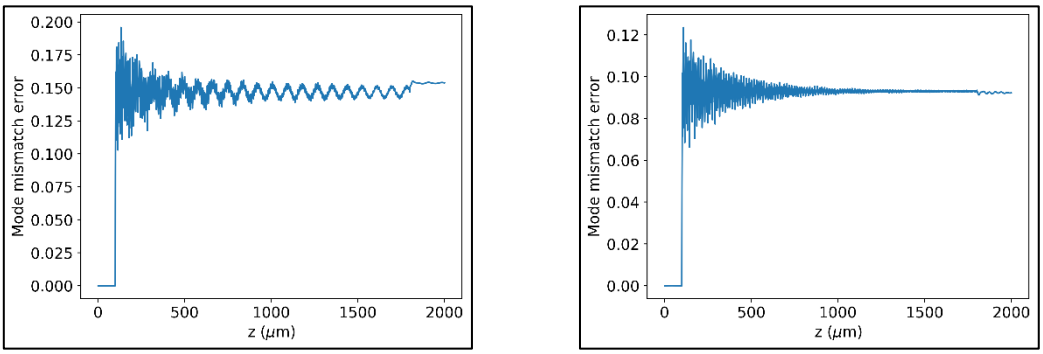

(a) H_y in the quasi-TE mode. (b) H_x in the quasi-TM mode.

Figure 6.2: Mode mismatch error between the initially propagated fundamental mode of the shallow-etched waveguide and the propagating field, as each field propagates through the shallow to deep and deep to shallow etch waveguide transitions.

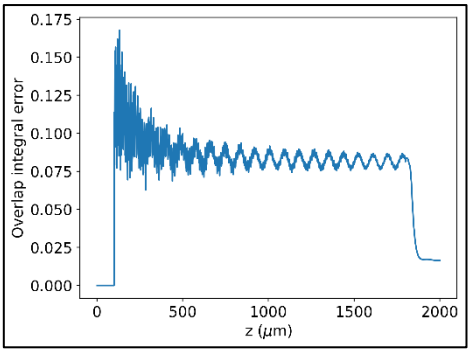

(a) H_y in the quasi-TE mode.

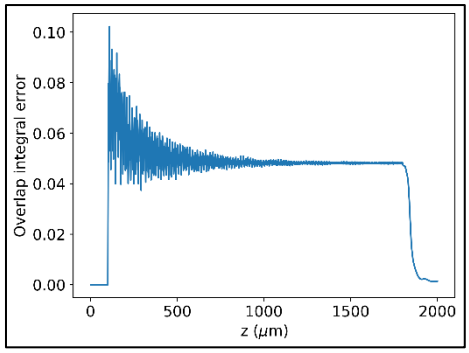

(b) H_x in the quasi-TM mode.

Figure 6.3: Overlap integral error between the initially propagated fundamental mode of the shallow-etched waveguide and the propagating field, as each field propagates through the shallow to deep and deep to shallow etch waveguide transitions.

6.2 Reducing the Loss from the Transition Between the Shallow-Etched and Deep-Etched Waveguides

As these transitions are necessary to connect shallow-etched waveguide devices to deep-etched waveguide bends, it is desirable to reduce the resulting loss from the transition as much as possible. This can be achieved if the deep-etched waveguide is modified so that the shape of the fundamental mode field of the deep-etched waveguide can be altered to be as close as possible to that of the shallow-etched waveguide. Figure 6.4 again shows the fundamental mode magnetic field in the quasi-TE mode for the both the shallow and deep-etched waveguides. From the graphs, it is clearly seen that the field is less confined along the $\hat{x}$ direction within the quantum well region, where the field amplitude is maximum, for the shallow-etched waveguide. This suggests that widening the deep-etched waveguide may result in a lower overlap integral error between the fundamental mode fields and therefore less loss would be achieved in the transition. To verify this, the width of the deep-etched waveguide was varied between 2.5 and 4 microns and the fundamental mode fields were calculated using the finite difference mode solver. The overlap integral error was then calculated between the fundamental mode fields of the original shallow-etched waveguide and the varying width deep-etched waveguide to find the width where the OIE was minimum. Figure 6.5 gives the value of this OIE with deep-etched waveguide width. The graphs show that the OIE can be minimised by increasing the waveguide width, with the minimum occurring at a width of 3.32 μm for the quasi-TE mode and a width of 3.08 μm for the quasi-TM mode. Unfortunately, for the quasi-TE mode, the slowly radiating second order mode, with most of its power confined at the top of the waveguide (Figure 5.8), becomes supported at a width of 2.82 μm, meaning that although the OIE has decreased, the excitations of the second order mode will no longer radiate away, potentially leading to more loss as the fundamental mode and the former radiation mode would beat together. Meanwhile, the third and higher order modes in the quasi-TE mode, as well as the second and higher order modes in the quasi-TM mode, do not become supported modes even at a waveguide width of 4 μm. They do, however, become more slowly radiating modes and therefore excitations must be minimised.

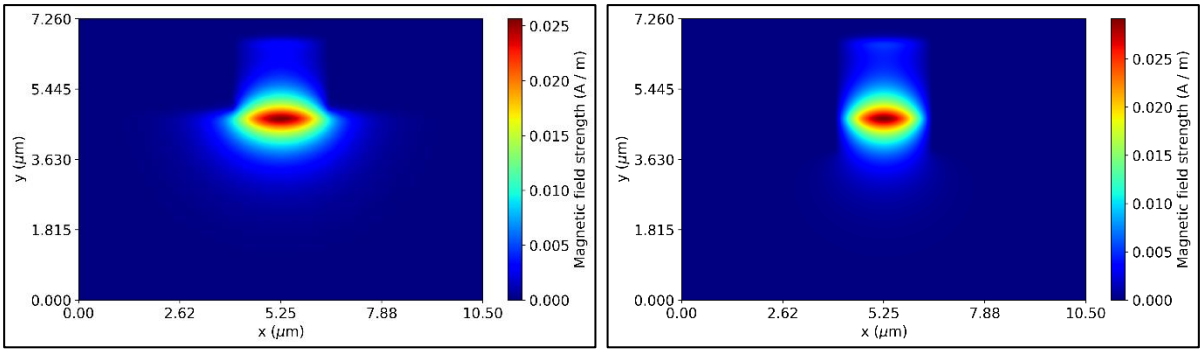

(a) Shallow-etched waveguide. (b) Deep-etched waveguide.

Figure 6.4: Fundamental mode field distributions of H_y in the quasi-TE mode for the shallow and deep-etched waveguides.

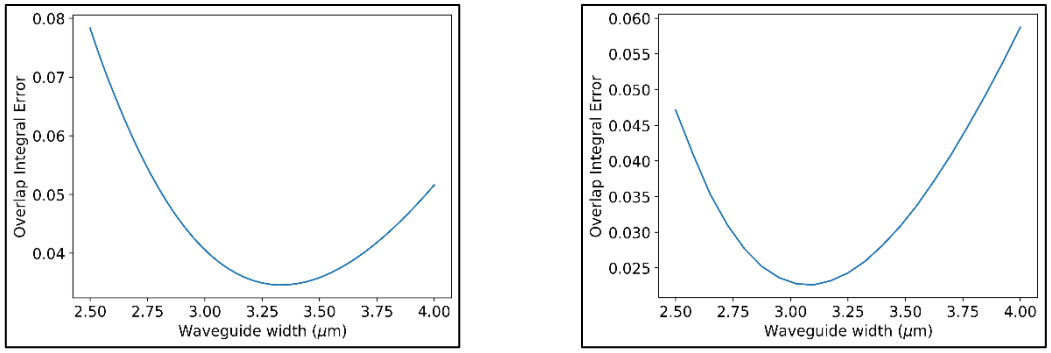

(a) H_y in the quasi-TE mode. (b) H_x in the quasi-TM mode.

Figure 6.5: Overlap integral error between the fundamental mode fields of the shallow-etched waveguide and the varying width deep-etched waveguide.

Although the OIE between fundamental modes is reduced by increasing the waveguide width, Figure 5.36 showed that a linearly changing curvature bend with an increased waveguide width is less capable of suppressing higher order mode excitations. It would therefore not be advisable to use the waveguide widths where the OIE was minimum for the bend, as suggested by the previous result, and another method of lowering the OIE after the transition must be considered.

Due to the shape of the mode profiles given by Figure 6.4, it was suggested that the OIE could also be lowered by only making one side of the waveguide deep etched, while keeping the other side shallow etched. The side to be deep etched would be the side on the outside of the bend, as the deep etch is far more effective at preventing the propagating field from leaking during the bend. The mode profiles of the shallow-etched and the deep-etched on one side waveguides are given by Figure 6.6. The deep etch on one side causes the field to shift slightly to the side with the shallow etch. This suggests increasing the waveguide size from the side with the deep etch may cause the field to better overlap with that in the shallow-etched waveguide. To verify this, Figure 6.7 gives a graph of the OIE between the fundamental mode magnetic field of the shallow-etched and the deep-etched on one side waveguides as the waveguide width increases from the side with the deep etch. The graphs show the OIE to be minimised at a width of 2.84 μm for the quasi-TE mode and a width of 2.76 for the quasi-TM mode, which are considerably smaller than what was observed for the OIE between the fields of the shallow-etched and deep-etched waveguides.

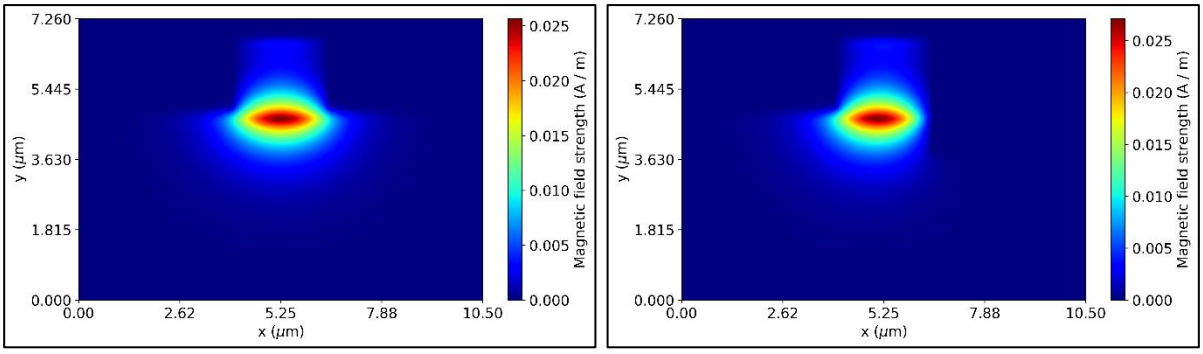

(a) Shallow-etched waveguide. (b) Deep-etched on one side waveguide.

Figure 6.6: Fundamental mode field distributions of H_y in the quasi-TE mode for the shallow and deep-etched on one side waveguides.

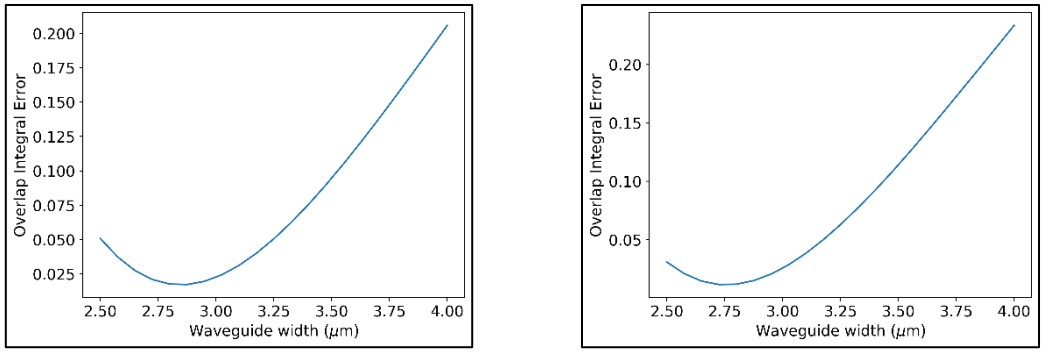

(a) H_y in the quasi-TE mode. (b) H_x in the quasi-TM mode.

Figure 6.7: Overlap integral error between the fundamental mode fields of the shallow-etched waveguide and the varying width deep-etched on one side waveguide.

As the OIE at the original 2.5 μm waveguide width is much closer to the minimum OIE for the deep-etched on one side waveguide in comparison to the deep-etched on both sides waveguide, it may make sense to keep the waveguide size at 2.5 μm and use the deep-etched on one side waveguide for the bend. Firstly however, the deep-etched on one side bend must be analysed to investigate how similarly it performs to the deep-etched on both sides bend. Figure 6.8 shows the propagating electric field in the quasi-TE mode, at y where the initial field amplitude was maximum, for a 180° circular bend and a 180° linearly changing curvature bend, both with an effective radius of curvature of 100 μm. Figure 6.9 and Figure 6.10 give the MME and OIE between the initially propagated field and the propagating field. The graphs appear very similar to the corresponding graphs in Section 5.2.2, which examined the propagating fields for the bend with the deep etch on both sides. The only differences appear to be the slightly different beat length between the fundamental mode and the radiation mode(s) of the circular waveguide as well as the linearly changing curvature waveguide appearing to be slightly less effective at suppressing higher order modes. To confirm this, Figure 6.11 shows the mode mismatch error between the fundamental mode field of the deep-etched on one side waveguide and the propagating field after the bend for the 180° circular and linearly changing curvature bends with effective radii of curvature between 10 and 200 microns for the electric field in both the quasi-TE and quasi-TM modes. Comparing it to Figure 5.29, which was the equivalent graph for the deep etch on both sides, the circular waveguide appears to perform worse for the

deep-etched on one side bends, with larger amplitude MME oscillations where the amplitude of the oscillations decreases much more slowly with respect to increasing radius of curvature. However, the MME at the minima of the oscillations are comparable to the MME at the minima for the circular deep-etched on one side bends, showing approximately the same amount of loss would be achieved if the bend was designed to end at one of these minima. For the linearly changing curvature waveguides, significant oscillations in the MME (which suggest significant excitations of higher order modes) do not begin until the effective radius of curvature has reached down to approximately 25 μm for the deep-etched on one side bend. This is in contrast to an effective radius of approximately 20 μm for the bend with the deep etch on both sides. Therefore, although making the waveguide deep etched on one side reduces the loss from the waveguide transition, it may lead to slightly higher bend loss for very small radii of curvature bends.

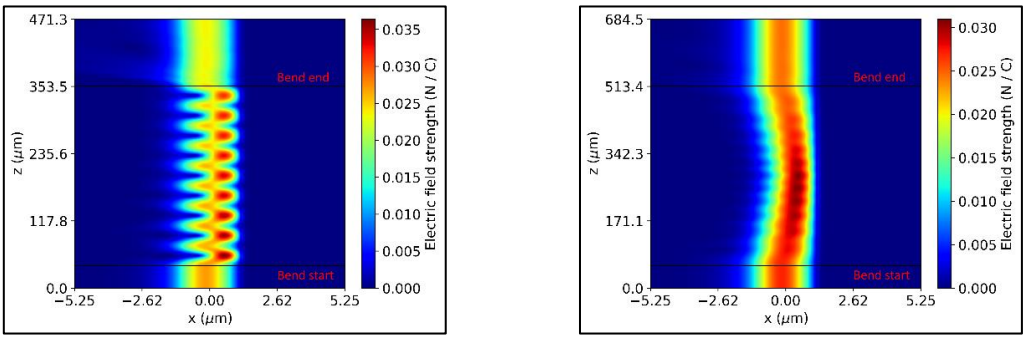

(a) Circular waveguide. (b) Linearly changing curvature waveguide.

Figure 6.8: Cross section of the electric field, at y where the initial field was maximum, as the electric field in the quasi-TE propagates through the circular and linearly changing curvature deep-etched on one side 180° waveguide bends with an effective radius of curvature of 100 μm.

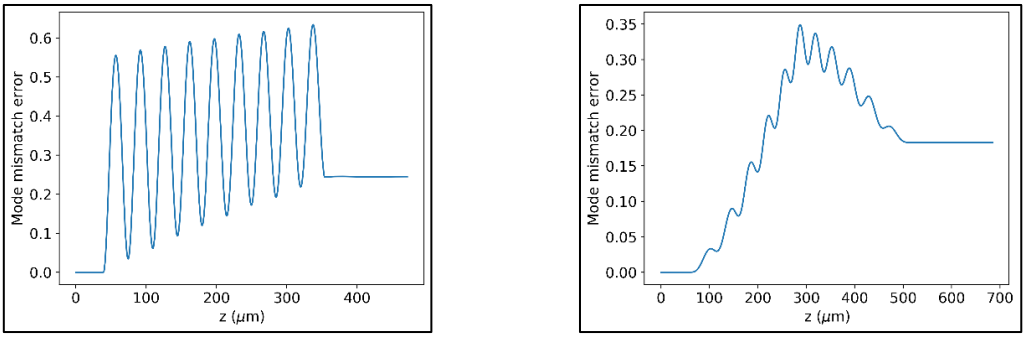

(a) Circular waveguide. (b) Linearly changing curvature waveguide.

Figure 6.9: Mode mismatch error as the electric field in the quasi-TE mode propagates through the deep-etched on one side 180° waveguide bends with an effective radius of curvature of 100 μm.

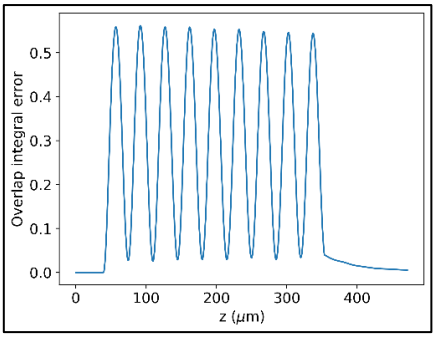

(a) Circular waveguide.

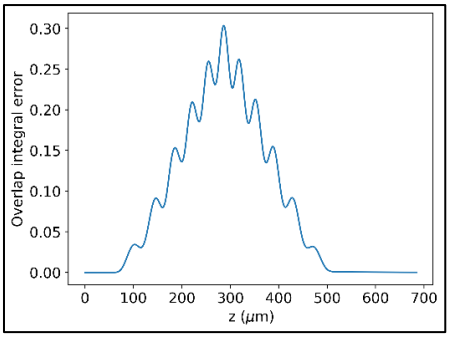

(b) Linearly changing curvature waveguide.

Figure 6.10: Mode mismatch error as the electric field in the quasi-TE mode propagates through the deep-etched on one side 180° waveguide bends with an effective radius of curvature of $100\ \mu m$.

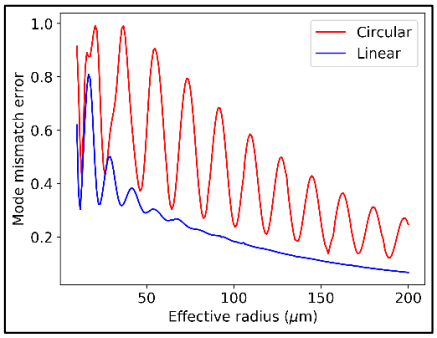

Figure 6.11: Mode mismatch error between the fields before and after the 180° bend as the effective radius of curvature increases for the circular and linearly changing curvature deep-etched on one side waveguides.

6.3 Shallow-Etched Waveguides Connected to Deep-Etched Bends

The previous section showed how less loss is observed in a transition between a shallow-etched waveguide and a deep-etched on one side waveguide than from a transition between a shallow-etched waveguide and a deep-etched on both sides waveguide, for a waveguide width of 2.5 μm. However, analysis of the deep-etched on one side bend showed the bend to perform slightly worse than the deep-etched on both sides bend in terms of loss and suppression of higher order mode excitations in the case of the linearly changing curvature waveguide. These bend simulations were done with the input and output straight waveguides also having the deep etch on one side and therefore did not consider the impact of the transition between the shallow-etched waveguide and the deep-etched on one side waveguide on the performance of the bend. Where this transition takes place could have an impact on the modes excited in the waveguide bend as the field after the transition could contain a superposition of modes due to the slowly radiating higher order modes. This superposition of modes could potentially better or worsen the excitation of the fundamental mode in the waveguide bend or potentially could also cause other higher order radiation modes to be significantly excited.

Firstly, the case of the waveguide transitions occurring at the beginning and the end of the bend is considered. Figure 6.12 shows the magnetic field in the quasi-TE mode as it propagates through the circular and linearly changing curvature deep-etched on one side waveguide bends with an effective radius of curvature of 100 μm. Figure 6.13 and Figure 6.14 show the MME and OIE between the initially propagated fundamental mode field of

the shallow-etched waveguide and the propagating field. For the circular waveguide, the amplitudes of the MME and OIE oscillations are actually smaller than what was observed in Figure 6.9 and Figure 6.10 when the connecting straight waveguides were also deep-etched on one side. This suggests the shape of the fundamental mode field of the shallow-etched waveguide is actually closer to the shape of the shifted fundamental mode field of the curved deep-etched on one side waveguide than the fundamental mode field of the straight deep-etched on one side waveguide is. This is suggested because less beating is observed between the modes if one mode receives more power, giving rise to the lower amplitude oscillations in the MME and OIE. This causes the straight shallow-etched waveguides connected to the circular deep-etched on the outside waveguide to actually perform better than the straight and circular waveguides all containing a deep etch on one side in general, except in cases where the bend ends on a MME minima, where the lower amplitude MME oscillations actually cause the lowest MME to occur for the case where the connecting straight waveguides and circular waveguide all contain a deep etch on only one side. Meanwhile, making the waveguide transition at the start and end of the bend is less effective for the linearly changing curvature. This is seen in Figure 6.13 (b) and Figure 6.14 (b), where the MME and OIE rise sharply once the bend starts. This occurs as the curvature is very small at the beginning of the bend due to the curvature linearly increasing, and as a result, the shallow to deep waveguide transition causes multiple radiation modes to be excited in the linearly increasing curvature waveguide. These excited radiation modes are initially slowly radiating as the curvature is initially too small to cause them to radiate away over a short propagating distance. This gives rise to the rapid oscillations in the MME and OIE at the beginning of the bend and causes the linear change in curvature to be less effective at retaining most of the power in the shifted fundamental mode.

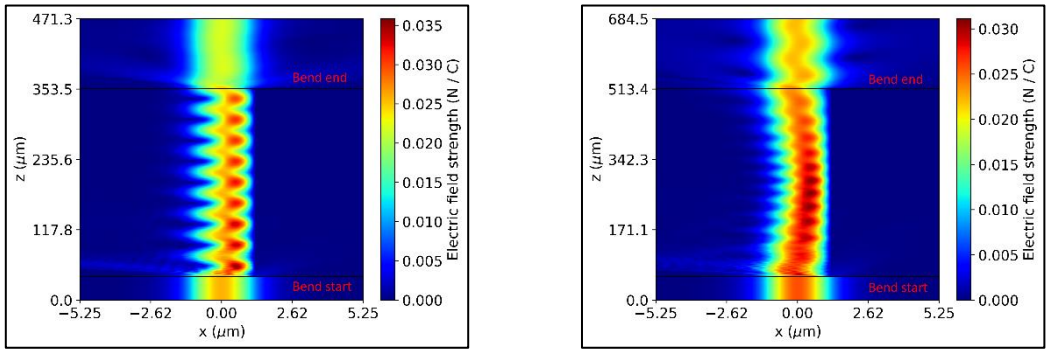

(a) Circular waveguide.

(b) Linearly changing curvature waveguide.

Figure 6.12: Propagating electric field in the quasi-TE mode, at y where the field amplitude was initially maximum, through the circular and linearly changing curvature deep-etched on one side waveguides with an effective radius of curvature of 100 μm that are connected by two straight shallow-etched waveguides.

Next, it must be determined if it is better to use the deep-etched on one side or both sides bend when connecting to the straight shallow-etched waveguides. Figure 6.15 gives the MME between the fundamental mode magnetic field of the straight shallow-etched waveguide and the propagating field as the effective radius of curvature increases for both a circular and linearly changing curvature 180° bend, where the deep etch is either made on one side or both sides. The graphs appear very similar, with the MME being in general

slightly lower for the deep etch on the outside of the bend in the case of the linearly changing curvature.

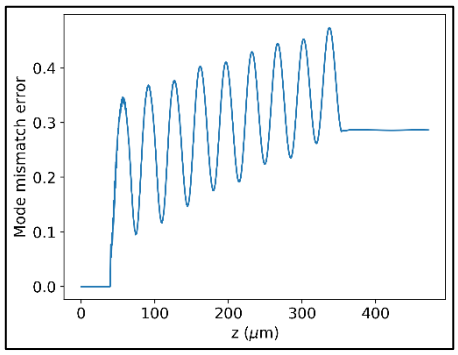

(a) Circular waveguide.

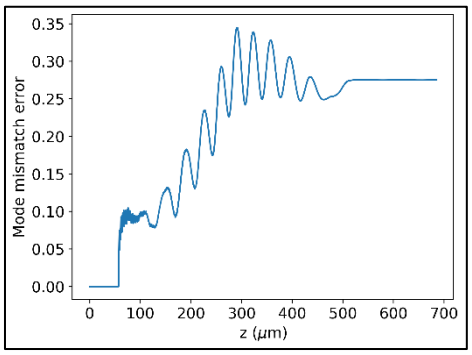

(b) Linearly changing curvature waveguide.

Figure 6.13: Mode mismatch error as the magnetic field in the quasi-TE mode propagates through the curved 180° deep-etched on one side waveguides with an effective radius of curvature of 100 μm that are connected at the ends to two shallow-etched waveguides.

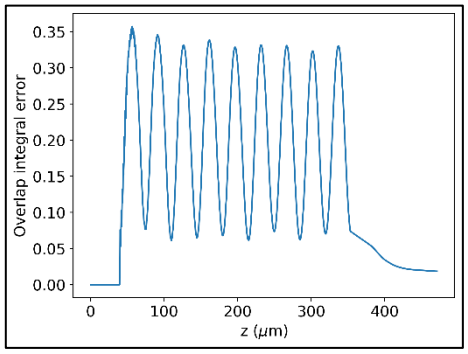

(a) Circular waveguide.

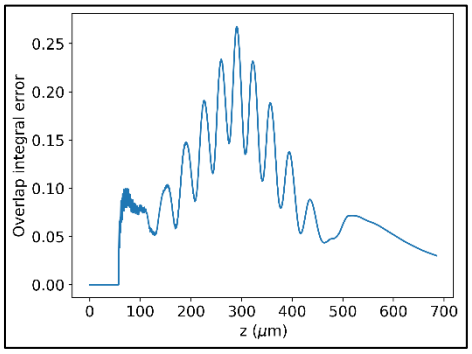

(b) Linearly changing curvature waveguide.

Figure 6.14: Overlap integral error as the magnetic field in the quasi-TE mode propagates through the curved 180° deep-etched on one side waveguides with an effective radius of 100 μm that are connected at the ends to two shallow-etched waveguides.

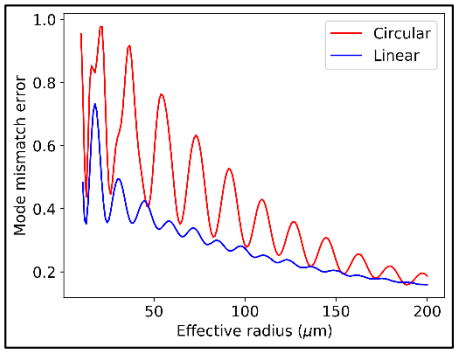

(a) Deep etch on outside of bend.

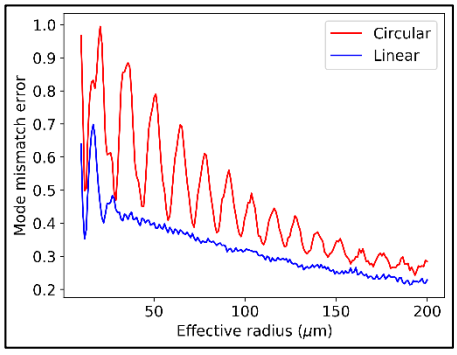

(b) Deep etch on both sides of bend.

Figure 6.15: Mode mismatch error as the effective radius of curvature increases for the circular and linearly changing curvature 180° waveguide bends where the bends are either deep etched on one side or both sides and the connecting straight waveguides are shallow etched.

For the above simulations, the waveguide transitions occur at the beginning and end of the waveguide bend. If the transition instead occurs at some point before the bend, the superposition of the excited slowly radiating higher order modes in the straight deep-etched waveguide could potentially cause different excitations of the shifted modes in the curved

waveguide, depending on where the waveguide transition takes place. Figure 6.16 shows the MME between the fundamental mode magnetic field of the straight shallow-etched waveguide and the propagating field in the straight shallow-etched waveguide after the bend for both a circular and linearly changing curvature deep-etched on one side bend with an effective radius of curvature of 100 μm, where the transitions between the shallow and deep-etched on one side waveguides take place at different distances from the beginning and end of the bend. For the circular waveguide, the MME is lowest when the transitions take place at the entry and exit points of the curved waveguide. For the linearly changing curvature waveguide, the MME does tend to decrease as the distance from the bend increases, however the reduction made to the MME is small suggesting it may not be worth the extra propagating distance. It also oscillates as the distance increases and the decrease may not hold for different radii of curvature. It would also not be advisable to make the waveguide transition after the bend begins, as Chapter 3 showed the shallow-etched bend to be much more lossy at lower radii of curvature. For these reasons, it would appear best to make the waveguide transitions at the immediate beginning and end of the bend.

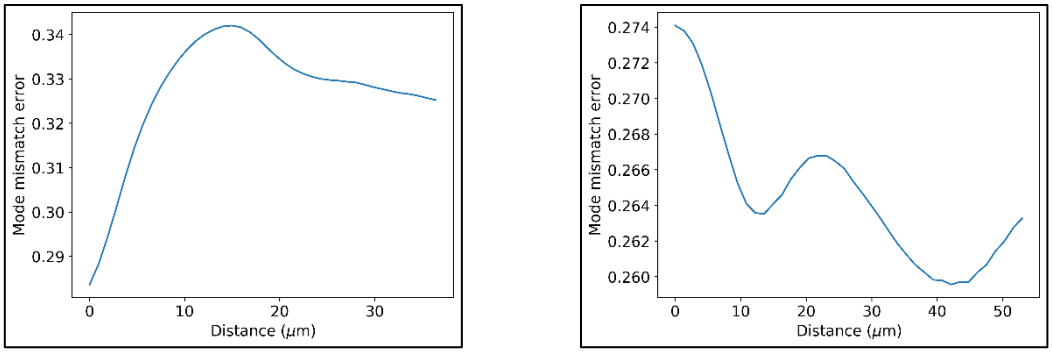

(a) Circular waveguide.

(b) Linearly changing curvature waveguide.

Figure 6.16: Mode mismatch error between the quasi-TE fundamental mode magnetic field of the shallow-etched waveguide and the propagating magnetic field after the circular and linearly changing curvature deep-etched on one side 180° waveguide bends with effective radii of curvature of 100 μm, which are connected by two straight shallow-etched waveguides, as the distance from the bend of the shallow etch to deep etch transition increases.

Another way to potentially reduce loss from the waveguide transition between the shallow and deep-etched waveguides and the bend would be to make the waveguide transition before the bend, setting the width of the deep-etched waveguide so as to minimise the loss from the transition, as shown in Figure 6.5 and Figure 6.7. However, as the increased waveguide width would lessen the ability of the linear change in curvature to prevent higher order mode excitations, the waveguide width would then need to be reduced before entering the waveguide bend. This would be achieved by introducing a waveguide taper, which would reduce the waveguide width gradually over a set propagating distance. An example of a waveguide taper is given by Figure 6.17. The taper would allow the fundamental mode of the wider waveguide to gradually take the shape of the fundamental mode of the narrower waveguide, with very little loss. After the bend, another taper of the same length would be used to increase the width of the waveguide back to its original width to minimise the mismatch error in the transition with the exit shallow-etched waveguide.

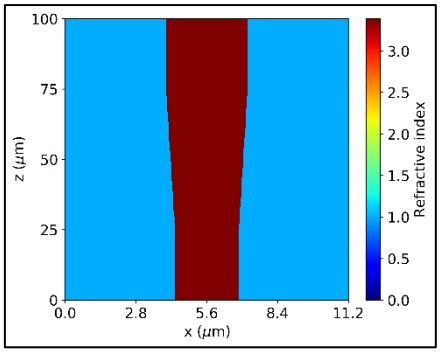

Figure 6.17: Waveguide taper of length 50 μm which increases the width of the deep-etched on both sides waveguide from 2.5 to 3.2 microns. The figure shows the refractive index profile at a y location in the quantum well region.

Firstly, the waveguide taper length must be selected to ensure minimal extra losses. This analysis will consider the waveguide transition from the shallow-etched waveguide to the deep-etched on one side waveguide. From Figure 6.7 it can be seen that the OIE between the fundamental modes is minimised at a width of 2.85 μm for the quasi-TE mode. A change in width between 2.85 and 2.5 μm will therefore be considered. To determine how long the taper must be to ensure minimal losses, the width of the deep-etched on one side waveguide was increased from 2.5 μm to 2.85 μm from the side of the deep etch using tapers of different lengths. If the taper works correctly, the field should slowly widen as the taper increases the width of the waveguide, and the OIE between the fundamental mode field of the wider waveguide and the propagating field should decrease as the field propagates through the taper. Figure 6.18 gives the propagating H_y field in the quasi-TE mode through the taper as well as the OIE between the fundamental mode of the wider waveguide and the propagating field. The OIE is very close to zero when the taper ends at $z = 75\ \mu m$, showing the taper to successfully transition the fundamental mode at a length of 50 μm.

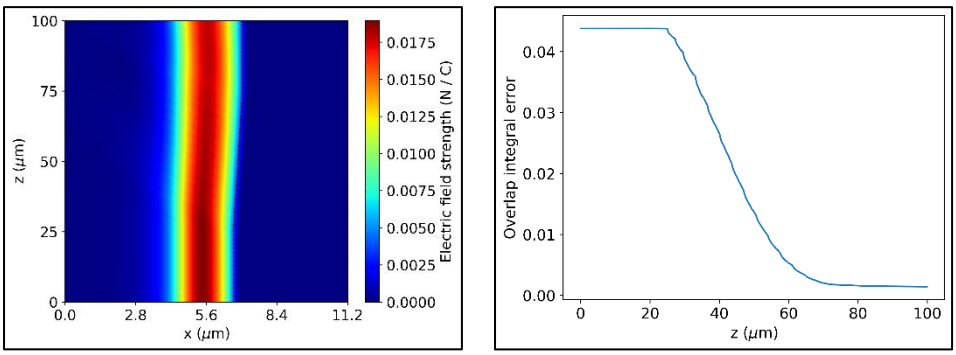

(a) Propagating H_y field. (b) Overlap integral error

Figure 6.18: (a) Propagating H_y field in the quasi-TE mode, at y where the initial field amplitude was maximum, as the width of the deep-etched on one side waveguide increases from 2.5 to 2.85 microns by means of a waveguide taper of length 50 μm between a propagating distance of 25 and 75 microns. (b) Overlap integral error between the fundamental mode of the wider waveguide and the propagating field.

To investigate if a shorter taper could be used, Figure 6.19 gives the OIE between the fundamental mode of the wider waveguide and the propagating field at the end of the taper. The graph shows that the longer the taper, the better the transition between fundamental modes and that the OIE initially drops sharply with increasing width. The curve begins to flatten at a length of approximately 50 μm.

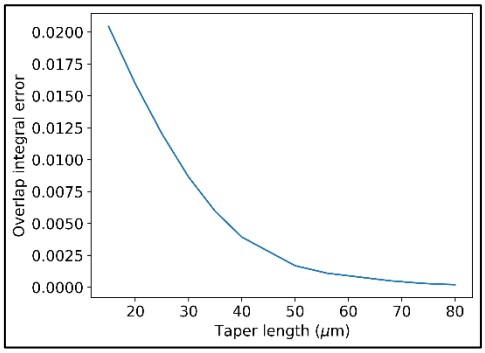

Figure 6.19: Overlap integral error between the fundamental mode of the wider waveguide and the propagating field at the end of the taper for different taper lengths where the width of the deep etch on one side waveguide is increased from 2.5 to 2.85 microns.

Finally, the taper is implemented into the structure containing the two shallow-etched waveguides connected to the deep-etched bend. The fundamental mode magnetic field in the quasi-TE mode is initially propagated through the straight shallow-etched waveguide of width 2.5 μm. This shallow-etched waveguide then transitions to the deep-etched on one side waveguide of width 2.85 μm, as this was where the OIE between the fundamental modes of the two waveguides was minimum as shown in Figure 6.7. The 2.85 μm width deep-etched on one side waveguide is then tapered down to a width of 2.5 μm using a 50 μm length taper. The narrower deep-etched on one side waveguide then undergoes a linearly changing curvature bend with an effective radius of 100 μm. After the bend, the width of the deep-etched on one side waveguide is again increased to 2.85 μm using a 50 μm long taper, and this wider waveguide then transitions to the exit shallow-etched waveguide of width 2.5 μm. Figure 6.20 (a) gives the magnetic field as it propagates through this structure, at y where the amplitude of the initially propagated field was maximum. The straight black lines indicate the locations where the waveguide transitioned, where the tapers began and ended, and where the bend began and ended. Figure 6.20 (b) gives the MME between the initially propagated field and the propagating field. The MME of approximately 0.225 at the end of the structure is lower than that for the corresponding structure without the tapers given by Figure 6.13 where it was approximately 0.275, showing the benefit of including the waveguide tapers.

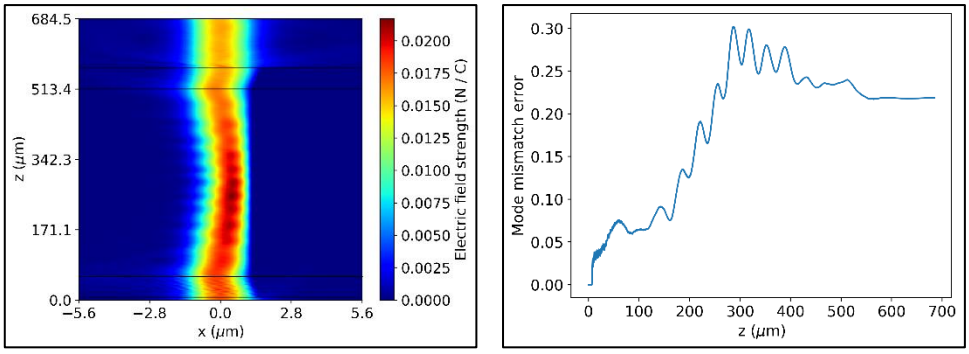

(a) Propagating H_y field. (b) Mode mismatch error

Figure 6.20: (a) Propagating H_y field in the quasi-TE mode, at y where the initial field amplitude was maximum, for the $180°$ deep-etched on one side bend with an effective radius of curvature of $100\ \mu m$, connected to two shallow-etched waveguides by means of two waveguide tapers. (b) Mode mismatch error between the initially propagated fundamental mode of the shallow-etched waveguide and the propagating field.

As the taper successfully transitions the field to the fundamental mode of the narrower waveguide, the taper could also be used to decrease the width to below 2.5 μm to take advantage of the lower loss and less excitations of higher order modes in the linearly changing curvature bend, as reported in section 5.3.1.

6.4 Examples of Optimised Bends

The following section will give examples of shallow-etched waveguide connected by deep-etched waveguide bends which produce very small amounts of loss, optimised according to the previous results.

Figure 6.21 (a) shows the cross section of the magnetic field in the quasi-TE mode as it propagates through an optimised 90° deep-etched on one side bend. The bend consists of linearly changing curvature with an effective radius of curvature of 22.5 μm. The width of the shallow etch waveguides is $2.5\ \mu m$ and the width of the deep-etch on one side waveguide is tapered down from 2.85 to 2.5 μm over a short propagating distance of 10 μm before the bend. This short taper length allows the total device footprint to be smaller albeit at the cost of slightly higher loss, as shown by Figure 6.19. The deep etch depth is 4 μm, which was shown to minimise propagation loss in Figure 5.38. The beating of modes can be observed in the waveguide bend. The MME between the initially propagated fundamental mode field of the waveguide before and after the bend was a low value of 0.159, which is shown by Figure 6.21 (b). The main contributing factors to this MME were the immediate loss from the transitions between the shallow-etched and the deep-etched on one side waveguides and the loss from the mismatch between the fields at the beginning and end of the bend. The propagation loss from the propagating field in the curved region was minimised by using the deeper etch.

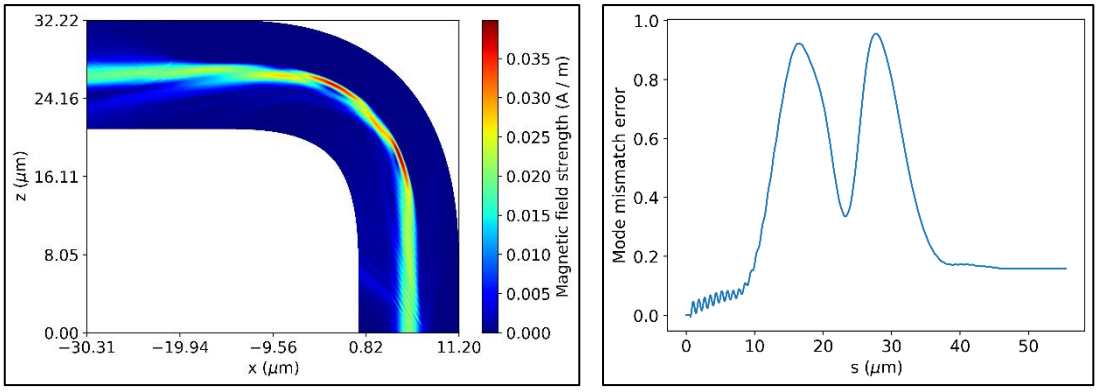

(a) Propagating H_y field. (b) Mode mismatch error

Figure 6.21: (a) Propagating H_y field in the quasi-TE mode, at y where the initial field amplitude was maximum, for the $90°$ deep-etched on one side linearly changing curvature bend, with an effective radius of curvature of 22.5 μm, connected to two shallow-etched waveguides by means of two waveguide tapers. (b) Mode mismatch error between the initially propagated fundamental mode of the shallow-etched waveguide and the propagating field.

The next optimized bend is that of the 180° deep-etched on one side bend. This bend consisted of half circular and half linearly changing curvature. The same parameters were used as for the previous bend apart from the effective radius of curvature which was 13.5 μm. The propagating field is given by Figure 6.22 (a). The MME after the bend was 0.122 and the evolution of the MME is given by Figure 6.22 (b).

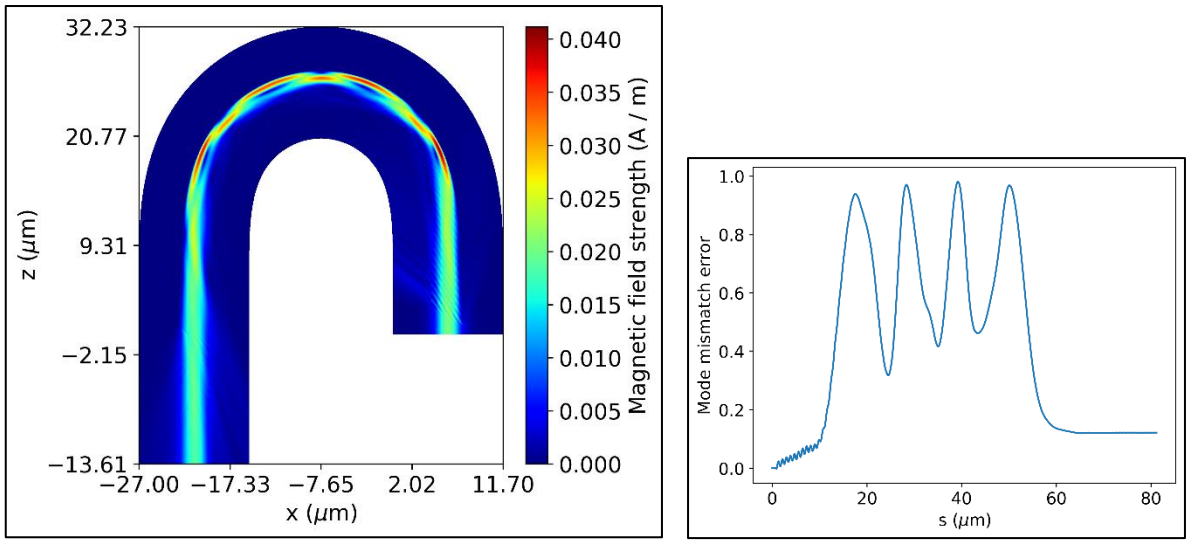

(a) Propagating H_y field. (b) Mode mismatch error

Figure 6.22: (a) Propagating H_y field in the quasi-TE mode, at y where the initial field amplitude was maximum, for the $180°$ deep-etched on one side, half circular, half linearly changing curvature bend, with an effective radius of curvature of 13.5 μm, connected to two shallow-etched waveguides by means of two waveguide tapers. (b) Mode mismatch error between the initially propagated fundamental mode of the shallow-etched waveguide and the propagating field.

The last optimised bend is for the wider 2.85 μm deep-etched on one side 180° bend. The bend consists of linearly changing curvature, has an effective radius of 11.5 μm, and connects the two standard 2.5 μm width shallow-etched waveguides. The etch depth was 4 μm. As the loss from the shallow-etched to deep-etched on one side waveguide transition is minimised at a width of 2.85 μm, no tapers are needed. Figure 6.23 (a) gives the cross

section of the propagating magnetic field in the quasi-TE mode through the curved waveguide and Figure 6.23 (b) shows the MME as it propagates. The MME between the initial field and the field after the bend was 0.166. Although tapers are not needed for this bend, this is larger than that for the optimised 2.5 μm width 180° bend, which is likely due to wider waveguide's inferior ability to supress higher order mode excitations, as shown in Figure 5.37.

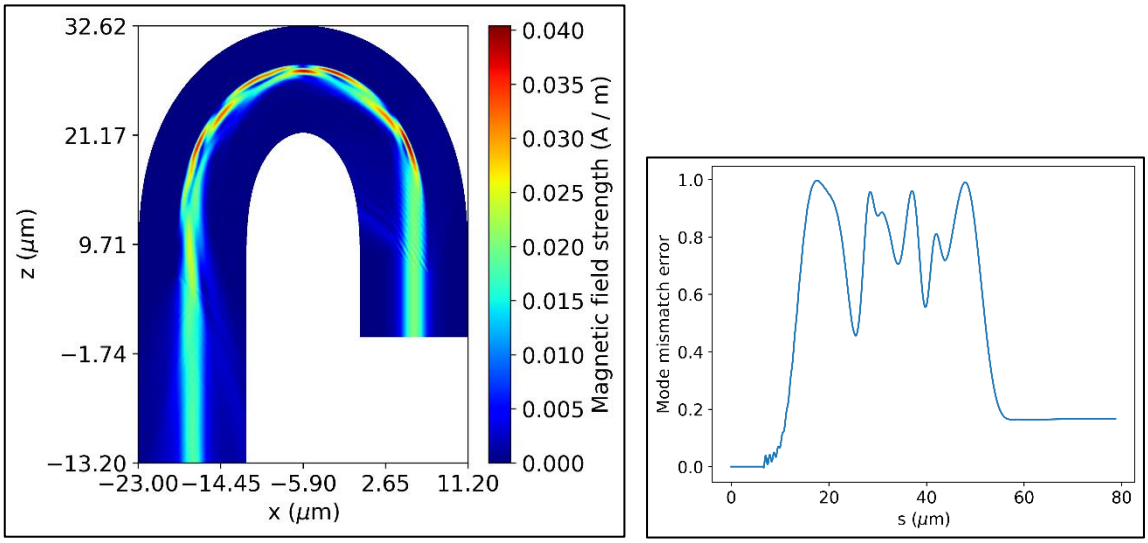

(a) Propagating H_y field. (b) Mode mismatch error

Figure 6.23: (a) Propagating H_y field in the quasi-TE mode, at y where the initial field amplitude was maximum, for the $180°$ deep-etched on one side 2.85 μm width linearly changing curvature bend, with an effective radius of curvature of 11.5 μm, connected to two shallow-etched waveguides by means of two waveguide tapers. (b) Mode mismatch error between the initially propagated fundamental mode of the shallow-etched waveguide and the propagating field.

6.5 Conclusions

Methods of combining shallow-etched waveguides with deep-etched bends have been investigated. The loss from the waveguide transitions and the bend were reduced by means of varying the waveguide width, the etch depth, and by implementing waveguide tapers. A number of optimised bends producing small amounts of loss were showcased.

7 Conclusions

Many conclusions can be drawn from the work done in this thesis. Firstly, the ability to analyse three-dimensional semi-vectorial wave equations through curved waveguides by a conformal transformation was shown. The method of finite difference was applied to the derivatives in these equations and the resulting finite difference equations could be solved easily and relatively quickly using modern numerical libraries and computer processors.

Modifying the curvature profile of the curved shallow-etched ridge waveguide did little to improve the overall loss from the bend. The weak confinement of the fundamental mode caused large amounts of propagation loss even at large radii of curvature. Increasing the width of the waveguide did somewhat improve the loss of the bend, but bends with effective radii of approximately half a millimetre were still required to prevent considerable loss.

On the other hand, modifying the curvature profile of the deep-etched waveguide bend caused considerable improvement of the curved waveguide loss. By implementing a linear change in curvature, excitations of multiple slowly radiating modes in the curved waveguide were prevented. This allowed the fundamental mode to slowly shift in its position as it propagated around the bend, with very little propagation loss on account of the deep etch causing high modal confinement. However, as the effective radius of curvature became small, the linearly changing curvature failed to prevent the excitations of multiple modes. The excitation of the multiple modes was found to be dependent on the slope of the change of the curvature with the path length, with the larger the slope, the more excitations of higher order modes. However, it was found that, like the matched bend, the linearly changing curvature bend also had effective radii of curvature where the initial input field would be reproduced at the end of the bend and that the overall loss of this bend was lower than that of the matched circular bend of similar radii of curvature.

Due to the superior performance of the deep-etched bend, the last chapter investigated the best approach of combining straight shallow-etched waveguides with deep-etched bends to take advantage of the lower loss. Methods to lower the loss from the transition between the shallow-etched and deep-etched waveguides were investigated, such as changing the waveguide width, changing the etch depth, introducing a waveguide taper, and only making the waveguide deep-etched on the outside. The analysis determined the best methods to minimise the overall loss and examples of optimised bends implementing the methods were shown.

The results of the analysis should allow low loss small radii ridge waveguide bends to be reliably fabricated. It was aimed to experimentally verify the findings of this thesis by fabricating and testing a variety of 180° ridge waveguide bends that were simulated in this thesis. The curved waveguide devices were designed using the program PICDraw which is used to design complex integrated photonic structures by the IPG in Tyndall. Examples of bends designed using this program are shown in Figure 7.1. Unfortunately, due to delays and access restrictions caused by the COVID-19 epidemic, it was not possible to test the

devices in the timeframe of this masters programme. It is therefore hoped that these results will be verified at some point in the future.

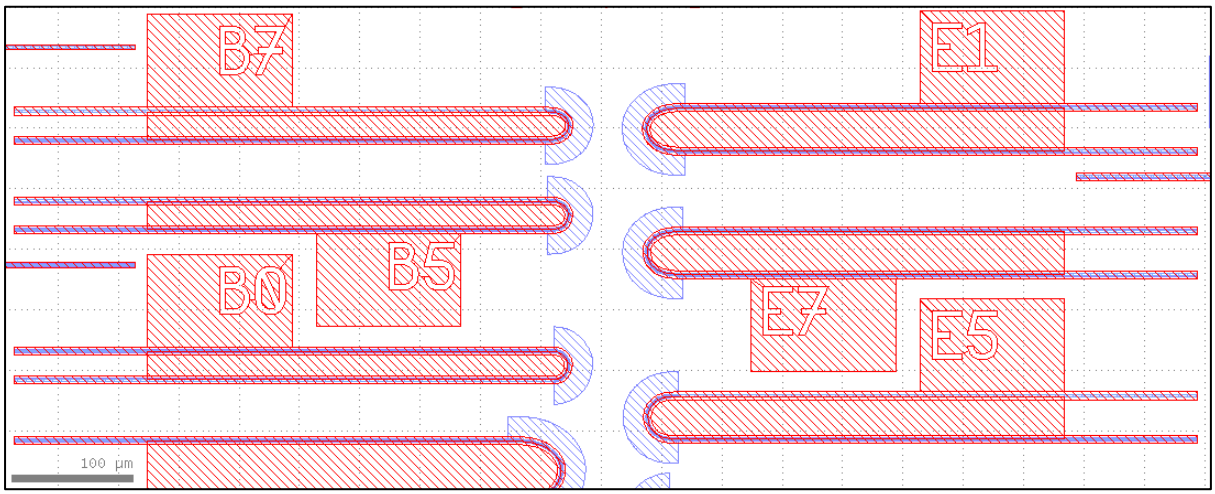

Figure 7.1: PIC waveguide bends designed using PICDraw.

Following on from this thesis, future work could involve a number of actions. Firstly, the developed 3D-SV-FD-BPM could be implemented into PICDraw which currently only contains a 2D BPM tool that does not support waveguide bends. This would allow greater accuracy for simulation of proposed photonic device designs, especially in the case of the deep-etched ridge waveguides. Secondly, the accuracy of the numerical simulations could be increased. This could be done by implementing a time domain beam propagation method (TD-BPM) [28], which would better analyse the effect of reflections along the propagation direction, at the cost of longer computation time. Derivatives in the wave equations could also be better approximated by using a more accurate higher order finite difference scheme, again at the cost of longer computation time [55]. With regard to waveguide bends, it was recently shown that varying the width of a waveguide over a non-constant curvature bend can lead to lower loss [56]. Making a bend of this type with the deep-etched ridge waveguides analysed in this thesis may improve the curved waveguide loss, as the waveguide width was shown to influence the excitations of higher order modes in the bend.

References

[1] C. Seo, Y. J. Sim: Optical bent rib waveguide with reduced transition losses*, IEEE Transactions on Magnetics,* vol. 32, pp. 930-933, 1996.

[2] T. Kitoh, N. Takato, M. Yasu, M. Kawachi: Bending loss reduction in silica-based waveguides by using lateral offsets*, Journal of Lightwave Technology,* vol. 13, pp. 555-562, 1995.

[3] Y. Wangqing, D. C. Hall: A general scaling rule for matched waveguide bends*, Journal of Lightwave Technology,* vol. 29, pp. 3786-3796, 2011.

[4] J. Ballato, P Dragic: Glass: The Carrier of Light – A Brief History of Optical Fiber*, Applied Glass Science,* vol. 7, pp. 413-422, 2016.

[5] B. Saleh, M. Teich, *Fundamentals of Photonics,* pp. 10, Wiley, 2007.

[6] K. Okamoto, *Fundamentals of Optical Waveguides,* pp. 2-7, Elsevier, 2006.

[7] F. Goos, H. Hänchen: *Ein neuer und fundamentaler Versuch zur Totalreflexion,* 1947.

[8] M. Born, E. Wolf, *Principles of Optics, pp. 65,* Pergamon Press, 1970.

[9] K. Kawano, T. Kitoh, *Introduction to Optical Waveguide Analysis,* pp. 1-20, Wiley, 2001.

[10] S. Selvaraja, P. Sethi: Review on Optical Waveguides, *Emerging Waveguide Technology*, Chapter 6, IntechOpen, 2018.

[11] L. Coldren, S. Corzine, M. Masanovic, *Diode Lasers and Photonic Integrated Circuits*, pp. 13-20, Wiley, 2012.

[12] C. Doerr, K. Okamoto, *Optical Fiber Telecommunications*, pp. 269-341, Academic Press, 2008.

[13] K. Worhoff, et al.: Silicon Oxynitride based photonics, Conference: *Transparent Optical Networks,* 2008.

[14] P. Kozma, F. Kehl, E. Ehrentreich-Förster, C. Stamm, F. Bier: Integrated planar optical waveguide interferometer biosensors: A comparative review, *Biosensors and Bioelectronics*, vol. 58, pp. 287-307, 2014.

[15] R. Steenbergen, *Everything You Always Wanted to Know About Optical Networking – But Were Afraid to Ask,* North American Network Operators' Group meeting 57, 2013.

[16] I. Chremmos, O. Schwelb, N. Uzunoglu, *Photonic Microresonator Research and Applications,* Springer Series in Optical Sciences, 2010.

[17] J. Yang, et al.: Characteristics of optical bandpass filters employing series-cascaded double-ring resonators, *Optics Communications,* vol. 228, pp. 91-98, 2003.

[18] A. Ramachandran: A universal biosensing platform based on optical micro-ring resonators, *Biosensors and Bioelectronics,* vol. 23, pp. 939-944, 2008.

[19] K. Kawano, T. Kitoh, *Introduction to Optical Waveguide Analysis,* pp. 21, Wiley, 2001.

[20] E. A. Marcatili: Dielectric rectangular waveguide and directional coupler for integrated optics, *Bell Syst. Tech. J.,* vol. 48, pp. 2071-2102, 1969.

[21] K. Okamoto, *Fundamentals of Optical Waveguides,* pp. 261-328, Elsevier, 2006.

[22] K. Kawano, T. Kitoh, *Introduction to Optical Waveguide Analysis,* pp. 117-164, Wiley, 2001.

[23] L. Thylén: The beam propagation method: An analysis of its applicability*, Opt. Quantum Electron,* vol. 15, pp. 433-439, 1983.

[24] Y. Chung, N. Dagli: Assessment of finite difference beam propagation*, IEEE J. Quantum Electron,* vol. 26, pp. 1335-1339, 1990.

[25] Y. Huang, C. L. Xu: Simulation of Three-Dimensional Optical Waveguides by Full-Vector Beam Propagation Method*, IEEE J. Quantum Electron,* vol. 26, pp. 1335-1339, 1990.

[26] G. L. Pedrola, *Beam Propagation Method for Design of Optical Waveguide Devices,* pp. 30, Wiley, 2016.

[27] K. Okamoto, *Fundamentals of Optical Waveguides,* pp. 316, Elsevier, 2006.

[28] M. J. Shibayama, M. Muraki, J. Yamauchi, H. Nakano: Comparative study of several time-domain methods for optical waveguide analysis*, Journal of Lightwave Technology,* vol. 23, pp. 2285-2293, 2005.

[29] K. Kawano, T. Kitoh, *Introduction to Optical Waveguide Analysis,* pp. 6, Wiley, 2001.

[30] C. Sanderson, R. Curtin: Armadillo: a template-based C++ library for linear algebra*, Journal of Open Source Software,* vol. 1, pp. 26, 2016.

[31] C. Sanderson, R. Curtin: A user-friendly hybrid sparse matrix class in C++*, Lecture Notes in Computer Science (LCNS),* vol. 10931, pp. 422-430, 2018.

[32] K. Kawano, T. Kitoh, *Introduction to Optical Waveguide Analysis,* pp. 160, Wiley, 2001.

[33] A. Cheng, D. T. Cheng: Heritage and early history of the boundary element method*, Engineering Analysis with Boundary Elements,* vol. 29, pp. 268-302, 2005.

[34] D. J. Griffiths*, Introduction to Electrodynamics,* pp. 344, Cambridge University Press, 2013.

[35] O. Schenk, K. Gartner: Solving unsymmetric sparse systems of linear equations with PARDISO, *J. of Future Generation Computer Systems,* vol. 20, pp. 475-487, 2004.

[36] G. R. Hadley: Transparent boundary condition for beam propagation, *Opt. Lett,* vol. 17, pp. 624-626, 1992.

[37] J. P. Bérenger: A perfectly matched layer for the absorption of electromagnetic waves, *Journal of Computational Physics,* vol. 114, pp. 185-200, 1994.

[38] B. Saleh, M. Teich, *Fundamentals of Photonics,* pp. 77, Wiley, 2007.

[39] W. P. Huang, C. L. Xu, W. Lui, K. Yokoyama: The perfectly matched layer (PML) boundary condition for the beam propagation method, *IEEE Photonics Technology Letters,* vol. 8, pp. 649-651, 1996.

[40] G. L. Pedrola, *Beam Propagation Method for Design of Optical Waveguide Devices,* pp. 42-44, Wiley, 2016.

[41] G. R. Hadley: Wide-angle beam propagation using Padé approximant operators, *Opt. Lett.,* vol. 17, pp. 1426-1428, 1992.

[42] G. R. Hadley: Multistep method for wide-angle beam propagation, *Opt. Lett.*, vol. 17, pp. 1743-1745, 1992.

[43] J. Yamauchi: Improved multistep method for wide-angle beam propagation, *IEEE Photonics Technology Letters,* vol. 8, pp. 1361-1363, 1996.

[44] G. L. Pedrola, *Beam Propagation Method for Design of Optical Waveguide Devices,* pp. 139-140, Wiley, 2016.

[45] G. L. Pedrola, *Beam Propagation Method for Design of Optical Waveguide Devices,* pp. 233, Wiley, 2016.

[46] D. Kulyabov, A. Korolkova: Maxwell's Equations in Arbitrary Coordinate System, Bulletin of People's Friendship University of Russia*,* Series Mathematics, no. 1, pp. 96-106, 2012.

[47] M. Heiblum, J. H. Harris: Analysis of Curved Optical Waveguides by conformal transformation, *IEEE Journal of Quantum Electronics,* vol. QE-11, pp. 75-83, 1975.

[48] R. V. Churchill, J. W. Brown, R. F. Verhey, *Complex Variables with Applications,* McGraw-Hill Book Co., 1974.

[49] A. Nesterov, U. Troppenz: A Plane-Wave Boundary Method for Analysis of Bent Optical Waveguides, *Journal of Lightwave Technology,* vol.21, No. 10, 2003.

[50] D. J. Struik, *Lectures on Classic Differential Geometry,* Dover, 1988.

[51] R. Sheehan, "The Design of Curved Optical Waveguides : analytical and numerical analysis", PhD thesis, 2013.

[52] R. Sheehan, F. Peters: Bends in the plane with variable curvature, *Irish Math Society Bulletin,* no. 78, pp. 61-80, 2016.

[53] M. Abramowitz, I. A. Stegun, *Handbook of Mathematical Functions with Formulas, Graphs, and Mathematical Tables,* National Bureau of Standards, 1965.

[54] E. C. Pennings, G. H. Manhoudt, M. K. Smit: Low-loss bends in planar optical ridge waveguides, *Electronics Letters,* no. 16, pp. 998-999, 1988.

[55] L. Sun, G. L. Yip: Modified finite-difference beam-propagation method based on the Douglas scheme, *Opt. Lett,* vol. 16, pp. 1229-1231, 1993.

[56] J. H. Song, et al.: Low-loss waveguide bends by advanced shape for photonic integrated circuits, *Journal of Lightwave Technology,* vol. 38, pp. 3273-3279, 2020.